

THE UNIVERSITY OF HULL

Iron Sulfide as a Sustainable Catalyst for the Selective Hydrogen
Transfer Reduction for the Synthesis of Fine Chemicals

being a thesis submitted for the degree of PhD

in the University of Hull

by

Jamie P. Southouse MChem (Hons)

September 2021

Abstract

Platinum group metals have been the most widely applied metals for hydrogenation catalysts used in the synthesis of fine chemicals; this has been due to their high catalytic activity and ease of preparation. However, platinum group metal-based catalysts are often overly active in the synthesis of complex molecules with multiple susceptible groups present. The aim of the work in this thesis was to synthesise metal sulfide catalysts for the selective hydrogenation of nitroarenes that are free from platinum group metals.

In this work, a simple solvothermal synthesis method was developed to produce a wide range of first row transition metal sulfides. By simply changing the precursor metal salt, the metal sulfide could be precipitated. Additional modifications to the product sulfides were achieved by changing the temperature and capping agent, resulting in a synthesis method by which composition and crystal structure could be modified to produce a range of potential products. Optimisation test work was carried out on the synthesis of FeS₂ pyrite and its characterisation by powder x-ray diffraction (PXRD) shows a single-phase product under the optimum conditions. Transmission electron microscopy (TEM) shows that the particles obtained are elongated with a width half that of their length which is between *ca.* 3-5 nm. The catalytic activity of these metal sulfides was characterised by their application in a heterogeneous hydrogen transfer reduction of substituted nitroarenes for the synthesis of substituted anilines. FeS₂ pyrite showed excellent catalytic activity towards the hydrogen transfer reduction of nitroarenes. Reaction conditions for the hydrogen transfer reaction were optimised before testing other potential sulfide catalysts. NiS₂ pyrite showed no catalytic activity when applied to the hydrogen transfer reaction. This was theorised to be due to the relatively small energy difference in Fe oxidation states allowing for chemical reactions to occur at low energy on the catalyst not present for Ni. FeS₂ pyrite was applied to other substituted nitroarenes to determine the broad applicability of the catalyst. FeS₂ pyrite maintained a high level of conversion of the

substrate material with complete selectivity towards the aniline product. Other hydrogen donors are also explored.

Acknowledgements

I would like to thank my supervisors for their support. Alex for showing me how to work under stress and pushing me to be better. Grazia for being the guidance I needed, helping me to develop into a well-rounded researcher, giving me the knowledge and advice on how best to progress my own work. Also, thanks Grazia for all the chats and laughs along the way.

I would like to thank the University of Hull for awarding my scholarship and funding my studies, providing me with the lab space to develop my work into something I can be proud of.

Thank you to Charlotte for the use of the GC and the endless chat in C315, whilst providing constant support in helping maintain the GC without which I simply wouldn't have been able to work. The constant strange chemistry and weird chemicals made it eye opening to work in the lab.

Thanks to the students I managed showing me never to underestimate a person.

Thanks to the guys in the office, Martin for being an ongoing support case, mentoring me and listening to my endless complaints, even if I did get the nickname of "Billy". The others for their love of cooking implements, providing much needed laughs throughout the process.

Abbreviations

ACN	Acrylonitrile
AN	Aniline
ATR	Attenuated Total Reflection
DCM	Dichloromethane
DMSO	Dimethyl sulfoxide
DRS	Diffuse Reflectance Spectroscopy
EDX	Energy Dispersed X-Ray Spectroscopy
EG	Ethylene Glycol
FAME	Fatty Acid Methyl Esters
FID	Flame Ionisation Detector
FTIR	Fourier Transform Infrared Spectroscopy
GC	Gas Chromatography
HAADF	High Angle Annular Dark Field
HDO	Hydrodeoxygenation
HRTEM	High Resolution Transmission Electron Microscopy
IR	Infrared
IS	Internal Standard
LOHC	Liquid Organic Hydrogen Carrier
MOF	Metal Organic Framework
p-CAN	4-Chloroaniline
p-CNB	4-Chloronitrobenzene
PGM	Platinum Group Metals
PXRD	Powder X-Ray Diffraction
SEM	Scanning Electron Microscopy
SS UVVIS	Solid State Ultraviolet-Visible Near Infrared
NIR	spectroscopy
TEM	Transmission Electron Microscopy
UVVIS	Ultraviolet-Visible spectroscopy
UVVIS NIR	Ultraviolet-Visible Near Infrared Spectroscopy

Table of Contents

Abstract	3
Acknowledgements	5
Chapter 1 Introduction and Literature Review	17
1.1 Sustainable chemistry and catalysis.....	17
1.2 Selective hydrogenation of nitroarenes.....	20
1.2.1 Hydrogenation of functionalised nitroarenes.....	20
1.2.2 The mechanism of nitrobenzene hydrogenation	21
1.3 Metallic catalysts for nitrobenzene hydrogenation.....	23
1.3.1 Classes of metallic catalysts	23
1.3.2 Preparation of metallic catalysts	28
1.4 Metal compound catalysts for nitrobenzene hydrogenation	32
1.4.1 Ceramic catalysts.....	32
1.4.2 Metal chalcogenide catalysts	35
1.4.3 Metal Borides, Nitrides and Phosphides.....	41
1.5 Hydrogenation Methods.....	42
1.5.1 Activation of Molecular Hydrogen	43
1.5.2 Transfer Hydrogenation.....	45
1.6 Chemical reactors for selective hydrogenation of nitrobenzenes	53
1.6.1 Batch Reactors	54
1.6.2 Continuous Microreactors	56
1.7 Aims.....	61
Chapter 2 Experimental Techniques	64
2.1 Material synthesis	64
2.1.1 Metal sulfide synthesis	67
2.2 Electromagnetic radiation characterisation	68
2.2.1 Crystallography	68
2.2.1.5 X-ray diffraction.....	76
2.2.2 Fourier Transformed Infra-Red Spectroscopy (FTIR)	84
2.2.3 Solid State Ultraviolet Visible Near Infra-Red Spectroscopy (UVVIS NIR)	86
2.2.4 Transmission Electron Microscopy (TEM) with Energy-Dispersive X-ray Spectroscopy (EDX) and Electron Diffraction.....	91
2.3 Catalyst Testing	94

2.3.1 Selective hydrogenation substituted nitrobenzenes.....	94
2.3.2 Gas Chromatography (GC).....	97
Chapter 3 Synthesis and characterisation of metal sulfide materials	104
3.1 Experimental	106
3.1.1 Materials	106
3.1.2 Preparation of FeS ₂ pyrite and optimisation synthesis	107
3.1.3 PXRD analysis	107
3.1.4 TEM and EDX analysis	107
3.2 Synthesis of iron sulfides	108
3.3 Optimisation of iron sulfide synthesis	109
3.3.1 Temperature of FeS ₂ synthesis.....	109
3.3.2 Sulfur content within the reaction	116
3.3.3 Reaction capping agent.....	120
3.3.4 Effect of solvent on the synthesis of FeS ₂	127
3.3.5 Further characterisation of optimum FeS ₂ synthesis.....	131
3.4 Substitution of iron within the pyrite structure	136
3.4.1 Nickel and cobalt.....	137
3.4.2 Copper and manganese.....	140
3.4.3 Vanadium, molybdenum and chromium	144
3.5 Conclusions	147
Chapter 4 Development and Optimisation of the FeS₂ pyrite catalytic hydrogen transfer reduction system	151
4.1 Experimental	153
4.1.1 Materials	153
4.1.2 Hydrogenation procedure	153
4.1.3 FTIR analysis	154
4.1.4 PXRD analysis	154
4.1.5 TEM and EDX analyses	155
4.2 Results and Discussion	155
4.2.1 Parameters for the optimisation of nitrobenzene hydrogenation	155
4.2.2 Mechanism of FeS ₂ heterogenous hydrogenation.....	180
4.3 Conclusions	188
Chapter 5 FeS₂ Catalytic Hydrogen Transfer Reduction System - Further Development	191
5.1 Experimental	192

5.1.1 Materials	192
5.1.2 Hydrogenation procedure	192
5.2 Results and Discussion	193
5.2.1 Effect of the substituent in the substrate.....	193
5.2.2 Screening of other potential hydrogen donors	202
5.3 Conclusions	206
Chapter 6 Conclusions and Future Work.....	209
6.1 Conclusions	209
6.1.1 Metal sulfide Synthesis.....	209
6.1.2 Optimisation of the FeS ₂ catalytic system.....	210
6.1.3 FeS ₂ catalytic system further development.....	211
6.2 Future Work	212
Appendices	214
References	224
Project Outputs.....	233
Research Articles.....	233
Oral Presentations.....	233
Poster Presentations.....	233

Table of Figures

Figure 1. 1: Approximate mass of chemicals produced in various chemical sectors with the use of catalysts in each sector increasing with specificity of the chemical application. ²	18
Figure 1. 2: Chemical structures of a) methyl orange and b) benzocaine, which are both synthesised from aryl amine intermediates obtained from nitroarene hydrogenation.	21
Figure 1. 3: Proposed reaction scheme in the synthesis of aniline from nitrobenzene, via a direct route and an indirect route. ^{16, 18}	22
Figure 1. 4: Schematic demonstration of the three general categories of metallic catalysts, monometallic, intermetallic and alloys.	23
Figure 1. 5: The relative chemisorption free energies for a hydrogen monolayer formation on various common transition metals used in hydrogenation catalysts, reproduced from Garcia-Garcia et al. using data produced by Nørskov et al. ^{22, 23}	24
Figure 1. 6: Schematic image of the raft formation in an alloy type catalyst particle under reduction conditions.	27
Figure 1. 7: Schematic diagram of the chemical reduction method for preparing a metallic catalyst from a metal precursor.....	28
Figure 1. 8: Schematic diagram of the thermal decomposition method in preparing a metallic catalyst from a metal precursor.....	30
Figure 1. 9: Schematic diagram of the ceramic synthesis method used in synthesising a range of solid-state materials.	33
Figure 1. 10: Schematic diagram of the solid-state method in synthesising metal chalcogenides via a) gas flow sulfurization and b) solid state reaction between metal oxide and elemental chalcogenide.....	36
Figure 1. 11: Common catalyst degradation/deactivation pathways observed in liquid phase catalysis.	39
Figure 1. 12: Schematic diagram of the hydrogen adsorption, dissociation and diffusion into the bulk on a noble metal (Pd) catalyst surface.	43
Figure 1. 13: Schematic mechanism of the dehydration of propan-2-ol to acetone with the hydrogen atoms becoming adsorbed to a catalyst surface.	46
Figure 1. 14: Schematic mechanism of formic acid dehydration to carbon dioxide, with the hydrogen atoms being adsorbed to a catalyst surface.	46
Figure 1. 15: Schematic mechanism of hydrazine decomposition over a catalyst surface with hydrogen atoms being adsorbed to the catalyst surface and nitrogen being the primary by product of the reaction. ¹³	48
Figure 1. 16: Reaction scheme for the spontaneous formation of the hydrazone product by a reaction between a carbonyl and hydrazine. R = CH ₃ , H, C _x H _{2x+1}	50
Figure 1. 17: Reaction scheme of tetralin (1,2,3,4-tetrahydronaphthalene) to naphthalene over a catalyst surface with hydrogen atoms becoming adsorbed to the catalyst. ^{160, 164}	51
Figure 1. 18: a) image of a Radleys 12 sample carousel batch reactor, b) schematic profile view of a carousel batch reactor, c) plain view of a carousel batch reactor.....	55
Figure 1. 19: Schematic diagram of the main components of a capillary microreactor.	57
Figure 1. 20: Schematic diagram of the process by which capillary channels may be coated and catalyst particles deposited on the capillary walls, reproduced from work carried out by N. Cherkasov. ^{186, 190}	57
Figure 1. 21: a) SEM image of the quartz capillary tube prior to catalyst impregnation, b) SEM image of the catalyst impregnated capillary wall showing a wall coating depth of 1.7	

µm, c) Elemental mapping of 1.21c, with Pd atoms shown in green, Zr atom shown in red and Si atoms shown in blue, reproduced from work carried out by J. Li et al.. ¹⁸⁷	58
Figure 1. 22: Schematic diagram of a thin film microreactor.. ¹⁹³	59
Figure 1. 23: Schematic diagram of the main components of a packed bed microreactor.	60
Figure 2. 1: Schematic of a solvothermal autoclave reactor.	66
Figure 2. 2: Image of Parr instrument company Teflon lined stainless steel autoclave reactor.	67
Figure 2. 3: Representation of a unit cell showing axes (x, y, z), unit cell parameters (a, b, c) and angles (α , β , γ).	71
Figure 2. 4: Examples of primitive (P), body-centred (I), all face-centred (F) and face centred (A shown) unit cell lattice types.	73
Figure 2. 5: Crystal structure of NaCl, with (111) lattice plane shown in pink. The purple spheres represent sodium cations, and the green spheres represent chlorine anions.	76
Figure 2. 6: The graphical illustration of how phase shift relates between two sine waves of identical amplitude.. ²⁰³	77
Figure 2. 7: Illustration of how the geometry of ray reflection is used in the derivation of the simplified Bragg equation. With the incoming and outgoing x-rays being reflected through angle 2θ between two parallel lattice planes, M and N, separated by lattice spacing d.. ²⁰³	79
Figure 2. 8: Cross section of a powder x-ray diffractometer with the components labelled...	81
Figure 2. 9: a) Flat surfaced sample holder for PXRD analysis with items labelled. b) The template is locked into the sample holder. c) The template filled with sample. d) baseplate is then connected to the template. e) Sample holder is then flipped over and e) sample is released to reveal a flat surface.....	83
Figure 2. 10: PANalytical Empyrean X-Ray diffractometer with key components labelled..	84
Figure 2. 11: IR active CO bond vibrating at its fundamental vibration mode when irradiated by infrared radiation, $\nu = 1720 \text{ cm}^{-1}$	85
Figure 2. 12: schematic of attenuated total reflectance FTIR with evanescent wave.	86
Figure 2. 13: Schematic of the diffuse reflection mechanism on a rough surface.....	87
Figure 2. 14: Schematic of the UVVIS NIR spectrometer with key components labelled.	88
Figure 2. 15: interior of UVVIS NIR instrument with key components labelled.....	89
Figure 2. 16: Sample with BaSO ₄ diluent prior to grinding and preparing for UVVIS NIR analysis.	90
Figure 2. 17: Schematic of a TEM instrument in both imaging and diffraction modes.	92
Figure 2. 18: Schematic of the operating principle of Energy Dispersed X-ray (EDX) spectroscopy.	93
Figure 2. 19: Reaction scheme of the selective hydrogenation of p-chloronitrobenzene (p-CNB) to p-chloroaniline (p-CAN) without forming aniline (AN) using hydrazine (N ₂ H ₄) as a hydrogen donor.	94
Figure 2. 20: Schematic of the apparatus used for the selective hydrogenation reactions in this work. The circles containing “X” represents taps which can be used to shut off and isolate parts of the reactor. The circles contain “L” represent multi-directional taps which can be used to connect the reactor to the left (N ₂ supply) or the right (vacuum) hand sides of the gas manifold or can be closed off from both sides.	96
Figure 2. 21: A schematic diagram of the gas chromatogram with gas bottle and attached computer.	98

Figure 2. 22: a) The Varian 430 gas chromatograph that was used to complete the analysis. b) The Varian CP-8400 autosampler with sample vials placed in the carrousel. c) The oven with Stabilwax® capillary column (Restek) attached to column hanger.....	99
Figure 2. 23: Column oven temperature progress against time for the GC method. $T_0=70\text{ }^{\circ}\text{C}$, $T_2=70\text{ }^{\circ}\text{C}$, $T_{11.17}=180\text{ }^{\circ}\text{C}$, $T_{15}=220\text{ }^{\circ}\text{C}$	101
Figure 3. 1: Crystal structures of a) FeS (NiAs type, $p6_2c$) ^{220, 221} and b) MoS ₂ (R3mH), Fe is at the centre of bronze polyhedra, Mo is at the centre of purple polyhedral. Yellow spheres represent sulfur. ²²²	105
Figure 3. 2: Crystal structure of FeS ₂ pyrite, space group Pa3. ^{222, 223}	106
Figure 3. 3: PXRD of FeS ₂ synthesised at 150 °C, with peaks indexed and amorphous sulfur region is highlighted. ²²³	109
Figure 3. 4: TEM images of product obtained using a lower temperature, a) low magnification image of the sulfur aggregates with hue dispersed between them, b) high magnification image of the nanoparticles dispersed between the sulfur aggregates.	110
Figure 3. 5: PXRD of FeS ₂ synthesised at 160 °C with peaks indexed. ²²³	111
Figure 3. 6: Proposed reaction scheme of oleylamine reacting with elemental sulfur to produce reactive sulfur species.	111
Figure 3. 7: Reaction scheme of FeS ₂ synthesis within the solvothermal reaction vessel. ⁷⁴	112
Figure 3. 8: PXRD pattern obtained of powder product from iron sulfide synthesis carried out at 180 °C for 12 hours, with peaks belonging to FeS ₂ indexed in blue and peaks belonging to Fe ₃ S ₄ indexed in red. ^{223, 225}	112
Figure 3. 9: Disproportionation reaction between Fe (II) ions and sulfur to produce FeS and FeS ₂	113
Figure 3. 10: Crystal structure of Fe ₃ S ₄ , greigite, space group Fd3mz. ^{222, 225}	113
Figure 3. 11: PXRD patterns of iron sulfide synthesis carried out at a) 160 °C and b) 180 °C for 48 hour reaction times, Fe ₃ S ₄ peaks indexed in red and FeS ₂ peaks indexed in blue, according to their respective models. ^{223, 225}	114
Figure 3. 12: TEM images of a) 160 °C reaction FeS ₂ product at a lower magnification, b) 160 °C reaction FeS ₂ product at higher magnification and particle diameter measured, c) 180 °C reaction product showing fern like entity common in the 180 °C sample, d) 180 °C particles of FeS ₂ with particle diameter measured.....	115
Figure 3. 13: PXRD patterns obtained from iron sulfide synthesis reaction products, a) 15 mmol sulfur, b) 7.5 mmol sulfur. With peaks corresponding to Fe ₃ S ₄ indexed in red and FeS ₂ indexed in blue. ^{223, 225}	117
Figure 3. 14: PXRD pattern obtained from iron sulfide synthesis reaction using 3.75 mmol sulfur, with peaks corresponding to Fe ₃ S ₄ indexed in red, FeS ₂ indexed in blue and unknown peaks identified with green. ²²⁵	118
Figure 3. 15: PXRD patterns obtained from iron sulfide synthesis using a) 2.5 mmol and b) 1.75 mmol of sulfur. A tentative assignment of peaks sees Fe ₃ S ₄ in red, unreacted iron (II) acetate in purple and peaks of possible iron sulfides highlighted in green.	119
Figure 3. 16: Crystal structures of a) FeS, space group Pnma and b) FeS, space group P6 ₂ c. ^{222, 227}	120
Figure 3. 17: Structures of a) oleylamine and b) dodecane thiol.	121
Figure 3. 18: PXRD of material obtained from reaction in absence of oleylamine.....	121

Figure 3. 19: TEM images of FeS ₂ nanoparticles prepared in the absence of oleylamine. a) aggregates of particles at low magnification, b) higher magnification of a large aggregate, c) high magnification of particles at the edge of an aggregate.	123
Figure 3. 20: PXRD pattern of FeS ₂ marcasite obtained by reaction with dodecane thiol capping agent with peaks indexed. ²²⁹	124
Figure 3. 21: TEM images of FeS ₂ marcasite obtained from reaction with dodecane thiol capping agent, a) region of low magnification showing 2 distinct morphologies with globular tubes (circled in red) and smaller distinct particles (circled in blue), b) higher magnification image of the particulate region, c) higher magnification of the globular region with particles visible within the globular clusters.	125
Figure 3. 22: EDX spectrographs of a) oleylamine capped FeS ₂ pyrite and b) dodecane thiol capped FeS ₂ marcasite.....	126
Figure 3. 23: PXRD pattern of material obtained after dodecane thiol capped reaction product was left for 2 weeks at 7 °C. Peaks corresponding to FeS ₂ pyrite indexed in blue and peaks corresponding to FeS ₂ marcasite indexed in red. ^{223, 229}	126
Figure 3. 24: Crystal structures of a) FeS ₂ pyrite, space group Pa3 and b) FeS ₂ marcasite, space group Pnnm. ^{222, 223, 229}	127
Figure 3. 25: PXRD patterns obtained from iron sulfide synthesis in different solvents, a) ethanol, b) ethylene glycol and c) water. FeS ₂ pyrite peaks indexed in blue and unknown sulfide peaks indexed in red.	131
Figure 3. 26: a) HAADF Scanning TEM image of nanoparticle dispersion. b) High resolution image of some nanoparticles showing their elongated shape. c) Selected Area Electron Diffraction (SAED) taken on a large agglomerate of FeS ₂ nanoparticles with diffraction rings indexed. d) EDS spectrum of sulfur and iron with their relative atomic abundancies expressed at a percentage.	132
Figure 3. 27: a) HAADF Scanning TEM of large aggregate of nanoparticles. b) Fe mapped	133
Figure 3. 28: a) High Resolution TEM image of FeS ₂ nanoparticles; b) Fourier Transform (FT) of the HRTEM image in a); c) Reconstruction of the FeS ₂ nanoparticles in a) using the FT in b). Reflections circled in colours in b) correspond to nanoparticles identified on c) with the same colour.	134
Figure 3. 29: FTIR spectrum of FeS ₂ catalyst prior to use in selective hydrogenation reactions.....	135
Figure 3. 30: a) SS-UV-VIS-NIR spectrum using wide wavelength scan from 200 nm to 2400 nm, b) SS-UV-VIS-NIR spectrum of the region corresponding to the band gap transition in FeS ₂	136
Figure 3. 31: Crystal structures of a) iron pyrite (FeS ₂) b) nickel pyrite (NiS ₂) and c) cobalt pyrite (CoS ₂), all structures are space group Pa3. ^{222, 223, 236}	137
Figure 3. 32: PXRD pattern obtained from cobalt sulfide synthesis, high background due to fluoresce of cobalt under Cu K _{α1} radiation.....	138
Figure 3. 33: PXRD pattern obtained from NiS ₂ synthesis. Peaks corresponding to Pa3 NiS ₂ indexed according to model. ²³⁶	139
Figure 3. 34: HRTEM images of a) NiS ₂ aggregates, b) dispersed NiS ₂ particles, particles have been ringed in red to aid in visibility.	139

Figure 3. 35: PXRD pattern obtained from copper sulfide synthesis with peaks corresponding to CuS indexed in blue, Cu ₂ S indexed in red and unknown peaks indicated by purple triangles. ^{64, 243}	141
Figure 3. 36: Crystal structures of obtained copper sulfides from CuS ₂ synthesis, a) CuS, space group P6 ₃ mmc, b) Cu ₂ S, space group P6 ₃ mmc, c) Cu ₇ S ₄ , space group pnma. ^{222, 244-246}	142
Figure 3. 37: PXRD pattern of material obtained from manganese sulfide synthesis, peaks corresponding to α -MnS (Fm3m) indexed in red and peaks corresponding to γ -MnS (P6 ₃ mc) indexed in blue. ^{75, 76}	143
Figure 3. 38: Crystal structures of a) α -MnS (Fm3m) and b) γ -MnS (P6 ₃ mc). ^{247, 248}	143
Figure 3. 39: PXRD pattern obtained from chromium sulfide synthesis.	144
Figure 3. 40: Crystal structures of the metal precursors a) sodium metavanadate, space group P2 ₁ mn and b) sodium molybdenum oxide, space group P2 ₁ c. Error! Bookmark not defined.	
Figure 3. 41: PXRD patterns obtained for a) vanadium sulfide synthesis and b) molybdenum sulfide synthesis.	146
Figure 4. 1: Decomposition of hydrazine to nitrogen and hydrogen in the presence of a heterogeneous catalyst.	151
Figure 4. 2: Reaction profile for the test reactions carried out. 4-CNB (blue graph) and increasing concentration for 4-CAN (orange graph) in time, during the FeS ₂ catalysed hydride transfer hydrogenation in ethanol, averaged across 3 test reactions.	157
Figure 4. 3: a) 1 st order kinetic plot for chloronitrobenzene consumption against time, b) 2 nd order kinetic plot for chloronitrobenzene consumption against time, using data shown in figure 4.48.	158
Figure 4. 4: graphical representation of 4-CNB binding to the FeS ₂ catalyst surface at two different angles 90° and 0/180°.	159
Figure 4. 5: Conversion percentages for hydrogenation reactions of 4-CNB at different reaction time points, using differing amounts of FeS ₂ catalyst.	161
Figure 4. 6: Conversion of CNB after 2 hours against catalyst loading.	162
Figure 4. 7: Normalised rate of reaction against catalyst mass.	163
Figure 4. 8: Normalised rate plotted against dielectric constant for the seven solvents trialled in the solvent study.	165
Figure 4. 9: Normalised rate against dielectric constant for the five remaining solvents after hexane and dimethylsulfoxide were removed.	166
Figure 4. 10: Conversion of 4-CNB for seven solvents against their associated dielectric constants.	167
Figure 4. 11: instantaneous conversion in the absence of a FeS ₂ catalyst for seven solvents against their associated dielectric constant.	168
Figure 4. 12: Conversion of 4-CNB in the absence of a catalyst plotted against the pK _a of the seven solvents tested, with areas corresponding to solvent classification highlighted.	169
Figure 4. 13: Normalised rate of reaction for the hydrogen transfer hydrogenation of 4-CNB against the pK _a of the reaction solvent.	170
Figure 4. 14: Conversion of 4-CNB with 25 mg catalyst (blue, left side y-axis) and without catalyst (orange, right side y-axis) in a two hour reaction timeframe against their respective pK _a (methanol left, butan-1-ol right).	171

Figure 4. 15: the reaction rate of 4-CAN synthesis in hexane (yellow) and ethanol (green) using various catalyst loadings.	173
Figure 4. 16: Conversion of 4-CNB in two hours against the catalyst loading for reactions carried out in hexane (yellow) and ethanol (green).	174
Figure 4. 17: Graphical depiction of how temperature (blue – low temperature, green – medium temperature, red – high temperature) affects the number of molecules with energy above the activation energy (purple region).	175
Figure 4. 18: Graphical representation of the effect of a catalyst on the activation energy of a given reaction, showing an uncatalyzed reaction pathway in red and a catalysed pathway in purple.	176
Figure 4. 19: Arrhenius plot $\ln(\text{rate})$ against $1/T$, for FeS_2 transfer hydrogenation of 4-chloronitrobenzene using hydrazine as the reducing agent across a temperature range of 25 °C to 80 °C.	177
Figure 4. 20: Variation of hydrazine concentration and its effect on conversion of 4-chloronitrobenzene within a 2 hour time frame.	179
Figure 4. 21: Reaction profiles of 4-CAN concentration for a filtered reaction (blue) and an unfiltered reaction (orange).	181
Figure 4. 22: recyclability of FeS_2 nanoparticles for the hydrogen transfer hydrogenation of 4-chloronitrobenzene, conversion of 4-chloronitrobenzene at 2 hours (blue) and selectivity towards 4-chloroaniline (orange).	182
Figure 4. 23: PXRD pattern of FeS_2 nanoparticle catalyst before and after recycled reactions, with peaks indexed. most intense iron based impurities are identified and overlapped with the patterns to emphasise their absence. ²⁷⁰⁻²⁷²	184
Figure 4. 24: FTIR spectra of FeS_2 catalyst before use (orange) and post reaction (blue). ..	185
Figure 4. 25: Crystal structures of FeS_2 and NiS_2 (pyrites) with the state d-electron configuration for the metals in 2+ oxidation state. ^{222, 223, 273}	186
Figure 4. 26: Reaction profiles obtained for the selective hydrogenation of 4-CNB via a hydrogen transfer reaction using 1 mL of hydrazine monohydrate and a) 25 mg of FeS_2 catalyst, b) 25 mg of NiS_2 catalyst and c) 0 mg of catalyst.	187
Figure 5. 2: Chemical structures of chloronitrobenzenes used in studying the effect of relative position on reaction characteristics.	194
Figure 5. 3: Initial rate of substituted aniline synthesis for ortho, para, meta chloronitrobenzenes plotted against their relative positions. Reaction profile plots shown in appendix 14-16.	195
Figure 5. 4: Resonance stabilised structures of a) 4-chloronitrobenzene (para) and b) 2-chloronitrobenzene (ortho).	196
Figure 5. 5: Resonance displayed by 3-chloronitrobenzene (meta).	196
Figure 5. 6: Initial rate of reaction for various para halogenated nitrobenzenes in a hydrogen transfer reaction over FeS_2 catalyst using hydrazine monohydrate as a reducing agent. Reaction profile plots shown in Appendix 16-19.	199
Figure 5. 7: Resonance structures from the electron withdrawing group in the para position relative to the nitro group.	200
Figure 5. 8: Inductive activation of moderately electron donating halogens in the para position relative to the nitro group.	200

Table of Tables

Table 1.1: Common precursor compounds used in the synthesis of borides, nitrides and phosphides.	41
Table 1.2: Examples of N ₂ H ₄ hydrogen transfer reactions over different catalysts, with respective reaction conditions.....	50
Table 2.1: Boiling point and vapour pressure of commonly used solvents in solvothermal synthesis.	65
Table 2.2: Equivalent improper rotations and inversion axes.	70
Table 2.3: The seven crystal systems.	72
Table 2.4: The fourteen Bravais lattices.....	74
Table 2.5: GC method conditions with the associated set point.....	101
Table 2.6: Concentration of all analyte solutions compared to the internal standard (IS) concentration.....	102
Table 4.1: Solvents studied with their associated dielectric constants and pK _a values.....	165
Table 5.1: Conversion of substrate and selectivity towards the substituted aniline product for reactions carried out using ortho, meta and para substituted chloronitrobenzenes, using hydrazine monohydrate as a reducing agent.....	194
Table 5.2: conversion of substrate and selectivity towards the desired substituted aniline product for hydrogen transfer reactions of various para halogenated nitrobenzenes, using hydrazine monohydrate as a reducing agent.....	198
Table 5.3: Hydrogen donor compounds used in the selective transfer hydrogenation of 4-chloronitrobenzene to 4-chloroaniline, a) 5 mmol addition of a KOH base co-catalyst. Reaction profile plots shown in Appendix 16,20-26.	203

Chapter 1 Introduction and Literature Review

The design of high-performance catalysts considering the environmental impact of the chemical transformations is at the forefront of industrial fine chemical production. This includes the reduction in the use of platinum group metals (PGMs) and reducing the harsh conditions required in these chemical transformations, such as reducing reaction temperatures and pressures.

Recent developments in catalysis have involved using more abundant elements in the synthesis of catalysts with a drive to achieve acceptable reaction performance at under more sustainable and less environmentally impactful conditions. This drive has emphasised a focus on metal oxides and sulfides as potential catalysts for fine chemical transformations.

1.1 Sustainable chemistry and catalysis

Sustainability in the efficient use of materials has become one of the driving forces in chemical synthesis in the 21st century, as our modern conveniences require vast quantities of bulk and fine chemicals, ranging in application such as dyes, agrochemicals and pharmaceuticals. The processes involved in the synthesis of these chemicals require a substantial amount of energy and demand for such chemicals expected to increase in the coming decades, there has been a focus on making these processes more efficient requiring less energy yet keeping up with the increased demand.¹ The primary means of driving this sustainability is the increased use of catalysts and the development of catalysts that do not impact the environment as severely in their synthesis.

The relative use of catalysts generally correlates with a decrease in production of chemicals, with bulk chemicals requiring less catalyst use compared to fine chemicals for a given production volume. This is depicted in shown in Fig. 1.1.

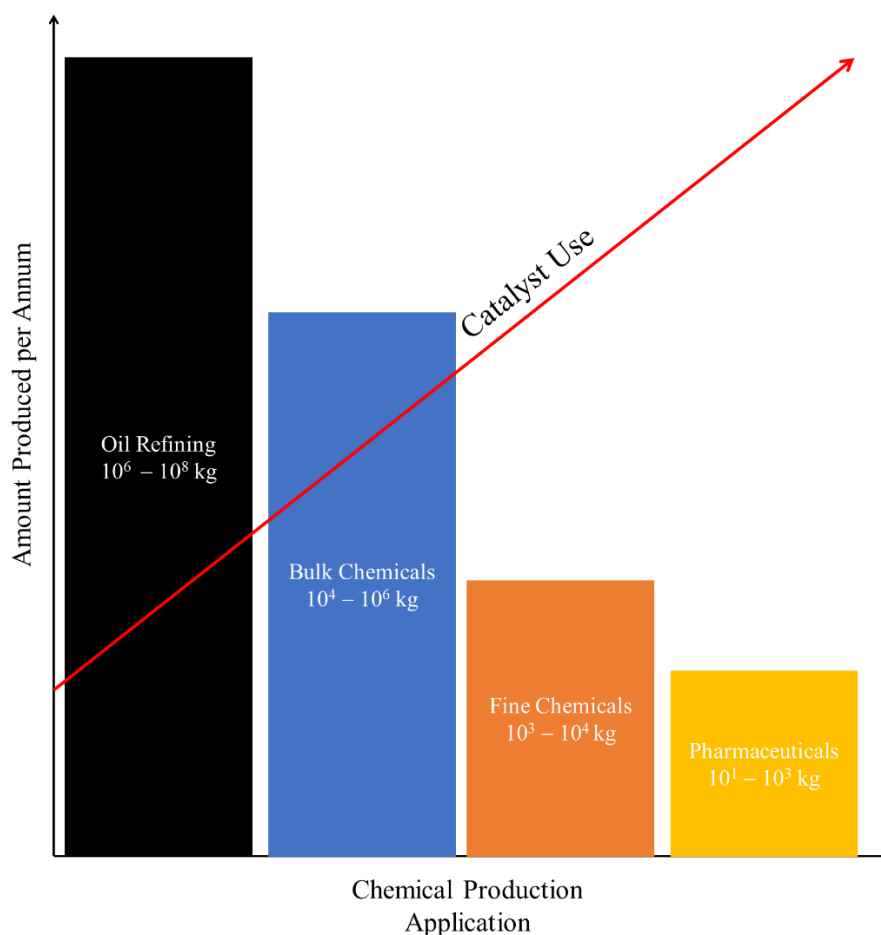


Figure 1. 1: Approximate mass of chemicals produced in various chemical sectors with the use of catalysts in each sector increasing with specificity of the chemical application, arrow indicate the use of catalysts.²

The industrial synthesis of bulk chemicals has largely remained unchanged for many decades using vast amounts of energy and inefficient catalyst technologies conceived in the 1950s.^{1, 2} One such example of this inefficiency within the chemical industry is the production of ammonia, more than 100 million metric tonnes of atmospheric nitrogen are extracted every year to make ammonia, with high reaction temperatures of 450 °C at 200 bar of pressure consuming 1-2 % of the global energy production and 5 % of the global natural gas production.^{3, 4} Another example is the selective hydrogenation of nitroarenes using supported poisoned PGM based catalysts, these catalysts contain a secondary metal within the active component to reduce the activity of the catalyst.⁵ However, this component is typically a toxic heavy metal in itself, such as lead within the so called Lindlar catalyst.^{6, 7} In addition to the lack of selectivity often displayed by these PGM based catalysts, the high costs of the precursor

materials and rapid poisoning after usage is driving the scientific interest into new catalyst compounds for the selective transformations of various compounds.

The intensive focus on these new compounds has driven a scrutineering of the traditional catalysts with a great emphasis on chemical and structural changes to the catalyst material, with many previously observed “poisoned state” materials such as PdS, FeS₂, NiS₂ and PdO being seen as potential catalysts for more efficient catalytic processes.⁸⁻¹¹

The key areas of sustainable catalysis that are being reviewed with increasing scrutiny are reducing the harsh reaction conditions; by reducing temperature and pressure, and by increasing the atomic efficiency of the reactions. The atomic efficiency of a reaction is a measure of how efficiently the reactant atoms are converted to useful atoms within the desired products. In an ideal reaction the atomic efficiency would be 100 %, where all reactant atoms are converted to desired products with no “wasted” atoms. In reality this is difficult to achieve, in part due to the nature of some chemical transformations such as the reduction of nitro or carboxylate groups, where water is always produced as a by-product. In these circumstances, it is known that a 100 % efficiency is impossible, as such the selectivity of the final product mixture and maintenance of the highest theoretical atomic efficiency is the focus.

Complex product mixtures are often achieved in the reduction of certain compounds with multiple reducible groups, such as aminostyrene or acrylonitrile synthesis. In these cases, the selectivity of the catalyst is paramount, with the activity of the catalyst often sacrificed in favour of selectivity towards a desired product. Selectivity is often favoured as the desired product is markedly more valuable than the other potential products, so increasing the yield of this product over the others is required.

Fine chemicals are typically synthesised in small batch processes requiring intensive purification and separation due to their complex synthesis often requiring a “work up” step to

ensure the final product is of sufficient quality.¹ Work up steps are wasteful in that vast amounts of solvent are required, and waste products are disposed of instead of recycling back into the reactor for further purification. This work up can be avoided using catalysts to selectively transform the target groups without the need for harsh reaction conditions. The area of focus in this thesis is the selective hydrogenation of aromatic nitro groups to anilines.

1.2 Selective hydrogenation of nitroarenes

The selective hydrogenation of substituted nitro arenes to substituted aryl amines is a vital process in the synthesis of various pharmaceuticals, agrochemicals and dye compounds. Substituted anilines are therefore of interest as their wide-ranging applications mean that the demand for their synthesis is rapidly increasing.^{5, 12-14}

1.2.1 Hydrogenation of functionalised nitroarenes

Simply reducing the nitro group of nitroarene is, in itself, not a complex chemical transformation, with this basic chemical reduction being used in the bulk production of “raw” aryl amine. Aniline, for example, is a commonly used solvent, organic base, and intermediate/precursor material in the preparation of countless other compounds. However, the key issue lies in the selective reduction of the nitro group when other groups, susceptible to hydrogenation, are present on the arene. These other substituent groups may be alkynes, alkenes, nitriles, halides, etc. The other substituent groups may be hydrogenated more easily than the nitro group, thereby removing the desired functionality in the end amine product.

As previously stated, these substituted aryl amines have near limitless uses within as agrochemicals, dyes and pharmaceuticals or as intermediates in the synthesis of these compounds. Common examples of these include benzocaine, a widely used local anaesthetic, and methyl orange, an indicator and dye compound widely used in the textile industry, the chemical structures of these compounds are shown in Fig. 1.2.

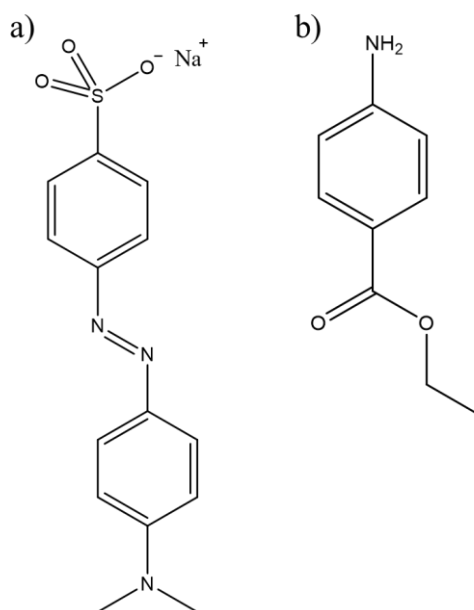


Figure 1. 2: Chemical structures of a) methyl orange and b) benzocaine, which are both synthesised from aryl amine intermediates obtained from nitroarene hydrogenation.

The production of substituted aryl amines requires highly selective catalysts that can target the nitro group for hydrogenation, while excluding the other groups, some of which may be susceptible to hydrogenation. This reduction process often involves the use of platinum group metal (PGM) based catalysts, these catalysts are often 5 % Pd/C for example using pressurised molecular hydrogen as a reducing agent.^{5, 15} However, the use of these common relatively cheap high PGM containing catalysts often lack the needed selectivity for the synthesis of substituted aryl amines. As previously discussed, due to an increasing drive for greater atomic efficiency in industrial chemical processes, there is a need to produce more selective catalysts for the synthesis of aryl amines.

1.2.2 The mechanism of nitrobenzene hydrogenation

The mechanism behind the selective hydrogenation of functionalised nitroarenes is somewhat mysterious.¹⁶ Across the literature there is a debate on the actual mechanism of the reduction, with the debate stemming from the direct synthesis route via forming the hydroxylamine intermediate or the indirect synthesis route via forming the hydroxylamine which condenses

and is then further reduced forming the azo product which is reduced to the amine product.^{17, 18}

A graphical display of the direct synthesis vs indirect synthesis is shown in Fig. 1.3.

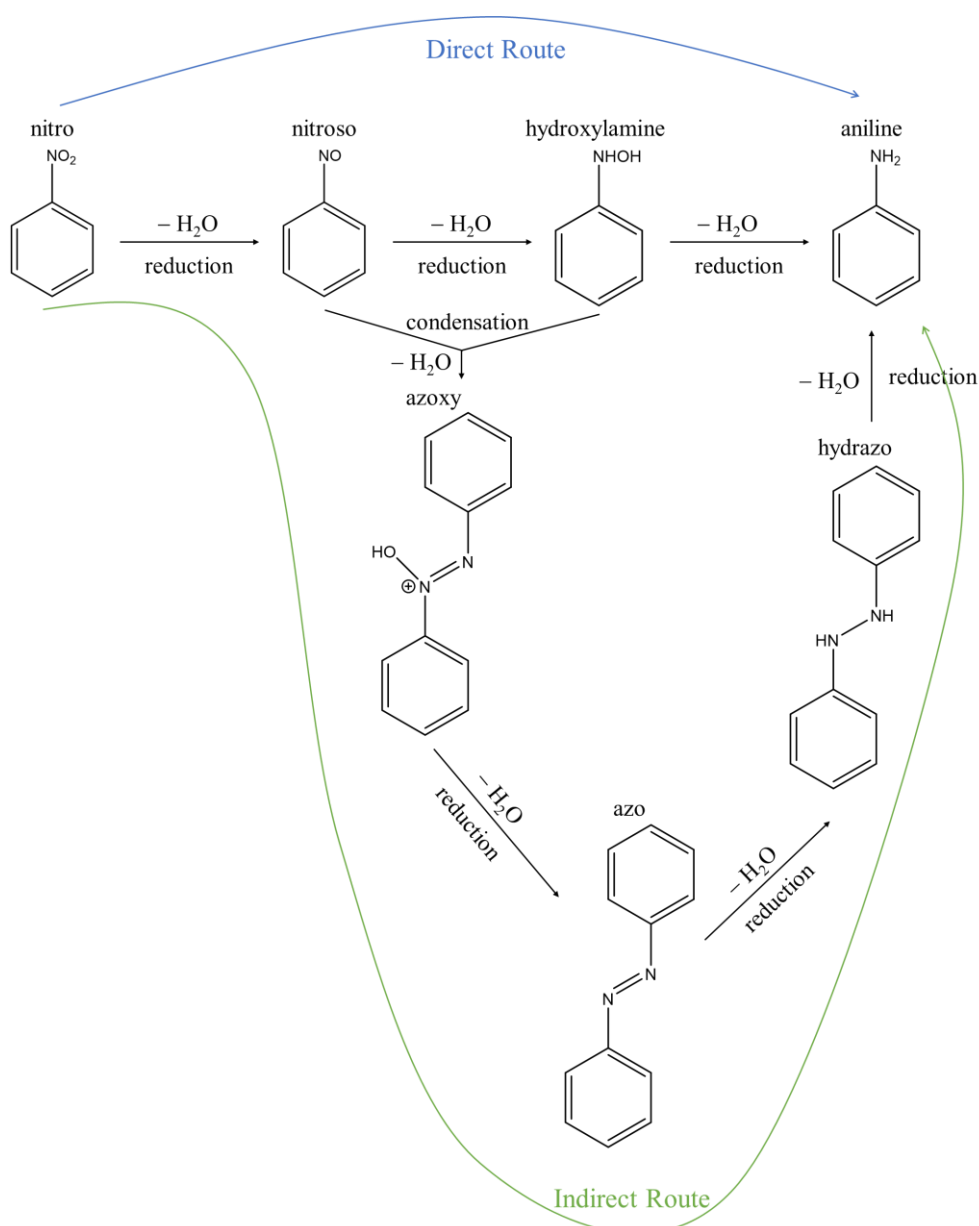


Figure 1. 3: Proposed reaction scheme in the synthesis of aniline from nitrobenzene, via a direct route and an indirect route.^{16, 18}

The direct route in the reduction of functionalised nitrobenzene is seen as the more efficient route for the synthesis of functionalised anilines, as it requires fewer chemical transformations. However, the indirect route is more energetically efficient, as the azo species represent a low energy stable intermediate, whereas in the direct route total conversion of the nitroso group to the unstable hydroxylamine intermediate.¹⁸ The total conversion of the nitroso to the

hydroxylamine intermediate requires a greater energy input than the condensation step, seen in the indirect step, however the energy gap between the hydroxylamine and aniline product is substantially reduced compared to the hydrazo product seen in the indirect route. As such, the energy gap between the two routes is negligible and they can be seen as equivalent in energy.

This equivalence in energy between the two systems can be differentiated when a catalyst is introduced. By stabilizing intermediates in either route, a catalyst causes a defined difference in the energy level, thus one route shows prevalence over the other.

1.3 Metallic catalysts for nitrobenzene hydrogenation

1.3.1 Classes of metallic catalysts

Metal based catalysts are often the go to materials for catalysts in the hydrogenation of organic compounds. More specifically, PGMs are highly sought after for their catalytic properties and ability to readily activate molecular hydrogen.¹⁹⁻²¹ However, these metals often lack the needed selectivity in these hydrogenation reactions, as they prove to be too active in the hydrogenation and activation of hydrogen leading to unwanted side reactions lowering the overall reaction efficiency.

Metal catalysts can be broken down into several distinct categories, monometallic, intermetallic and alloys. A visual demonstration of these categories is shown in Fig. 1.4.

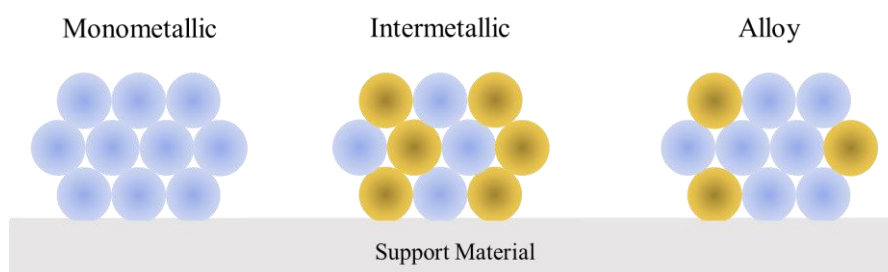


Figure 1. 4: Schematic demonstration of the three general categories of metallic catalysts, monometallic, intermetallic and alloys.

1.3.1.1 Monometallic catalysts

Monometallic catalysts feature only a single metal element in their active component, ordinarily supported on an oxide such as silica or alumina. These metals are typically PGMs due to PGMs being highly active in the activation of molecular hydrogen, shown in Fig. 1.5, and the hydrogenation of organic compounds. Yet, some non-PGM metals are used in the reduction of organic compounds such as iron, cobalt, nickel and copper, these metals have a lower activity in the activation of molecular hydrogen and are often employed when selectivity is key in a reaction. However, due to their decreased activation of hydrogen these catalysts require longer reaction times to produce sufficient conversion of substrates.

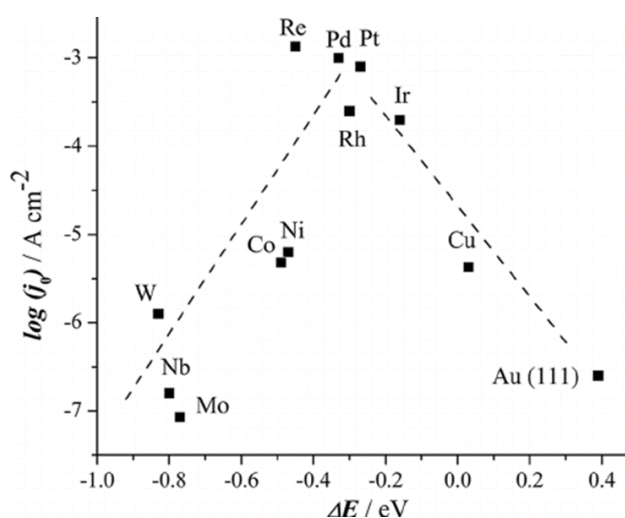


Figure 1. 5: The relative chemisorption free energies for a hydrogen monolayer formation on various common transition metals used in hydrogenation catalysts, reproduced from Garcia-Garcia et al. using data produced by Nørskov et al.^{22, 23}

The activation of hydrogen is highly energetically favoured by PGMs demonstrated by the tip of the volcano plot shown in Fig. 1.4. Palladium, platinum and rhenium show the greatest activation of hydrogen with the other commonly used metals showing a relative decreased free energy.

PGM monometallic catalysts have been demonstrated for a wide array of uses, with the hydrogenation of nitro arenes being of key interest to this work.^{12, 24-26} As previously discussed in section 1.2, the hydrogenation of substituted nitro arenes is a key challenge within catalysis

and industrial synthesis scale up. PGM based monometallic catalysts have been employed in many applications such as alkyne reduction, however, the reduction of substituted nitroarenes is challenging to achieve with monometallic catalysts.²⁶⁻²⁸ This is often due to the excessive activity of these catalysts, which causes excessive reduction of the nitroarene. In other words, the reduction is not limited to the nitro group but also results in the removal of the desired functionality in the aniline product. By removing the functionality of the final aniline, the valorisation of the desired product is lost, this reduces both the atomic efficiency of the reaction and the economic efficiency of the reaction. PGMs are expensive and difficult to process as such any loss in efficiency has a drastic effect on the economics of the reaction.^{29, 30}

1.3.1.2 Intermetallic catalysts

A route for increasing the selectivity of a given reaction, yet still provide an acceptable activity of reaction is to use an intermetallic catalyst. The active component of an intermetallic catalyst contains more than one metal element.^{6, 31, 32} Secondary, or even tertiary, metals are added to the catalyst in order to produce favourable characteristics in the catalyst, such as increased activity or, more typically, to increase selectivity towards a desired product.^{28, 33}

Intermetallic compounds have a defined crystal structure with long range order displayed between the active metal, typically a PGM, and the secondary metals, which can be transition metals or poor metals.^{27, 34, 35} These compounds often share the same basic arrangement of metals atom centres to the bulk metal but the “dopant” metal substitutes the active metal within the structure. The substitution of the active metal with the dopant reduces the relative concentration of catalytic metal leading to reduced catalytic activity. Pd₃Sn and PdZn described by S. K. Johnston *et al.* and L. B. Okhlopko *et al.* respectively showed a small doping of tin or zinc into the structure of palladium greatly increased the selectivity of the catalyst by altering the relative adsorption energies of alkyne and alkene reactants during the reduction of 2-

methyl-3-butyn-2-ol.^{36, 37} The adsorption of the alkene product was decreased relative to the alkyne product thus increasing the selectivity towards 2-methyl-3-buten-2-ol.

The catalyst phases used in the previously described work used a concentrated active metal component, with palladium content above 50 %. In such cases there is a high degree of next nearest neighbour atoms being the active metal, thus the active sites are in close contact. Close contact of active sites presents problems with selective reductions of substituted nitroarenes, as the close active sites may reduce groups other than the nitro group, reducing the overall selectivity of the catalyst. This effect was demonstrated by S. Xu et al using a platinum catalyst doped with cobalt, forming a Pt₅Co catalyst material, that showed comparable conversion of a substituted nitroarene substrate with increased selectivity towards a substituted aniline product.³⁸ High selectivity towards the substituted aniline product from the substituted nitrobenzene would have been impossible to achieve using a monometallic PGM based catalyst.

1.3.1.3 Alloy catalysts

There are even more dispersed catalysts used in the hydrogenation of various organic compounds. These compounds fall into the class of alloys, they do not display a regular long range order and can show active site isolation with no next nearest neighbours being the active metal.^{39, 40}

In terms of hydrogenation catalysis, the active metal is responsible for adsorbing and deposition of the hydrogen on the surface of the catalyst, yet the secondary metal can accept the adsorbed dissociated hydrogen on the surface in a spill over effect.⁴¹ The spilled hydrogen is then stored on the surface of the catalyst. Thus, if the secondary metal displays some catalytic activity towards the reduction of organic groups, then this spilled hydrogen may be used in the reduction of various groups in a more efficient manner than using an intermetallic catalyst.

Alloy and intermetallic catalysts tend to show the greatest selectivity in the hydrogenation of organic molecules; however, this often comes with compromised activity.^{27, 33, 42, 43} Yet, some intermetallic and alloy-based catalysts can be metastable. Under repeated use under hydrogenation reaction conditions, the single PGM atoms on the surface of the catalyst can form rafts of the active metal, i.e. dimers, trimers and extended structures, can be formed via a structural rearrangement of the metals.^{41, 44} The PGM component, under reaction conditions, can be forced from the bulk material to the surface of the catalyst particles forming rafts of highly active metal, shown in Fig. 1.6. This has been widely demonstrated using highly dispersed platinum and palladium atoms within a copper nanoparticles where after repeated use PGM rafts become visible on the catalyst surface under TEM analysis and the selectivity of the catalyst begins to decline with activity increasing, due to the no longer isolate active sites.⁴⁴

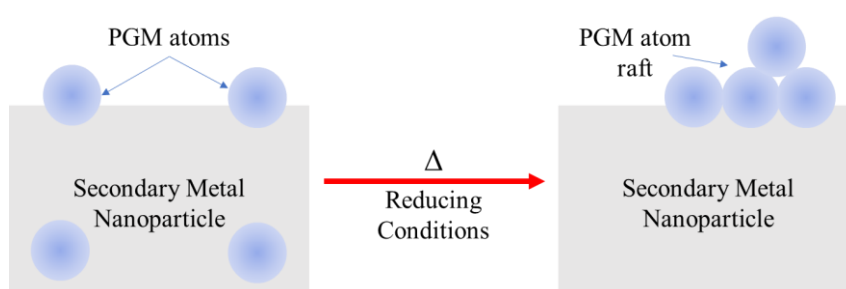


Figure 1. 6: Schematic image of the raft formation in an alloy type catalyst particle under reduction conditions.

The sharp increase in activity of the “rafts” drives a corresponding decrease in the selectivity of the product distribution, is characteristic of long-term use of intermetallic and alloy-based catalysts. The use of metal compounds is one such way of avoiding the rafting observed in metallic catalysts. These catalyst materials are discussed in section 1.4.

1.3.2 Preparation of metallic catalysts

In general, the preparation of metallic catalysts follows one of three primary methods of preparation: chemical reduction of metal salt precursors into metal particles, thermal decomposition of metal precursors into metal particles and templated synthesis.^{29, 45}

1.3.2.1 Chemical reduction

Chemical reduction preparation of metallic catalysts is shown schematically in Fig. 1.7.

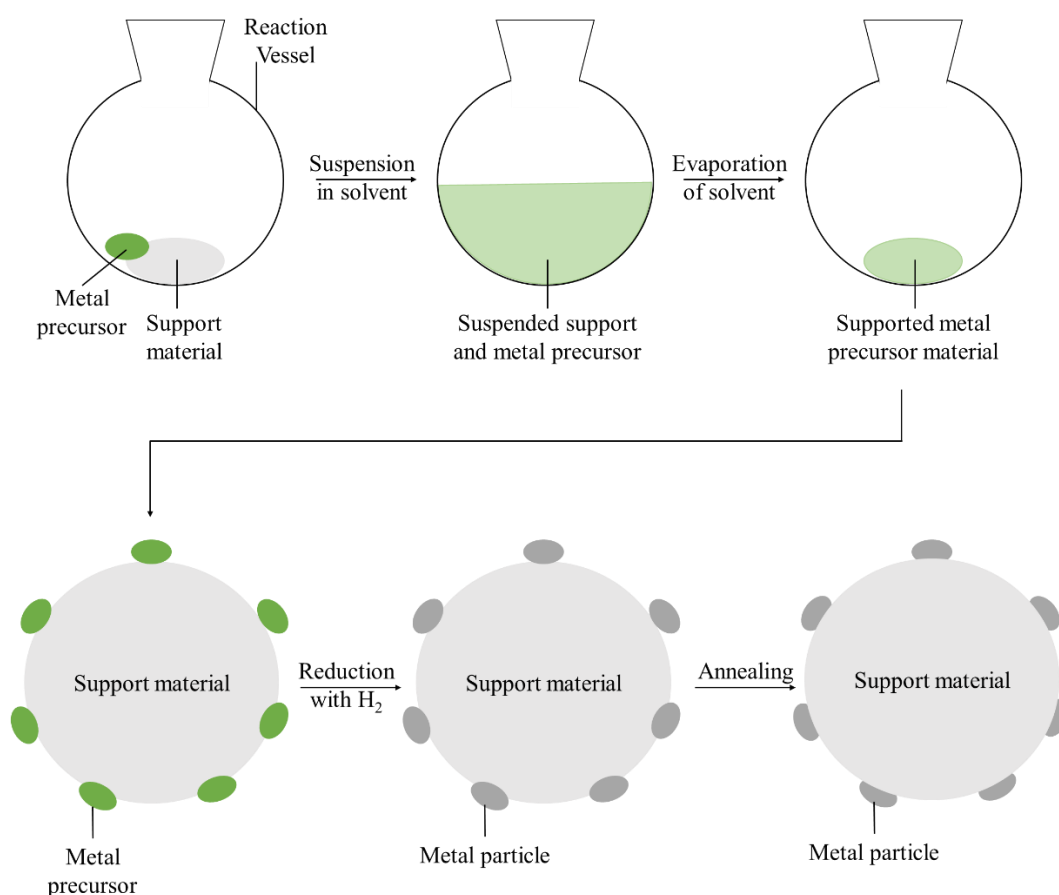


Figure 1. 7: Schematic diagram of the chemical reduction method for preparing a metallic catalyst from a metal precursor.

Chemical reduction route commonly involves the chemical deposition of a measured weight percent of metal precursor(s) onto a support.^{20, 29, 30} Metal precursors can range in metal salt, e.g., nitrates, sulfates, chlorides, etc.⁴⁶ The support material is typically an oxide, namely silica (SiO₂), alumina (Al₂O₃), titania (TiO₂) or ceria (CeO₂), however, other support materials are known and widely used for example, activated carbon, graphene and silicon carbide (SiC).^{19,}

^{31, 47-52} A surfactant or stabilizer is often used to prevent particle aggregation, such as oleylamine, yet is not required for the synthesis.^{53, 54} Once the metal precursor is suspended with the support material, the solvent is evaporated leaving the metal precursor on the support surface.

The supported metal precursor is then reduced at high temperature ($> 500\text{ }^{\circ}\text{C}$) in a stream of dilute H_2 in N_2 , typically 10-20 % H_2 , or by using a wet chemical method such as NaBH_4 or hydrazine, for a set period of time until the metal precursor is reduced to the metal.²⁹ This process leaves the metal particles attached to the support surface. The catalyst material is then annealed to bind the metal particles to the support.

1.3.2.2 Thermal Decomposition

The thermal decomposition method for preparing metal catalysts shares many similarities with the chemical reduction method.^{16, 40, 52} Metal precursor(s) materials are adhered to a support surface, via suspension in a solvent and deposition by evaporation of the solvent, however, after this point the metal precursor is pyrolyzed in order to create metal oxides on the surface of the support.⁵⁵⁻⁵⁸ Due to the metal precursor requiring pyrolysis, the metal salt is generally present as an organic salt or MOF compound, which can be pyrolyzed leaving the metal oxide behind.^{56, 59-61}

The metal oxide is then reduced and annealed in a similar process to that of the chemical deposition method. A schematic diagram of thermal decomposition preparation is shown in Fig. 1.8.

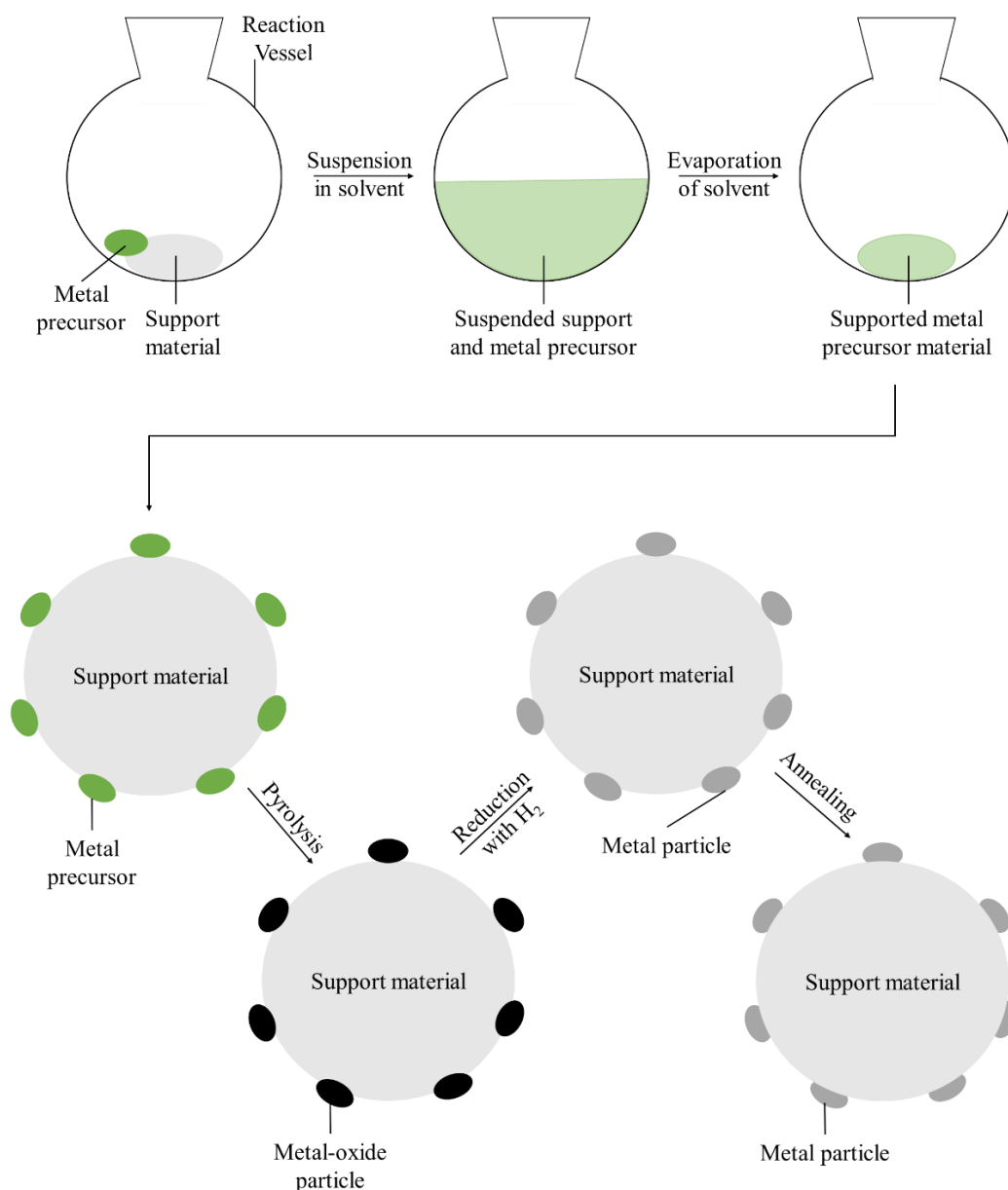


Figure 1. 8: Schematic diagram of the thermal decomposition method in preparing a metallic catalyst from a metal precursor.

Both chemical deposition and thermal decomposition methods can be used in preparing monometallic, intermetallic and alloy catalysts. However, control over the composition of intermetallic and alloy catalysts is difficult due to the uncontrolled nucleation in the evaporation deposition step,⁵⁷ in addition to the uncontrolled nature of the pyrolysis and reduction steps, where uncontrolled rearrangements of the crystal structures of the metals can lead to phase separation.⁵⁶ Thus, another method of preparation is needed for the controlled

synthesis of selective intermetallic compounds which can be achieved using a templated synthesis.²⁹

1.3.2.3 Templated synthesis/gelation

Less widely used, yet a much more versatile tool in the synthesis of metallic catalytic materials, are templated gelation methods; in particular, sol-gel methods. Sol-gel methods typically involve suspensions of colloidal particles (sols) which are converted via polymerisation or attraction between the particle to gels. The final process is aging and drying, to the useable solid material. The principal advantage of using sol-gel methods in the synthesis of metallic catalysts, is it allows for the greatest control in the overall stoichiometry of the final product, allowing for accurately controlled crystal growth for a targeted active material. The stoichiometry of the catalyst material is what gives rise to the advantageous properties of intermetallic and alloy catalysts. This precision in the synthesis of the active phase is achieved by careful control of factors such as cooling/freezing time (aging of the sol-gel), concentration of the particles and even the amount of solvent used. This allows for accurate control over the desired solid, including porosity, pore size, morphology and particle size.⁶²

The primary use of sol-gel methods within heterogeneous catalysis lies with the ability to produce highly structured and controlled support materials using a range of elements such as Si, Zr, Al, W, Ce or Mg, yielding their oxides or mixed metal oxides.⁶³⁻⁶⁵ These supports are generated with fine control over the porosity, pore size and distribution and even the distribution of activity promoting groups such as hydroxyls, thiols, sulfates and carboxylates on the surface of the support material. These materials may then be impregnated in the same way as described in previous sections 1.3.2.1 and 1.3.2.2.

1.4 Metal compound catalysts for nitrobenzene hydrogenation

As previously discussed in section 1.3, a range of catalytically active structures are possible for metals, with one or more metals being present. However, these structures have a tendency to phase separate under the reaction conditions required for catalytic transformations. Thus, the isolated active sites become aggregated, increasing activity of the material yet decreasing the desired chemoselectivity.

Intermetallic and alloy compounds are one primary way of attempting to create a fixed structure of isolated active sites, yet the breakdown of these sites into islands of active metal poses a risk in the potential life span of the catalyst material. Due to this, an increasing level of attention is being directed to more fixed metal-non-metal compounds, such as oxides, nitrides and sulfides. This classification of catalysis being the use of mineral and mineral like materials for their potential catalytic performance. In this section, the synthesis and the potential catalytic use of such materials will be explored.

1.4.1 Ceramic catalysts

Strictly intermetallics and alloys are metal compounds, yet in this section ceramic catalysts refer to mineral and mineral-structure materials used in catalysis. These materials are commonly found naturally in rock formations and metal ores; however, they are often synthesised for use in catalysis. Common structures used in catalysis are perovskite (ABX_3), pyrite (MX_2) and spinel (AB_2X_4), with many other structures being considered for a range of potential catalytic applications.^{10, 66-73} As such the use and demand for such catalytic materials has increased.

1.4.1.1 Synthesis of ceramics

Traditional synthesis of metal oxide materials follows a ceramic style synthesis where, high temperatures ($\sim 1000\text{ }^{\circ}\text{C}$) are employed with repeated grinding of the ceramic precursor material (oxides, carbonates, oxalates, etc.) in order to obtain a homogeneous material. This process is shown schematically in Fig. 1.9.

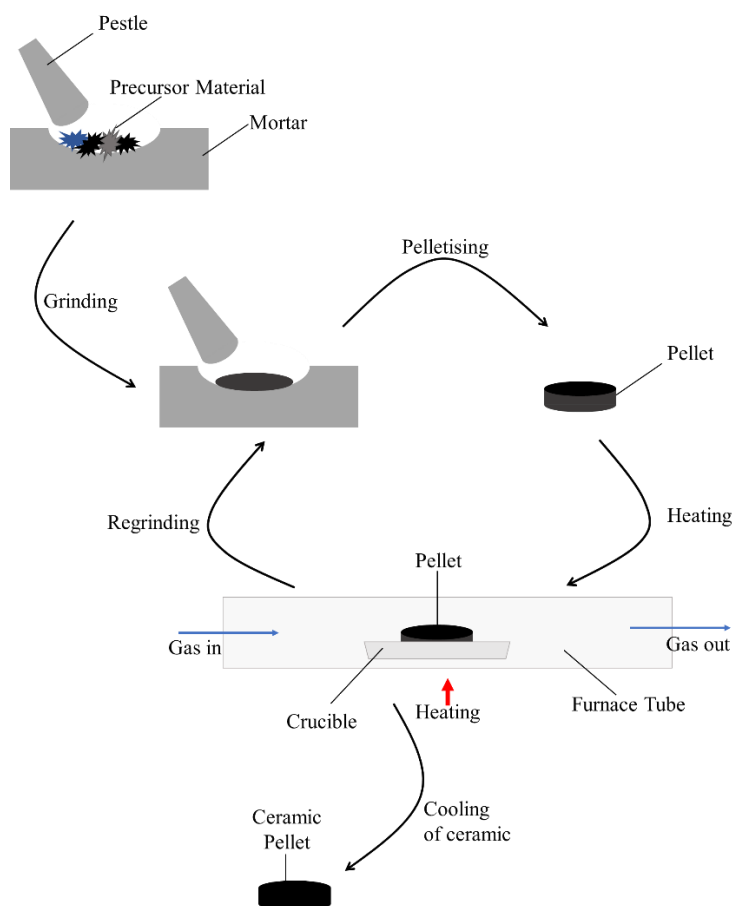


Figure 1. 9: Schematic diagram of the ceramic synthesis method used in synthesising a range of solid-state materials.

Ceramic synthesis can in some cases use various anaerobic gases (N_2 or argon) or reactant (N_2 , H_2 , O_2 , H_2S , etc.) gas flows to alter the end material. Thus, this method of synthesis is varied in the possible end products. However, solid-state reactions need energy, time, controlled regrinding, pelletising and heating to produce a homogeneous material, which can be a lengthy process.

The materials synthesised by ceramic synthesis can be a variety of metal compounds, and due to the flexibility and range of precursor materials, mixed metal oxides can be easily synthesised with their stoichiometries varied to suit a particular application. However, due to the high reaction temperatures and lengthy cooling periods, materials with a refined nanostructure, as needed for higher surface area materials used in catalysis, are difficult to synthesise. As such sol-gel synthesis can be employed in the synthesis of structured mixed metal oxides for use as catalysts.

1.4.1.2 Ceramic compounds as catalysts

Ceramic oxide materials have seen an increased screening for their potential uses within multiple catalytic disciplines. Examples include the oxidation of alcohols to aldehydes, hydrogenation of nitro groups or water splitting. S. Farhadi showed the applicability of LaFeO_3 nanoparticles in the transfer hydrogenation of a nitrobenzene substrate under microwave irradiation.⁷³ The hydrogen transfer reaction with LaFeO_3 as a catalyst was shown to be rapid with 100 % conversion of the substrate in <20 minutes whilst maintaining 100% selectivity to the functionalised aniline product, far exceeding the reactivity and selectivity obtained using PGM catalysts with pressurised hydrogen.

The metals within ceramic materials are in a non-zero oxidation state, such as Fe within LaFeO_3 being 3+. This is key to the activity of these compounds in their catalytic properties. Using LaFeO_3 as an example, Fe (III) can be reduced to Fe (II) via the donation of an electron from either a substrate or reducing agent, which is then used to propagate the reaction via an electron transfer process. Thus, materials containing iron are highly desirable due to the redox reactions of the Fe (III/II) ion.

1.4.2 Metal chalcogenide catalysts

Metal chalcogenides have similarly seen an increasing interest as catalysts for a range of chemical transformations, including oxidation and hydrogenation reactions. This increased interest in metal chalcogenides has been driven by the fossil fuel industries where the resistance to sulfur poisoning is of interest in the processing of natural gas and petroleum products. In addition to maintaining activity under problematic reaction conditions, metal chalcogenides show good thermal stability as demonstrated by the natural minerals that they are derived from.

1.4.2.1 Synthesis of chalcogenides

Metal chalcogenides are synthesised through a variety of routes, primarily traditional solid state route using a sulfurization gas flow or via solvothermal reactor.⁷⁴⁻⁷⁶ These techniques allow for a controlled growth of differing chalcogenide phases in addition to a great deal of control over the size and shape of the resultant particles.

Solid state synthesis of sulfide phases traditionally involves the use of a metal oxide phase that is heated and reacted with a sulfurization gas at high temperature, >400 °C. The general process of solid-state sulfurization is shown in Fig. 1.10. The sulfurization can be achieved by reaction of metal oxides with different gases, such as CS₂, H₂S, or via a solid-state reaction between elemental sulfur, selenium or tellurium with the metal oxide.

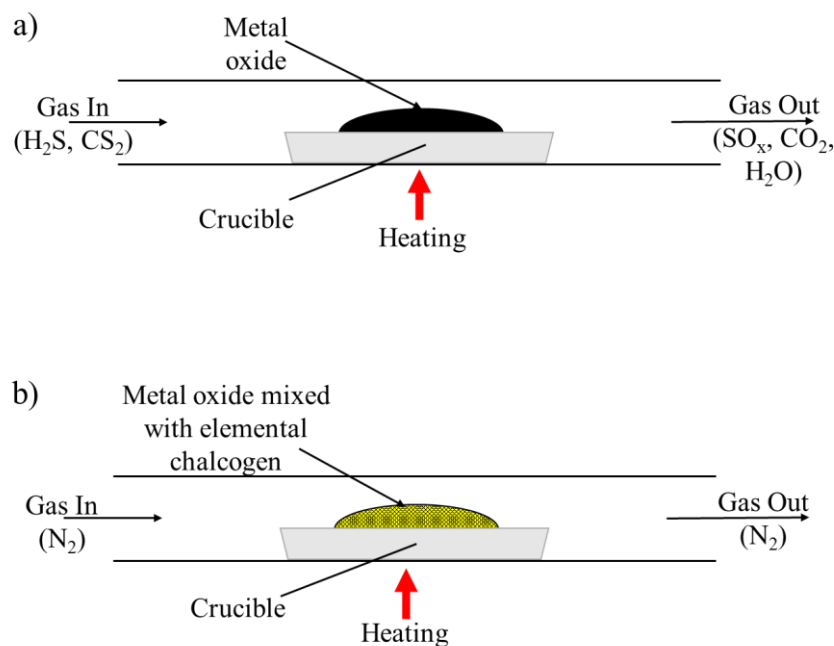


Figure 1. 10: Schematic diagram of the solid-state method in synthesising metal chalcogenides via a) gas flow sulfurization and b) solid state reaction between metal oxide and elemental chalcogenide.

The second method of chalcogenide preparation is using the solvothermal approach. Solvothermal synthesis involves the use of an autoclave reactor. The primary advantage of utilising solvothermal reaction methods is that reactions can be carried out at pressures higher than ambient pressure.⁷⁷⁻⁷⁹ When synthesising chalcogenides the autoclave reactor is pressurised with the H₂S or a side reaction within the reactor is used to generate reactive chalcogenide species which react with the metal ions to precipitate the metal chalcogenide.⁸⁰ Solvothermal autoclave reactions are typically carried out at temperatures less than 200 °C, as the pressure of most reactors is limited to ~124 bar. However, the pressure is significantly higher than that obtainable using other reaction methodologies. As such reactive or unstable species may be generated in situ which can be utilised in the synthesis of meta stable chalcogenide species. Solvothermal synthesis has several disadvantages in the synthesis of chalcogenides primarily in the equipment required for the synthesis which can be prohibitively expensive and often produces only small amounts of material per synthesis run.

Solvothermal synthesis is highly flexible in the synthesis of chalcogenide catalysts due to the range of solvents and metal precursor materials available. Solvents can be used to modulate the solubility of the metal precursors and other reactants, in addition to the tuneable boiling point or pressure of the reaction.^{75, 78, 81} Traditionally only three solvents are used in autoclave reactors, water (hydrothermal synthesis), ethanol and ethylene glycol. Additionally, combinations of these solvents can be used to obtain a desired boiling point and reactor pressure.

1.4.2.2 Chalcogenide Catalysts

Metal chalcogenides have shown an increasing potential as catalysts for a wide range of chemical transformations. Through hydrogenation and oxidation reactions, along with uses in electrocatalysis and photocatalysis.^{8, 10, 13, 82} They have a wide variety of crystal structures and accessible metals. These materials can range in their electronic properties from metallic, semiconductor and insulator properties, as such modulating the metal used and the target crystal structure the activity of the end material can be easily manipulated to obtain specific properties.

The applications of chalcogenides in this work focuses on the use of such materials in hydrogenation catalysis, where chalcogenide materials have been shown to possess properties that are difficult to obtain using traditional metallic catalysts. One such example is the use of a supported palladium sulfide (Pd₄S) catalyst in the reduction of a mixed alkene/alkyne stream to select for alkenes.⁸ The Pd₄S material was selected due to its increased selectivity towards the alkene product, this increased selectivity is due to the relative deactivation of the palladium via active site isolation by surrounding sulfur atoms. As such alkyne substrates are preferentially reduced over alkene substrates. The primary reason for utilising Pd₄S as a catalyst was highlighted by similar work with intermetallic catalysts, as described in section 1.3.1.2, where the secondary metal is used in a defined crystal structure to ensure a relative

deactivation of the primary metal. Thereby increasing the relative selectivity of the intermetallic compound was increased when compared to the monometallic catalyst. This work demonstrated the excellent thermal and chemical stability displayed by palladium sulfide as the reduction takes place at elevated temperature, 250 °C, and high-pressure hydrogen, 18 bar, with minimal deactivation of the catalyst over time. The low degree of deactivation of Pd₄S, compared to Pd metal catalysts in this reaction conditions was attributed to the stability of Pd₄S with the forming of rafts/islands of palladium not observed. This islanding process, described in section 1.3.1.3, showed how across time alloy and intermetallic catalysts may structurally rearrange leading to islands of active metal causing a sharp decrease in selectivity with a noted increase in catalytic activity.^{27, 32, 83} Yet, Pd₄S showed that the bonding within the crystal structure prevented such rearranging of the ions, potentially due to the ionised nature of the Pd within the crystal structure.

The advantageous properties of metal chalcogenide catalysts are more greatly demonstrated in liquid phase reduction reactions where the interaction of the catalyst and solvent often present challenges not faced in gas phase catalysis. These challenges are often induced by catalyst deactivation by the reduced adsorption of substrate from the solvent onto the catalyst surface, the decreased desorption of products from the catalyst into the reaction mixture and the solvent attacking the catalyst surface binding to the surface or stripping vital active material away leaching the catalyst into the reaction mixture. These effects are demonstrated in Fig. 1.11.

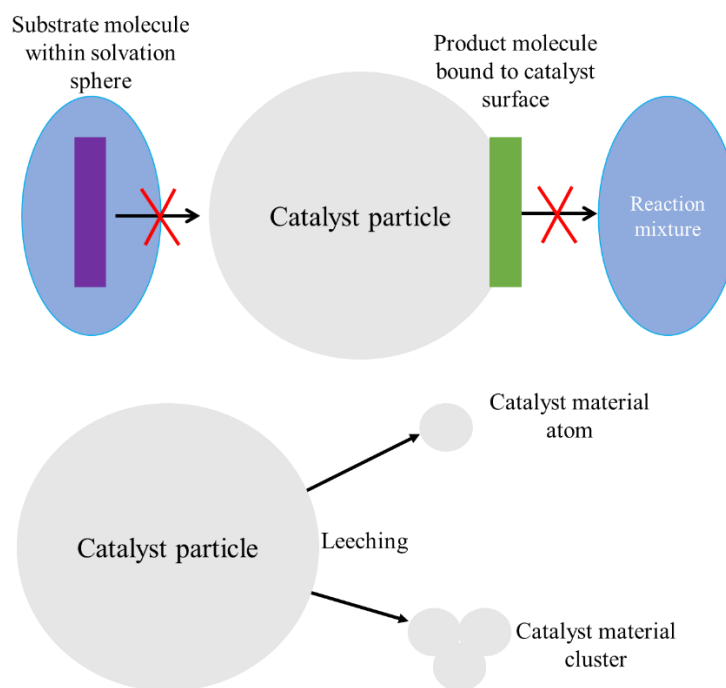


Figure 1. 11: Common catalyst degradation/deactivation pathways observed in liquid phase catalysis.

Due to these potential methods of deactivation, liquid phase hydrogenation catalysis requires catalysts resilient to the build-up of surface contaminants and resistant to leaching material from the surface. Leached atoms or clusters of atoms have been observed to show greatly increased catalytic activity when compared to the bulk catalyst particle due to the vastly increase surface area of the material available to react. However, this increase activity often leads to a sharp decrease in the required selectivity of a given chemical transformation, therefore, minimising the amount of active material leaching from the catalyst has to be paramount in designing new catalysts for fine chemical synthesis.⁸⁴⁻⁸⁶ Using compounds with a defined crystal structure such as chalcogenide materials the leaching of active material can be minimised. This is achieved as the energy required to strip an active atom/ion from the catalyst surface far exceeds the stabilisation energy of the atom/ion in solution. As the bonding within common chalcogenide materials is relatively strong, relative to traditional metallic catalysts, the energy required to desorb atoms or groups of atoms from the catalyst surface is greatly reduced.

The reduction of nitroarenes is one such liquid phase selective hydrogenation reaction that has been greatly studied as a model reaction to compare catalysts. This is due to the range of potential products that may be formed in the reaction as shown by Fig. 1.3. Metal sulfides have been employed in this reaction to increase the selectivity of the hydrogenation towards an aniline product that maintains an unaffected substituting group.^{8, 9, 13, 15, 72, 87, 88} As described previously, the role of the sulfide in the vast majority of these cases is to provide a selective method of poisoning the catalyst material to provide a relative decrease in activity thereby providing an increase in selectivity. However, some materials, such as pyrites (MS_2), graphite-like MoS_2 and greigites (M_3S_4), have recently shown catalytic properties in the selective hydrogenation of nitroarenes. The metal centres within these sulfide materials, unlike poisoned PGMs, do not show appreciable catalytic performance unless subjected to extreme temperatures and pressures.⁷⁴ Yet, within the sulfide structure they have been demonstrated to show excellent activity whilst maintaining high selectivity to the desired product. This is exemplified by the work conducted by J. Morse *et al.* where a bulk off the shelf iron pyrite (FeS_2) was ground to produce particles $<20\text{ }\mu\text{m}$ and employed in a hydrogenation reaction using conditions currently employed by PGM based catalysts.⁷² The reaction was carried out using nitrobenzene substrate dissolved in 50:50 water:THF with 50 mg of powdered pyrite, this solution was then pressurised with 50 bar of hydrogen and heated to $120\text{ }^\circ\text{C}$ for 18 hours. The conversion and selectivity of the off the shelf iron pyrite was comparable to that of the PGM based catalyst under the same reaction conditions.

Due to the resistance to potential poisoning metal sulfide-based catalysts have seen increasing scrutiny for applications within selective hydrogenation of nitroarenes. However, when compared to more traditional catalysts, discussed in section 1.3, the reaction conditions are typically harsher in order to drive the reaction towards completion. These harsh reaction conditions can include increased hydrogen pressure, increased temperature or increased

catalyst loading.^{9, 21, 72, 88-90} Yet, with increased stability and lower affinity towards side reactions metal sulfide catalysts have been shown to provide increased selectivity in the selective hydrogenation of nitrobenzenes, with a wide variety of substituent groups.

1.4.3 Metal borides, nitrides and phosphides

Metal borides, nitrides and phosphides are other classes of compounds that have seen an increased interest within catalysis, not only within hydrogenation catalysis but electrocatalysis and photocatalysis. In part this is due to the high stability observed comparable to that of metal sulfide catalysts but the excellent selectivities shown in the selective reduction of numerous organic compounds.⁹¹⁻⁹⁶

1.4.3.1 Synthesis of borides, nitrides and phosphides

The synthesis of metal borides, nitrides and phosphides follow the general methodologies described in the solid-state synthesis of ceramic and sulfide materials. Metal precursors and boron or phosphorus source are ground together to form a homogenous powder, this is then heated at high temperatures >700 °C under a reducing atmosphere, such as hydrogen diluted in nitrogen, in order to reduce and react the precursor materials.^{92, 95-98}

Precursor materials are tailored to the intended product material. A summary of common precursor materials for the synthesis of borides, nitrides and phosphides is shown in Table 1.1.

Boride (M_xB_y)	Nitride (M_xN_y)	Phosphide (M_xP_y)
$Me_2NH.BH_3$⁹⁷⁻⁹⁹ (dimethylamine borane)	5% - 30% v/v N_2/H_2^{100, 101}	phytic acid¹⁰⁵
$NaBH_4$^{97, 99} (sodium borohydride)	NH_3^{102, 103}	$(NH_4)_2HPO_4$¹⁰⁶ (diammonium hydrogen orthophosphate)
	$H_2N(C=O)NH_2$¹⁰⁴ (urea)	$(NH_4)H_2PO_4$¹⁰⁷ (ammonium dihydrogen orthophosphate)

Table 1.1: Common precursor compounds used in the synthesis of borides, nitrides and phosphides.

1.4.3.2 Uses as catalysts

Metal borides, nitrides and phosphides are used in a wide variety of catalytic processes, primarily electrocatalysis, for water splitting and oxygen reduction processes, yet there are increasing examples of effective application of these compounds in hydrogenation catalysis.^{91, 93, 96, 98, 99, 102} Recent application of borides and hydrides have shown limited application within the selective hydrogenation of some organic molecules, such as cinnamaldehyde and alkynes. Yet important to this work, an increasing number studies have shown that under harsh reaction conditions, >120 °C and >11 bar H₂ pressure, metal borides, nitrides and phosphides do demonstrate appreciable conversion of nitroarenes with a high degree of selectivity.^{95, 108-110} However, when phosphides, nitrides and borides are compared to other potential catalysts such as intermetallics, metal sulfides and some ceramic compounds, the catalytic performance in the reduction of nitroarenes requires a far greater energy input to obtain similar conversions and selectivities.

In addition to the relatively poor catalytic performance of borides, nitrides and phosphides, their synthesis is often lengthier, requiring high synthesis temperatures to obtain a pure final compound. The high temperature used the synthesis of pure compounds, makes these compounds unsuitable for larger scale production methods. Yet, for highly specialised synthesis of fine chemicals, such as functionalised anilines, the use of these catalysts may be of interest.

1.5 Hydrogenation Methods

The work presented in this thesis focuses on the selective hydrogenation of substituted nitrobenzenes to substituted anilines. There are two primary methods utilised in the reduction of nitrobenzenes, the activation of molecular hydrogen and transfer hydrogenation. This section

will discuss the differences between the two systems in addition to the advantages each hydrogenation route possesses over the other.

1.5.1 Activation of molecular hydrogen

The most widely utilised method for hydrogenation reactions is the activation of molecular hydrogen. Molecular hydrogen activation involves the adsorption of hydrogen on the catalyst surface and activation of the hydrogen molecule; this activation typically takes the form of homolytic cleavage of the hydrogen bond leaving desorbed hydrogen atoms on the surface of the catalyst. The general process for molecular hydrogen activation is shown in Fig. 1.12.

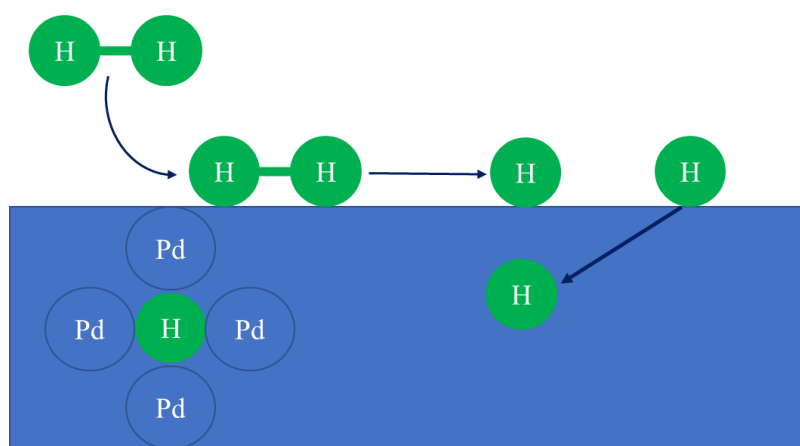


Figure 1. 12: Schematic diagram of the hydrogen adsorption, dissociation and diffusion into the bulk on a noble metal (Pd) catalyst surface.

Hydrogen activation is most energetically favourable for Pt and Pd metals and this is due to the diffuse outer shells of these metals easily forming metal hydrides on the surface of the catalyst.¹¹¹⁻¹¹³ These hydrides/dissociated hydrogen atoms are highly mobile across the surface of the catalyst, and are known to jump between energetically favourable sites. The relative energy and likelihood of occupation of these sites is related to the reaction temperature and catalyst material.¹¹³ Defects within the crystal structure of the catalyst and high pressure of hydrogen can lead to the dissociated hydrogen being taken into the bulk of the catalyst material, via the formation of metal hydride species.^{111, 113} This hydrogen may then be utilised in

hydrogenation reactions that have higher energy requirements or reduce the overall selectivity of the catalyst material.¹¹⁴⁻¹¹⁷

The key limiting step in the activation of molecular hydrogen is the solubility of hydrogen in the solvent and the energy difference between this solvated hydrogen and the hydrogen adsorbed to the catalyst surface.^{118, 119} The greater this energy difference, the lower the rate. In addition to the relative solubilities of the substrate and product materials where the polarity of the solvent can heavily influence the product distribution and the mechanism by which the hydrogen is added to the substrate molecule. Hydrogen (H₂) itself is nonpolar, yet, during the adsorption can become polarised by the catalyst surface, through a heterolytic cleavage of the H – H bond.¹²⁰⁻¹²² This is highly unfavourable within nonpolar solvents, such as n-hexane, toluene and cyclohexane.^{121, 123, 124} This polarisation of the hydrogen during the dissociation leads to nonpolar solvents showing a slower rate of substrate conversion, when compared to polar solvents. Polar solvents tend to show an increase in the rate with an increase in the polarizability of the solvent, this may be due to a wider range of substrate – catalyst – product solubilities or an increased stabilisation of the polarised hydrogen bond cleavage.¹²⁴⁻¹²⁶ This gives greater conversion than nonpolar solvents, however, selectivity achieved can be sporadic and unpredictable.

Hydrogenation via activation of molecular hydrogen gas is often achieved using high pressure, to overcome many of the mass transfer hydrogen solubility limitations, in addition to high pressure being required in many cases to obtain meaningful conversion of the substrate material.^{8, 26, 72, 115, 127} However, this can lead to over saturation of the reaction solution further adding to erratic selectivity in the final product distribution.^{51, 115, 116} The effect of pressure on the product distribution is compounded by the explosive potential of hydrogen gas, which has led to the development of efficient transfer hydrogenation processes, utilising alcohols, hydrides and hydrazines.^{67, 128, 129}

1.5.2 Transfer hydrogenation

Transfer hydrogenation refers to the addition of hydrogen to a compound from a molecule that is not molecular hydrogen, known as the hydrogen donor source. Transfer hydrogenation via a hydrogen donor is a powerful and often convenient method for the synthesis of various hydrogenated compounds.^{67, 87, 128-130} It is an attractive alternative to direct molecular hydrogen activation for many potential benefits, as such it has become a methodology at the forefront of hydrogenation catalysis. These benefits include, transfer hydrogenation not requiring hazardous and potentially explosive pressurised hydrogen gas. Hydrogen donor compounds are generally readily available, inexpensive and easy to handle with standard laboratory practice. The major side products of the hydrogen donor compound either do not interfere with the hydrogenation or can be recycled into value added products themselves useful in future chemical transformations.¹²⁹⁻¹³¹

In general, three classes of hydrogen donor compounds are used in the transfer hydrogenation process. These are alcohols and acids, hydrides and hydrazines and anoxic organic compounds. Each classification of compound has a specific compound group for which it can be most effective in transferring hydrogen to and certain cases where these hydrogen donors are not the ideal hydrogen source.¹²⁹ However, due to the range of possible hydrogen donor compounds the potential of this method is only limited by the catalyst efficiency in transferring the hydrogen.

1.5.2.1 Alcohols and Acids

Alcohols and acids are the most used hydrogen donor compounds in part due to being relatively inexpensive but having a wide range of potential target substrates.^{13, 73, 132-135} The primary mechanism of action observed within alcohol based hydrogen donors is the formation of carbonyl products, essentially oxidising the alcohol in order to reduce a substrate.^{40, 134} The general mechanism of this transfer process is shown in Fig. 1.13.

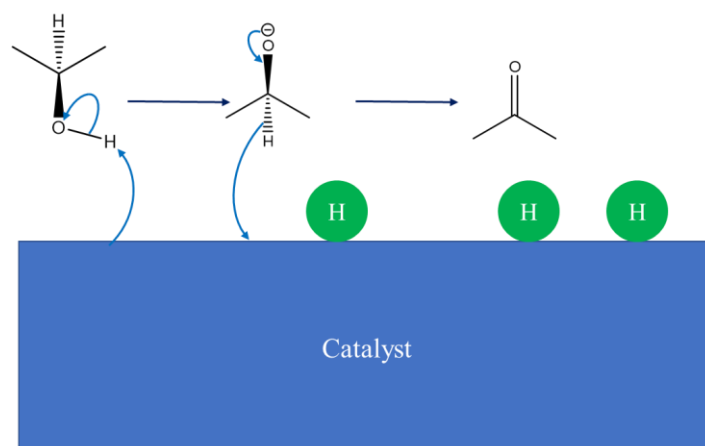


Figure 1. 13: Schematic mechanism of the dehydration of propan-2-ol to acetone with the hydrogen atoms becoming adsorbed to a catalyst surface.

Acidic hydrogen donors are less commonly utilised when compared to alcohol hydrogen donors but have been demonstrated to show great potential in the reduction of various organic groups.¹³⁶⁻¹⁴³ Acid hydrogen donors can be organic acids, such as formic (methanoic) acid, and selected mineral acids, such as hypophosphorus (phosphinic) acid (H_3PO_2); these function in a similar mechanism to that of alcohols, yet possess a far lower pKa value.^{137, 138} These, are deprotonated more easily making the cascading oxidation reaction much more efficient, yet more unpredictable than alcohol hydrogen donors. The mechanism of action for acidic hydrogen sources is shown in fig. 1.14.

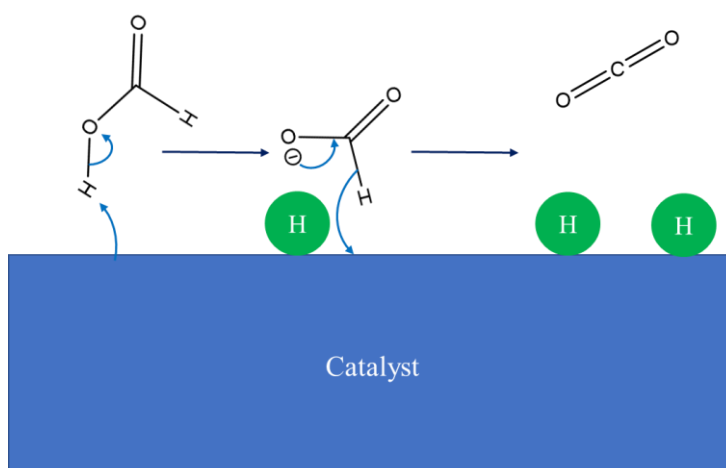


Figure 1. 14: Schematic mechanism of formic acid dehydration to carbon dioxide, with the hydrogen atoms being adsorbed to a catalyst surface.

In some rare cases, the end product of the hydrogen donor oxidation exists in a different state from that of the ongoing reaction. Examples include formic acid being oxidised to carbon

dioxide and hypophosphorus acid being oxidised to phosphorus oxides, that crash out of solution (solids) or diffuse out from the reaction solution (gases), thereby removing the “spent” hydrogen donor compound.^{138, 143} This removal of the “spent” hydrogen donor compound drives the reaction equilibrium forcing the consumption of the hydrogen donor compound, which in turn drives the conversion of the substrate.

Alcohols and acids has been utilised in limited studies for the reduction of nitro compounds yet due to the potential coupling of the desired aniline product with excess hydrogen donor forming potential side products these compounds have largely been avoided.¹²⁹ However, an increasing number of studies have shown that isopropanol, cyclopentanol and formic acid can be applied, in conjunction with a highly selective catalyst, to the reduction of nitro compounds in both batch and continuous flow reactors.^{13, 132, 144, 145} These systems have demonstrated that near complete substrate conversion, >95 %, with high selectivity, >95 %, towards the substituted aniline product, thus showing the applicability of alcohols and acids in the selective reduction of nitroarenes.

1.5.2.2 Hydrides and Hydrazines

A popular method for the reduction of organic compounds is the use of sodium borohydride (NaBH_4) and lithium aluminium hydride (LiAlH_4) as sources of hydride ions for the reduction of various susceptible groups.¹⁴⁶⁻¹⁴⁸ These materials form cyclic intermediates where the substrate group coordinates to the Al or B centre allowing for transfer to occur in localised position within the substrate. Transfer hydrogenation utilising hydrides are generally shown to be rapid in the transfer of hydrides to the substrate molecule, achieving high conversions of the substrate within 30 minutes.^{147, 148} However, the process tends to show reduced selectivity in product distribution, in part due to the high reactivity of free hydride ions. Loss of selectivity in the product distribution, specifically for nitrobenzene reduction, has been demonstrated in several studies showing rapid formation of the substituted aniline product.^{146, 148} Yet, as the

reaction progresses substantial quantities of azoxybenzene, azobenzene and aniline are formed, via an indirect hydrogenation route as discussed in section 1.1, see fig. 1.1.

Some catalyst species, such as Raney nickel, FeNi intermetallic compounds and some Au based catalysts, have shown great potential in directing the hydrogenation of nitro groups using hydride donors.^{147, 149-152} The materials show controlled surface formation of metal hydride species, that reduce the nitro group in a more controlled fashion increasing selectivity but also increasing reaction time.¹⁵² This compromise still produces rapid reactions, with high conversion of substrates achieved within 2 hours, yet maintaining high selectivities towards substituted aniline products.^{147, 149, 150}

Hydrazines are widely used source of hydrogen for transfer hydrogenation reactions, which is due to the high hydrogen density of these compounds. Unsubstituted hydrazine is the most hydrogen dense being comprised of 12.5 % hydrogen by weight, releasing four hydrogen atoms per molecule of hydrazine consumed in the transfer reaction.^{87, 153} The final product of this decomposition reaction is nitrogen.^{13, 154} Unlike carbonyl and hydrocarbon by-products, nitrogen does not strongly adsorb to catalyst surfaces being readily released from the reactor in the form of nitrogen gas, thus driving the equilibrium to consuming more hydrazine. This decomposition over a catalyst with the ultimate removal of nitrogen from the reaction is shown schematically in Fig. 1.15.

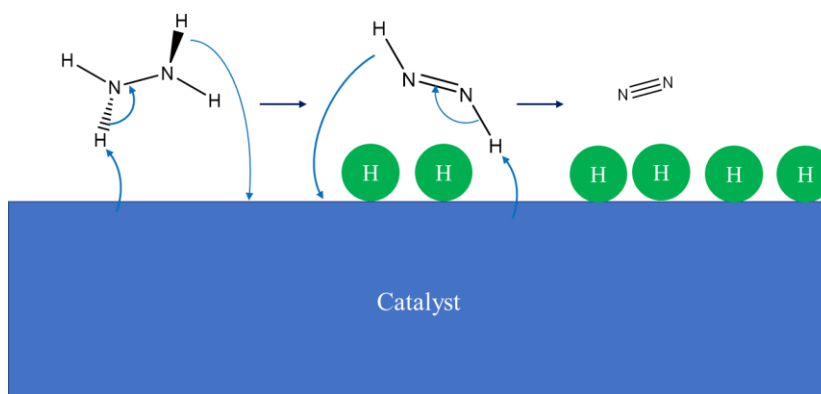


Figure 1. 15: Schematic mechanism of hydrazine decomposition over a catalyst surface with hydrogen atoms being adsorbed to the catalyst surface and nitrogen being the primary by product of the reaction.¹³

Despite the high hydrogen density of hydrazine, it is not often implemented within hydrogenation systems in its pure form.¹⁵⁵ This is due hydrazine being highly toxic and unstable when non-solvated, making handling procedures difficult and expensive. Yet, when solvated in water hydrazine becomes stable and far less hazardous to handle, as such hydrazine hydrates have been shown to display great effectiveness in the selective reduction of various organic molecules and groups.^{15, 155} Most commonly hydrazine has been utilised as hydrazine monohydrate ($\text{N}_2\text{H}_4\cdot\text{H}_2\text{O}$), even in this diluted state, it comprises of ~65 % hydrazine by mass. Thus, a millilitre of hydrazine monohydrate contains 163 mmol of hydrogen; this hydrogen is more easily available than that stored within alcohols and acids as such is more effective at being transferred to potential substrates.¹⁵

It has been demonstrated by numerous studies that hydrazine hydrate can be used in as a hydrogen donor for the selective reduction of nitro groups.^{154, 156-159} The catalysts utilised in these cases are varied from metal nanoparticles, oxides and sulfide materials. See table 1.2, for comparison between differing catalysts and reaction conditions for nitrobenzene transfer hydrogenation using hydrazine as a hydrogen source.

Catalyst	Reaction Conditions	Ref
Pd – C nanospheres	EtOH:H₂O, 80 °C	158
Co – Co₂B Nanocomposites	MeOH, r.t.	156
Rh – Fe₃O₄ Nanocrystals	EtOH, 80 °C	159
Ni/Co PVP Stabilised Nanoparticles	H₂O, r.t.	154
MoS₂ – C	EtOH, 80 °C	13

Co – Mo₂C – C Nanocomposite	H₂O, reflux	157
O – MoS₂ Nanoparticles	EtOH, 50 °C	87

Table 1.2: Examples of N₂H₄ hydrogen transfer reactions over different catalysts, with respective reaction conditions.

These materials have all shown great potential in the reduction of various nitro substituted substrates, maintaining a high selectivity with rapid conversion of the substrate. Molybdenum sulfide (MoS₂) shows the greatest catalytic potential for transfer hydrogenation to synthesise substituted nitroarenes.^{13, 87, 96} The activity of molybdenum sulfide in the reduction of nitroarene substrates was shown to be comparable if not superior to that of the metal nanoparticle-based catalysts. Iron, nickel and cobalt doped materials also display great potential in the reduction of nitro groups via hydrazine transfer hydrogenation, with many of the previous studies showing a marked promotion in activity and selectivity with the inclusion of first row transition metal within the catalyst material either doped into the crystal structure of the catalyst or as a composite additive within the catalyst material.¹⁵⁴⁻¹⁵⁷ In each case, this additive first row transition metal aids in the selectivity of the catalyst for hydrazine transfer hydrogenation.

Transfer hydrogenation using hydrazine does possess some major deficiencies when compared to other hydrogen sources, one such example is the difficulty in the reduction of carbonyl compounds.^{15, 155} The reduction of carbonyl compounds cannot be achieved via a hydrazine hydrogen source due to the formation of hydrazone compounds as shown in Fig. 1.16. The formation of the hydrazone product is spontaneous and not reversible in the presence of hydrazine.

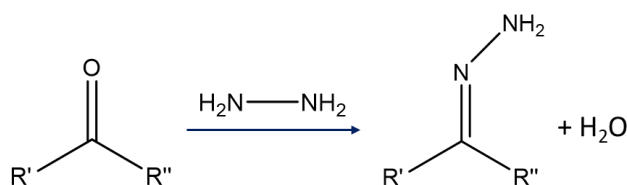


Figure 1. 16: Reaction scheme for the spontaneous formation of the hydrazone product by a reaction between a carbonyl and hydrazine. R = CH₃, H, C_xH_{2x+1}.

As a result of this spontaneous hydrazone formation, carbonyl containing species are to be avoided when attempting hydrogen transfer reactions in the presence of hydrazine. Unreactive carbonyls, such as those present within amide and ester containing compounds are not susceptible to the formation of a hydrazone group, as such substrates containing these groups are possible substrates in the hydrazine mediated hydrogen transfer reaction.

1.5.2.3 Liquid Organic Hydrogen Carriers

The final and least widely applied category of hydrogen donor compounds are the so called Liquid Organic Hydrogen Carriers (LOHC) compounds.^{129, 160-162} These include cyclohexane, tetralin (1,2,3,4-tetrahydronaphthalene), 1,3-cyclohexadiene, bicyclohexyl and their derivatives. These compounds are dehydrogenated to form highly stable aromatic compounds with the hydrogen being adsorbed to the catalyst surface. The high stability of the dehydrogenated product drives the reaction forward, with the dissociated hydrogen then being free to be consumed within a transfer hydrogenation process.^{160, 163} This dehydrogenation process is demonstrated in Fig. 1.17, where tetralin is dehydrogenated to naphthalene, with the hydrogen atoms becoming adsorbed to the catalyst surface.

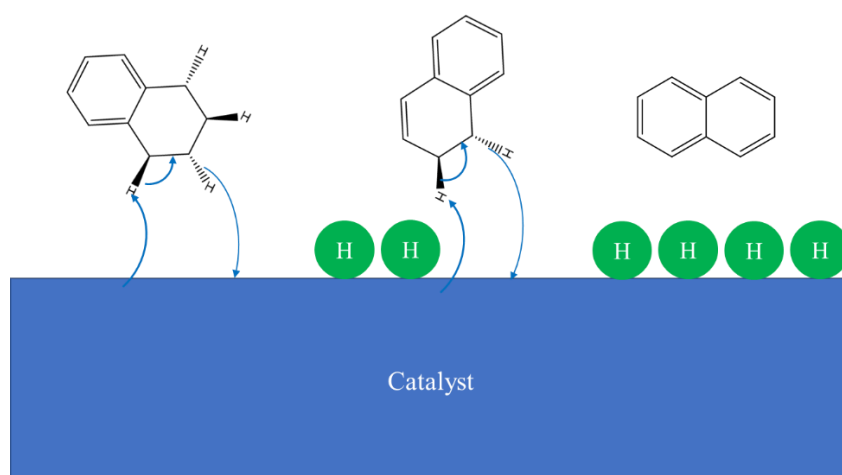


Figure 1. 17: Reaction scheme of tetralin (1,2,3,4-tetrahydronaphthalene) to naphthalene over a catalyst surface with hydrogen atoms becoming adsorbed to the catalyst.^{160, 164}

LOHCs have been demonstrated to show potential in the reduction of fatty acid methyl esters (FAME) to biodiesel like hydrocarbons and in the cracking of FAME into smaller hydrocarbon

units.^{83, 160, 163} Hydrodeoxygenation (HDO) reactions removing oxygen from substrates through hydrogen addition are one such route where LOHCs are being widely applied, as traditionally this has been achieved using high pressure hydrogen (>50 bar H₂) and other hydrogen transfer reagents such as isopropanol.¹²⁰ However, these processes typically require the use of platinum or palladium catalysts, high temperatures and have potential side reactions via the products of alcohol transfer hydrogenation. LOHCs have been employed due to the relative inertness of the aromatic product and the high thermal stability, low vapour pressure and relatively low flammability of these materials.

Despite the potential benefits of LOHC based transfer systems, they are limited by the high activation energy of the dehydration process and the high degree of catalyst poisoning observed within these systems.^{129, 164, 165} The energy required to strip hydrogen atoms from LOHCs often limits their uses to energy intensive applications such as coal and biomass liquefaction and HDO reactions, making them unsuitable for lower energy processes such as nitro group reduction and aniline synthesis.^{129, 166} In addition to this, the poisoning of the catalyst is more prevalent with the application of LOHCs, due to the so called “coking” process.^{166, 167} Coking of a catalyst is the formation of carbonaceous deposits on the catalyst surface and occurs within most catalytic processes however is often more prevalent with LOHCs. Coking of the catalyst occurs when highly stable carbon deposits adhere to the catalyst surface thereby blocking the active sites from functioning, resulting in a marked decrease in catalytic activity.^{165, 167, 168} The coking process occurs via one of two potential routes, white coking and black coking.¹⁶⁹ White coking involves the formation of long chain, paraffin like, hydrocarbon species, this can occur via a polymerisation/ring opening reaction of the LOHC where the highly reactive particularly dehydrate species quickly reacts with surrounding LOHC species forming long chains.^{166, 170} White coke is easily removed via a solvent flushing process and merely poses a nuisance in the reaction system. Black coking is far more poisoning to the catalyst and may result in sustained

activity reduction even after reprocessing the catalyst.¹⁷⁰ Black coking involves the formation of graphitic sheets from the LOHCs to form extended networks of carbon layers, these can be highly stable and highly adsorbing to the catalyst surface, often requiring oxidative treatment to facilitate the removal of the coking.¹⁶⁹ Yet, this may introduce some imperfections into the catalyst, as such, the catalyst used in LOHC transfer hydrogenation often has a limited lifetime of activity and must be resynthesized regularly making the use of catalytic material highly inefficient.

1.6 Chemical reactors for selective hydrogenation of nitrobenzenes

When considering the pilot and production scale synthesis of fine chemicals, the reactor used must also be considered in addition to the catalyst applied to the synthesis, as with many chemical processes, scale-up can produce side reactions not observed in lab scale production.^{133, 171, 172} Chemical reactors generally fall into two main categories, batch reactors and continuous reactors. With many fine chemicals, such as substituted anilines, it is often more beneficial to utilise scaled up batch processes in pilot scale synthesis, in part due to the value of the end product, as such time and scale become lesser factors when compared to a similar scale bulk chemical.¹³³ Bulk chemicals, such as ethylene, often require continuous production in order to make their synthesis cost effective, in part to due to the lower value per unit of synthesised product.^{31, 173}

Due to these factors, it is important to first understand the final industrial scale of the model/target reaction and the value of the desired product.^{1, 2, 174, 175} For instance, if the final product is highly valuable, time inefficiency such as the use of batch reactors may be overlooked in favour of producing high purity product. Yet should the final product be required

in a bulk quantity or have a low market value, continuous synthesis may be required to make the product economically viable.¹⁷⁵ However, should the reaction form many side products, losing desired product selectivity, inefficiencies are introduced as the final product purification is required. Thus, alternative catalysts and reactor designs may be considered to boost the final product purity to increase the market value of the product.

The hydrogenation of nitroarenes to anilines, as previously discussed, is one of the most important hydrogenation reactions used industrially as these are key intermediates and products used in the manufacture of a wide range of fine chemicals.^{176, 177} As such there has been a key focus on balancing the value of the end aniline product and the reactors employed in their synthesis. Not all functionalised anilines are created equally; some aniline derivatives are final products used as pharmaceuticals and agrochemicals and these are generally more complex compounds, thus yielding a higher market value when compared to bulk aniline derivatives.^{174, 175} With aniline derivatives used as intermediates in the synthesis of dyes and polymers, generally yielding a lower market value requiring larger production volumes to be considered cost effective. Due to this dichotomy in the value of anilines, the end industrial use has a great impact on the reactor used in full scale synthesis. However, most laboratory scale testing of catalysts in the hydrogenation of nitroarenes is carried out using batch reactor techniques in order to quickly screen potential catalysts for their usefulness in the selective synthesis of anilines.

1.6.1 Batch reactors

The most widely utilised reactor type in the synthesis of aniline derivatives is the batch reactor. Batch reactors often take the form of a closed reaction vessel to which the solvent, catalyst and substrates are added, with the reactor requiring emptying and cleaning after each reaction. Batch reactors can synthesise a fixed quantity of product with each production run due to the capacity of the vessel.^{133, 178, 179} These reactors are widely employed with laboratory scale

synthesis of various products in part due to modern carousel batch reactors, see Fig. 1.18, where numerous batch reactions can be carried out in tandem in order to screen different reaction conditions to rapidly optimise the reaction conditions or determine the initial usefulness of a catalyst material.¹¹⁶ These reactors can be fed with differing gases to tailor the reaction conditions to the desired product distribution for a given reaction.

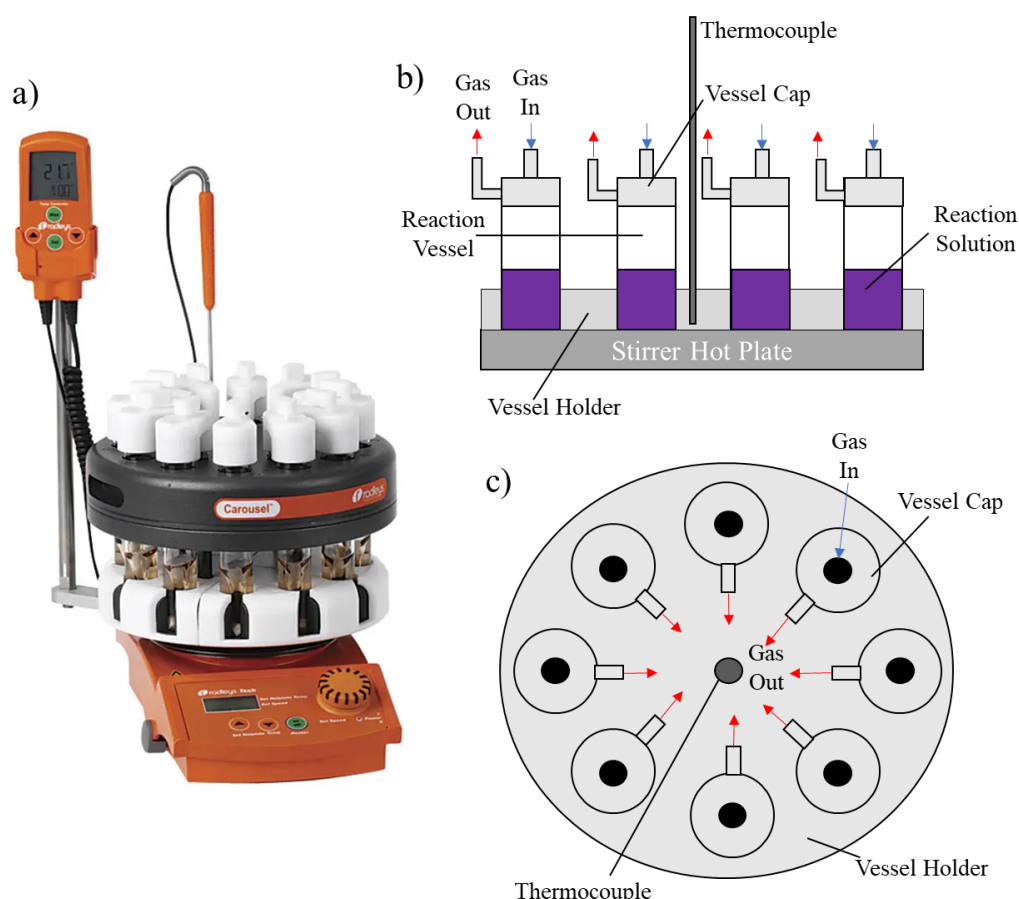


Figure 1. 18: a) image of a Radleys 12 sample carousel batch reactor, b) schematic profile view of a carousel batch reactor, c) plain view of a carousel batch reactor.

Scale up of batch reactors is generally the simplest of the main reactor types, in that a scaled-up reactor involves using a large volume vessel. However, with extreme industrial scale batch reactors mass transfer limitations become evident as a large volume of solvent being heated can result in a temperature differential between the outer edges of the reactor and the centre point.^{1, 2} In these cases, only highly valuable products are produced due to the inefficiency in solvent and energy usage. Batch reactions are easily monitored continuously by

chromatography to determine the ideal reaction time at which the reaction become most selective to maximise the desired product and limit impurities within the product.¹⁸⁰

1.6.2 Continuous microreactors

Continuous reactors do not have a fixed reaction capacity as the substrate is continually passed through the reactor without interruption, the products are collected at the effluent point with further purification if needed. Since the 1990s there has been a drastic increase in the use of micro reactors for fine chemical synthesis.^{171, 172, 181} Continuous microreactors have many advantages when compared to batch reactors, namely greater contact between catalyst and substrate phases i.e. reduction in mass and thermal transfer limitations, yet, providing an increase in the safety when utilising hazardous substances.^{182, 183} Scale-up is also a simple affair with continuous flow microreactors in that increasing the number of microreactors increases the amount of product that can be produced.^{171, 184, 185} However, this method of scale-up is expensive requiring an array of pumps and high-pressure systems to accurately control the reactors. For bulk chemical production microreactors often output an insufficient amount of effluent to make them economically viable in large scale production as such they are limited in application.¹³³

1.6.2.1 Capillary microreactors

Capillary microreactors, or wall coated microchannel reactors, are widely utilised due to their similarity to many liquid chromatography systems.^{182, 186, 187} Being comprised of a substrate reservoir, gas or transfer agent inlet, a high-pressure pump, reactor column, back-pressure regulator and effluent collection, see Fig. 1.19 for schematic of this reactor type.¹⁸⁷

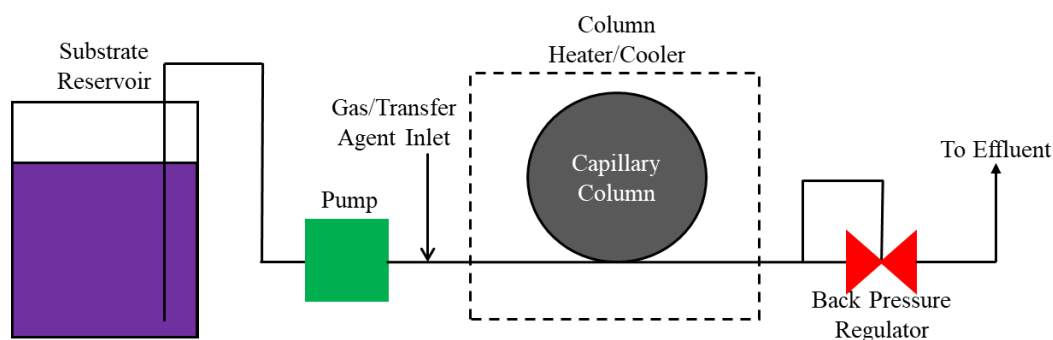


Figure 1. 19: Schematic diagram of the main components of a capillary microreactor.

The reactor column used is generally in the form of a fused silica capillary column, similar to those used in gas chromatography, alternatively microfluidic chips may be manufactured with channels tailored to a specific application, with the surface modified to deposit a catalyst on the capillary walls.^{48, 187} The reactor column can be heated or cooled dependent on the required reaction conditions within the column and reactor pressure modulated by a back-pressure regulator situated at the end of the column. Catalyst preparation follows the same general procedure to that when preparing a catalyst in an open environment, however, the support and catalyst precursors are pumped into the capillary tube instead of external impregnation as traditional supported catalysts are produced.^{48, 188, 189} See Fig. 1.20 for the preparation of a wall coated microchannel reactor column.

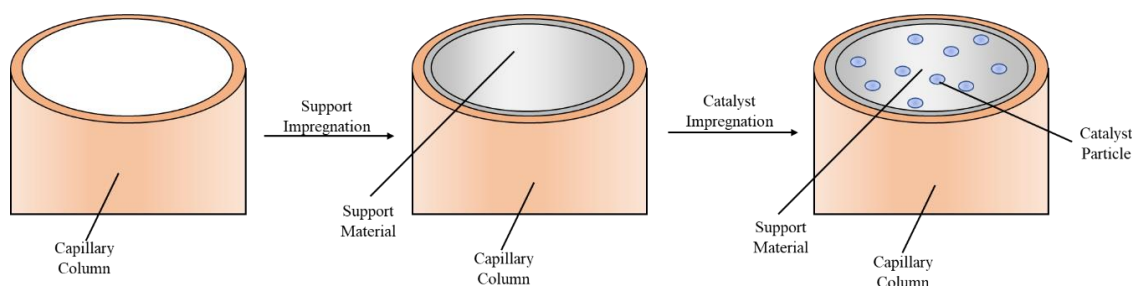


Figure 1. 20: Schematic diagram of the process by which capillary channels may be coated and catalyst particles deposited on the capillary walls, reproduced from work carried out by N. Cherkasov.^{186, 190}

The walls of the capillary may be coated in a variety of potential materials to facilitate chemical reactions within the microreactor. Fig. 1.21, reproduced from a recent example by Li *et al.*, who demonstrated that metal organic framework (MOF) supported Pd nanoparticles may be impregnated into a quartz capillary to facilitate the selective reduction of 4-nitrostyrene.¹⁸⁷ The

support and catalyst show a clear distinction from the capillary wall. When the elements are mapped onto the SEM image (Fig. 1.21c) no “bleed over” of Si from the capillary wall is observed within the supported catalyst material.¹⁸⁷

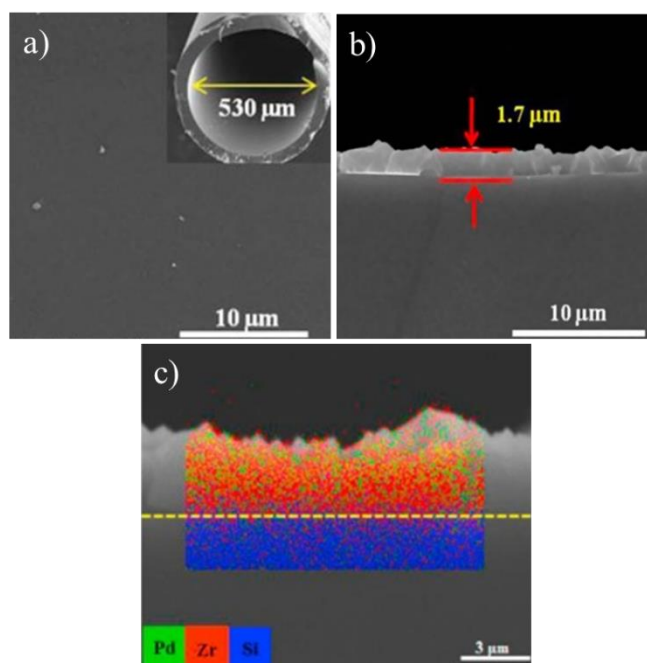


Figure 1. 21: a) SEM image of the quartz capillary tube prior to catalyst impregnation, b) SEM image of the catalyst impregnated capillary wall showing a wall coating depth of 1.7 μm , c) Elemental mapping of 1.21c, with Pd atoms shown in green, Zr atom shown in red and Si atoms shown in blue, reproduced from work carried out by J. Li *et al.*¹⁸⁷

In the work by Li *et al.*, a high conversion (>95 %) of 4-nitrostyrene was observed with a short residence time (<5 minutes) of the substrate within the capillary column, thus showing the potential that capillary microreactors have for the rapid throughput and continuous synthesis of low value 4-aminostryrene.¹⁸⁷

However, microreactors are all generally limited in their output per minute of use to the flow rate which is generally less than 100 $\mu\text{L min}^{-1}$. This results in lengthy times to produce any great volume of product without the so called “numbering up” process where multiple wall coated capillary reactors are stacked together to increase the overall output of products.^{186, 187} Numbering up is expensive when compared to the large batch alternative and so is currently not widely employed for industrial production of substituted anilines.

1.6.2.2 Film microreactor

Thin film microreactors are an emerging microreactor with high substrate through put with interfacial surface areas per reaction volume of $9000 - 15000 \text{ m}^{-1}$.^{191, 192} In thin film microreactors, alternatively called falling film microreactors, two plates coated in a catalyst are held at a fixed separation typically $<100 \text{ }\mu\text{m}$ and liquid, containing the substrate, is fed from the top of these plates falling due to gravity creating a thin film of substrate over the catalyst coated plates. ^{193, 194} The combination of a thin film of substrate in contact with catalyst plates in the presence of gas or transfer agent promotes mass and thermal transfer between the phases allowing for more efficient reaction engineering. A schematic of a thin film reactor is shown in Fig. 1.22.

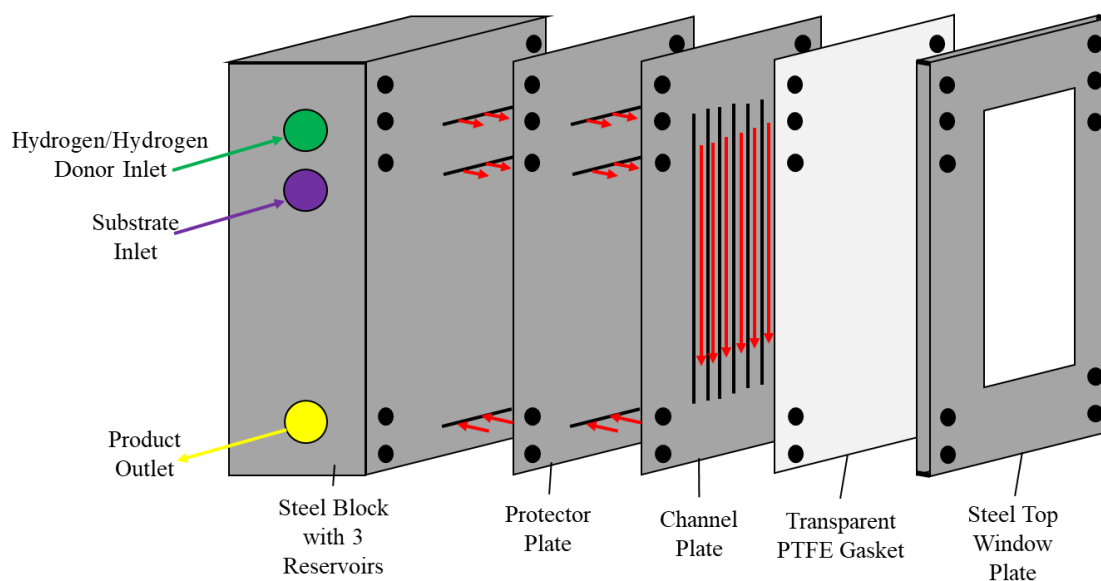


Figure 1. 22: Schematic diagram of a thin film microreactor.¹⁹³

Thin film microreactors have been demonstrated to show potential in the hydrogenation of nitrobenzenes for a variety of selective process, such as the formation of aniline and azoxyl products.^{191, 192, 194} The preparation of these thin film microreactors followed a similar methodology to the preparation of capillary microreactors. However, instead of requiring complex wall coating preparations, the catalyst and support can be grafted directly onto the

plate using traditional methods such as wet impregnation, chemical vapour deposition and photodecomposition of precursor materials.^{191, 192, 195}

The microreactors produced for the hydrogenation of nitrobenzenes showed successful conversion of the substrate and that it was indeed possible to tailor the reactor to produce a specific product from the substrate material.^{191, 192} Yet, in all cases deactivation issues were prevalent. Imperfections within the plate formation by cracking of the catalyst surface, formation of organic adherents, followed by loss of the catalyst material limited all reactor lifetimes to <50 hours reactor time on stream.¹⁹² However, in some cases it was observed that the microreactor produces a comparable daily output of products to batch reactor systems, under optimal conditions. Yet this beneficial output could be offset in the lengthy downtimes described in reparation of the plates after extended usage.¹⁹¹

1.6.2.3 Packed bed microreactor

The primary disadvantage of capillary and thin film microreactors stem from the difficulty in achieving uniformity of the substrate flow and/or the catalyst coating/loading process.^{178, 183, 196} This lack of uniformity in the reactor walls can lead to uneven reaction completion by irregularities in the mass/thermal transfer in parts of the system, thus leading to the formation of by-products and, in turn, potential catalyst deactivation.^{197, 198} These limitations may be overcome in many cases by the use of packed-bed microreactors, in which the substrates flow through a packed bed of solid catalyst.^{199, 200} Schematic of a packed-bed microreactor is shown in Fig. 1.23.

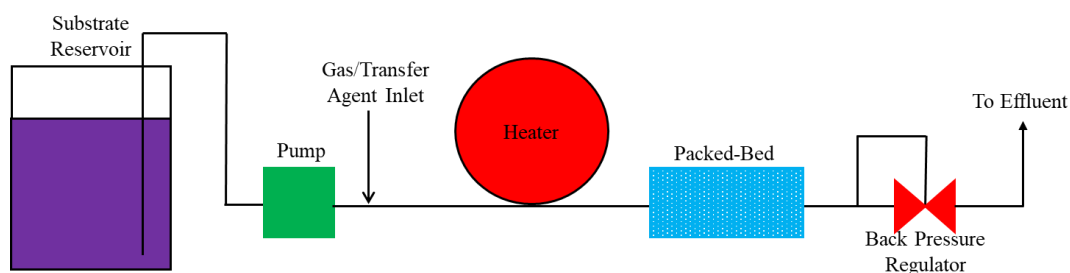


Figure 1. 23: Schematic diagram of the main components of a packed bed microreactor.

The packed bed is of known thickness and diameter, with catalyst mass being controlled to alter the product distribution of the reaction. The catalysts used in packed-bed type reactors are the simplest in terms of preparation with the catalysts used in traditional batch type processes being utilised in the packed-bed, as such no complex catalyst preparation methods are required.^{196, 197, 201} Due to the possibility of utilising more traditional catalysts, taking advantage of the rapid preparation of numerous catalysts for a given reaction, rapid screening of potential catalysts can be achieved using packed-bed style reactors, allowing for efficient optimisation of reaction conditions and extraction of kinetic parameters.^{197, 199} However, packed-bed are limited by the uncontrolled fluid dynamics, poor thermal transfer and significant drops in pressure, through sheer forces within the uncontrolled packed-bed.

Large scale industrial synthesis of anilines utilises macro packed bed reactors in the gas phase, liquid-phase hydrogenation of nitrobenzenes has not been widely deployed extensively due to the difficulties in removing heat from the reaction.¹⁹⁷ This is mainly due to the previously described poor thermal transfer of packed-bed reactors. However, by designing structured catalysts and better optimising the reactor catalyst usage nitrobenzenes could be efficiently reduced within a packed-bed reactor.¹⁹⁶ Importantly these studies both demonstrate poor conversion and inconsistent selectivity when compared to liquid-phase batch hydrogenation reactions.^{200, 202} Yet pack beded microreactors may still show potential in screening potential nitrobenzene hydrogenation catalysts across a variety of reaction conditions.

1.7 Aims

The aims of this work were to research and develop metal sulfide catalysts to potentially replace current supported noble metal catalysts for the reduction of nitroarenes to anilines. The metal sulfides developed should pose a lesser environmental impact and show superior performance,

in both activity and selectivity, than the current state of the art on the selective hydrogenation of nitroarenes.

Due to the environmental challenges of noble metal extraction and wide-ranging substrate incompatibility, such as sulfur and carbonyls, presented by supported noble metal catalysts, replacements for these are sought. The focus of my efforts has been to produce first row transition metal sulfides as these have shown great potential in the reduction of nitroarenes under a wide range of reaction conditions.

The preparation of metal sulfide compounds is traditionally carried out at high temperature (often $> 700\text{ }^{\circ}\text{C}$) through a so-called sulfurization reaction reacting a precursor material with a sulfurizing gas as previously described. However, metal sulfides may be prepared at lower temperatures through a solid-state reaction of a sulfur source and metal precursor allowing for relatively mild reaction conditions. These more traditional methods often lead to the synthesis of large crystalline materials with little to no nanostructure. Recent work has shown the potential of synthesising metal sulfides using solvothermal methods, in which metal precursors and a sulfur source are dissolved in a solution containing a capping agent.¹³

The reaction group studied is that of the selective hydrogenation of nitroarenes to anilines, whilst avoiding the non-selective route synthesising aniline (Fig. 1.3). To optimise the reaction conditions for the hydrogen transfer reduction using the metal sulfide catalysts for the reduction of nitroarenes, the reduction of 4-chloronitrobenzene to 4-chloroaniline is used as a model reaction. This reaction is optimised with regards to various critical reaction parameters such as temperature, catalyst loading, reaction solvent, etc. Once the optimum conditions have been reached various other nitroarene substrates will be studied to show the general applicability of metal sulfides in the reduction of nitroarenes. Other hydrogen donors will also be explored in order to determine whether hydrazine is the most suitable for the application.

Chapter 2 Experimental Techniques

2.1 Material synthesis

For the synthesis of all materials in this work, solvothermal synthesis techniques were used, rather than traditional solid-state routes based on high temperature calcination.

Solvothermal synthesis is used in the preparation of a wide variety of materials such as ceramics, polymers and metal oxides.⁷⁷⁻⁷⁹ The reaction involves the use of moderate to high pressure and elevated temperatures, in a solvent. If water is used as the solvent, it is referred to as “hydrothermal synthesis”. When using non aqueous solvents, the technique is referred to as “solvothermal synthesis”. Solvothermal synthesis allows for greater control of parameters such as particle size and particle aggregation, which is crucial in heterogeneous catalysis. This control is due to the manipulation of the cooling rate and reaction dwell time. Due to the extreme reaction environment, both thermodynamically stable and metastable states can be prepared by solvothermal synthesis; the solubility of reactants can be achieved by the elevated pressures and temperatures within the autoclave which may not be possible with more traditional synthesis methods.

The use of a solvothermal autoclave for this synthesis allows for much higher reaction pressures than within traditional glassware reactors. The high-pressure environment of the solvothermal reactor allows for a more efficient reaction between volatile precursors or intermediate products.

Two key factors control reaction outcome in solvothermal synthesis outcomes, the chemical nature of precursors and the solvent selected for the synthesis.

The chemical nature of the precursors must be consistent with that of the target materials. In addition, the concentration of the precursors plays a role in controlling size, shape and crystal

phase of the resulting material. The interaction between solvent and reagent plays an additional role in solvothermal reactions.

Therefore, the choice of solvent can play a key role in solvothermal synthesis. Solvent-reagent incompatibility is a key aspect in all liquid phase reactions. In the closed solvothermal reactor environment, incompatibility or solvent-reagent interaction can lead to loss of reaction efficiency. Yet, in some cases the solvent may be used as an initiator or activator of inert reagents.

In general, alcoholic solvents are preferred for solvothermal synthesis due to their lower boiling points and higher vapour pressures. A higher boiling point solvent allows for a higher temperature reaction, generally leading to a more efficient reaction with shorter reaction times. Table 1 shows the most widely applied solvents for solvothermal synthesis with their associated boiling points and vapour pressures.

Solvent	Boiling point (°C)	Vapour pressure at 25 °C (kPa)
Water	100	3.1710
Ethanol	78	8.1060
Ethylene glycol	198	0.0120
Glycerol	290	0.0002

Table 2.3: Boiling point and vapour pressure of commonly used solvents in solvothermal synthesis.

Water and ethanol are most widely used in solvothermal synthesis due to their ease of use and availability. However, in certain cases, these solvents are not ideal, either due to their low boiling points or higher vapour pressures, see table 2.1. In certain circumstances a more reducing environment is required and ethylene glycol or glycerine is used. A more reducing atmosphere can be useful in maintaining oxidation state of reagent materials during the reaction.

Due to the high pressure used in solvothermal synthesis specialised reactors are used. A solvothermal autoclave is used in such reactions, schematic shown in figure 2.1.

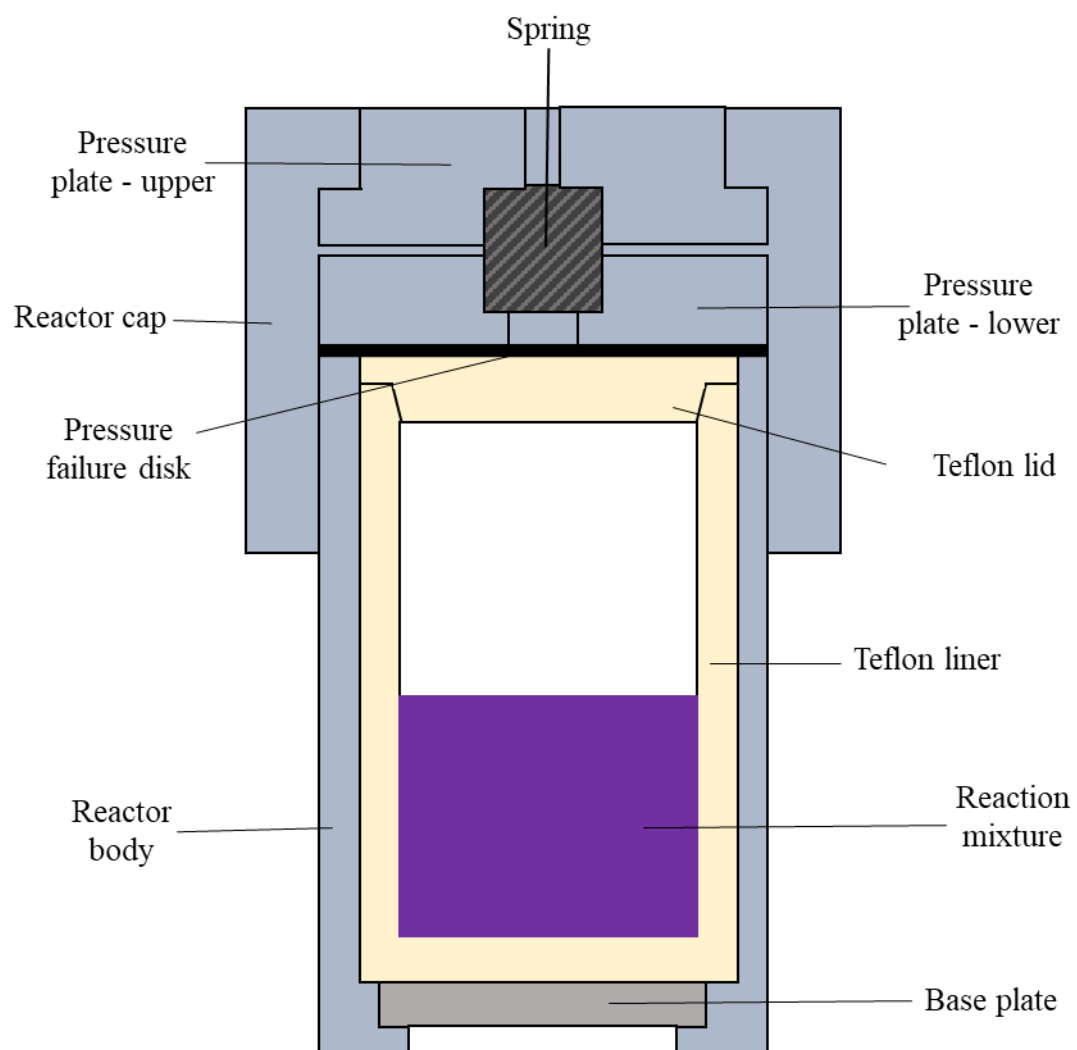


Figure 2. 1: Schematic of a solvothermal autoclave reactor, not drawn to scale.



Figure 2. 2: Image of 50 mL Parr instrument company Teflon lined stainless steel autoclave reactor.

The autoclave reactor is made up of two primary components, a stainless-steel body and a Teflon liner, see figure 2.1 and 2.2. These two components are used to create a reactor capable of containing the high-pressure reaction inside. In order to prevent catastrophic failure of the reactor vessel, a safety pressure disc is used. This disc allows for the venting of pressure upon the Teflon liner rupturing.

2.1.1 Metal sulfide synthesis

The method for synthesising transition metal sulfides was the direct reaction between elemental sulfur and the acetate (II) salt of the metal. This process would require the use of a surfactant and templating, in the form of oleylamine.

The reaction proceeds by the reduction of elemental sulfur to hydrogen sulfide (H_2S) and other active sulfur species, which upon pressurisation within the autoclave, react with the metal salt thereby precipitating the metal sulfide nanoparticles from solution.

The general method for producing the metal sulfide nanoparticles was to prepare an ethanol-based suspension of the metal (II) acetate and sulfur powder that was then sonicated to suspend all solids before adding the oleylamine. The suspension was then added to the Teflon liner before placing the liner in the stainless-steel body and sealing the reactor. The reactor was then placed in a thermostatically controlled oven for up to 24 hours.

Once the required reaction time had elapsed, the oven was cooled to room temperature at a cooling rate of $5\text{ }^\circ\text{C}/\text{min}$ after which the autoclave was removed. The solid material was obtained from the reaction mixture by centrifugation at 2500 rpm, washing first with ethanol and then hexane ($3 \times 15\text{ mL}$ each) and dried at room temperature, under vacuum, for 12 hours. The materials were then stored in a vacuum desiccator until use.

2.2 Electromagnetic radiation characterisation

2.2.1 Crystallography

In this thesis, the catalyst material prepared consists of a solid material with a fixed regular repeating lattice of atoms, ions or molecules, as opposed to random free floating atoms, ions or molecules. Solid materials generally have a fixed, long-range order in the arrangement of atoms that make up the crystal structure. The crystal structure can be described in terms of the symmetry of the structure.

2.2.1.1 Symmetry operations

The specific arrangements of atoms and ions within a crystal structure is described by the symmetry operations present. These operations fall into one of two broad categories; point symmetry and translational symmetry.

Different point symmetry operations are described by the Hermann-Mauguin symbols as follows:

Axis of rotation – A rotation around an axis by $360^\circ/n$, where integer n represents the order of the axis (the number of times this rotation operation can be applied around the axis in 360°). This operation is represented by the symbol C_n .

Planes of symmetry – Mirror planes in which both sides of a plane are the mirror image of each other, given the symbol m .

Inversion – A centre of inversion, is an operation whereby inversion of coordinates (x, y, z) will generate an identical point at $(\bar{x}, \bar{y}, \bar{z})$, where bar represents the negative or opposite value, given symbol $\bar{1}$.

Inversion axis – A combination of an axis of rotation and an inversion, given symbol \bar{n} , where rotations around an axis by $360^\circ/n$ is followed by an inversion.

Improper rotation axis – A combination of an axis of rotation and a plane of symmetry, given symbol \tilde{n} , where rotation around an axis by $360^\circ/n$ is followed by a reflection in a mirror plane, that is perpendicular to the rotation axis.

Improper rotation axes are generally not used to describe crystal structures, this is in part due to their innate similarity to inversion axes. Equivalent inversion and improper rotation axes are shown in table 2.2.

Improper rotation axis	Inversion axis
$\tilde{1}$	$\bar{2}$ (m)
$\tilde{2}$	$\bar{1}$
$\tilde{3}$	$\bar{6}$
$\tilde{4}$	$\bar{4}$
$\tilde{6}$	$\bar{3}$

Table 2.4: Equivalent improper rotations and inversion axes.

Translational symmetry operations are only found in the solid state and consist of two primary operations.

Glide plane – A combination of translation with a plane of symmetry, reflection in the plane of symmetry is followed by a translation parallel to the plane by a distance of $\frac{1}{2}$. The direction of the plane along the axes (a, b, c) is dependent on the spacegroup symbol. n represents the translational distance with respect repeat distance parallel to the translation. The notation of this operation for example $a/2$ represents a translation along the a axis by a distance of $\frac{1}{2}$ the unit cell a parameter e.g. Pn is $P1n1$; hence there is a reflection perpendicular to b and the glide is an n-glide along a and c.

Screw axis – A combination of rotations with translation. A rotation of $360^\circ/n$, where integer n represents the order of the axis, is followed by a translation. Given the symbol n_m , where m represents the distance of the translation. m depends on the repeat distance parallel to the axis, t, such that $m = n \times t$. For instance, 2_1 represents rotation of 180° followed by a translation of $\frac{1}{2}$ the repeat distance, and 6_3 represents a rotation of 60° followed by a rotation of $\frac{1}{2}$ the repeat distance.

2.2.1.2 Crystal Systems

In order to visualise the crystal structure of a solid material, the material is broken up into continuous repeating units referred to as the unit cell. The unit cell is the simplest three-

dimensional “building block” of a solid crystalline structure that can be repeated in all planes in a regular way to correspond to the long-range crystal structure of the material.

The unit cell is defined in terms of the cell parameters, length of the cell edges (a , b and c), and the angles α , β and γ , shown in figure 2.3.

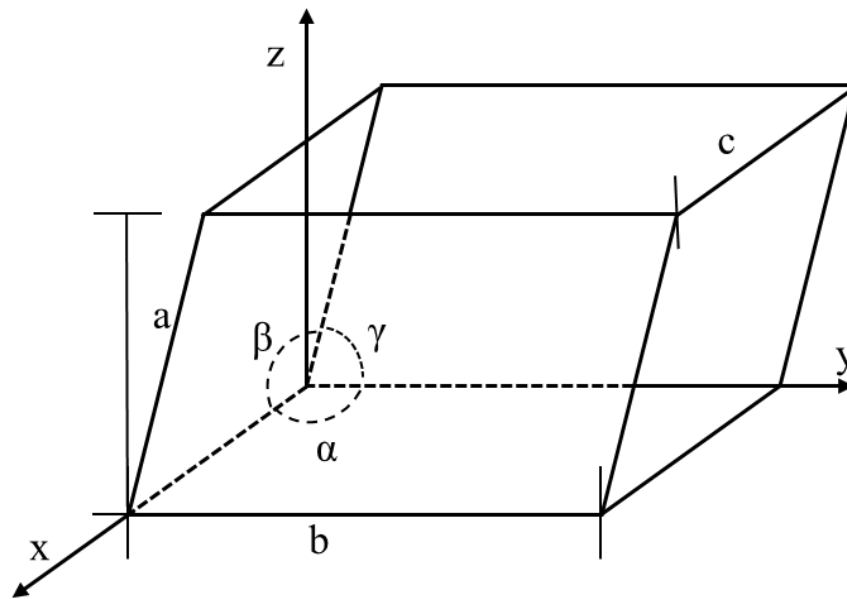


Figure 2. 3: Representation of a unit cell showing axes (x , y , z), unit cell parameters (a , b , c) and angles (α , β , γ).

Unit cells are categorised into one of seven distinct “crystal systems” depending on the relationship between the unit cell parameters a , b and c ; and the angles α , β and γ . These relationships and requirements that correlate to each crystal system is shown in Table 2.3.

System	Unit cell restrictions	Minimum symmetry requirements
Triclinic	$\alpha \neq \beta \neq \gamma \neq 90^\circ$ $a \neq b \neq c$	None.
Monoclinic	$\alpha = \gamma = 90^\circ$ $\beta \neq 90^\circ$ $a \neq b \neq c$	One twofold axis or one symmetry plane.
Orthorhombic	$\alpha = \beta = \gamma = 90^\circ$ $a \neq b \neq c$	Any combination of three mutually perpendicular twofold axes or planes of symmetry.
Trigonal	$\alpha = \beta = \gamma \neq 90^\circ$ $a = b = c$	One threefold axis.
Hexagonal	$\alpha = \gamma = 90^\circ$ $\beta = 120^\circ$ $a = b \neq c$	One sixfold axis or one sixfold improper rotation axis
Tetragonal	$\alpha = \beta = \gamma = 90^\circ$ $a = b \neq c$	One fourfold axis or one fourfold improper rotation axis
Cubic	$\alpha = \beta = \gamma = 90^\circ$ $a = b = c$	Four threefold axes along the unit cell diagonals

Table 2.5: The seven crystal systems.

2.2.1.3 Lattices

When equivalent points are evenly spaced in a regular array, in one, two or three dimensions, this is known as a lattice. A unit cell is the smallest translational repeat of the lattice. Points may have ions, ionic groups, atoms or molecules placed on each point to make a structure. Within a unit cell, there are four possible lattice types.

These four lattice types are shown in figure 2.4. The primitive lattice type (given the symbol P) is the simplest three-dimensional lattice type, consisting of a single lattice point per unit cell. Lattices can be characterised by their packing density of the points contained within. The packing density of a primitive cubic lattice is 52 %. The body centred lattices (given the symbol

I) equals the primitive lattice with the addition of a single lattice point at the centre of the unit cell, thereby consisting of a total of two lattice points per unit cell. The maximum packing density of a body centred cubic unit cell is 68 %. The all face-centred cubic unit cell (given the symbol F) consists of a lattice point at all corners of the unit cell, as well as a lattice point at the centre of each face of the unit cell, thereby giving a total of four lattice points per unit cell. The corresponding maximum packing density in an all face-centred cell is 74 %. This is the highest possible packing density of any crystal structure using a rigid sphere model. Finally, side-centred unit cell (given the symbol A, B or C) consists of a lattice point on all four corners, as well as a lattice point on a pair of opposite faces, e.g., the b and c planes for an A type. Face centred unit cells consist of two lattice points per unit cell, thereby giving a maximum packing density of 74 %.

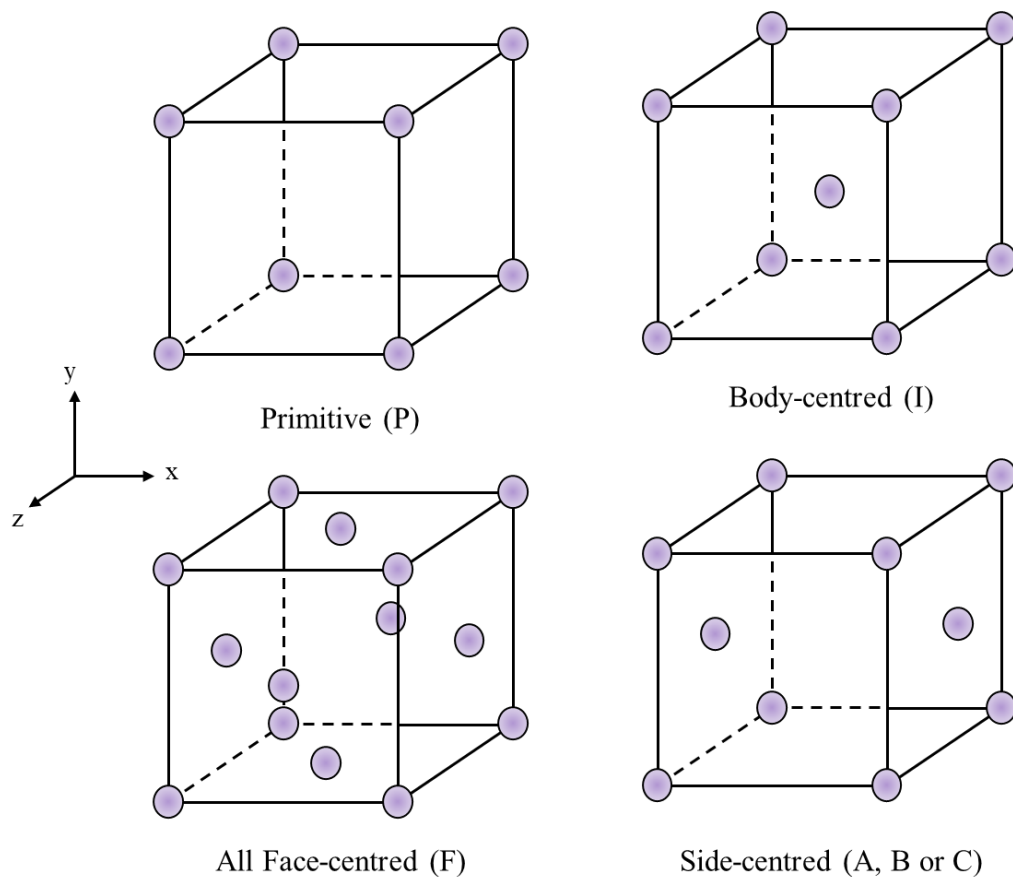


Figure 2. 4: Examples of primitive (P), body-centred (I), all face-centred (F) and side centred (A shown) unit cell lattice types.

The seven crystal systems (section 2.2.1.2) can be combined with the four lattice types (section 2.2.1.3) to result in fourteen distinct groups, known as Bravais lattices. These fourteen result from the combination of various symmetry operations required for the seven crystal systems, which exclude certain combinations. These fourteen Bravais lattices are listed in Table 2.4.

Crystal system	Lattice symbol
Triclinic	aP
Monoclinic primitive	mP
Monoclinic centred	mC
Orthorhombic primitive	oP
Orthorhombic C-face-centred	oC
Orthorhombic body-centred	oI
Orthorhombic face-centred	oF
Tetragonal primitive	tP
Tetragonal body-centred	tI
Trigonal (Rhombohedral)	hR
Hexagonal primitive	hP
Cubic primitive	cP
Cubic body-centred	cI
Cubic face-centred	cF

Table 2.6: The fourteen Bravais lattices.

In theory, a three-dimensional shape can have an unlimited number of symmetry elements of its own, therefore being categorised by an unlimited number of possible point groups. However, the number of possible point groups, when combined with the seven possible crystal systems, is reduced. The reduction of possible point groups is due to the crystal system consisting of an array of interconnected polygons with no voids between them or overlapping of the polygons. From these reductions, a total of 32 point groups remain possible, when combined with the 7 crystal systems.

Finally, the 32 possible point groups are combined with the 14 Bravais lattices and the translations symmetry operations resulting in the 230 “space groups”. These space groups are used to describe the crystal structures of all crystalline solid materials.

2.2.1.4 Space groups and notation

Each of the 230 space groups is described by combining the notation for each of the crystal systems (P, F, I, R, C) with the Hermann-Mauguin symmetry operations along the x , y and z axes. For example, the space group $Fm\bar{3}m$, corresponds to a face-centred cubic crystal system, there is a mirror plane perpendicular to the $\langle 100 \rangle$ direction and a $\bar{3}$ rotation along $\langle 111 \rangle$ axis, and a mirror plane perpendicular to the $\langle 110 \rangle$ axis.

In addition to describing the overall crystal structure of a solid material, it is also important when discussing diffraction (section 2.2.2) to describe specific points or planes within the crystal structure of a solid material.

Lattice planes are parallel sets of planes along a lattice which intersect many lattice points in the crystal structure. Lattice planes are described using Miller indices. Miller indices use three points at which the plane intersects the a , b and c unit cell parameters. Lattice planes are referred to using the h,k,l notation, where h , k and l are a reciprocal of the distance along the cell parameter, a , b and c respectively. For example, a cross section which intersects along $\frac{1}{2} \times a$, $1 \times b$ and $\frac{1}{3} \times c$, is given the index (213). The crystal structure of NaCl ($Fm\bar{3}m$) with the (111) lattice plane is shown in Fig. 2.5.

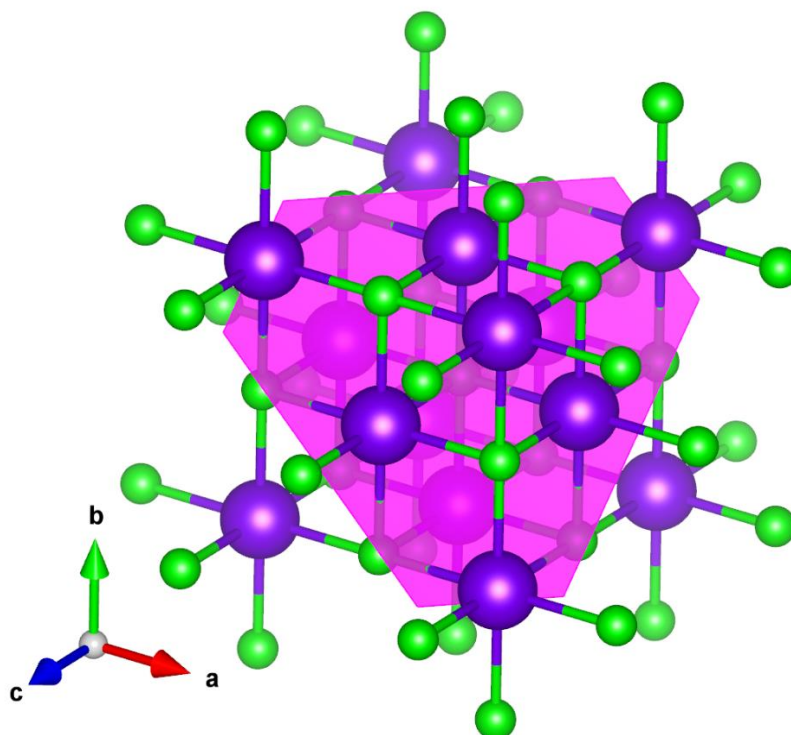


Figure 2. 5: Crystal structure of NaCl, with (111) lattice plane shown in pink. The purple spheres represent sodium cations, and the green spheres represent chlorine anions.

In certain cases, several different lattice planes within a crystal structure are equivalent, for example in a face centred cubic (*fcc*) unit cell (space group $Fm\bar{3}m$) as shown by NaCl (Fig. 2.5) the (100), (010) and (001) planes are equivalent, due to the symmetry operations of the space group.

2.2.1.5 X-ray diffraction

X-ray diffraction is a non-destructive analytical technique used in the analysis of the crystal structure of solids using electromagnetic radiation. The first use of x-rays to analyse a compound was carried out by Friedrich, Knipping and Max von Laue in 1912 analysing single crystals of copper and zinc sulfates.²⁰³⁻²⁰⁸ X-rays are a type of EM radiation with a wavelength, λ , significantly shorter than that of visible light on the scale of approximately 1 \AA (10^{-10} m) this scale happens to also be on the scale of the separation of lattice planes within a crystal.^{205, 207-}

2.2.1.5.1 Theory of diffraction

X-ray diffraction relies on the occurrence of “phase shift”, this occurs when two or more waves arrive at the same point however waves are out of phase. Phase shift is measured as difference in the phases of the two incoming waves with respect to their wavefronts.^{203, 205, 206} Due to the waves being transverse this shift is measured as linear shift, Δ measured in wavelength units, or equivalently phase shift, $\delta\phi$ on an angular scale. This relationship between linear shift and phase shift is shown in figure 2.6. The relation between these units and the incident x-ray wavelengths is shown in equation 2.1.²⁰³

$$\frac{\Delta}{\lambda} = \frac{\delta\phi}{2\pi} \rightarrow \delta\phi = \frac{2\pi}{\lambda} \Delta \quad \text{Equation 2.1}$$

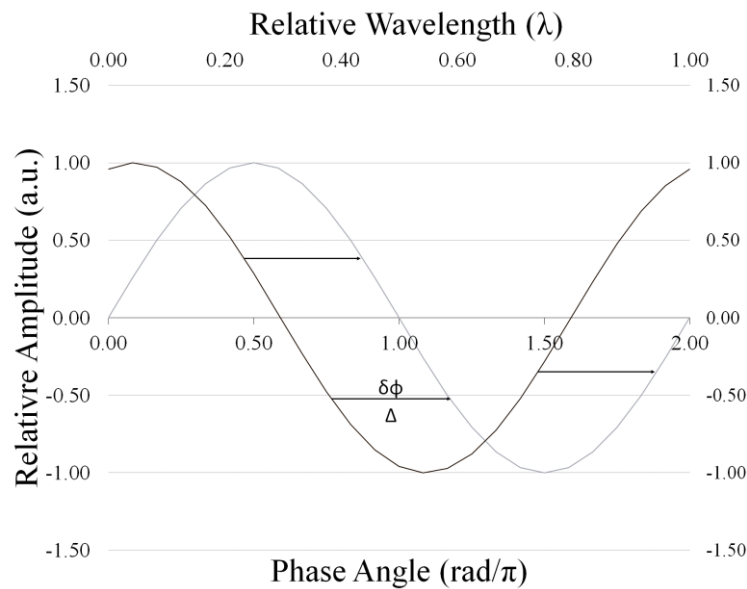


Figure 2. 6: The graphical illustration of how phase shift relates between two sine waves of identical amplitude.²⁰³

X-ray diffraction is the measurement of the intensity of reflected x-rays. The x-rays are reflected by the electrons bound to atoms/ions within a unit cell. Waves reflected by electrons at different positions collect at the detector with a relative phase shift. This data can then be interpreted to determine relative atomic positions. The measured intensity is related to the

phase shift ($i\phi$) and the amplitudes of the sum of all incoming waves (A_j), equation 2.2 demonstrates how this relationship is approximated, where.^{203, 205}

$$I = [\sum_j A_j \exp(i\phi_j)]^2 \quad \text{Equation 2.2}$$

In XRD the Fraunhofer approximation is used to calculate the relative intensities with respect to the lattice d spacings. The distances between the lattice planes within the crystal are many orders of magnitude lower than the distance from the sample to the detector. In equation 4 this is approximation of intensity and the phase shift (ϕ) depend on the position of the atoms present at the convergence point j . Therefore, since in incoming and outgoing x-ray vectors are known the inter atomic/ionic distances can be inferred based on the detected intensities at specific angles of 2Θ .^{203, 205, 210}

Bragg analysis treats a crystallographic plane like a mirror with x-rays behaving like visible light, reflecting from these “mirror surfaces”.^{203, 205} However since x-rays are far more energetic than visible light the x-ray penetrates thousands of mirror planes deep into the material, where additional reflections may occur. Since all mirror planes are separated by the same distance and in the same direction, superposition of scattered x-rays occurs, this constructive interference only occurs if the distance between the planes are a multiple of the wavelength.

Since there is always a deeper plane for which there is an exactly 180-degree phase shift, perfect destructive interference occurs at all angles on an x-ray diffraction pattern.²⁰⁷⁻²⁰⁹ Therefore equation 3 can be altered to give equation 2.3, the Bragg equation where n is an integer, λ is the wavelength, d is the inter-atomic spacing and Θ is the incident angle of the x-rays relative to the sample.^{203, 205}

$$n\lambda = 2d \sin \Theta \quad \text{Equation 2.3}$$

Sharp maxima seen in x-ray diffraction, relate to the angle and wavelength, λ , of the incident and outgoing x-rays, 2θ . This is shown in Fig. 2.7.

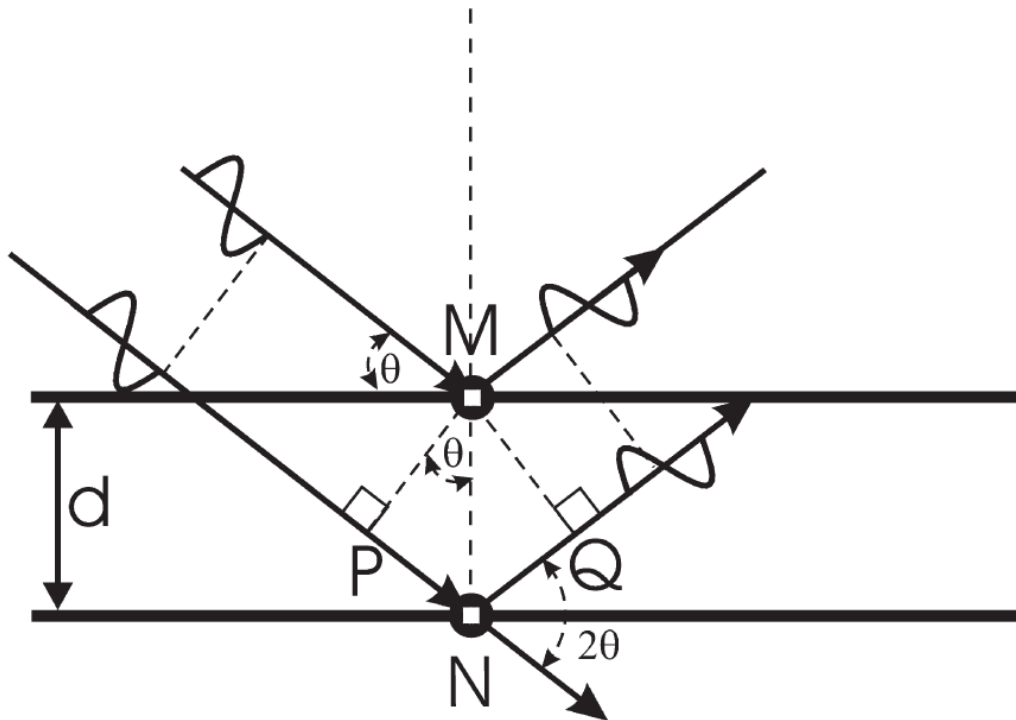


Figure 2. 7: Illustration of how the geometry of ray reflection is used in the derivation of the simplified Bragg equation. With the incoming and outgoing x-rays being reflected through angle 2θ between two parallel lattice planes, M and N, separated by lattice spacing d .²⁰³

The simplified Bragg equation has a serious drawback, as x-rays are not reflected by planes but are scattered by the electrons bound to atoms in a crystal structure. Crystal planes are not perfect mirrors but are made up of discrete atoms with regions of much lower electron density between. However, due to the fundamentals of geometry the Bragg equation is a good approximation and therefore is still useful despite this drawback.^{203, 204, 210-213} It can be used in determining the d spacings within lattices which are then used to give the hkl values useful in identifying a crystal structure.

2.2.1.5.2 Coherent diffraction domain size estimation in XRDFor infinitely sized crystals there is a majority of the unit cells present in the bulk of the material compared to the surface. Therefore, the majority of the unit cells are uniform in shape and are unstrained by the surface morphology

of the crystal.^{203, 204, 212, 213} In a finitely sized crystal, on the size order of tens to hundreds of unit cells, such as nanoparticles, those unit cells present on the surface are highly strained and compose a larger percentage of all unit cells present. Another factor influencing peak broadening within PXRD patterns can be attributed to the interference of electromagnetic waves which is key to the operation of x-ray diffraction. In materials with a theoretically infinite potential reflection planes, total destructive interference of the x-rays occurs creating sharp well-defined peaks. However, when the number of these reflection planes becomes finite, total destructive interference of the x-rays does not occur thus losing resolution of the peak resulting in broadening. Due to the strain and finite reflection planes within a nanoparticle, the peaks observed within a PXRD pattern tend to show broadening.

This broadening can be summarised using the Scherrer equation, shown in equation 2.4. Where the broadening of the peak at half height, β , can be related to the mean size of the crystallites, τ , by the shape factor, K , and wavelength of the x-ray radiation, λ .²⁰³

$$\tau = \frac{K\lambda}{\beta \cos\theta} \quad \text{Equation 2.4}$$

This would be useful in the interpretation of the PXRD data as an approximation in the size of the obtained particles prior to confirmation by TEM analysis.

The mode of operation of a powder x-ray diffractometer is generally the same for all diffractometers, a source of x-rays, a sample stage and a detector. A cross sectional schematic of a powder diffractometer is shown in Fig. 2.8.

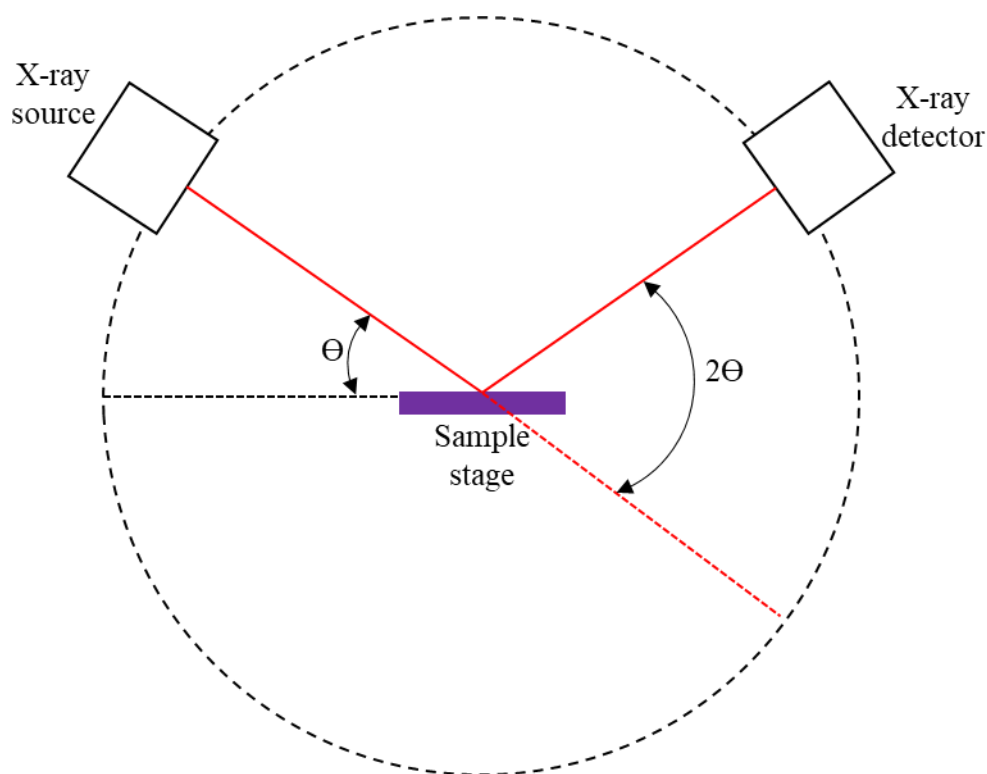


Figure 2. 8: Cross section of a powder x-ray diffractometer with the components labelled.

The x-ray source is typically an x-ray tube, consisting of electron gun and a metal target. Inside the x-ray tube the electrons from the gun are accelerated towards the metal target, copper or molybdenum in most cases. When the electrons collide with the target high energy photons are emitted in the form of x-rays. These x-rays are then focused and reflected by a monochromator, to ensure the x-ray beam is of uniform energy.

The x-ray beam is reflected from the sample surface, as described earlier in this section, and then passes into the detector. Modern PXRD instruments typically use a strip detector, such as the PIXcel detector from Empyrean. In these detectors, x-rays enter and excite a strip of n-type silicon producing a voltage that is read out by the instrument. The advantages of strip detectors versus older Geiger-Muller detectors are the higher count rate and increased spectral resolution.

2.2.1.5.2 PXRD equipment and procedure

Powder X-ray Diffraction was carried out on all obtained compounds using a PANalytical Empyrean X-ray diffractometer using Cu $K\alpha_1$ radiation. Results were recorded using the

instruments inbuilt software. Obtained patterns were analysed using PANalytical Highscore Plus.

The sample was placed in a sample holder as shown in Fig. 2.9 and placed in the diffractometer's autosampler. The program for the diffractometer to collect the pattern was collecting data from 2θ angles 20° to 80° with the collection time at each point being 1521 s and a step of 0.02626° . To prevent system variance between samples all samples, would also be analysed using a 1° fixed slit at the x-ray tube and using a Ni anti-scatter filter, to prevent the fluorescence of certain first row transition metals under $\text{Cu K}\alpha_1$ radiation. During the data collection the sample was rotated at 0.5 rotations per minute.

Sample preparation for PXRD analysis required a flat surface obtained using a specialised sample preparation device, shown in Fig. 2.9. The sample preparation device involved the use of 3 components shown in figure below, the sample preparation holder which held the sample template in place during sample addition and when attaching the sample baseplate. The data collected were analysed to determine phase purity of the sample, unit cell parameter determination and particle size estimation.

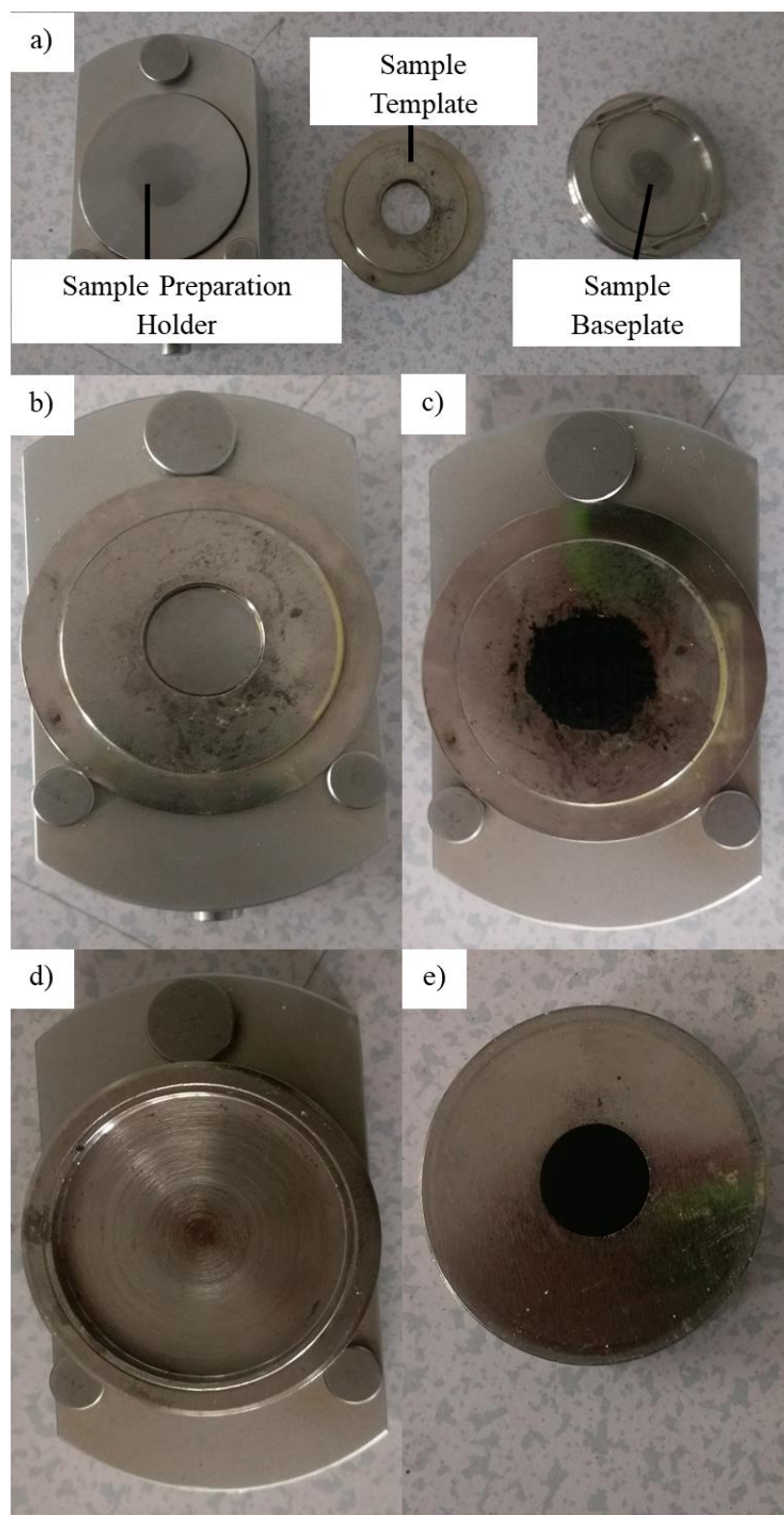


Figure 2. 9: a) Flat surfaced sample holder for PXRD analysis with items labelled. b) The template is locked into the sample holder. c) The template filled with sample. d) baseplate is then connected to the template. e) Sample holder is then flipped over and e) sample is released to reveal a flat surface.

Once the sample filled the sample template, the baseplate is attached to the template. This is then turned over and released to reveal the flat sample surface. The sample template was then

placed in the diffractometer, an image of the diffractometer interior with the key components labelled is shown in Fig. 2.10.

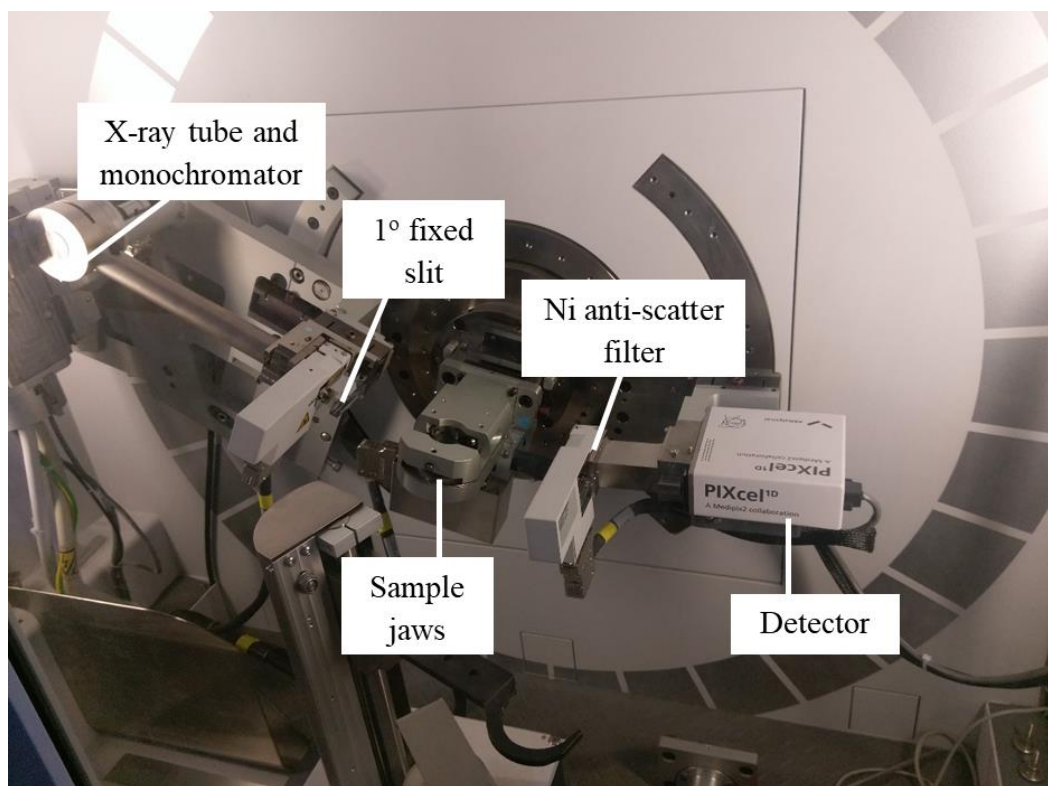


Figure 2. 10: PANalytical Empyrean X-Ray diffractometer with key components labelled.

2.2.2 Fourier Transformed Infra-Red Spectroscopy (FTIR)

Fourier Transformed Infra-Red spectroscopy is a widely used spectroscopic technique which relies on the discrete stretching energies of various bonds. This spectroscopic technique uses light in the energy range between 800 cm^{-1} and 4000 cm^{-1} . The mid infrared region of the electromagnetic spectrum is used to study the fundamental vibrations associated with chemical structure and bonding. Infrared spectroscopy exploits the inherent resonance frequencies of chemical bonds by measuring the absorbance specific frequencies associated with a bond vibration. These bond vibrations are determined by the bond strength, mass of the atoms involved and the associated vibronic coupling.

For a bond to be considered “IR active”, throughout its vibrational mode there must be a change to its permanent dipole moment. Shown in Fig. 2.11 is an example carbonyl bond which upon irradiation by IR radiation, $\nu = 1720\text{ cm}^{-1}$, it begins to vibrate in its fundamental frequency. This stretch is “IR active” due to the permanent dipole of the bond being changed by the vibration of the bond length.

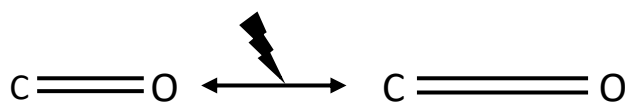


Figure 2. 11: IR active CO bond vibrating at its fundamental vibration mode when irradiated by infrared radiation, $\nu = 1720\text{ cm}^{-1}$.

FTIR analysis was carried out using attenuated total reflectance (ATR). ATR is a technique used for analysing solid and liquid samples with minimal sample preparation. The technique requires contact between the sample and diamond ATR crystal. Due to the differing refractive indices, of the sample and ATR crystal, total internal reflection occurs. In principle, the sample and IR light only interact at the point of internal reflection, the so called “evanescent wave”.

The evanescent wave cannot properly propagate into the sample, due to the total internal reflection of the IR beam (shown in Fig. 2.12). As this wave cannot propagate into the sample, it becomes focused on the point of internal reflection and starts decaying exponentially. Thereby, causing the evanescent wave to protrude into the sample, see figure for ATR schematic. With the sample in contact with the evanescent wave, specific regions of the IR beam are absorbed based on the sample’s composition. Therefore, the reflected IR beam has the absorbed regions missing and thus is attenuated, hence “attenuated total reflectance”.

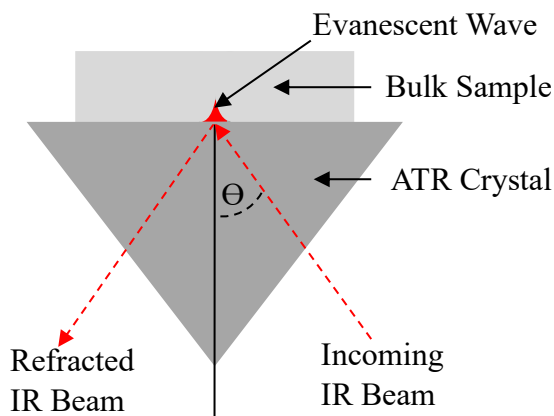


Figure 2. 12: schematic of attenuated total reflectance FTIR with evanescent wave.

Samples for ATR FTIR analysis were dried in vacuo prior to analysis. FTIR spectra were obtained using a ThermoScientific Nicolet iS5 spectrometer fitted with a Pike Miracle diamond ATR scanning from 800 cm^{-1} to 4000 cm^{-1} . The spectra were analysed using Omnic software.

2.2.3 Solid State Ultraviolet Visible Near Infra-Red Spectroscopy (UVVIS NIR)

Ultraviolet Visible spectroscopy (UVVIS) analysis is traditionally accomplished by measuring transmission of UVVIS light in solution/suspension making analysis of solids difficult. Transmission spectroscopy of solids often yields little information outside of particle size, but this is limited to particles with diameters equal to the smallest UV wavelength. UVVIS therefore requires a different method to obtain useful information from the spectroscopy. Diffuse reflectance is used to determine the band gap of semiconductor materials along with other electronic effects.

In principle, diffuse reflectance spectroscopy (DRS) is independent of the incidence angle of the light on a non-smooth surface, therefore a specific angle is not required to analyse this diffuse reflected light. Some of the incoming light waves are absorbed by the analyte material while others are reflected, thus allowing for the analysis of the electronic structure of the material. According to the theory of P. Kubelka and F. Munk presented in 1931, the measured

reflectance spectra can be transformed to the corresponding absorption spectra by applying the Kubelka–Munk function. The region showing a steep, linear increase of light absorption with increasing energy is characteristic of semiconductor materials. The x-axis intersection point of the linear fit of the Tauc plot gives an estimate of the band gap energy. This sharp transition occurs when electrons from the valence bands are given energy by photons, equal to the band gap, and transition into the conduction band.

Diffuse reflection requires a shallow penetration of the surface material, which then interacts with the material absorbing certain wavelengths whilst others pass through the material. In this way it can be seen as similar to the previously discussed ATR FTIR spectroscopy (section 2.2.2), however, in ATR FTIR the specular reflected wave is measured. Whereas in DRS, the diffuse reflected wave is measured. A schematic of how the incident beam is split into the specular reflected beam and the diffuse beams is shown in Fig. 2.13.

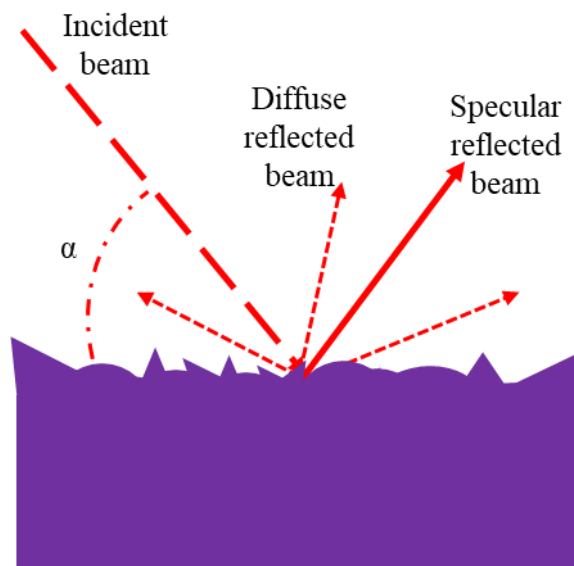


Figure 2. 13: Schematic of the diffuse reflection mechanism on a rough surface.

Diffuse reflected beams are reflected in all directions from the sample yet are all seen to be equivalent. Therefore, when concentrated together by a concave parabolic mirror, these collated beams constructively interfere amplifying the features of the absorbed regions. A

schematic of how the incident beam is reflected and the diffuse reflections are collated is shown in Fig. 2.14.

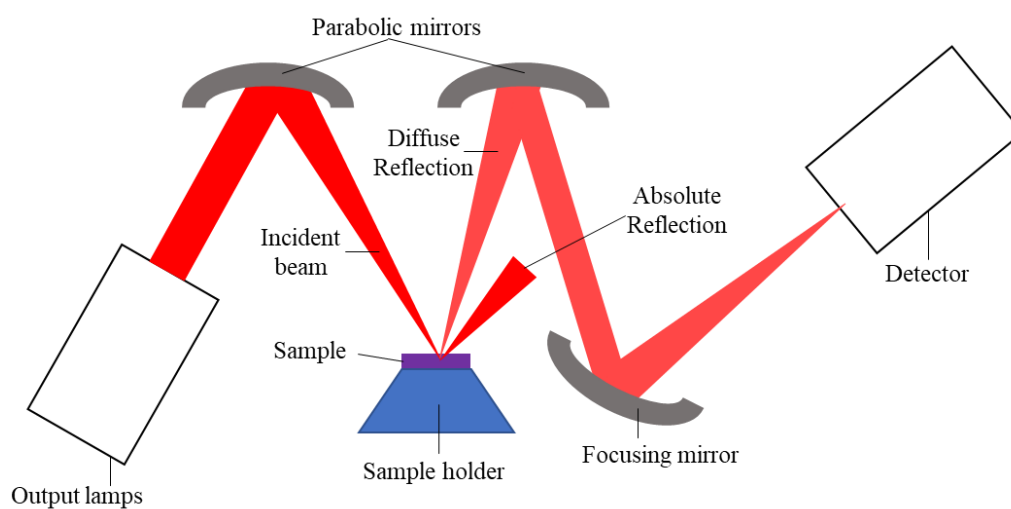


Figure 2. 14: Schematic of the UVVIS NIR spectrometer with key components labelled.

UVVIS NIR spectroscopy was carried out using a Varian Cary 5E UV-Vis-NIR Spectrometer equipped with a Harrick Praying Mantis diffuse reflectance device, Fig. 2.15.

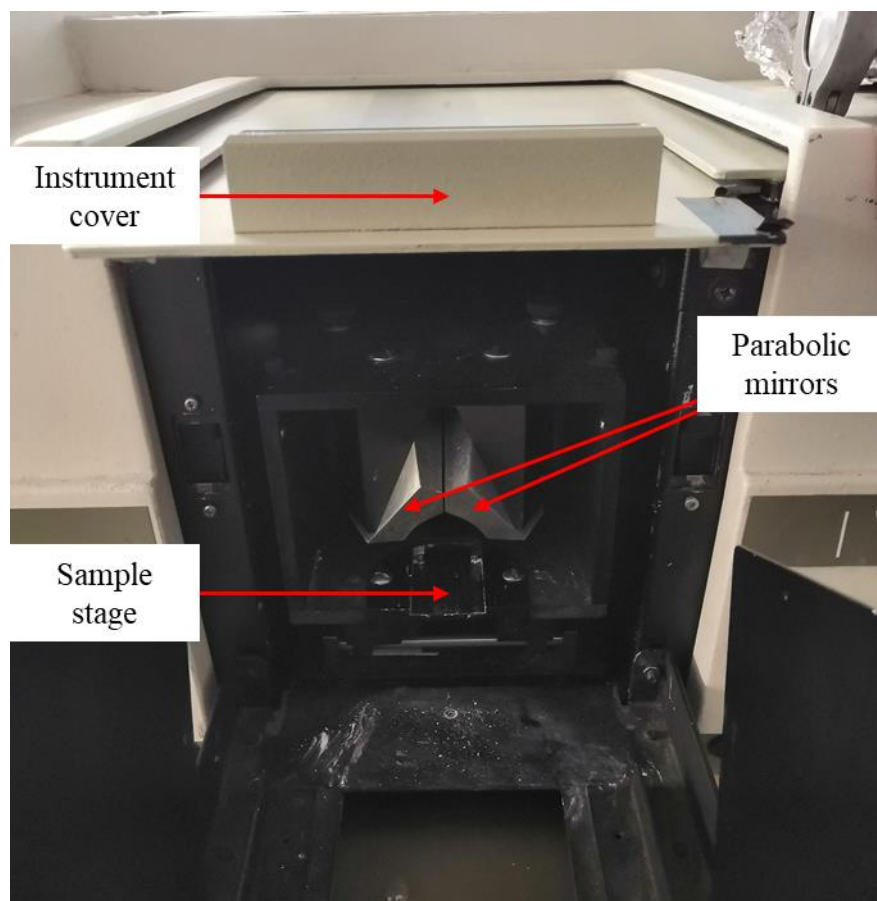


Figure 2. 15: interior of UVVIS NIR instrument with key components labelled.

The UVVIS NIR instrument was first calibrated using BaSO_4 to obtain a reference reflectance i.e., 100 % reflectance. BaSO_4 was used as a calibrant as it exhibits excellent reflectivity across the EM spectrum. Samples for UVVIS NIR spectroscopy were diluted in BaSO_4 (4:1 ratio of BaSO_4 :Sample by weight) shown in Fig. 2.16.

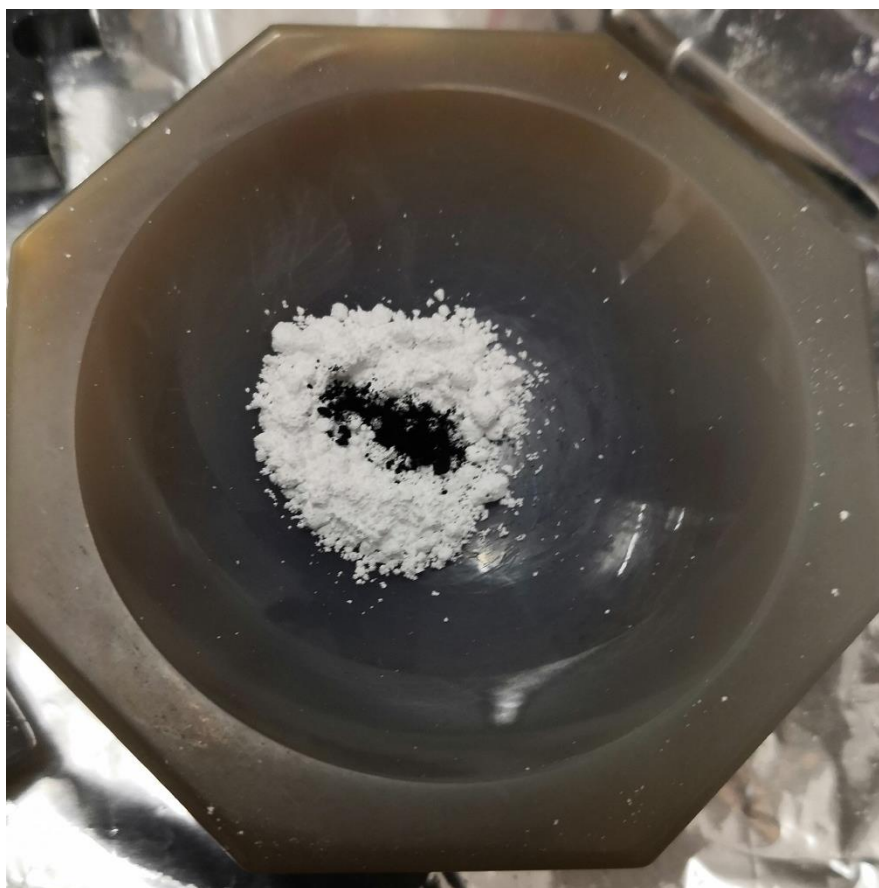


Figure 2. 16: Sample with BaSO₄ diluent prior to grinding and preparing for UVVIS NIR analysis.

Data were recorded in the range of 200 nm to 2500 nm, band gap was estimated using the Kubelka-Munk function plotting wavelength versus F(R).

$$F(R) = \frac{(1-R)^2}{2R} \quad \text{Equation 2.5}$$

Equation 2.5 shows the calculation of F(R) where R is the reflectance. Kubelka-Munk relies on the measurement of the gradient maximum to determine the band gap of the material. At the gradient maximum, a tangential line is taken which intersects the x-axis at specific wavelength of light and by extension a specific energy of light (equation 2.6).

$$E = h \frac{c}{\lambda} \quad \text{Equation 2.6}$$

Equation x shows how a specific wavelength (λ) in nm can be converted to its respective energy (E) in Joules, using the speed of light (c) and Planck's constant (h). This energy is then converted to electron volts (eV) for standardised band gap measurements.

2.2.4 Transmission Electron Microscopy (TEM) with Energy-Dispersive X-ray Spectroscopy (EDX) and Electron Diffraction

Transmission electron microscopy (TEM) utilises electrons focused onto a sample, instead of photons used in more traditional microscopy. These electrons are then reflected or absorbed based on the imaging technique. TEM relies on the transmission of electrons through the sample with dark areas on the image showing area where more electrons are absorbed by the sample. Due to this transmission, samples for TEM are required to be thin (100 nm thick or less) for fine details to be resolved. The schematic of how a TEM instrument operates is shown in Fig. 2.17.

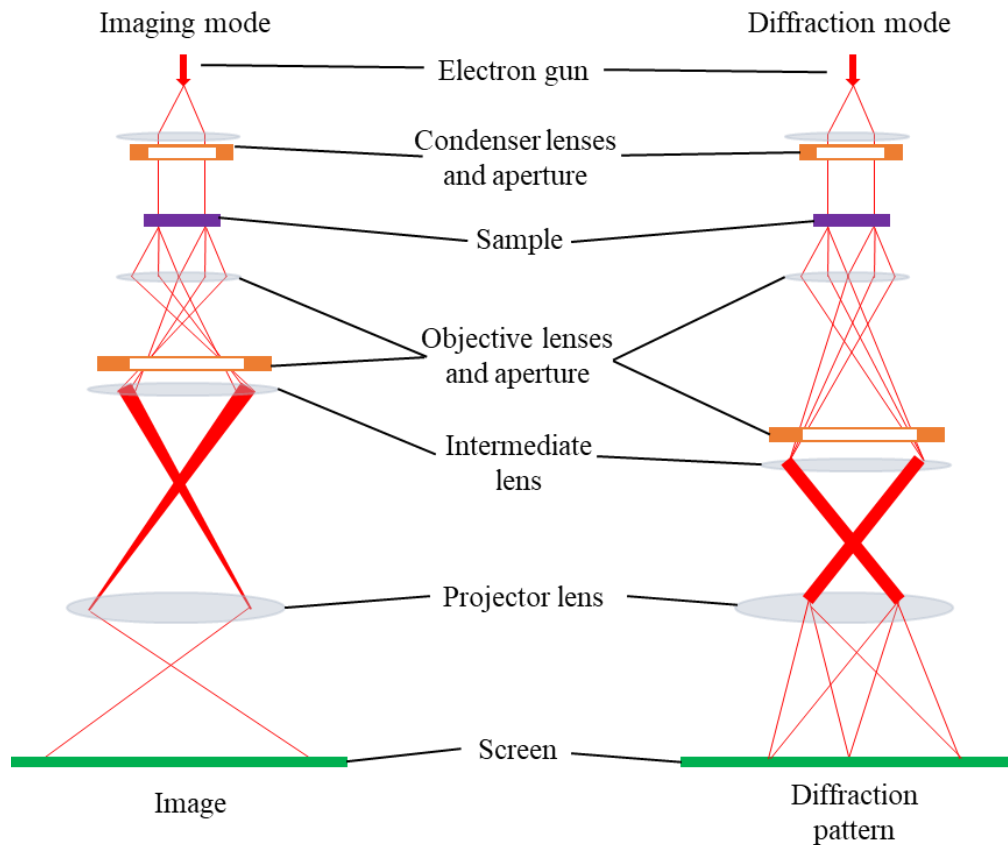


Figure 2. 17: Schematic of a TEM instrument in both imaging and diffraction modes.

Energy Dispersive X-ray spectroscopy (EDX) is a technique for analysing the elemental make up of a sample. This technique is used for elements with an atomic number greater than that of carbon. EDX involves the use of the electron beam used in the imaging process. The intense electron beam causes core electrons within the sample to be ejected creating an electron hole. These electron holes are then filled by electrons falling from higher energy levels emitting a characteristic x-ray photon, these photons are specific to each electron shell within an element producing a “fingerprint” for the element. This fingerprint is then interpreted from the spectrum of these photons. A schematic of an EDX set up is shown in Fig. 2.18.

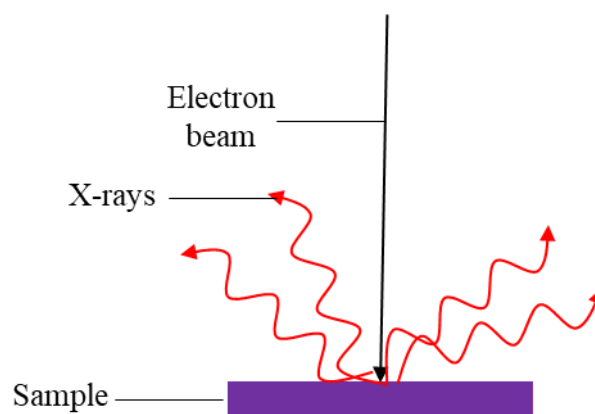


Figure 2. 18: Schematic of the operating principle of Energy Dispersed X-ray (EDX) spectroscopy.

Samples for transmission electron microscopy (TEM) were dispersed in acetone using an ultrasonic bath and a drop of this dispersion was placed on a carbon coated copper grid. These grids were then imaged by a Gatan Ultrascan 4000 digital camera with digital micrograph software, attached to a JOEL 2010 TEM instrument running at 200 kV. Nanoparticle sizes were determined by comparing several particles present in different areas of the grid using the Gatan Digital Micrograph software.

High Resolution Transmission Electron Microscopy (HRTEM) studies were performed in a high-resolution (HR) (0.18 nm) field emission JEOL 2200FS microscope operating at 200 kV, equipped with an in-column Ω energy filter, two High-Angle Annular Dark Field (HAADF) detectors for the so-called ‘Z-contrast’ imaging and an Energy Dispersive X-ray Spectrometer (EDX) for collecting X-ray spectra and X-ray mapping. The nanostructures were dispersed on holey copper grids for the observation. The particles were dispersed on the copper grids by dispersing the particles in ethanol, followed by evaporation to deposit the particles onto the grid.

2.3 Catalyst Testing

2.3.1 Selective hydrogenation substituted nitrobenzenes

Hydrogenation of substituted nitrobenzenes, via a hydride transfer mechanism, was carried out to test the performance of the catalyst material prepared in this work (Fig. 2.19).

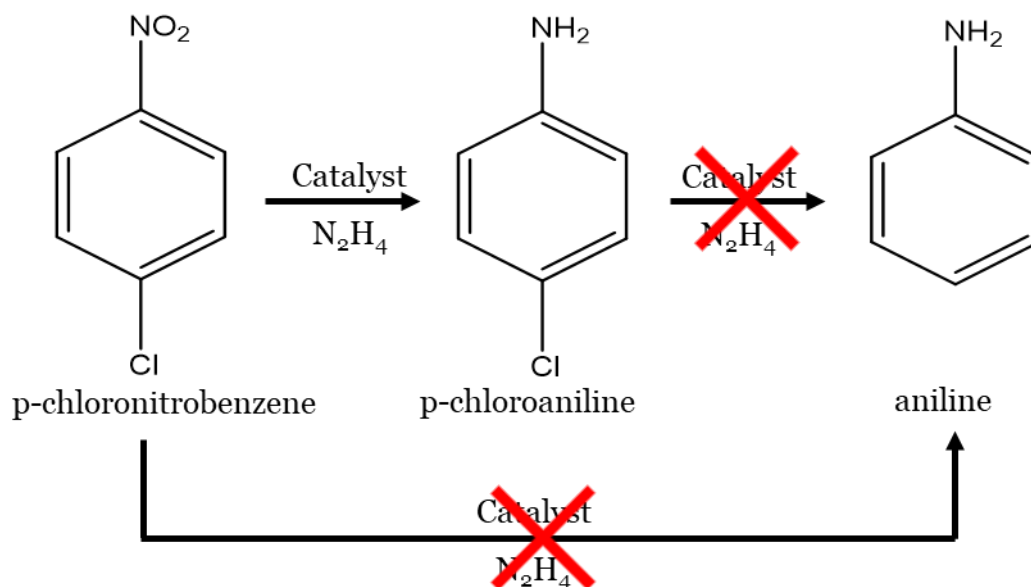


Figure 2. 19: Reaction scheme of the selective hydrogenation of p-chloronitrobenzene (p-CNB) to p-chloroaniline (p-CAN) without forming aniline (AN) using hydrazine (N_2H_4) as a hydrogen donor.

2.3.1.1 Apparatus and reactor

The hydrogenation of nitrobenzenes was carried out using a batch reactor, schematic shown in Fig. 2.20.

A standardised solution of the substituted nitrobenzene was prepared and added to a 3 necked round bottom flask fitted with suba seals on the side necks. A suba seal was used for the injection of hydrazine at the start of reaction, and the other to withdraw aliquots ($\sim 250 \mu\text{L}$) for off-line gas chromatography (GC) analysis of reaction progression.

The use of vacuum grease at the connections within the reactor was found to leach from the joints and contaminate the reaction and disrupt the GC results. Hence, the joints at the top and

bottom of the condenser was fitted with rigid PTFE sleeves and ground glass join clips (Fisher) to make the reactor gas tight. Vacuum grease was used at all other joints, in combination with ground glass joint clips.

A gas burette was used to monitor the volume of gas produced by the reaction. At the reaction start, the burette was filled with KCl saturated ethylene glycol (EG). The salt saturated ethylene glycol was used in order to avoid the dissolution of O₂, CO₂, etc. EG was selected to use in the gas burette due its low vapour pressure (0.0120 kPa at 25 °C), thus limiting the risk of EG vapour contaminating the reaction. When the reactor is open to the atmosphere, the EG level is maintained at the same height as the level of ethylene glycol in the EG feed flask. However, once the reactor is closed, and the reactor is subjected to pressure changes due to vacuum or gas release from the reaction, or when the reactor is purged, the height of the EG inside the burette changes to compensate for this pressure differential inside and outside the reactor. Therefore, the pressure during the reaction is maintained at ambient pressure. Further to this, prior to the start of a reaction the gas burette is filled, as close as possible, to "300 mL" at the top of the gas burette. Since N₂, and some unused H₂, is produced in the reaction, the level of EG falls to maintain ambient pressure. This drop in EG volume can be used as a crude measurement of reaction progress.

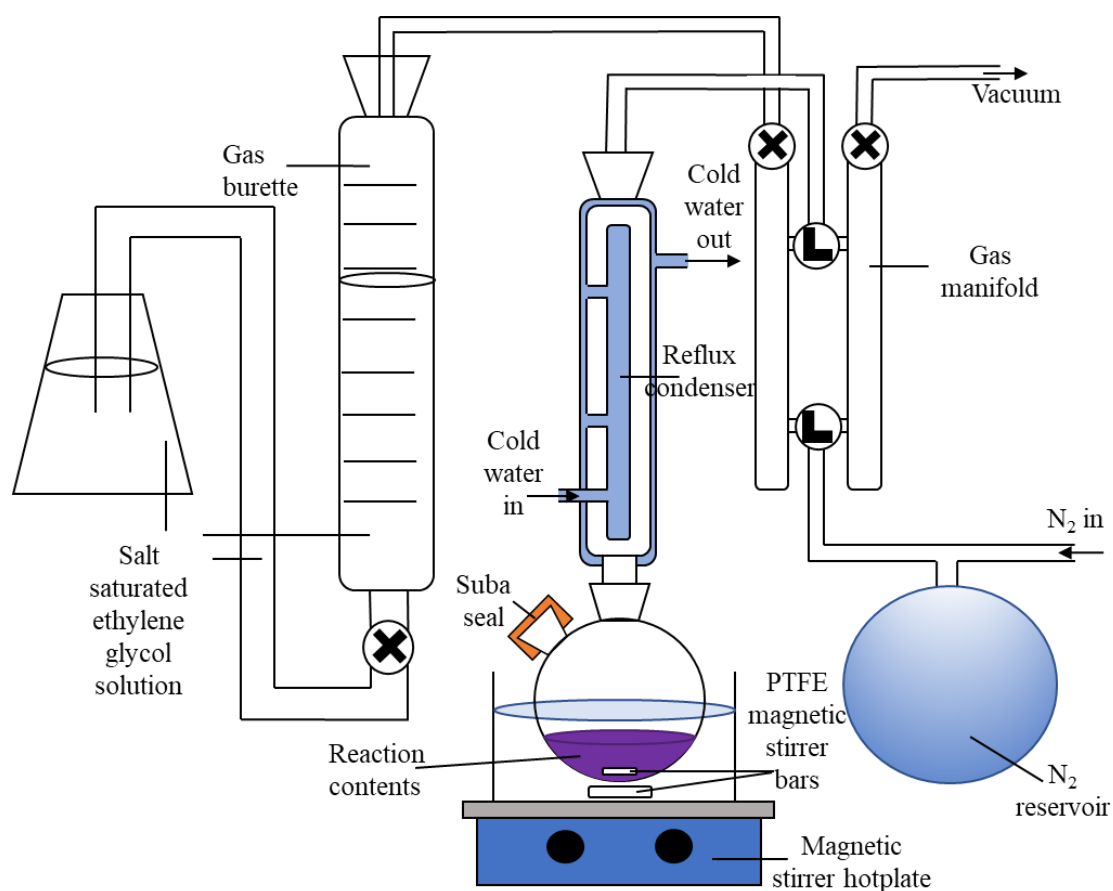


Figure 2. 20: Schematic of the apparatus used for the selective hydrogenation reactions in this work. The circles containing "X" represents taps which can be used to shut off and isolate parts of the reactor. The circles contain "L" represent multi-directional taps which can be used to connect the reactor to the left (N_2 supply) or the right (vacuum) hand sides of the gas manifold or can be closed off from both sides.

2.3.1.1.1 Determination of catalyst activity and selectivity

Conversion of substituted nitrobenzene substrate and selectivity towards the desired substituted aniline at different levels of conversion were calculated using Equations 2.7-2.9, where C_t = concentration of substituted nitrobenzene benzene substrate at time t , C_0 = initial concentration of substituted nitrobenzene substrate, C_{XAN} = concentration of substituted aniline product, $C_{products}$ = concentration of all products, aniline, substituted aniline and nitrobenzene, t = reaction time elapsed, respectively. Equations 2.8 and 2.9 imply that no other components other than, the substituted aniline, aniline and nitrobenzene were obtained. This was confirmed by the carbon balance for all reactions of $100 \pm 2\%$

$$\text{Conversion (\%)} = \left(\frac{C_0 - C_t}{C_0} \right) * 100 \quad \text{Equation 2.7}$$

$$\text{Selectivity (\%)} = \left(\frac{C_{XAN}}{C_{products}} \right) * 100 \quad \text{Equation 2.8}$$

The activity of a given reaction was characterised using the rate of substituted nitrobenzene substrate conversion, as in Equation 3, where C_0 = initial concentration of substituted nitrobenzene substrate, C_t = concentration of substituted nitrobenzene benzene substrate at time t , t = reaction time elapsed. This initial rate was taken at a set reaction time elapsed between 0 minutes and 20 minutes.

$$\text{Initial rate} = \frac{C_0 - C_t}{t} \quad \text{Equation 2.9}$$

2.3.2 Gas Chromatography (GC)

Chromatography is used to separate a range of different chemical compounds from an unknown mixture based on their interactions with the mobile and stationary phases. This technique is also used for the quantification of the chemicals based on a data compared to a standard calibration curve.

The technique involves the flow of a “mobile phase” comprised of a gas or liquid through a medium known as the “stationary phase”. The stationary phase for chromatography is typically a porous silica-based compound immobilised on a glass capillary, the mobile phase can either be a gas, gas chromatography (GC), or liquid, liquid chromatography (LC). Components of a chemical mixture will have differing polarities, causing an adsorption/desorption of the compound to the surface of the stationary phase. From this adsorption/desorption some compounds are retained for a longer on the stationary phase and so elute from the column later in the analysis. This enables the separation of different chemical species from the mixture to be analysed.

The technique used for the separation and quantification of chloronitrobenzene, chloroaniline, aniline and nitrobenzene would be gas chromatography (GC). For this work a calibration curve would need to be plotted, for each analyte, in order to quantify the compounds during a hydrogenation reaction.

The sample in GC can either be using a headspace technique or using a liquid sample, in either case the injector is heated to a specified temperature in order to force all compounds, including solvent, into the gas phase. This gas is then carried through the injector into the capillary column by an inert carrier gas, in this case it was helium. The column outer wall is typically made of fused silica glass with the interior coated with the stationary phase which can be modulated depending on the polarity of the compounds which were to be analysed. A Schematic of a typical gas chromatography set up is shown in Fig. 2.21.

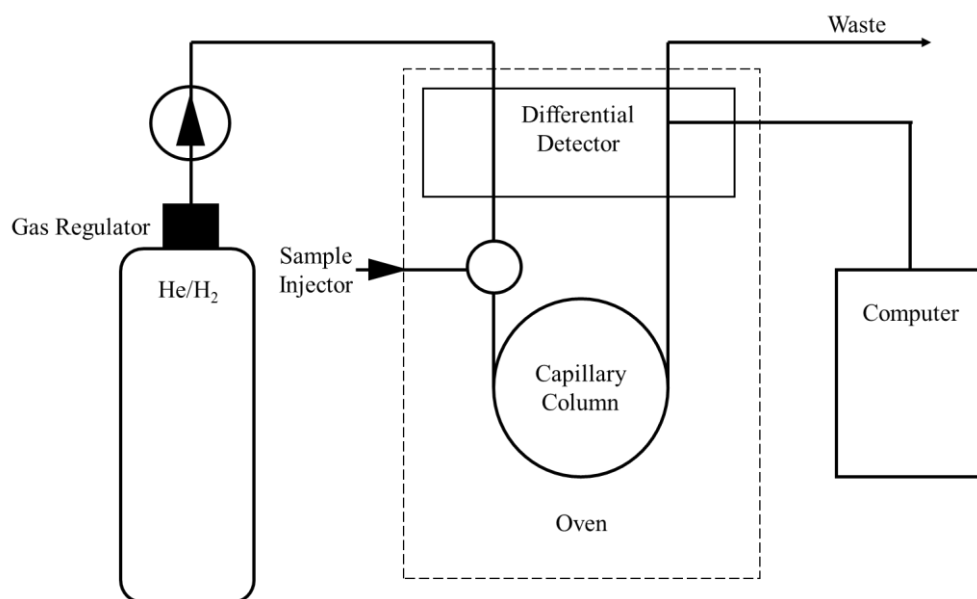


Figure 2. 21: A schematic diagram of the gas chromatogram with gas bottle and attached computer.

2.3.2.1 Equipment for GC

Gas Chromatography of compounds was carried out using a Varian 430 gas chromatograph, with a 30 m Stabilwax® capillary column (Restek) and a Varian CP-8400 autosampler shown in Fig. 2.22.



Figure 2. 22: a) The Varian 430 gas chromatograph that was used to complete the analysis. b) The Varian CP-8400 autosampler with sample vials placed in the carousel. c) The oven with Stabilwax® capillary column (Restek) attached to column hanger

2.3.2.2 GC analysis procedure

Analysis of reaction progress (Section 2.3.1.1) was carried out by taking an aliquot of the reaction solution, filtering through glass wool and placing solution in 2 mL vials with a rubber septum before being placed into the Varian CP-8400 autosampler. Data was then written into the Varian Galaxie software to automatically take samples from the vials in the carousel analysing them sequentially.

The program for analysis of all samples was as follows: a wash cycle was programmed, so that the GC was flushed with a 2.0 μL injection of pure ethanol (other wash solvents used in different reactions, wash solvent matched the reaction solvent, see section 4.2.1.3) twice before each sample was injected, 1.0 μL of sample was taken for injection, with an injector temperature of 250 °C. The column flow rate was 2.0 mL min^{-1} with a helium carrier gas. The oven temperature program had several stages of heat ramping. Initially, the temperature was held at 70 °C for 2 minutes. The temperature was then increased at a rate of 12 °C min^{-1} until the temperature reached 180 °C. The temperature then ramped further at a rate of 10.4 °C min^{-1} until the temperature reached 220 °C, at which point the GC run would end. The in-situ detector inside the GC instrument was a flame ionisation detector (FID), which utilised H_2 gas a flow rate of 20 mL min^{-1} , and compressed air at a flow rate of 200 mL min^{-1} , whilst operating at 350 °C. The method developed for the GC analysis is summarised in table 2.5 and Fig. 2.23.

GC Condition	Set Point
Injector Temperature	250 °C
Injection Volume	1.0 µL
Run time	15.0 minutes
Flow rate	2.0 mL min ⁻¹
Detector Temperature	350 °C
Wash Solvent	Reaction dependant

Table 2.7: GC method conditions with the associated set point.

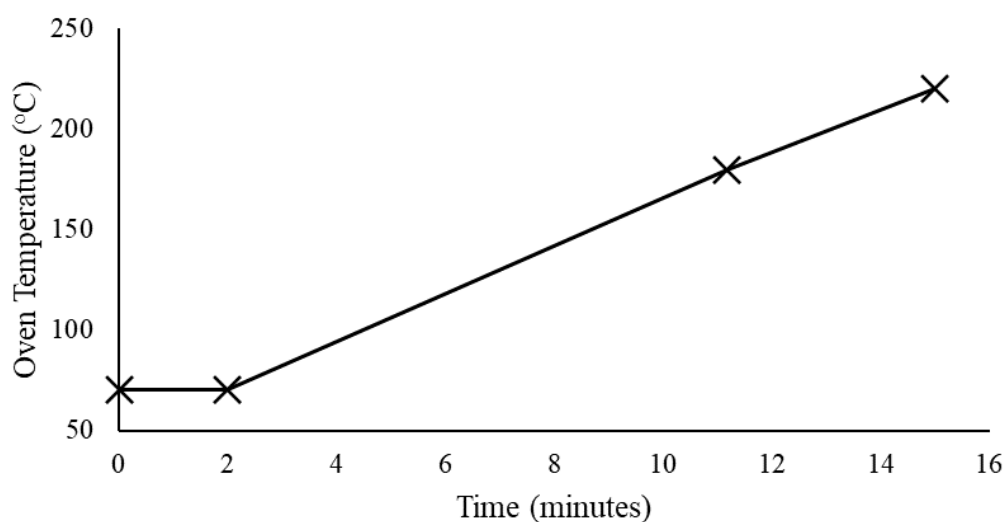


Figure 2. 23: Column oven temperature progress against time for the GC method. $T_0=70\text{ }^{\circ}\text{C}$, $T_2=70\text{ }^{\circ}\text{C}$, $T_{11.17}=180\text{ }^{\circ}\text{C}$, $T_{15}=220\text{ }^{\circ}\text{C}$.

2.3.2.3 GC calibration

To calculate concentrations of reaction components from reaction aliquots (Section 2.3.1.1), a calibration had to be performed using standard solutions of each analyte compound, as well as a fixed, known concentration, of toluene (0.1 M). Toluene was selected as an internal standard for this work due to its miscibility with solvents used and its inertness in the reduction reaction, therefore, its concentration would not change regardless of reaction progress. Since the concentration of toluene in the gas chromatographs remains constant, the peak area

corresponding to toluene can be used as a comparison for the peak areas corresponding to the product compounds. Considering the peak areas of both reactant and products relative to that of the fixed toluene concentration therefore compensates for any changes in the peak area due to inconsistencies in injection volume of sample.

Each analyte compound pairs, i.e., 4-chloronitrobenzene and 4-chloroaniline, was first prepared in an approximately 1 mg mL^{-1} solution in ethanol and were analysed in sequence to determine the relative peak positions from each other and from other potential product compounds. Example of this separation is shown in Appendix 1. Once all peaks were sufficiently resolved from one another calibration curves of all compounds were prepared by first preparing stock solutions of all of the compounds which were to be analysed, in a concentration range of 0 – 100 mM. Shown in table 2.6, are the concentrations of the various stock solutions prepared for the calibration of the GC for the hydrogenation compounds.

IS Concentration (M)	Analyte Concentration (M)
0.100	0.000
0.100	0.025
0.100	0.050
0.100	0.075
0.100	0.100

Table 2.8: Concentration of all analyte solutions compared to the internal standard (IS) concentration.

For each of the compounds a series of dilutions were prepared to ensure the GC would be calibrated for the range of expected concentrations that would be used in the hydrogenation reaction. These concentrations were 0 M, 0.025 M, 0.050 M, 0.075 M and 0.100 M, with the toluene internal standard maintained at 0.100 M. The broad concentration range would ensure

there were sufficient data points on the calibration curves for all compounds to produce a valid calibration curve, all calibrant solutions were injected 3 times to ensure valid standard deviation of samples was taken into account.

Chapter 3 Synthesis and characterisation of metal sulfide materials

Metal sulphides have been side-lined in studies in catalysis because they are considered the products of catalyst poisoning in traditional catalysis fields such as crude oil cracking, where the noble metal catalysts are poisoned by a surface layer of sulphide material. The poisoning of the catalyst surface leads to a decrease in activity and a lower turnover of the catalyst. However, in recent years, metal sulphides have been shown to display promising catalytic properties such as enhanced selectivity towards a desired product.^{8, 9, 13, 72, 84, 214, 215} For instance Pd₄S has been studied for its uses as a semi-hydrogenation catalyst for alkyne gas streams.²¹⁶ Various transition metal sulphides have also been assessed for their use as photocatalysts in hydrogen evolution.^{10, 217}

Some transition metal sulphide compounds have shown great potential for hydrogenation of nitrobenzene derivatives, including MoS₂,^{13, 218} CoS₂,⁸² FeS₂,^{9, 72} and various Ni_xS_y derivatives.²¹⁹ The wide range of elements, compounds, crystal structures and oxidation states among transition metals allows for a tailored approach to their catalytic applications. Some materials such as FeS can be amorphous (making their catalytic active sites difficult to determine), but under certain reaction conditions FeS can be synthesised with an NiAs type structure and others such as MoS₂ have a distinct layered structure thus making the determination of catalytic properties simpler. The crystal structures of FeS (NiAs type) and MoS₂ are shown in Fig. 3.1.

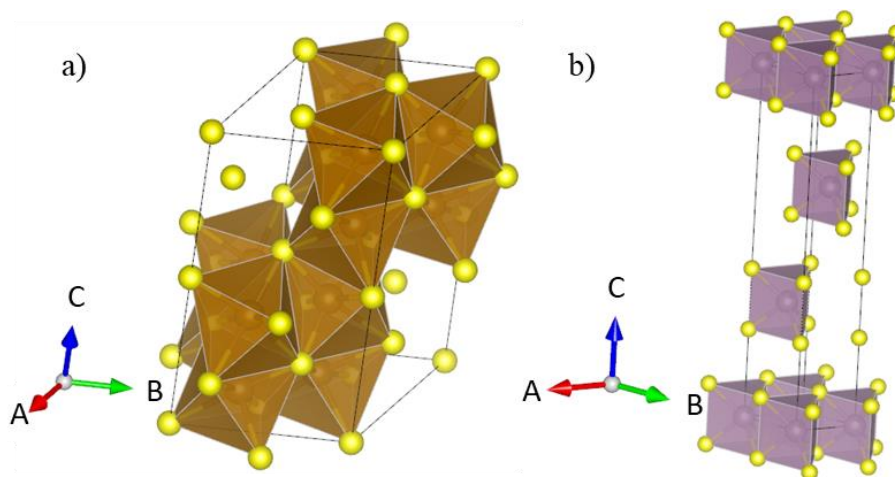


Figure 3. 1: Crystal structures of a) FeS (NiAs type, $p\bar{6}_2c$)^{220, 221} and b) MoS₂ (R3mH), Fe is at the centre of bronze polyhedra, Mo is at the centre of purple polyhedral. Yellow spheres represent sulfur.²²²

Generally metal sulfides do display direct metal-metal bonds. These metal centres tend to be more isolated than those in nanoalloys and intermetallic materials. Limited metal-metal interactions in theory means that catalytic sites are highly dispersed across the catalyst surface and, unlike nanoalloys of dispersed active metals, the metal centres are fixed in the crystal structure, hindering unfavourable migration under extreme reaction conditions.

The focus of this thesis revolves around the pyrite structure and developing new non-noble metal containing catalysts for the hydrogenation of substituted nitrobenzenes. The aristo type compound for the pyrite structure is the mineral pyrite, FeS₂, which is commonly found, naturally occurring, in iron deposits globally.^{9, 72} Iron metal centres within the pyrite structure may be substituted, partial or complete, with other metal ions, most commonly Ni, Co and Cu.¹⁰ Recent work by B. Ma et al.,⁹ building on the work of C. Guo et al.,⁷¹ showed that pyrite (FeS₂) (Fig. 3.2) has shown great potential as a hydrogenation catalyst for nitroarene reduction.

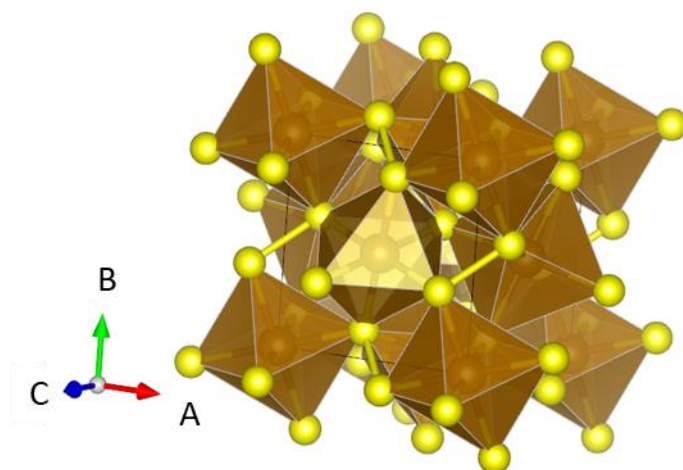


Figure 3. 2: Crystal structure of FeS_2 pyrite, space group $Pa\bar{3}$.^{222, 223}

In this chapter, the preparation of various metal sulfides was developed by optimisation of the solvothermal synthesis of FeS_2 pyrite.¹⁴ This was achieved by further development of previously reported methods. Once an efficient method for pyrite synthesis was achieved substitution of iron within the pyrite structure was attempted with the aim of developing a method by which the pyrite structure could be adapted to the needs of the catalysis being conducted.

3.1 Experimental

3.1.1 Materials

The metal sources used in the preparation of potential sulfide catalysts were iron (II) acetate anhydrous (Fe 29.5 % min, Alfa Aesar), nickel (II) acetate tetrahydrate (98 %, Alfa Aesar), cobalt (II) acetate tetrahydrate (98 %, Alfa Aesar), copper (II) acetate monohydrate (98 %, Alfa Aesar), manganese (II) acetate anhydrous (98 %, Alfa Aesar), sodium molybdenum oxide dihydrate (98%, Alfa Aesar), sodium metavanadate (96 %, 38 % V content, Alfa Aesar), chromium (III) acetate hydroxide (24% Cr content, Alfa Aesar). Sulfur (325 mesh powder, 99.5 %, Alfa Aesar) was used as the source of sulfur. Oleylamine (C-18 content 80-90 %, Fisher Scientific) and 1-dodecanethiol (98 %, Alfa Aesar) were used as templating agents. Ethanol

(absolute, Honeywell), ethylene glycol (laboratory reagent grade, Fisher Scientific), n-hexane (laboratory reagent grade, Honeywell) were used as solvents without any pre-treatment.

3.1.2 Preparation of FeS₂ pyrite and optimisation synthesis

The method used in the synthesis of FeS₂ pyrite was adapted from the method reported by C. Guo et al.⁷¹ This method was altered to produce a single phase FeS₂ pyrite material, described in Section 2.1. This was achieved by altering the stoichiometric amount of iron (II) acetate and sulfur and by using oleylamine as a capping agent in ethanol or ethylene glycol.

Synthesis of other transition metal sulfides followed the method developed for the synthesis of single phase FeS₂ nanoparticles, substituting the iron acetate with an appropriate salt for the target metal sulfide. The capping agent was changed in order to determine the effect of an acidic capping agent, in this case oleylamine was replaced with dodecane thiol, see Section 3.3.3.

3.1.3 PXRD analysis

Powder X-Ray Diffraction (PXRD) was carried out using a PANalytical X-ray diffractometer using monochromatic Cu K α_1 radiation and line PIXcel detector. Results were recorded using the instruments in-built software as described in section 2.2.1.5.2.

3.1.4 TEM and EDX analysis

Transmission Electron Microscopy (TEM) was carried out samples after PXRD analysis on selected single-phase samples. TEM was carried out using a JOEL 2010 TEM instrument running at 200 kV, with images captured by a Gatan Ultrascan 4000 digital camera. Particle sizes were analysed using the Gatan Digital Micrograph software. Energy Dispersive X-ray spectrometry (EDX) was carried out on each sample to determine phase composition. High Resolution Transmission Electron Microscopy (HRTEM) was carried out using high resolution (0.18 nm) field emission JOEL 2200FS microscopy operating at 200 kV. High-Angle Annular

Dark Field (HAADF) detectors for z-contrast imaging and EDX for elemental mapping. TEM, HRTEM and EDX analysis is described in detail in section 2.2.4.

3.2 Synthesis of iron sulfides

The preparation of iron pyrite (FeS_2) was achieved by modifying a previously reported method by C. Guo et al. and implemented in the synthesis of iron pyrite catalysts by B. Ma et al.^{9,71} In their route to synthesize single phase unsupported FeS_2 , 5 mmol of iron (II) acetate ($\text{Fe}(\text{CH}_3\text{COO})_2$) and 30 mmol of sulfur was dispersed in a mixture of 40 mL of ethanol and 20 mL of oleylamine. The dispersion was then added to a 100 mL autoclave before heating at 220 °C for 10 hours, after which the solution was cooled, the black precipitate was collected and dried.

The modified method adopted in this work used a lower reaction temperature, between 150 °C and 180 °C, the molar ratio of iron and sulfur altered and the reaction time varied to determine the optimum conditions for single phase FeS_2 . To synthesize FeS_2 , 2.5 mmol (0.43 g) of iron (II) acetate anhydrous and 2.5 to 15 mmol (0.08 g to 0.48 g) of elemental sulfur powder were dispersed in a mixture of 20 mL of ethanol and 10 mL of capping agent (oleylamine or dodecanethiol). The dispersion was then sonicated for 5 minutes to ensure a good dispersion of reagents, before placing into a 50 mL Teflon lined stainless steel autoclave (Parr Instrument Co.). The autoclave was then heated to reaction temperature for 12 hours, before cooling to room temperature. A black precipitate was collected by repeated centrifugation at 4500 rpm for 5 minutes, washing first with ethanol followed by hexane. Black solid then allowed to dry in vacuo at room temperature for 8 hours.

3.3 Optimisation of iron sulfide synthesis

3.3.1 Temperature of FeS₂ synthesis

The initial reaction to synthesise FeS₂ used a reaction temperature of 150 °C for a reaction time of 12 hours. The reaction temperature was lowered from the literature method in order to produce smaller nanoparticles with more defined morphology. T. Li et al. reported that lowering the synthesis temperature of FeS₂ nanoparticles from 260 °C to 180 °C resulted in a drastic decrease in particle size, from 18 nm to 3.5 nm, whilst making the resultant particles more uniform in size and shape.²²⁴ Upon PXRD analysis, it was found that the sample contained predominantly FeS₂ (Fig. 3.3). However, very poorly crystalline sulfur was present in the sample, possibly due to the low reaction temperature (Fig. 3.3)

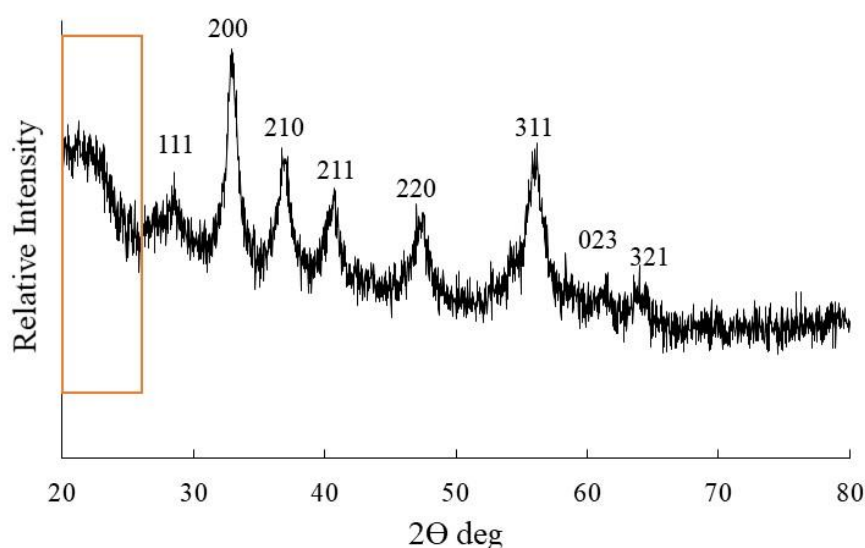


Figure 3. 3: PXRD of FeS₂ synthesised at 150 °C, with peaks indexed and amorphous sulfur region is highlighted.²²³

These amorphous sulfur impurities became evident under TEM analysis, where clear large aggregates of sulfur can be seen in the images (Fig. 3.4). These sulfur aggregates range in size from 200 nm to 500 nm in diameter. These sulfur aggregates are separated by regions of FeS₂ nanoparticles showing an even dispersion.

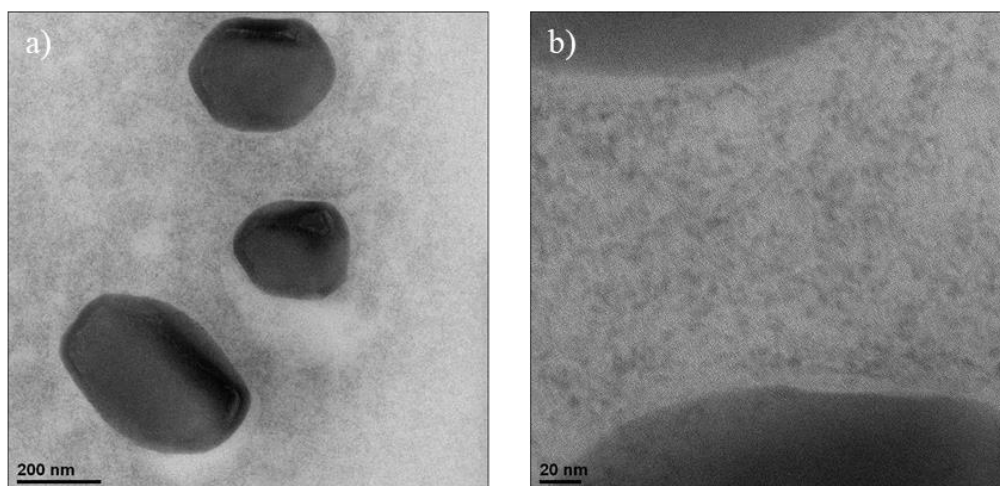


Figure 3. 4: TEM images of product obtained using a lower temperature, a) low magnification image of the sulfur aggregates with hue dispersed between them, b) high magnification image of the nanoparticles dispersed between the sulfur aggregates.

The lower reaction temperature, compared with that of the method as reported was determined to be the primary reason for the sulfur impurities found in the final product. As such the reaction temperature was raised to 160 °C to initiate all the sulfur to react. At this higher temperature the sulfur would be above its melting point and able to freely diffuse throughout the reaction. Diffusion of the sulfur would allow for a more complete reaction/interaction between the sulfur and other reagents.

Increasing the reaction temperature to 160 °C, was found to remove this sulfur impurity (Fig. 3.5). This removal of the sulfur region was determined to be due to the increased reaction between sulfur and oleylamine, and by extension sulfur insertion into the FeS occurring more efficiently at this higher temperature.

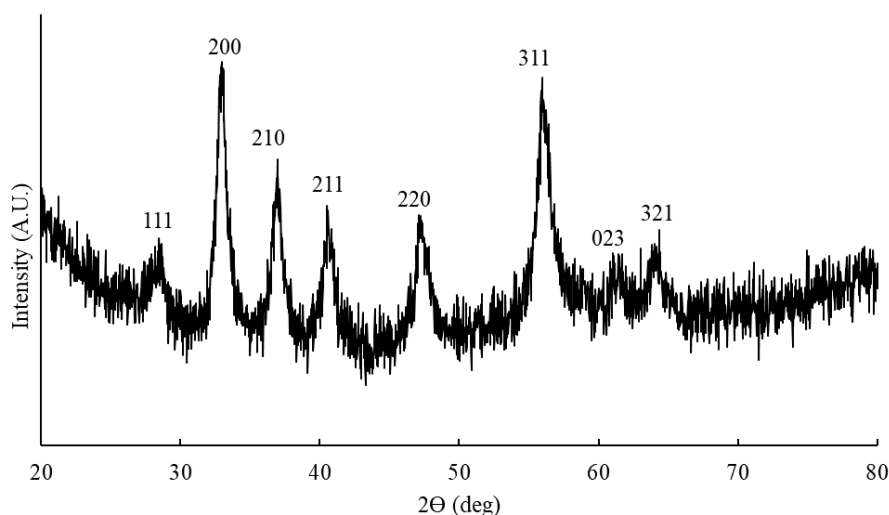


Figure 3. 5: PXRD of FeS_2 synthesised at $160\text{ }^\circ\text{C}$ with peaks indexed.²²³

These two reagents readily react forming a sulfur containing oleylamine species and hydrogen sulfide (H_2S), Fig. 3.6.⁷⁴

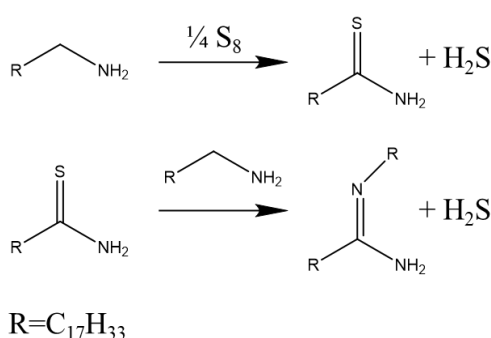


Figure 3. 6: Proposed reaction scheme of oleylamine reacting with elemental sulfur to produce reactive sulfur species.

The synthesis of FeS_2 requires the insertion of a disulfide (S_2^{2-}) group. However, this insertion does not occur instantaneously, a disulfide group cannot be inserted in this form. The disulfide group is built from a monosulfide. In the initial reaction Fe^{2+} in solution reacts with the H_2S , formed by the reaction between oleylamine and sulfur, forming FeS which is often amorphous.⁷⁷ FeS then reacts with either H_2S or elemental sulfur in the reaction vessel, inserting the S into the structure and thus forming the disulfide ion. This reaction scheme is summarised in Fig. 3.7.

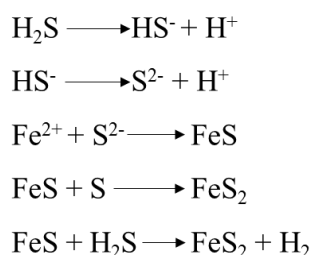


Figure 3. 7: Reaction scheme of FeS_2 synthesis within the solvothermal reaction vessel.⁷⁴

The reaction was further repeated at higher temperatures, 180 °C and 200 °C, to determine if any further phase changes occur. Increasing the reaction temperature to 180 °C did not produce a purer FeS_2 phase but produce a secondary phase of Fe_3S_4 . Fe_3S_4 is a thio-spinel structure, isostructural to Fe_3O_4 . The PXRD pattern obtained from the reaction carried out at 180 °C is shown in Fig 3.8.

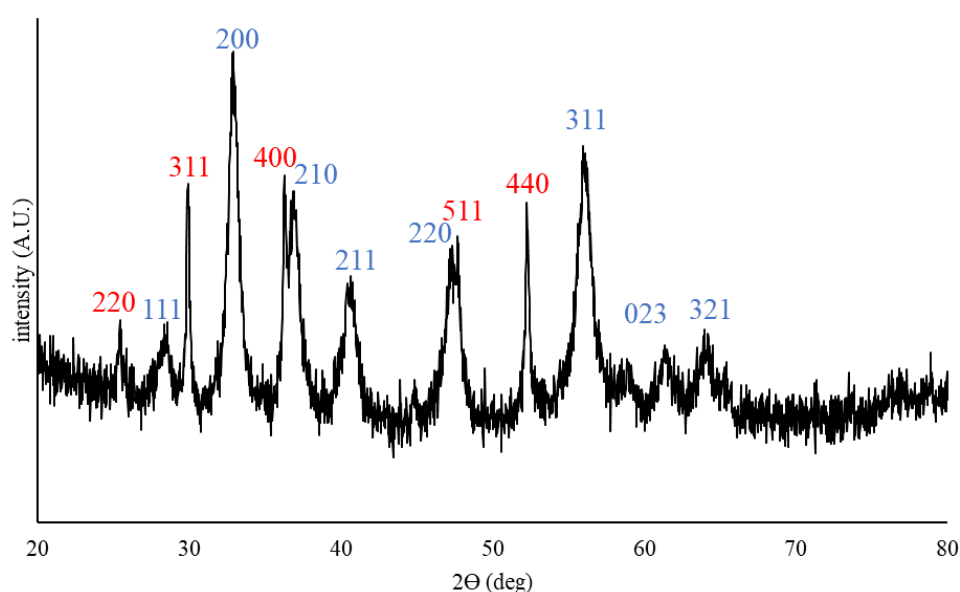


Figure 3. 8: PXRD pattern obtained of powder product from iron sulfide synthesis carried out at 180 °C for 12 hours, with peaks belonging to FeS_2 indexed in blue and peaks belonging to Fe_3S_4 indexed in red.^{223, 225}

The Fe_3S_4 phase, so called greigite, was unexpected due to the reducing nature of oleylamine. Greigite contains iron in a mixed oxidation state both Fe (II) and Fe (III) in a 1:2 ratio. The presence of greigite in the sample showed that some of the Fe (II), from the iron acetate, had

been oxidised in the reaction. This was possibly caused by the higher temperature initiating side reactions producing an excess of Fe (III), as summarised in Fig 3.9.

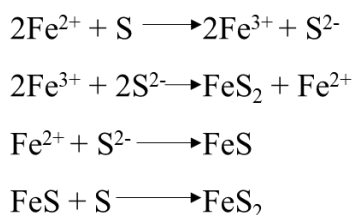


Figure 3. 9: Reaction between Fe (II) ions and sulfur to produce FeS and FeS₂.

Some free Fe (III) may have reacted to produce Fe₃S₄ as well as FeS₂. Alternatively, the higher temperature may have caused some of the S₂²⁻ dumbbells to be cleaved further reducing the FeS₂ formation in favour of S²⁻ ions, which are present in the greigite structure. The crystal structure of greigite is shown in Fig. 3.10.

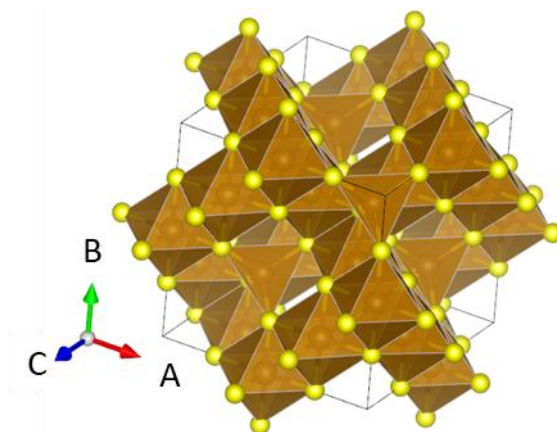


Figure 3. 10: Crystal structure of Fe₃S₄, greigite, space group $Fd\bar{3}m$.^{222, 225}

Due to the production of Fe (III) ions at higher temperatures, it was speculated that at further elevated temperatures (200 °C) may either produce a purer greigite phase or produce α-Fe₂S₃.

The increased temperature did not produce a purer phase, nor a new phase but a partially tar-like product, which could not be identified and possibly deriving from the polymerisation of oleylamine followed by vulcanisation of the resultant polymer by the excess sulfur within the

reaction. The resultant products only contained trace amounts of FeS_2 with a large amount of background. This high background could be attributed to this polymerised product.

As 200 °C did not produce a pure phase of Fe_3S_4 it was decided to return the reaction temperature to 180 °C and 160 °C but lengthen the reaction time from 24 to 48 hours. (Fig 3.11).

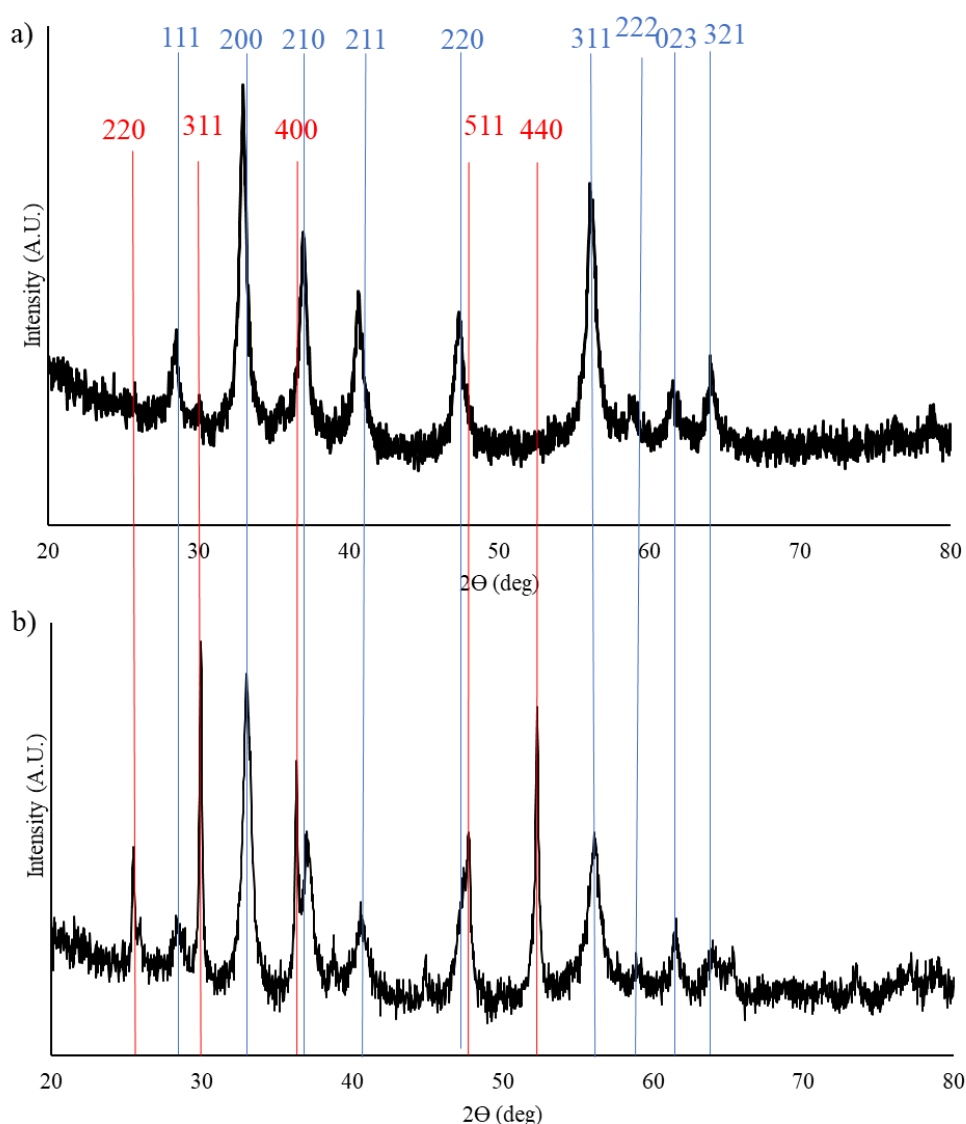


Figure 3. 11: PXRD patterns of iron sulfide synthesis carried out at a) 160 °C and b) 180 °C for 48 hour reaction times, Fe_3S_4 peaks indexed in red and FeS_2 peaks indexed in blue, according to their respective models.^{223, 225}

Increasing the reaction length from 12 hours to 48 hours at 160 °C had little effect on the outcome of the reaction. A single phase FeS_2 was obtained showing this temperature was the

ideal temperature for FeS_2 synthesis. When the reaction time was extended to 48 hours at 180 °C, there was a noticeable increase in the content of Fe_3S_4 in the product mixture. This phase was probably more crystalline in comparison to the FeS_2 as the peaks corresponding to Fe_3S_4 are far sharper. Conversely in both 160 °C and 180 °C reactions FeS_2 peaks were broadened by the distortion of the unit cells within the FeS_2 nanoparticles. Scherrer line analysis of these broadened peaks indicated a crystallite size of approximately 5 nm, subsequently confirmed by TEM analysis (Fig 3.12).

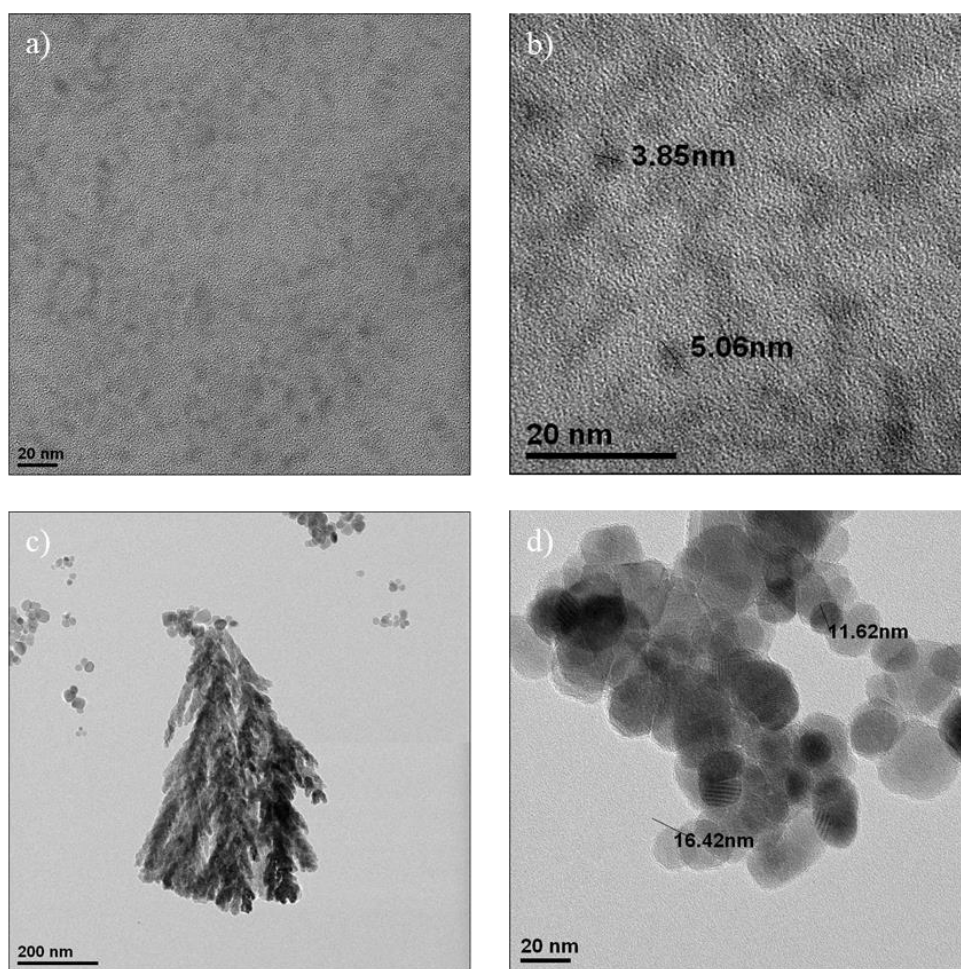


Figure 3. 12: TEM images of a) 160 °C reaction FeS_2 product at a lower magnification, b) 160 °C reaction FeS_2 product at higher magnification and particle diameter measured, c) 180 °C reaction product showing fern like entity common in the 180 °C sample, d) 180 °C particles of FeS_2 with particle diameter measured.

From the obtained TEM images of the particles from each reaction it was determined that smaller particles were produced at lower reaction temperature. As Fig. 3.12b shows the FeS₂ particles obtained at 160 °C reaction temperature were significantly smaller than those obtained from a higher temperature reaction, (Fig. 3.12d) with an average size across numerous particles of 4 ± 1 nm. The size discrepancy observed between these two sets of nanoparticles may have been due to the breakdown/loss of capping effectivity of the oleylamine. The loss of oleylamine, at higher temperature, was hypothesized as the reason behind the observed Fe₃S₄ product. The reduction oleylamine allows for more Fe (III) to be free in the reaction, which react to form the observed Fe (III) containing species, Fe₃S₄. The effect of oleylamine and another capping agent is discussed in section 3.3.3.

No single phase Fe₃S₄ was successfully isolated from attempting the synthesis at elevated temperatures. Elevated reaction temperatures were found only to reduce the purity of the obtained FeS₂ material and it was decided that all synthesis would be carried out at 160 °C. This was done in order to prevent the formation of other sulfide materials that may interfere with catalytic characteristics of FeS₂.

3.3.2 Sulfur content within the reaction

The content of sulfur within the reaction was altered to determine the minimum quantity necessary to synthesise a single phase FeS₂ material, to avoid the excess sulfur observed in lower temperature reactions. It is possible that the sulfur impurity is hidden within the background of the PXRD pattern showing the product of the synthesis reaction carried out at 160 °C (Fig. 3.5). In this case, the sulfur impurity is difficult to detect. A series of sulfur reactions were carried out with sulfur content ranging from 1.75 mmol to 15 mmol, to determine if sulfur content has an outcome on the products. The hypothesis was that more sulfur rich reactions would produce a higher proportion of FeS₂, whereas lower proportions of sulfur expected to produce more Fe₃S₄, Fe₂S₃ or FeS phases.²²⁶

With all previous reactions 15 mmol of sulfur was used as such this would become the baseline for the synthesis of iron sulfides, Fe:S ratio 1:6, meaning reactions had a sixfold excess of sulfur which proved difficult to remove consistently. The product of the reaction carried out using halved concentration of sulfur, 7.5 mmol, is shown in Fig. 3.13, which also shows a comparison with the PXRD pattern of the product of the baseline reaction.

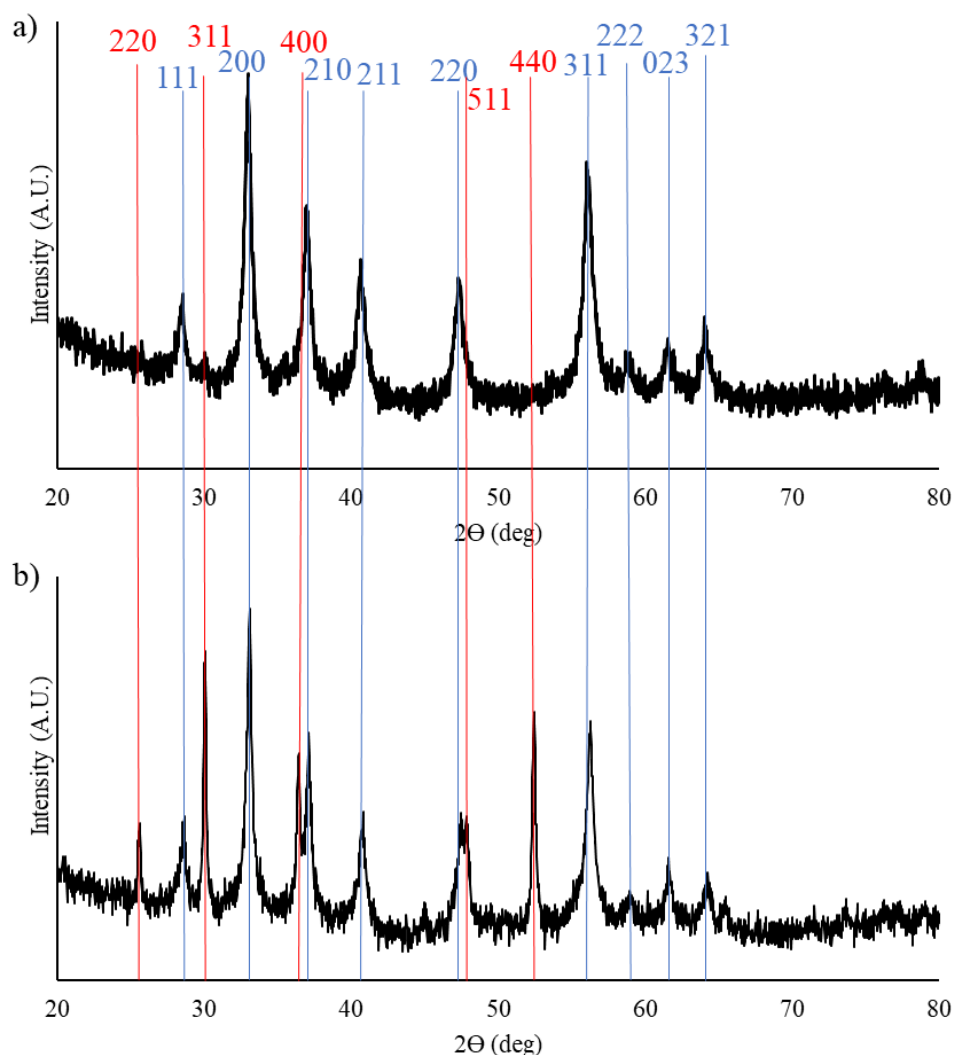


Figure 3. 13: PXRD patterns obtained from iron sulfide synthesis reaction products, a) 15 mmol sulfur, b) 7.5 mmol sulfur. With peaks corresponding to Fe_3S_4 indexed in red and FeS_2 indexed in blue.^{223, 225}

As the sulfur concentration within the reaction is halved, the sulfur to iron ratio is lowered to 3:1 compared from 6:1. The PXRD pattern (Fig 3.13 b)) shows that peaks attributed to Fe_3S_4 have become pronounced. Hence, reducing the sulfur excess in the reaction allowed for the

synthesis of less sulfur rich compounds such as the observed Fe_3S_4 phase. Yet when the sulfur content of the reaction was reduced further to 3.75 mmol the resultant phase mixture became more complex (Fig. 3.14).

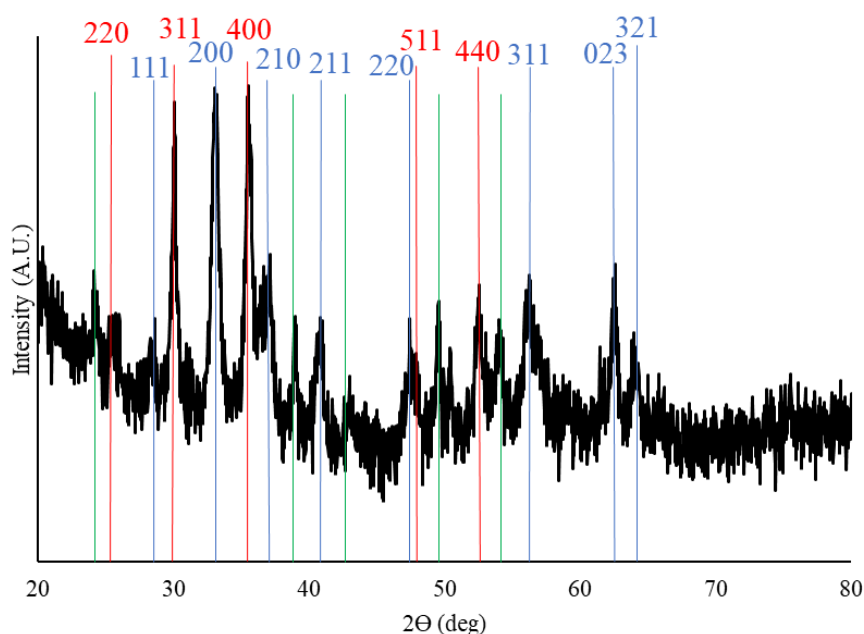


Figure 3. 14: PXRD pattern obtained from iron sulfide synthesis reaction using 3.75 mmol sulfur, with peaks corresponding to Fe_3S_4 indexed in red, FeS_2 indexed in blue and unknown peaks identified with green.²²⁵

The PXRD pattern of the product obtained using 3.75 mmol sulfur content, shows that many iron sulfide phases were produced, predominantly Fe_3S_4 and FeS_2 (Fig. 3.14). A few of the peaks were not assignable to a specific iron sulfide phase, these may belong to sulfur deficient pyrite or greigite phases, FeS_{2-x} and $\text{Fe}_3\text{S}_{4-x}$ respectively.

It appears that when there is enough sulfur present to form FeS_2 , that this phase would form preferentially compared to other iron sulfides.²²⁶ The sulfur content of the reaction was lessened to just 2.5 mmol, in a 1:1 molar ratio with the iron acetate, and to 1.75 mmol, half of the equivalence of the iron acetate. Many peaks in the PXRD patterns could not be assigned to any phase present in the database used. The formation of significant quantities of amorphous FeS , which raised the background of the patterns obscuring fine details, may also contribute to the lack of clarity on which phases are formed (Fig. 3.15).

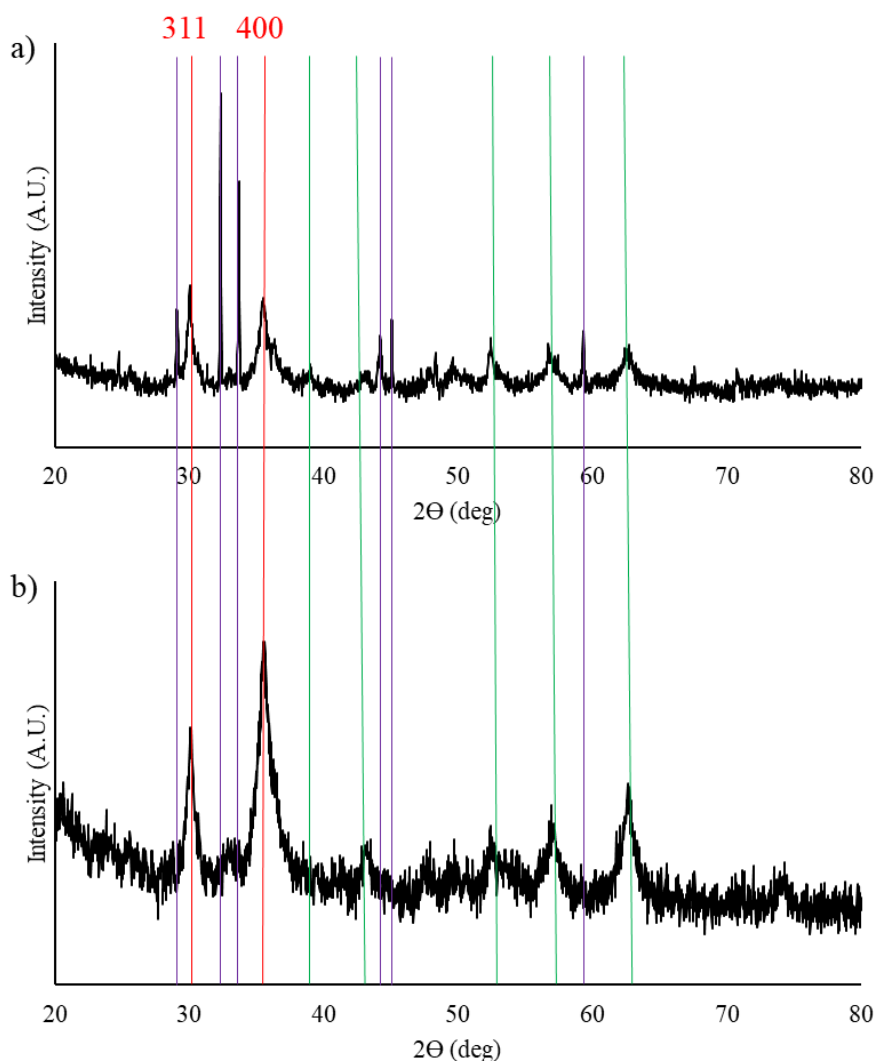


Figure 3. 15: PXRD patterns obtained from iron sulfide synthesis using a) 2.5 mmol and b) 1.75 mmol of sulfur. A tentative assignment of peaks sees Fe_3S_4 in red, unreacted iron (II) acetate in purple and peaks of possible iron sulfides highlighted in green.

Phases obtained from the reaction containing 2.5 mmol of sulfur (Fig. 3.15a), equivalent to the concentration of iron (II) acetate, showed that there was unreacted iron acetate remaining in the reaction vessel. This was unexpected due to the absence of iron (II) acetate in the reaction with 1.75 mmol of sulfur (Fig. 3.15b). Both reaction products showed an increased background, possibly due to the increased amorphous FeS concentration within each sample. Some of the peaks can be tentatively attributed to an Fe_3S_4 phase. From the broad peaks observed in the PXRD pattern and the nature of amorphous FeS an accurate phase determination could not be defined. However, it is believed that this may be a mixture of the possible FeS ($P\bar{6}2c$), FeS

($Pnma$), Fe_3S_4 ($Fd\bar{3}m$) and FeS_2 ($Pa\bar{3}$) phases, with no dominant phase present in the final product. The structures of FeS ($P\bar{6}2c$) and FeS ($Pnma$) are shown in Fig. 3.16.

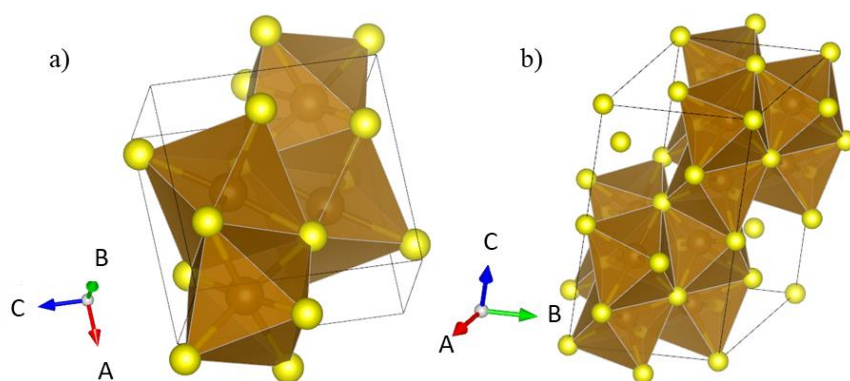


Figure 3. 16: Crystal structures of a) FeS , space group $Pnma$ and b) FeS , space group $P\bar{6}2c$.^{222, 227}

These two distinct FeS phases may have been present within the sample yet due to the large amorphous FeS background, but this remained undetermined.

Due to the results obtained across various sulfur contents, it was decided to use 15 mmol of sulfur. This was selected due to the minimal by-product formation as this reaction resulted in a single phase FeS_2 nanoparticle material with uniform particle size of 4 ± 1 nm. This was further studied by analysis of the effect of the oleylamine capping agent on the structure of the obtained material.

3.3.3 Reaction capping agent

Oleylamine plays a vital role as both a reactant and a capping agent within the FeS_2 synthesis.^{9, 71, 74} As discussed in section 3.3.1, the effect oleylamine has on the crystal structure and morphology of the obtained material was studied. Firstly, a reaction was carried out in the absence of oleylamine, secondly a reaction was carried out using a comparable acidic capping agent, dodecane thiol. The chemical structures of oleylamine and dodecane thiol are shown in Fig. 3.17. Dodecane thiol was selected as a potential capping agent due to its inherent acidity, as sulfide phase can be directed by the pH of the surrounding material.

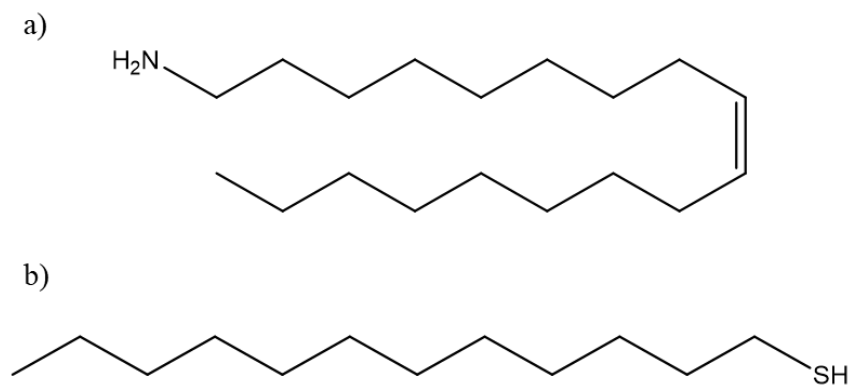


Figure 3. 17: Structures of a) oleylamine and b) dodecane thiol.

To test the effect oleylamine has on the obtained material a reaction was carried out using similar conditions to previous syntheses yet in the absence of oleylamine replacing it with excess ethanol. The reaction was carried out over 12 hours as with previous experiments before collecting the nanoparticles by centrifugation. The reaction obtained a black powder which upon drying remained black in colour. PXRD of obtained material shown in Fig. 3.18.

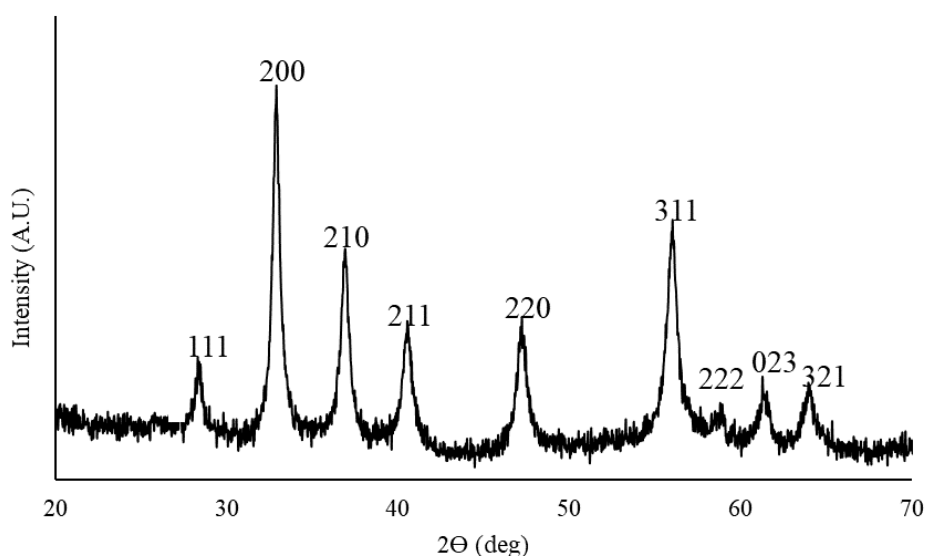


Figure 3. 18: PXRD of material obtained from reaction in absence of oleylamine.

The PXRD obtained from the reaction in absence of oleylamine (Fig. 3.18), showed that the FeS₂ synthesis was successful. The FWHM of the 200 and 311 peaks for the material obtained without the use of oleylamine were found to be 1.2° and 1.6°, respectively, compared to 1.7°

and 2.3° for the 200 and 311 peaks obtained from the material capped by oleylamine indicating an increase in particle size in the absence of oleylamine. From what has previously reported this was unexpected, as without oleylamine present in solution there should not have been a reaction.^{74, 79} However, the initiation of this reaction may have been due to other factors, such as a partial oxidation of the Fe^{2+} ions present in the solution. Fe^{2+} may reduce some sulfur in a redox reaction, (Fig. 3.9).

This redox reaction between the dissolved Fe (II) ions and the S_8 rings may be a supporting mechanism for the FeS_2 synthesis, however there was a distinct H_2S smell, when opening the reaction vessel from the reaction without oleylamine. H_2S is not produced by the proposed interaction between the Fe (II) ions and S_8 , yet there may be another potential reduction of the sulfur rings by the ethanol under the high temperature of the reactor, thereby forming some H_2S which then reacts. Due to the formation of H_2S in the reactor FeS_2 is formed during the reaction, without oleylamine facilitating sulfur activation.

The particle size of the obtained FeS_2 material was studied to determine what effect the lack of oleylamine had on the particle size and morphology. It was determined that oleylamine effectively capped the particle size. Where in a reaction including oleylamine the particle size of FeS_2 is, 4 ± 1 nm, in the absence of oleylamine the particle size increases by some 400 % to a size of 16 ± 1 nm (Fig 3.19). Yet, nanoparticles retain a spherical morphology as shown in Fig 3.19.

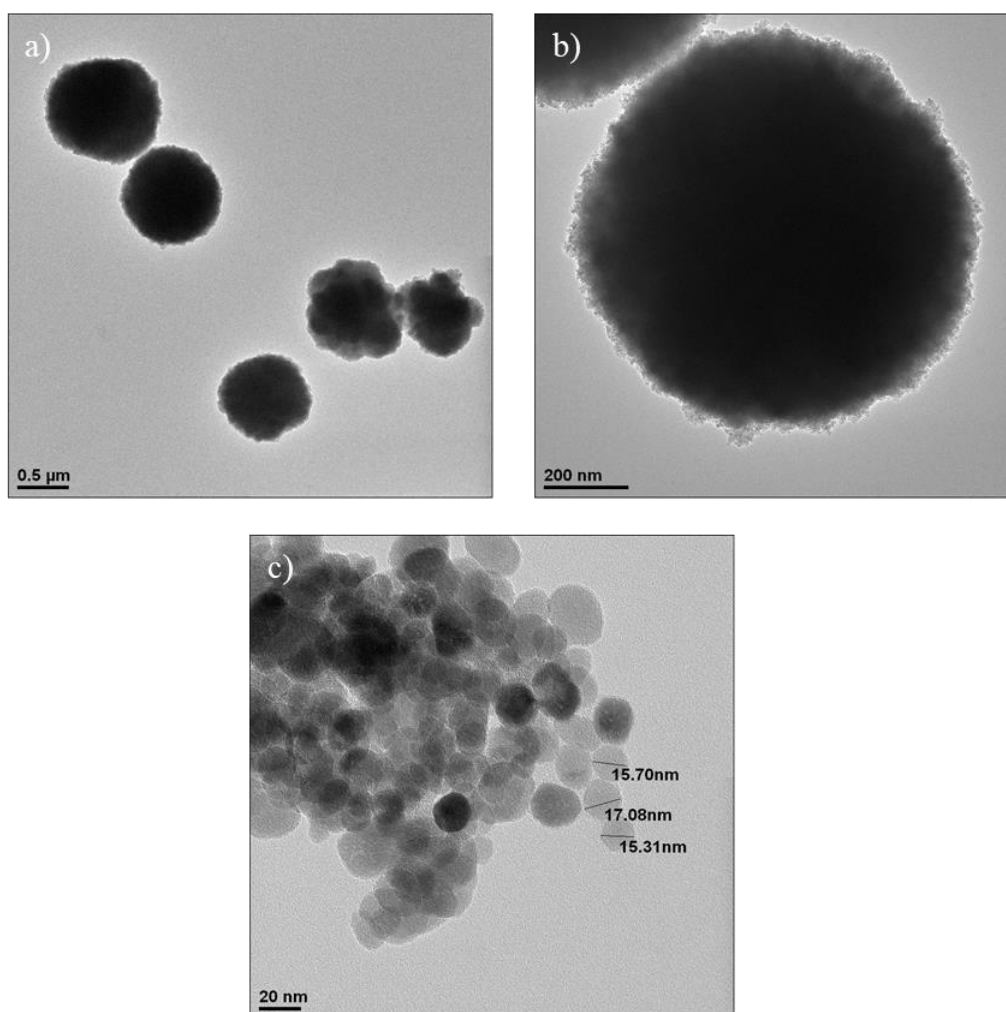


Figure 3. 19: TEM images of FeS₂ nanoparticles prepared in the absence of oleylamine. a) aggregates of particles at low magnification, b) higher magnification of a large aggregate, c) high magnification of particles at the edge of an aggregate.

The spherical particles obtained in the absence of oleylamine showed a tendency to aggregate together forming large clumps of FeS₂ nanoparticles. The size range of these aggregates was found to be $0.75 \pm 0.15 \mu\text{m}$. There were few distinct nanoparticles free from the aggregates. This highlights the second important role of oleylamine, preventing aggregation of the particles by creating a boundary layer thus limiting particle-particle attraction. This limitation of particle aggregation, in practical catalysis, means that more of the surface of each particle is in contact with the surrounding substrate solution allowing for an increased catalytic performance observed in the catalyst.

To determine the effect an acidic capping agent would have on the structure and morphology of the obtained material; a reaction was carried out replacing oleylamine with dodecane thiol. Dodecane thiol consists of a 12 carbon chain terminated at one end with a thiol group ($\text{C}_{12}\text{H}_{27}\text{SH}$, $\text{pK}_a \sim 10.5$), this thiol group dissociates weakly in solution forming a thiolate group, which may act on the surface of particles limiting growth.^{224, 228} The deprotonation of thiol lowers the pH of the solution to approximately pH 5, whereas in a typical reaction with oleylamine as a capping agent the pH is approximately pH 9.

The reaction was carried out at 160 °C for 12 hours, after which the obtained black powder was dried and analysed via PXRD (Fig. 3.20). The obtained material was determined to be a single-phase marcasite FeS_2 from the indexed peaks of the PXRD. However, the amount of material obtained was significantly less than reactions carried out using an oleylamine capping agent, yielding 0.2 g compared to 0.45 g when oleylamine had been used.

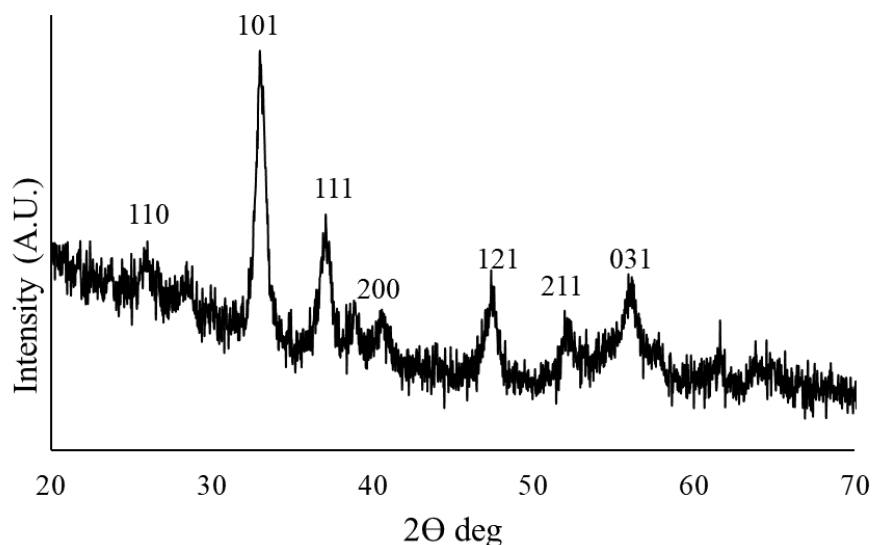


Figure 3. 20: PXRD pattern of FeS_2 marcasite obtained by reaction with dodecane thiol capping agent with peaks indexed.²²⁹

However, under TEM analysis the purity of the marcasite phase was determined to be mixed with two phases present as two distinct particle morphologies could be observed. A globular

structure was observed across the samples with regions of distinct separate particles (Fig. 3.21). The morphology of the crystalline region, shown in Fig. 3.21b and 3.21c, was irregular with crystallites no fixed morphology with seemingly random shape. The globular regions have no defined boundary as shown in Fig. 3.21a. Yet at the fringes of these globular regions there are embedded crystalline particles visible within (Fig. 3.21c).

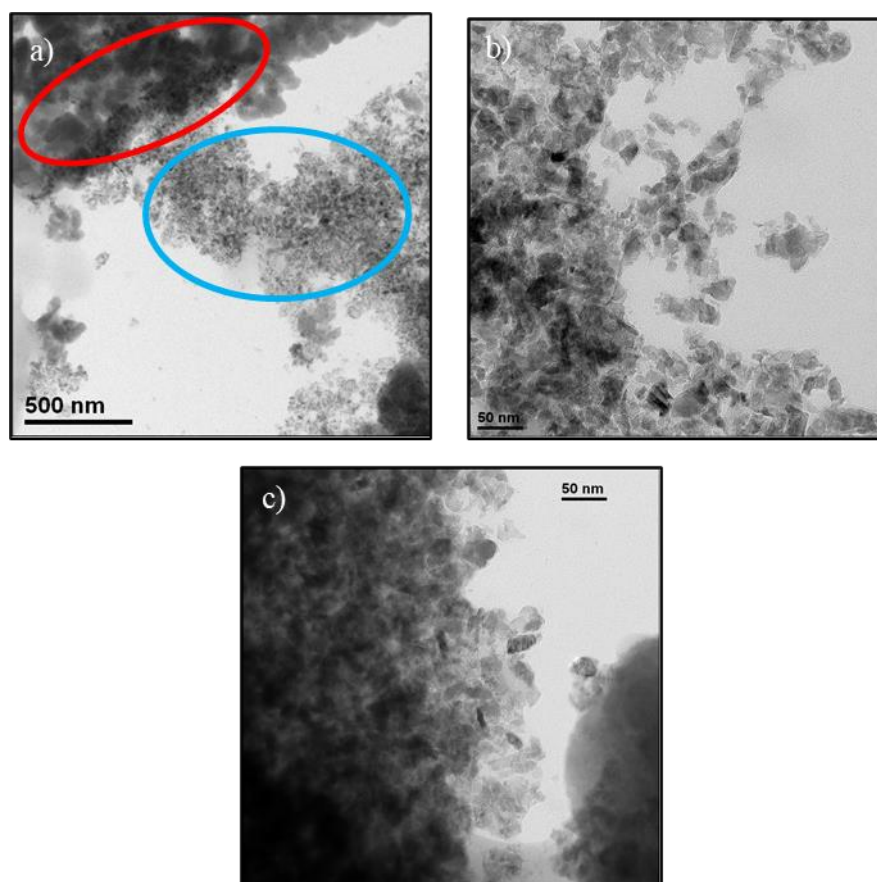


Figure 3. 21: TEM images of FeS_2 marcassite obtained from reaction with dodecane thiol capping agent, a) region of low magnification showing 2 distinct morphologies with globular tubes (circled in red) and smaller distinct particles (circled in blue), b) higher magnification image of the particulate region, c) higher magnification of the globular region with particles visible within the globular clusters.

It can be inferred that the crystalline material is the FeS_2 marcassite, and the globular regions were potentially amorphous FeS encapsulating particles of marcassite. Comparing the EDX spectra of the oleylamine capped and dodecane thiol capped reactions (Fig. 3.22) there is little difference in the atomic abundancies of sulfur and iron, both maintain a sulfur to iron ratio of 2:1 which is to be expected for iron disulfide materials.

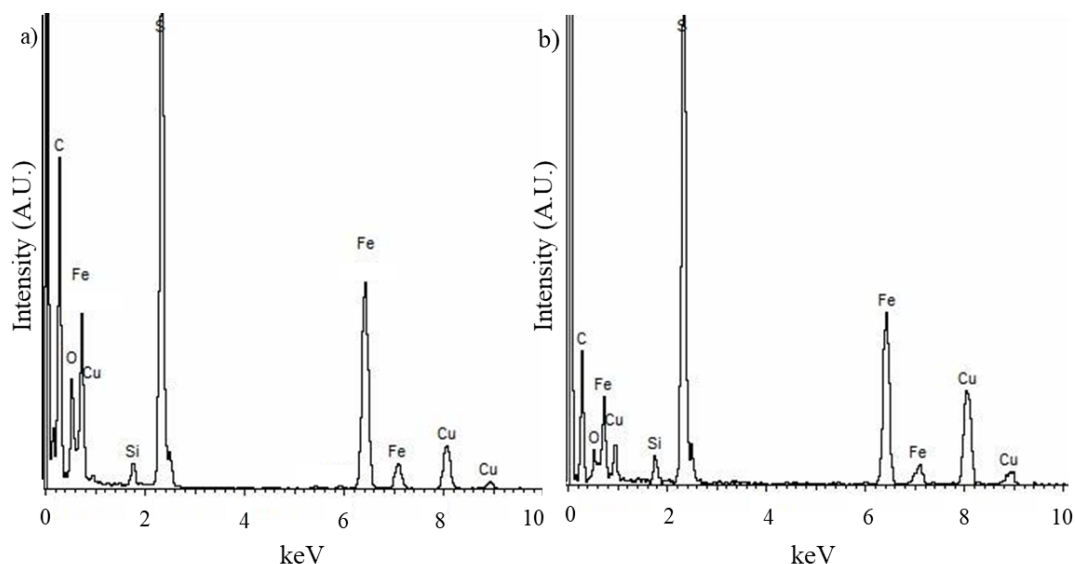


Figure 3. 22: EDX spectrographs of a) oleylamine capped FeS_2 pyrite and b) dodecane thiol capped FeS_2 marcasite.

The marcasite sample was left in a fridge at 7 °C for two weeks before use in a selective hydrogenation reaction. Before the hydrogenation reaction was carried out PXRD analysis was carried out on the material to determine any structural changes prior to use. The PXRD of the marcasite material, shown in Fig. 3.23, showed considerable decomposition of the material with clear growth of peaks belonging to pyrite.

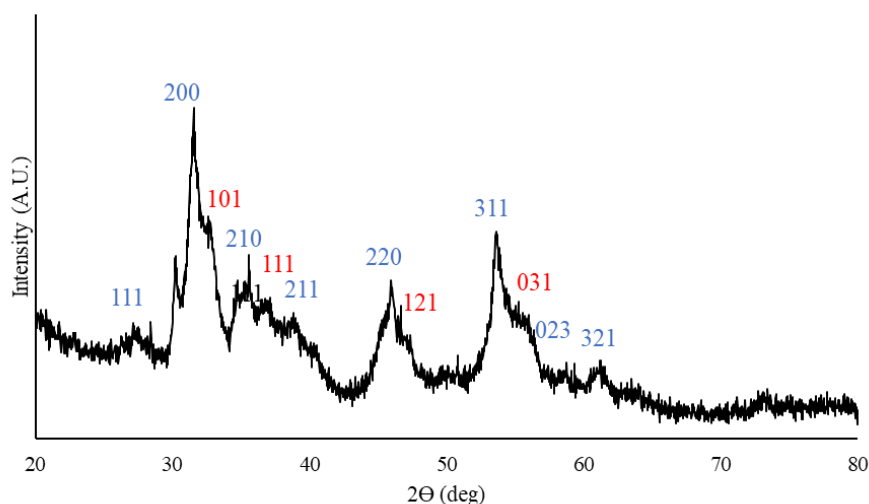


Figure 3. 23: PXRD pattern of material obtained after dodecane thiol capped reaction product was left for 2 weeks at 7 °C. Peaks corresponding to FeS_2 pyrite indexed in blue and peaks corresponding to FeS_2 marcasite indexed in red.^{223, 229}

This decomposition was due to the metastability of the marcasite structure. The marcasite structure changes into the pyrite structure overtime due to the greater lattice energy of pyrite.^{228,}

²³⁰ The structures of marcasite and pyrite are shown in Fig. 3.24.

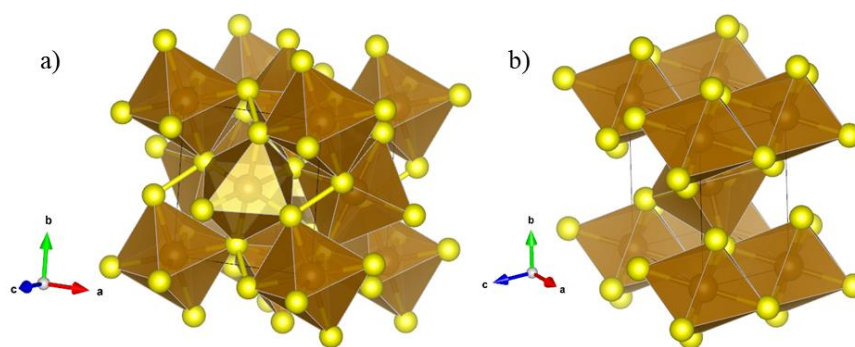


Figure 3. 24: Crystal structures of a) FeS_2 pyrite, space group $\text{Pa}\bar{3}$ and b) FeS_2 marcasite, space group Pnnm .^{222, 223, 229}

The pyrite structure has a lower energy than marcasite due to the closer packing of the iron polyhedra, which share more vertices. Therefore, the sulfur dumbbells are shared across more polyhedra dissipating the strain they place on the structure of marcasite.^{226, 227}

The use of dodecanthiol clearly favours the formation of the FeS_2 marcasite polymorph over the pyrite, hence it was decided that oleylamine should be used as a capping agent to prepare pyrite nanoparticles. The further advantage of using oleylamine is the even distribution of particles observed in an oleylamine capped nanoparticles, which were prevented from aggregating, unlike uncapped particles.

3.3.4 Effect of solvent on the synthesis of FeS_2

The solvent used in solvothermal synthesis plays an important role in the end material obtained. The solvent influences the pressure within the solvothermal reactor at a specific temperature and the solvent interacts with the reactants differently based on its nature. This interaction between solvent and reactant is vital in this reaction as discussed in section 3.3.1, where it was

shown that ethanol plays a role in the activation of sulfur. As such solvents considered for the reaction to compare with ethanol were ethylene glycol and water. These solvents are commonly used in solvothermal synthesis due to their range of properties.^{71, 77, 78, 80} Ethanol had been used as a solvent in previous reactions in line with what was reported by B. Ma et. al.⁹

Solvent	Vapour Pressure at 25 °C (kPa)	Boiling Point (°C)	Density at 25 °C (kg m⁻³)
Ethanol	8.106	78	789
Ethylene glycol	0.011	197	1110
Water	3.171	100	997

Table 3.1: The three solvents used in pyrite synthesis with relevant properties.

Ethylene glycol (EG) is often selected as a solvent in solvothermal reactions due to its high boiling point, 197 °C, and low vapour pressure as shown in table 3.1. These two properties allow for high temperature lower pressure synthesis. However, another property of EG is its reducing potential, that increases as temperature increases. As such high temperature reductions are often carried out to produce metallic catalysts.^{78, 231} In the case of sulfides, EG may facilitate the reduction of S (0) to S²⁻ thereby skipping the S₂²⁻ required for disulfide synthesis in the pyrite structure.

Water was also chosen as a potential solvent due to its relative inertness and low environmental impact compared to the alcohol solvents, whilst providing a higher boiling point for reaction relative to ethanol.

The reactions were carried out as previously described using 2.5 mmol iron (II) acetate and 15 mmol of sulfur with 20 mL of solvent and 10 mL of oleylamine, the reactions were heated at 160 °C for 12 hours before cooling to room temperature. The products were collected by centrifugation and dried *in vacuo*. Fig. 3.26 shows the PXRD patterns obtained from the

reactions in each solvent. As shown previously, ethanol (Fig. 3.25a) produces a single phase FeS₂ pyrite phase.

The reaction solvated by EG (Fig. 3.25b), produced a largely amorphous product with a few peaks present. These peaks marked in red were not observed in other reactions and may be attributed to either a crystalline FeS phase or a dilute Fe₃S₄ phase. Yet, due to the low intensity these peaks could not be definitively attributed to either phase, with the bulk of the material largely being amorphous in nature. This lack of an identifiable phase, within the EG pattern, suggested that the EG had been too strongly reducing not allowing for the formation of the S₂²⁻ ion required for the pyrite structure. Instead, a high abundance of S²⁻ was formed by the reaction which explained the high abundance of amorphous FeS indicated by a high background observed within these samples and small quantities of an undefined crystalline FeS/Fe₃S₄ phase.

Similarly, in water the reaction did not produce a predominant phase of FeS₂ pyrite, a low yield of product was obtained from this reaction of 0.05 g of black product which may have been poorly crystalline oxides. This is likely due to the immiscibility of liquid sulfur with water, even at high temperature, reducing the reaction, with the sulfur dissolving into the oleylamine phase. The iron (II) acetate dissolves more readily in the water phase, resulting in a partitioning of the reactant. Thus, reactions only occurred at the interface between the oleylamine-water phase boundary. This reduction in phase contact reduced the likelihood of reaction between the two reactants, resulting in a lowering of overall product obtained from the reaction. PXRD analysis of the obtained product (Fig. 3.25c) shows peaks that are in line with an FeS₂ pyrite phase yet they are not as intense as those seen in the ethanol reaction (Fig. 3.25a). In addition to the lack of intensity, there was a potential underlying amorphous product obscuring the presence of other products that may have formed in the synthesis.

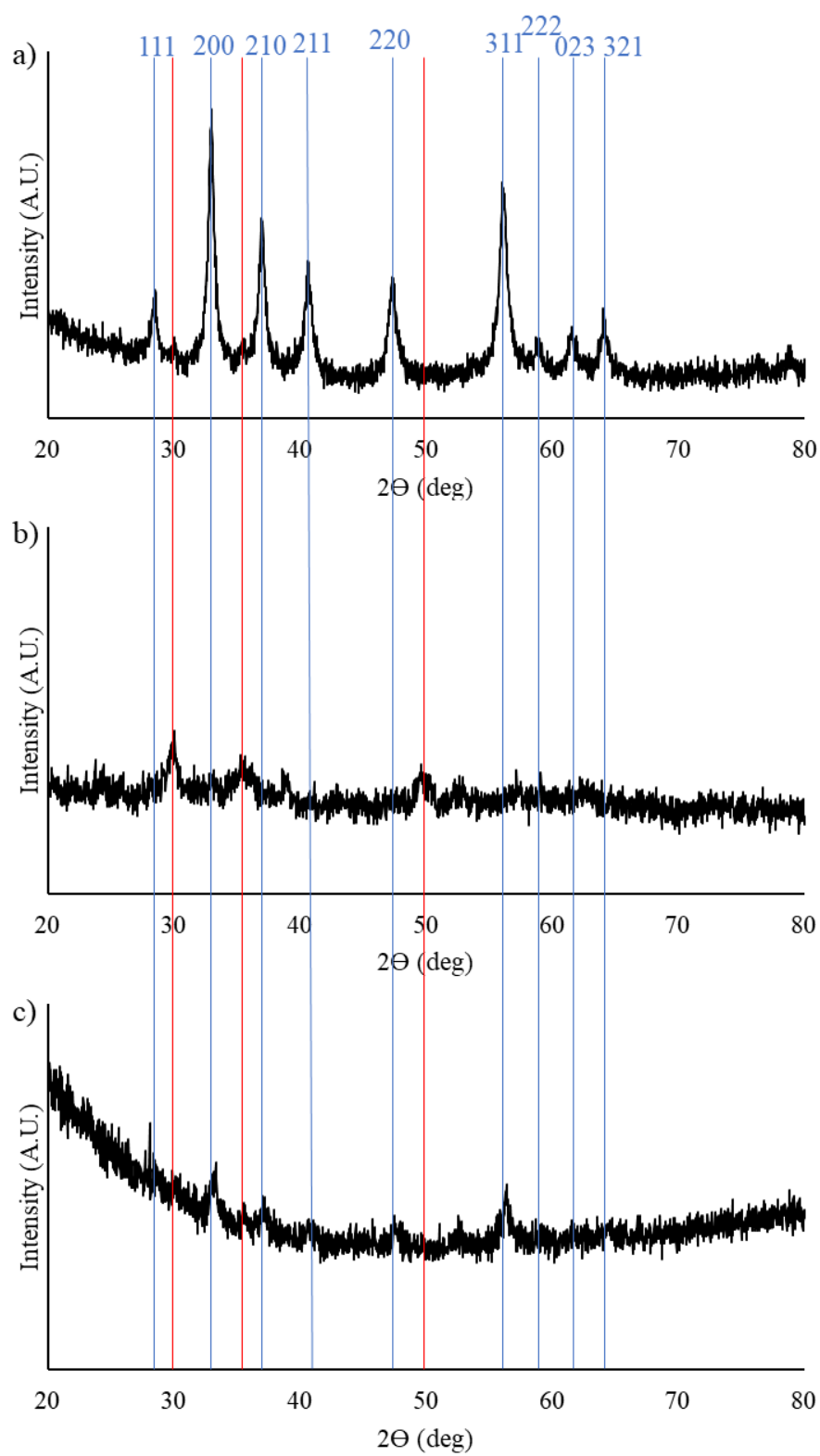


Figure 3. 25: PXRD patterns obtained from iron sulfide synthesis in different solvents, a) ethanol, b) ethylene glycol and c) water. FeS₂ pyrite peaks indexed in blue and unknown sulfide peaks highlighted in red.

Ethanol would be continued to be used as a solvent in the synthesis of the sulfide materials due to the phase purity of the product obtained. This would be implemented in future syntheses in chemical substitutions of iron within the pyrite structure (section 3.4).

3.3.5 Further characterisation of optimum FeS₂ synthesis

From the results described in section 3.3.1 to 3.3.4 the best reaction for the formation of pyrite nanoparticles is a solvothermal reaction with a mixture of 2.5 mmol of anhydrous iron (II) acetate and 15 mmol of sulfur, with 10 mL oleylamine capping agent in 20 mL of ethanol. The heating step is carried out at 160 °C for 12 hours before cooling to room temperature and FeS₂ nanoparticles are separated by centrifugation.

Further characterisation on the optimised particle synthesis was carried out to determine physical, optical and electronic properties of the obtained FeS₂ pyrite nanoparticles. Characterisation of the particles was carried out using TEM, electron diffraction, elemental mapping, infrared spectroscopy and solid state UVVIS spectroscopy.

High resolution transmission electron microscopy (HRTEM) was carried out to determine morphology of the particles in detail. Selected area electron diffraction (SAED) was carried out to cross reference the structural data obtained using X-Ray diffraction techniques. HRTEM shows that the shape is mainly elongated, and the length is more than twice the width. Their average size (length) has been measured around 5.0 ± 0.5 nm. The SAED pattern (Fig. 3.26c) was indexed using the model reported by Finklea et al. for FeS₂ and the reflections are in agreement with the model.²²³

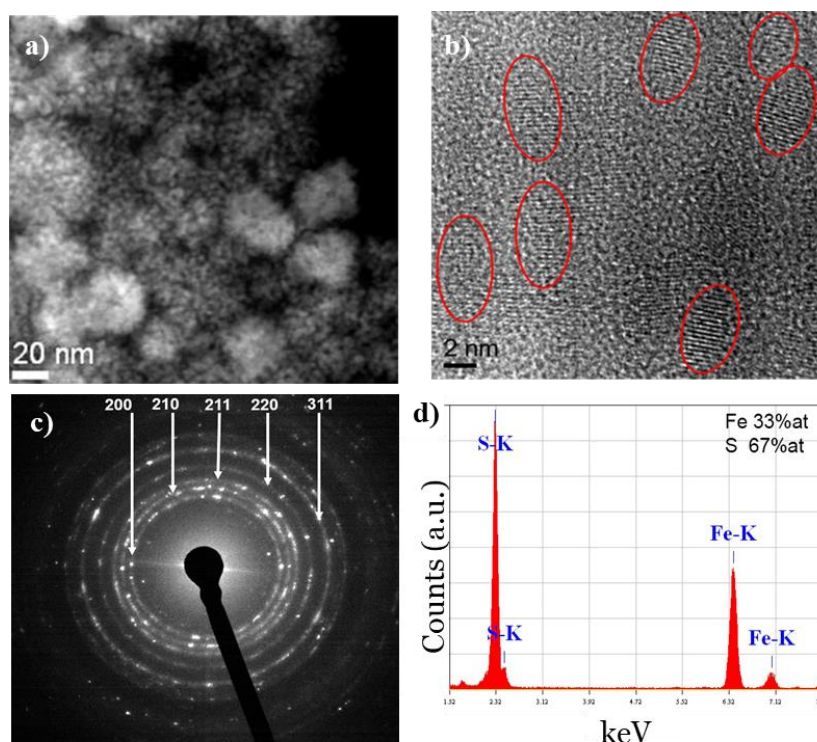


Figure 3. 26: a) HAADF Scanning TEM image of nanoparticle dispersion. b) High resolution image of some nanoparticles showing their elongated shape. c) Selected Area Electron Diffraction (SAED) taken on a large agglomerate of FeS_2 nanoparticles with diffraction rings indexed. d) EDS spectrum of sulfur and iron with their relative atomic abundances expressed at a percentage.

EDS analysis was used to confirm the chemical composition of the material. Analyses have been performed in different regions and identified a consistent abundance of 67% of sulfur and 33% iron by atomic percentage, in line with the expected values for FeS_2 (fig. 3.26d). High Angle Annular Dark Field (HAADF) image and HRTEM images show that the dispersed nanoparticles tend to form agglomerates while maintaining their individuality (Fig. 3.26a, b).

The elemental mapping of the FeS_2 material (fig. 3.27b and 3.27c) showed homogeneous distribution of Fe and S within the catalyst material. Isolated pockets of iron, potentially detrimental for catalytic performance, were not detected.^{67, 232}

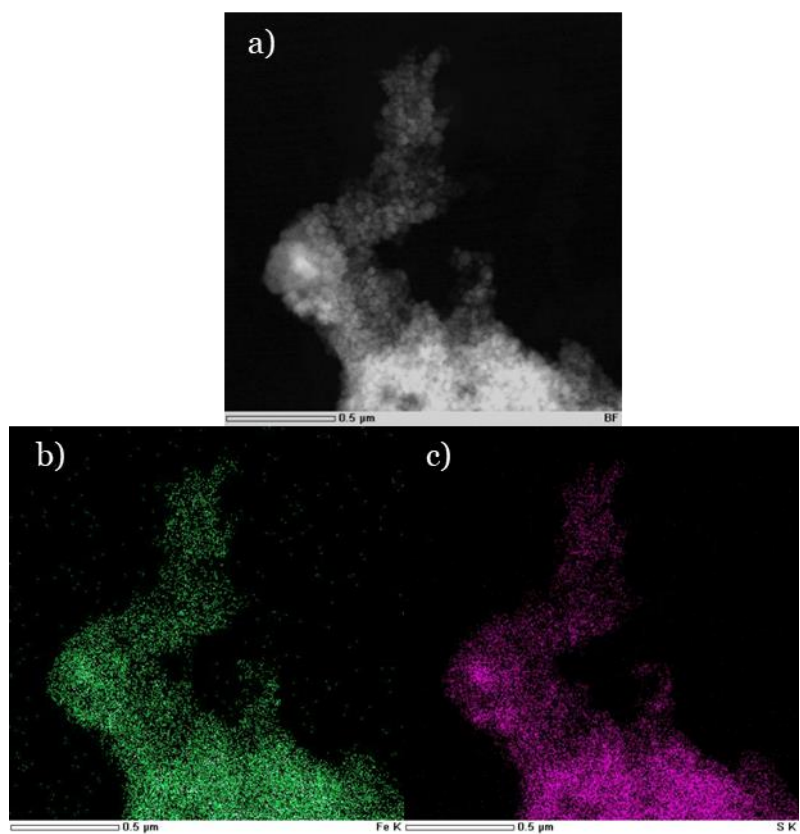


Figure 3. 27: a) HAADF Scanning TEM of large aggregate of nanoparticles. b) Fe mapped

The dimensions of the particles were studied by the inverse Fourier transform of the HRTEM pictures diffractogram with one reflection at a time and by measuring the thickness of the diffraction pattern rings.

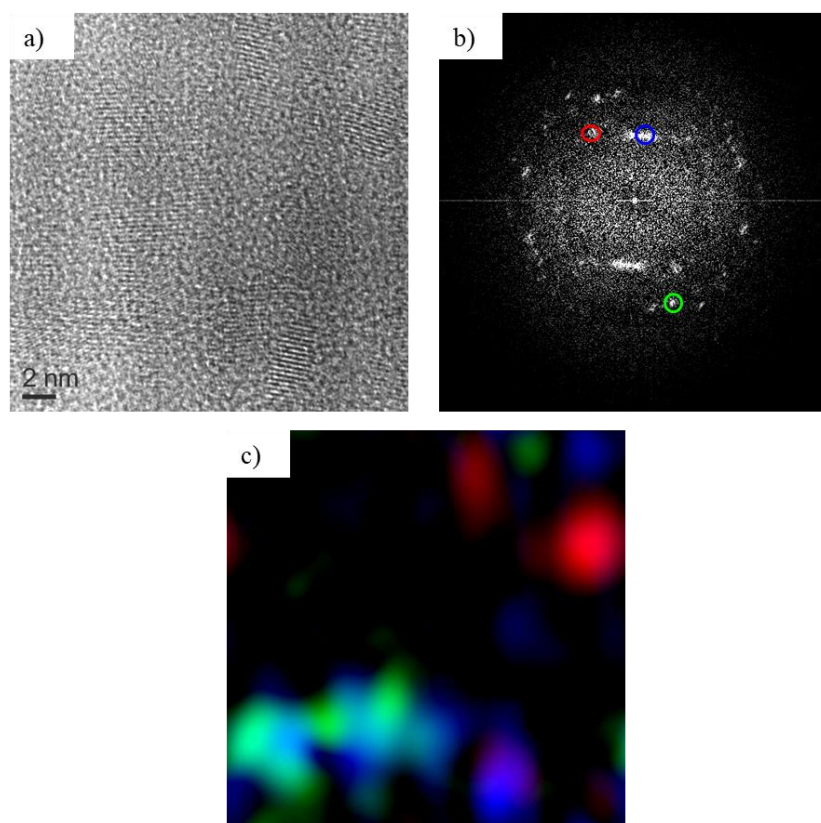


Figure 3. 28: a) High Resolution TEM image of FeS₂ nanoparticles; b) Fourier Transform (FT) of the HRTEM image in a); c) Reconstruction of the FeS₂ nanoparticles in a) using the FT in b). Reflections circled in colours in b) correspond to nanoparticles identified on c) with the same colour.

Inverse FT mapping of HRTEM image showing the FeS₂ particles, Fig. 3.28a, produced an image, Fig. 3.28c, that corresponded well to the original. The simulated d spacing of the material matched well with the model data for FeS₂, lending credence to the presence of single phase FeS₂ particles.

The FTIR spectrum of the catalyst material (fig. 3.29) shows residual amounts of elemental sulfur, and sulfur oxygen species around (1400 cm⁻¹). Sulfur oxygen species are expected due to the highly reactive and oxophilic nature of transition metal disulfides, which readily oxidise in the presence of oxygen.²²⁶ In addition thiol is present in the sample (2800 cm⁻¹) due to the surface terminating disulfide groups of pyrite and, in general, of metal sulphide materials.²²⁶

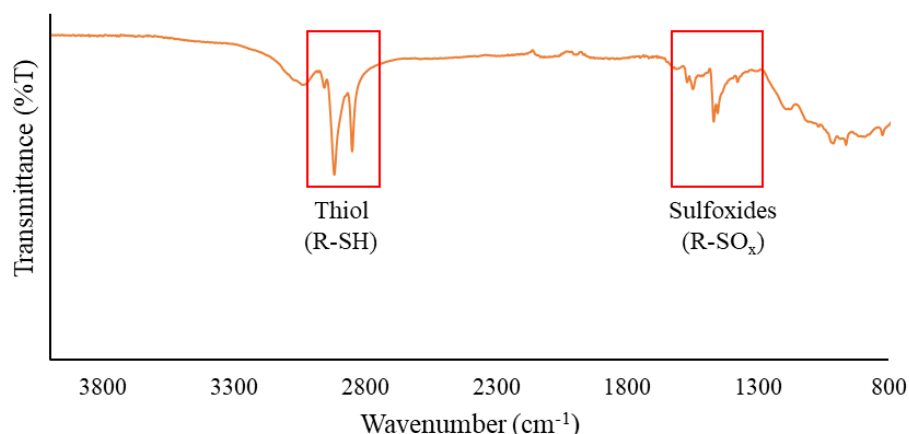


Figure 3. 29: FTIR spectrum of FeS₂ catalyst prior to use in selective hydrogenation reactions.

Solid State Ultra-Violet VISible Near InfraRed (SS-UVVIS-NIR) spectroscopy was carried out on the FeS₂ nanoparticles to determine what effect the decreased particle size and morphology had on the electronic properties of the material. SS-UVVIS is a method for determine certain electronic interactions within the analyte material, this data can be interpreted using Kubelka-Munk theory to determine the so called “band gap” of the material.²³⁴ The band gap of a semiconductor material is the energy required to cause an electron to jump from the valence band of a material to the conduction band. In the case of FeS₂ the reported band gap of the bulk material is ~0.75 eV.^{71, 228}

The wide wavelength scan of the FeS₂ nanoparticles (Fig. 3.30a) shows several features associated with FeS₂ and its reflectance at lower wavelengths. From 700 nm to 200 nm, there is an increase in the reflectance associated with FeS₂. The primary feature of interest in the sharp transition associated with the band gap of FeS₂ pyrite at 1900 nm. This transition is shown in greater detail in Fig. 3.31b. Using the Kubelka-Munk equations shown in section 2.2.3, the band gap of the FeS₂ pyrite nanoparticles was determined to be 0.57±0.08 eV. This band gap is lower than the literature value of ~0.75 eV and this was theorised to be due to the distortion of the FeS₂ pyrite unit cells within the nanoparticles and potential error within the measurement as the FeS₂ had to be highly diluted to produce any features in the spectrum. The deformation

of the unit cells causes some electronic transformations become less energetic.^{82, 235} Reducing these energetic transformations therefore, closes the gap between the conduction band and valence band in the FeS₂ material.

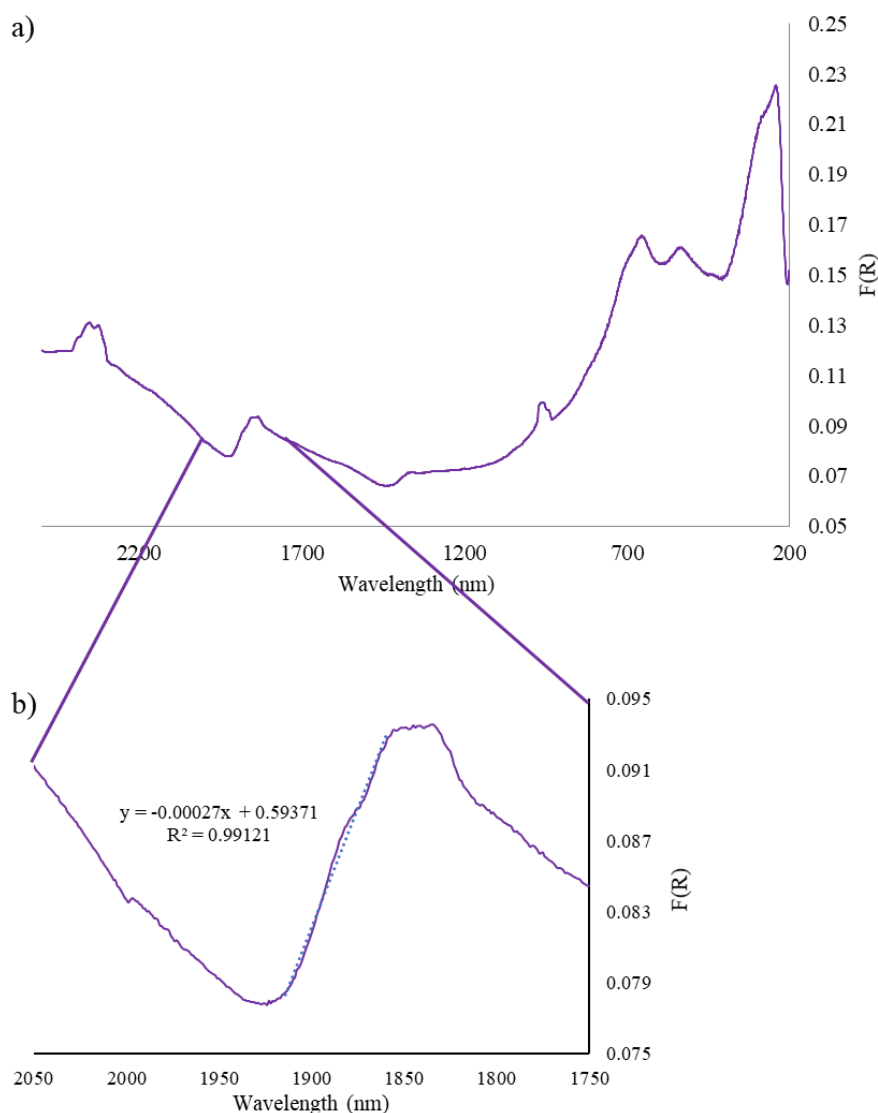


Figure 3. 30: a) SS-UV-VIS-NIR spectrum using wide wavelength scan from 200 nm to 2400 nm, b) SS-UV-VIS-NIR spectrum of the region corresponding to the band gap transition in FeS₂.

3.4 Substitution of iron within the pyrite structure

The pyrite structure is known to be able to host numerous other metals, in place of iron. These include nickel and cobalt.^{223, 236, 237} However, other metals such as manganese, copper, chromium, vanadium and molybdenum also show varied metal sulfide phases in a similar way

to that of iron.¹³ These compounds may show catalytic properties in the reduction of nitrobenzenes. Yet, due to the novelty of metal sulfides these compounds have not been widely tested for their catalytic applicability.

3.4.1 Nickel and cobalt

Nickel and cobalt pyrites are widely known to exist within ore deposits and are distributed globally. These two metals are situated next to iron in the periodic table with the number of d electrons in their 2+ ions being, Fe d⁶, Co d⁷ and Ni d⁸. Nickel and cobalt can take the place of iron within the pyrite structure due to their atomic radii being similar to Fe (II) and being stable in a 2+ ion.^{10, 226} The crystal structures of these sulfides are shown in Fig. 3.31. These compounds have been studied for their potential electrochemical performance for hydrogen generation but have not been studied for their potential as a hydrogenation catalyst.

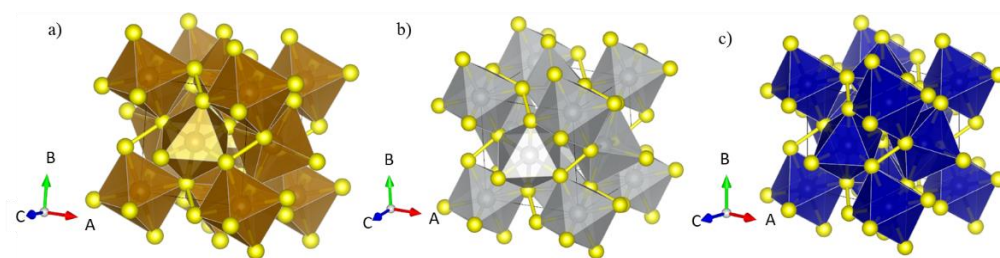


Figure 3. 31: Crystal structures of a) iron pyrite (FeS_2) b) nickel pyrite (NiS_2) and c) cobalt pyrite (CoS_2), all structures are space group $\text{Pa}\bar{3}$.^{222, 223, 236}

The synthesis of nickel and cobalt pyrites followed the optimised route for FeS_2 pyrite synthesis. 2.5 mmol of the metal (II) acetate and 15 mmol of sulfur was added to a Teflon lined stainless steel autoclave to which 10 mL of oleylamine was added along with 20 mL of ethanol. The autoclave was then heated at 160 °C for 12 hours before cooling to room temperature. The obtained nanoparticles were then separated by centrifugation washing with ethanol and hexane. Cobalt disulfide synthesis was unsuccessful after numerous attempts no clear phases could be observed in the PXRD although there was a clear background shift due to the high fluorescence

of cobalt under Cu $K_{\alpha 1}$ radiation (Fig. 3.32).²³⁸ No peaks corresponding to the CoS_2 pyrite phase could be identified, nor other cobalt sulfide phases such as Co_3S_4 or Co_2S_3 .

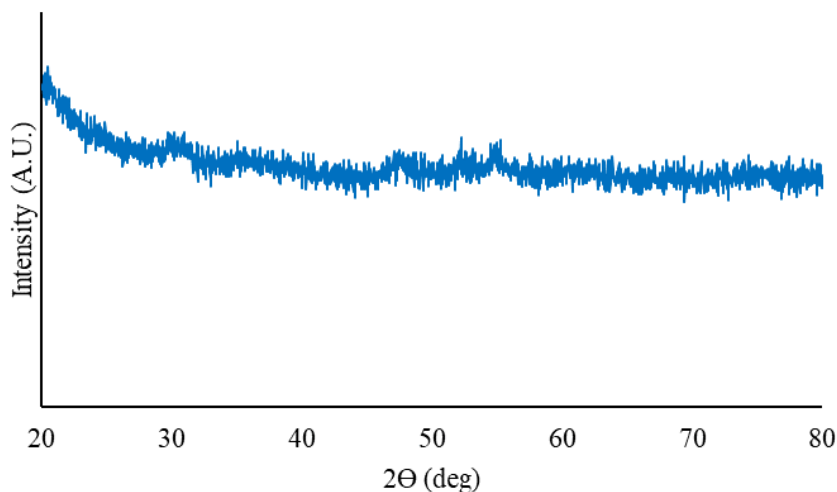


Figure 3. 32: PXRD pattern obtained from cobalt sulfide synthesis, high background due to fluoresce of cobalt under Cu $K_{\alpha 1}$ radiation.

It may have been possible that the obtained black material from attempted CoS_2 synthesis may have been an amorphous CoS material. As such it was deemed to be similar to the previous material proposed to be FeS at low temperature reactions. It was thus determined that the synthesis temperature for CoS_2 was significantly higher than that of FeS_2 .

Nickel disulfide synthesis was successful and repeatable; as shown by the PXRD pattern of obtained NiS_2 shown in figure 3.33. The obtained NiS_2 nanoparticles contained a small unidentified impurity which has been attributed to alternative nickel sulfide phases such as NiS or Ni_2S_3 , the peaks corresponding to these additional phases could not be properly indexed but shouldering is present on the NiS_2 200, 211 and 220 peaks.

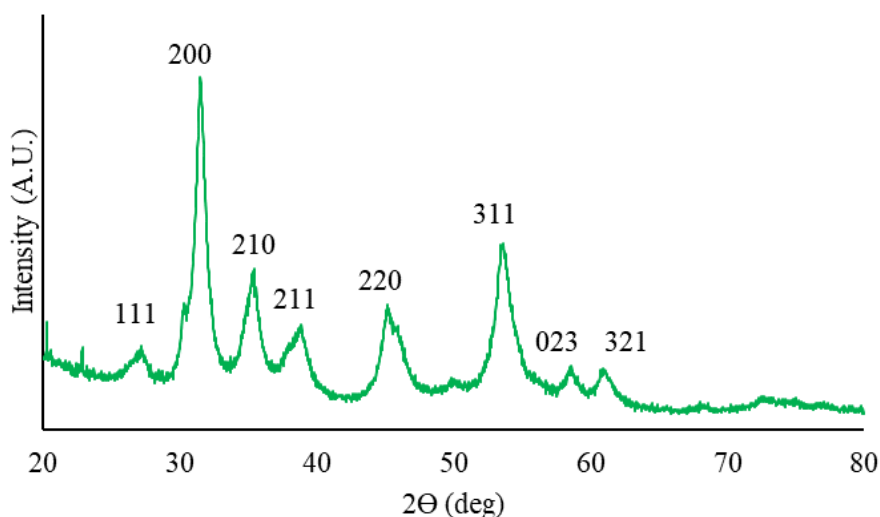


Figure 3. 33: PXRD pattern obtained from NiS_2 synthesis. Peaks corresponding to $\text{Pa}\bar{3} \text{NiS}_2$ indexed according to model.²³⁶

Further characterisation was carried out on the NiS_2 nanoparticles via HRTEM. The images obtained by HRTEM (Fig. 3.35) were found to be very similar to those obtained from FeS_2 pyrite (Fig. 3.34).

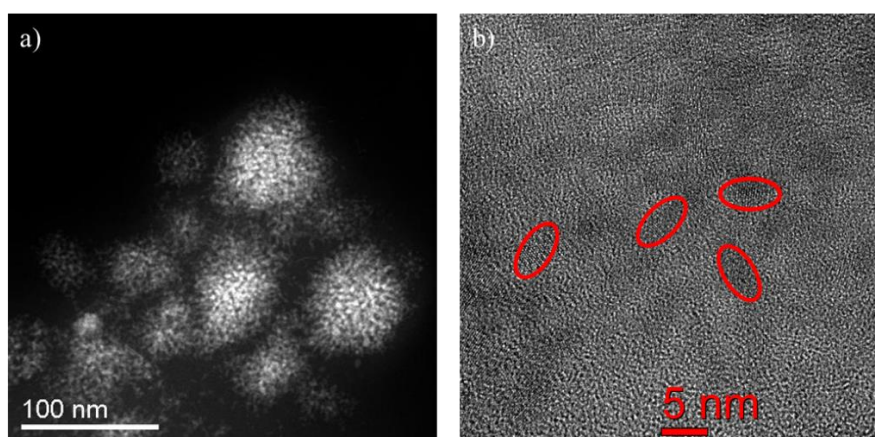


Figure 3. 34: HRTEM images of a) NiS_2 aggregates, b) dispersed NiS_2 particles, particles have been ringed in red to aid in visibility.

The FeS_2 and NiS_2 nanoparticles obtained were found to be very similar in shape both displaying an elongated form with lengths $5.0 \pm 0.5 \text{ nm}$. As such these two materials have very similar surface areas and surface characteristics. These similarities in morphology and surface

characteristics would allow for a controlled analysis in the differing catalytic performance of each material, which is discussed in section 4.2.2.3.

3.4.2 Copper and manganese

Copper and manganese were also studied as potential metals to test within the pyrite structure as marcasites of both metals are well known.^{239, 240, 242} In addition to this both metals have favourable catalytic properties that have been widely studied.^{70, 241} Due to the catalytic potential of copper and manganese pyrites it was decided to attempt to synthesise them using the same method used to prepare iron and nickel pyrites.

Copper pyrite is known to exist yet is only meta stable with rapid decomposition to various copper sulfides releasing sulfur as a biproduct.^{240, 242} However, it was still decided to attempt synthesis of CuS_2 pyrite as it may potentially show catalytic properties and may become more stable as the particle size becomes constrained.

The synthesis followed the previously described methodology with heating to 160 °C for 12 hours followed by separation by centrifugation. PXRD analysis was carried out on the obtained material (Fig. 3.35). From the PXRD pattern obtained from the material it was determined that CuS_2 pyrite synthesis was unsuccessful.

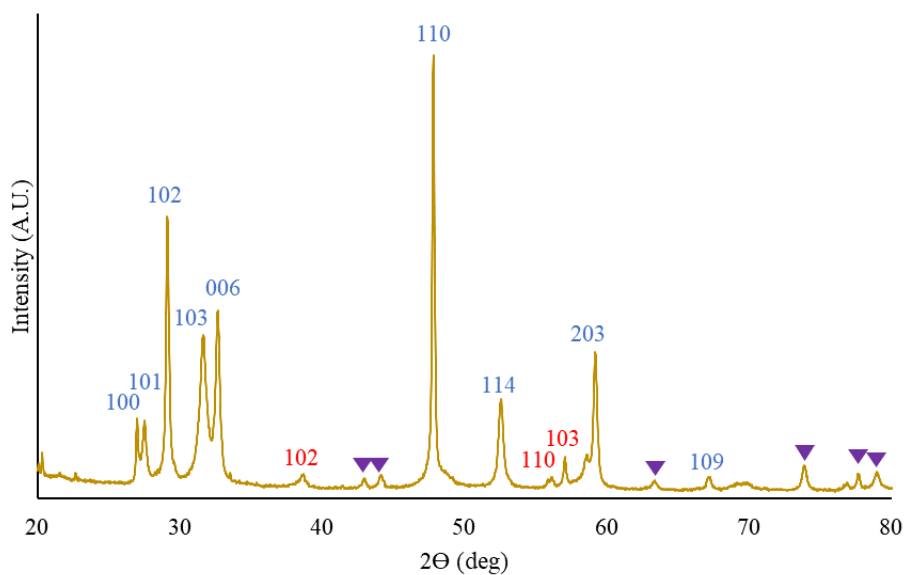


Figure 3. 35: PXRD pattern obtained from copper sulfide synthesis with peaks corresponding to CuS indexed in blue, Cu₂S indexed in red and unknown peaks indicated by purple triangles.^{64, 243}

However, an interesting largely pure phase of CuS ($P6_3mmc$) had been synthesised, with dilute quantities of Cu₂S ($P6_3mmc$) and other copper sulfides. This unidentified copper sulfide was deemed to mostly likely be Cu₇S₄ ($Pnma$), but peaks could not be assigned to Cu₇S₄ to determine this accurately. The crystal structures of CuS, Cu₂S and Cu₇S₄ are shown in Fig. 3.36.

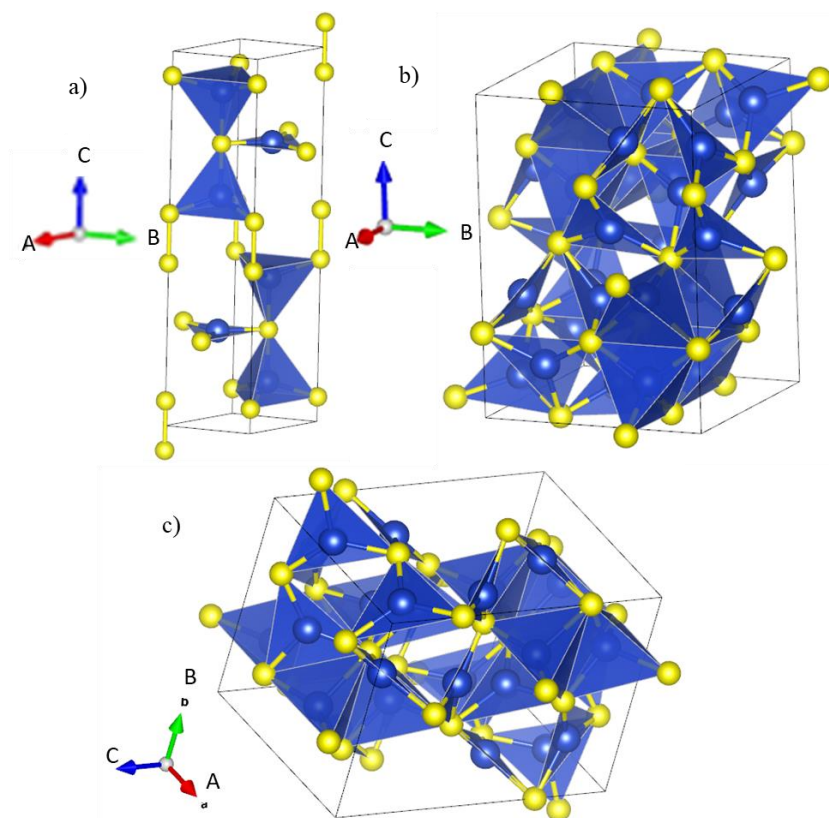


Figure 3. 36: Crystal structures of obtained copper sulfides from CuS_2 synthesis, a) CuS , space group $P6_3mmc$, b) Cu_2S , space group $P6_3mmc$, c) Cu_7S_4 , space group $Pnma$.^{222, 244-246}

Manganese disulfide synthesis was also carried out using the same reaction conditions. PXRD pattern of the obtained material is shown in Fig. 3.38. From the PXRD pattern obtained from the manganese sulfide synthesis, no evidence of manganese pyrite was obtained. Yet, there was a clear phase of α -MnS with a γ -MnS impurity, as shown by the peak indices on the pattern.

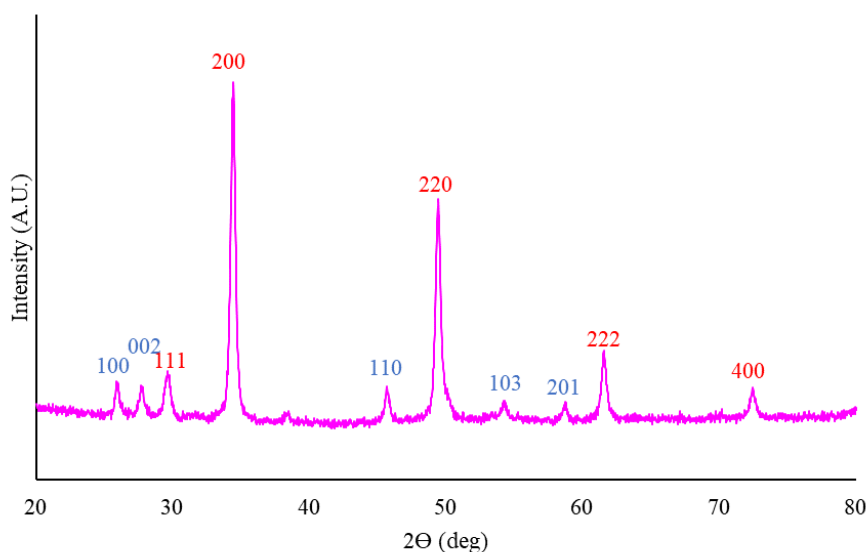


Figure 3. 37: PXRD pattern of material obtained from manganese sulfide synthesis, peaks corresponding to α -MnS ($Fm\bar{3}m$) indexed in red and peaks corresponding to γ -MnS ($P6_3mc$) indexed in blue.^{75, 76}

Although the pyrite structure of manganese was not obtained, these two polymorphs of MnS, crystal structures shown in Fig. 3.38, are still of interest in catalysis. As α -MnS is a rock salt (NaCl) type sulfide structure (Fig. 3.38a) this is contrasted by γ -MnS which is a hcp packed structure with manganese tetrahedra as opposed to the octahedra seen in α -MnS. Should these compounds display any catalytic performance the differences in structure may play a role in the catalysis and the selectivity towards a given product.

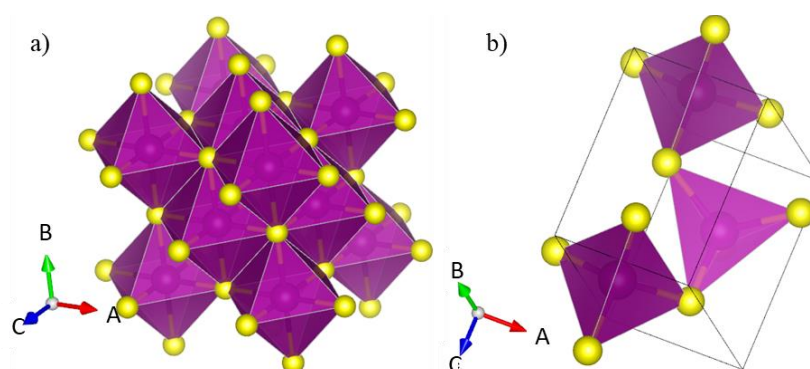


Figure 3. 38: Crystal structures of a) α -MnS ($Fm\bar{3}m$) and b) γ -MnS ($P6_3mc$).^{247, 248}

No manganese or copper pyrites were successfully synthesised in this work and the synthesised manganese sulfides will not be used in catalysis. However, in section 6.1.1, future work will

focus on purifying these phases to obtain a single phase of CuS, Cu₂S, α -MnS and γ -MnS. These single-phase sulfides will then be compared to the work carried out in chapter 4, to determine the applicability of these phases in hydrogenation of nitrobenzenes.

3.4.3 Vanadium, molybdenum and chromium

Molybdenum disulfide (MoS₂) is known to have catalytic properties in the hydrogenation of organic compounds.^{13, 87} Due to the properties displayed by MoS₂ it was decided that, using the previously optimised method for iron pyrite synthesis, MoS₂, Cr₂S₃ and VS₂ would be synthesised to determine if they had any applicability in the hydrogenation of nitrobenzenes.

Chromium sulfide synthesis was attempted first using chromium (III) acetate hydroxide, as chromium (II) salts are highly reactive and are air sensitive making them difficult to work with. It was decided that chromium (III) acetate hydroxide would be a suitable alternative as the final oxidation state of the chromium is 3+ in the sulfide. The chromium (III) acetate hydroxide was added to the auto clave with the other reagents and reacted at 160 °C for 12 hours. Once the reaction was cooled to room temperature the material was separated by centrifugation. The PXRD pattern of the material obtained from the reaction is shown in Fig. 3.39.

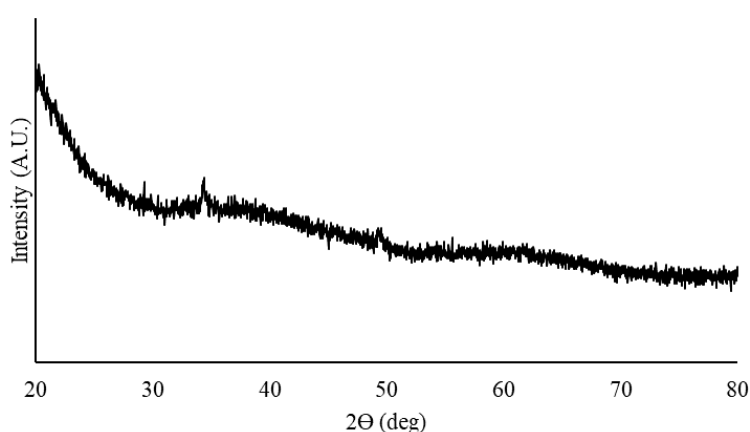


Figure 3. 39: PXRD pattern obtained from chromium sulfide synthesis.

The PXRD pattern obtained from the material obtained in chromium sulfide synthesis did not show defined peaks. This suggested that the material obtained was largely amorphous in nature. As the material could not be characterised and its phase identified definitively chromium was abandoned as a potential catalyst material.

For vanadium and molybdenum sulfide synthesis different metal precursors were required. These precursors were sodium metavanadate and sodium molybdenum oxide dihydrate.

2.5 mmol of the precursor was added to an autoclave as in previous reactions, with the other reagents and heated at 160 °C for 12 hours. After reaction was complete the material was separated by centrifugation. The materials were characterised by PXRD (Fig. 3.40) to determine the phases that had been synthesised.

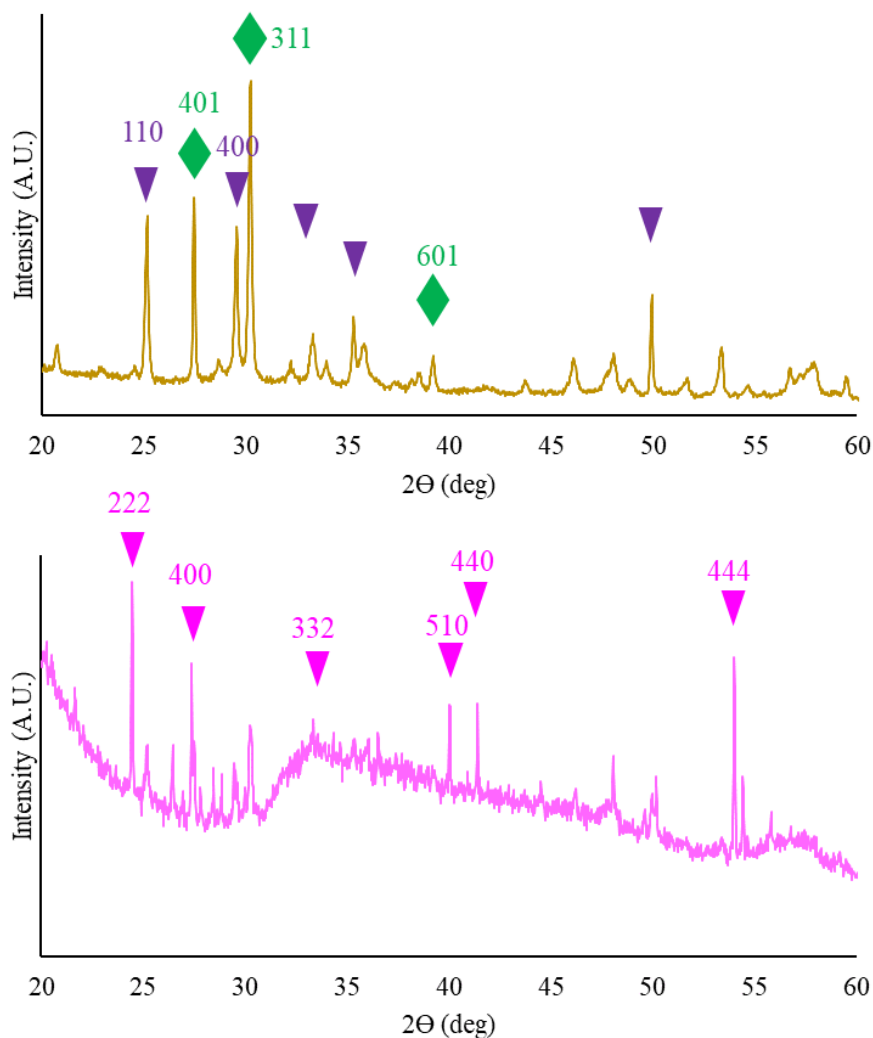


Figure 3. 0: PXRD patterns obtained for a) vanadium sulfide synthesis with sodium metavanadate peaks indexed in green and vanadium (V) oxide in purple and b) molybdenum sulfide synthesis with sodium molybdate peaks indexed in pink.

The PXRD patterns for both materials showed that no reaction had occurred with the starting metal precursors or their decomposition products, sodium metavanadate and vanadium (V) oxide (Fig. 3.40a) and sodium molybdenum oxide (Fig. 3.40b), being the dominant phase within the patterns. This lack of reaction observed using these metal precursors to be due to the stability of the metal oxygen bonds in both compounds. These metal oxygen systems dissociate from the sodium in solution forming vanadate and molybdate ions respectively. These two complexes are stable in solution and require a high energy to break the oxygen metal bonding. It was

determined that the reaction conditions were insufficient to break these bonds therefore no reaction occurred. As such the metals would not be used to test catalytic properties.

3.5 Conclusions

A successful and repeatable iron pyrite (FeS_2 , $Pa\bar{3}$) synthesis was developed and optimised to minimise the presence of other work at these reaction temperatures. This was achieved by optimisation of the reaction temperature across a range of 150 °C to 200 °C. The lower reaction temperatures were insufficient for the synthesis of a single phase FeS_2 material; lower temperatures left an impurity of sulfur within the final product. The temperature for the reaction was raised to 160 °C, at which point a single phase FeS_2 pyrite was produced. Increasing reaction temperature further to 180 °C generated a new greigite phase, Fe_3S_4 , mixed with FeS_2 pyrite phase. This phase mixture was maintained at a reaction temperature of 200 °C. The ideal reaction temperature for FeS_2 pyrite synthesis was deemed to be 160 °C, as this produced a single-phase pyrite.

Sulfur content of the reaction was optimised next with sulfur content ranging from 15 mmol to 1.75 mmol. The lower sulfur content, 1.75-3.75 mmol, produced a complex mixture of iron sulfides, with FeS_2 pyrite, Fe_3S_4 and other unknown sulfur deficient sulfides synthesised. A sulfur content of 7.5 mmol produced a binary phase mixture of FeS_2 pyrite and Fe_3S_4 , this was contrasted to a sulfur content of 15 mmol that produced a single phase FeS_2 pyrite. Due to the single phase FeS_2 pyrite produced by the reaction with 15 mmol of sulfur this was selected as the ideal sulfur content in future reactions.

Capping agent effects were studied by determining what effect no capping agent and capping agent acidity had on the synthesis products. Oleylamine capping agent was selected due to its prior use in nanoparticle synthesis and dodecane thiol was selected as an acidic capping agent to observe the effect a low reaction pH has on the product distribution. It was found that

oleylamine capped particles were single phase FeS₂ with an elongated shape, length 5.0 ± 0.5 nm. The particles obtained in the absence of a capping agent were a single phase FeS₂ nanoparticle material, particles have a spherical morphology with size of 16 ± 1 nm. Particles in the absence of oleylamine showed a tendency to aggregate together forming large ~ 0.75 μ m aggregates, this is seen to a much lesser degree with oleylamine present. Material obtained from reaction capped with dodecane thiol was determined to be FeS₂ marcasite, a differing polymorph of FeS₂ showed an irregular shape with large globular structures present throughout the sample. These globular structures were undetermined in their nature. After approximately 2 weeks the marcasite sample was reanalysed showing that it had degraded significantly forming an FeS₂ pyrite phase. The oleylamine capped reaction product would be used in catalytic testing.

Reaction solvent was studied to determine the effect this has on the phase of the material obtained. All reactions to this point had used ethanol as a solvent, as such reactions in water and ethylene glycol would be compared to this. In both, ethylene glycol and water, the obtained material phase changed from that of single phase FeS₂ pyrite to that of a mostly amorphous material believed to be FeS. Due to this the solvent was maintained as ethanol.

From these results it was determined that the optimum reaction conditions for single phase FeS₂ pyrite synthesis was 15 mmol sulfur and 2.5 mmol of iron (II) acetate, with 20 mL of ethanol as a solvent and 10 mL of oleylamine capping agent. Reaction temperature was 160 °C for 12 hours, with particles separated by centrifugation.

Attempting to substitute the metal centre within the pyrite structure with nickel formed an impure NiS₂ pyrite material and it is believed that this product contained either NiS or Ni₂S₃ but these could not be properly indexed. This material would be tested to determine its catalytic performance in relation to FeS₂ pyrite. The obtained NiS₂ material showed particle morphology

comparable to that of FeS₂ pyrite with particles showing an elongated form with length of 5.0 ± 0.5 nm. The substitution of iron with cobalt was unsuccessful the material obtained was believed to be amorphous CoS, as such cobalt was not tested further.

Substituting iron with copper and manganese obtained CuS and MnS phases, respectively. CuS phase obtained showed an impurity of Cu₂S and was suspected to contain a small impurity of Cu₇S₄. The MnS product showed a mixture of polymorphs with both α-MnS (rock salt type structure) and γ-MnS (wurtzite type structure) being present. As these phases were not of the pyrite structure they were not developed further in this work. However, future development on purifying these phases could yield a new hydrogenation catalyst.

Vanadium, molybdenum, and chromium sulfide synthesis was unsuccessful. Chromium sulfide synthesis was unsuccessful with no crystalline product obtained. Vanadium and molybdenum compounds did not react, as such the PXRD analysis of the compounds found that no metal sulfide had been formed. This was deduced to be due to the stability of the starting metal salt which mean that no reaction took place with the sulfur.

In conclusion, a method for repeatable iron disulfide (FeS₂) has been optimised to produce a single phase FeS₂ pyrite. The optimisation of this process included the temperature of reaction, sulfur content, capping agent and reaction solvent. Once optimised the method was implemented with several other metals, with nickel disulfide (NiS₂) pyrite being successfully synthesised. The nickel sulfide showed similar structural and morphological properties to the obtained FeS₂ pyrite, providing a direct comparison in the catalytic properties of the two materials. Copper and manganese sulfides were successfully synthesised; however, they did not show the pyrite structure. As such they would be excluded from this work.

In the next chapter, the catalytic properties of FeS₂ pyrite are explored in a transfer hydrogenation reaction for the reduction of 4-chloronitrobenzene. The reaction conditions are

optimised, and comparisons are drawn between the catalytic activities of FeS_2 pyrite and NiS_2 pyrite.

Chapter 4 Development and Optimisation of the FeS₂ pyrite catalytic hydrogen transfer reduction system

FeS₂ has shown great potential for use as a catalyst in the selective hydrogenation of nitrobenzenes via activation of hydrogen gas.^{9, 72} However, this process occurs at an elevated pressure of 10-50 atmospheres, requiring a great amount of energy in the production and pressurisation of the hydrogen gas. Recent advances have shown that hydrogen transfer routes may be used as a more environmentally friendly route to hydrogenation of organic molecules.¹²⁹

As discussed in section 1.5.2, hydrogen donor compounds take many forms, such as hydrazine monohydrate, tetralin and isopropanol.^{13, 134, 161} These hydrogen donor compounds all possess differing reaction pathways, producing products that may present incompatibilities with the substrate material.

For this work hydrazine monohydrate was selected as a hydrogen donor compound. Hydrazine monohydrate was selected due to its prevalent usage in industrial processes, in addition to its decomposition products (reaction scheme shown in Fig. 4.1) being inert and non-interfering in the hydrogenation reaction.

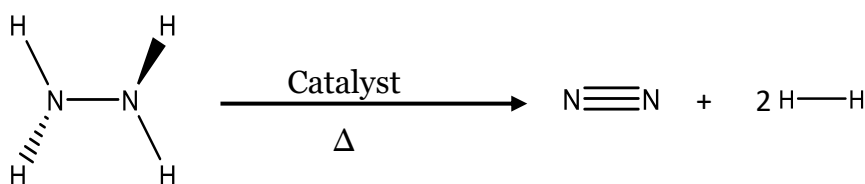


Figure 4. 1: Decomposition of hydrazine to nitrogen and hydrogen in the presence of a heterogeneous catalyst.

Hydrazine is not a perfect solution to ambient pressure hydrogenation reactions as it is known to be toxic and corrosive, therefore, careful handling procedures are required. Yet hydrazine monohydrate has numerous advantages compared to other potential hydrogen donor compounds, it contains 8 % hydrogen by weight, compared to approximately 3 % available hydrogen in tetralin and isopropanol, also being highly miscible with many solvents, as such

issues observed with hydrogen solubility are further reduced when hydrazine is used as a hydrogen donor.^{135, 160, 164} The hydrogen transfer reaction using hydrazine was demonstrated by Wang et al. to be a rapid tool for low temperature and low pressure reduction of nitroarenes.¹³ This work also showed that in the presence of the substrate minimal ammonia was produced from the decomposition of hydrazine, with nitrogen being the dominant product of decomposition.

In this chapter, the initial transfer hydrogenation of 4-chloronitrobenzene is studied with extrapolation and cross analysis for the potential reaction mechanism. Once the reaction was shown to be successful, the reaction parameters were optimised in order to obtain a reaction system in which catalytic performance and selective product production was maximised. Yet, the environmental considerations of the system were taken into account to reduce the potential impact of the system.¹⁴

The parameters that were optimised for the chemoselective transfer hydrogenation were the solvent used in the reaction, the catalyst loading, reaction temperature and the hydrazine monohydrate concentration. These parameters all effect the reaction characteristics, which drive the overall conversion of 4-CNB and the selectivity of the reaction.

Once the reaction is optimised to compromise between the reaction performance and environmental considerations, the reaction could be studied in greater depth. This includes a hot filtration of the reaction; this involves the removal of the catalyst from an in-progress reaction. This is useful in determining whether leached catalyst material plays a role in the catalysis, this is important due to previous studies suggesting the semi homogeneous nature of metal sulfides in catalysis. Once the reaction was confirmed to cease after the removal of the catalyst material, studies were carried out to determine how recyclable the FeS₂ catalyst is under repeated use in hydrogen transfer reactions with minimal catalyst processing between

reaction cycles. The results from the hot filtration and recyclability study would then be fed into a study of the catalytic activity of the pyrite structure, this was achieved by comparing the catalytic activity of the FeS₂ and NiS₂ pyrite nanoparticles synthesised in Section 3.4.1. The comparative reactions were carried out by applying the NiS₂ pyrite nanoparticles to the optimised transfer hydrogenation conditions. Studying the metal within the pyrite structure and the effect on the reaction shows how the electronic configuration of the metal effects the catalytic properties of the pyrite material.

4.1 Experimental

4.1.1 Materials

1-chloro-4-nitrobenzene 98+ %, 4-chloroaniline, aniline 99+ %, nitrobenzene 99+ % and hydrazine monohydrate 98+ %, were purchased from Alfa Aesar.

Methanol (analytical grade), absolute ethanol, butan-1-ol (analytical grade), hexane (analytical grade), dimethyl sulfoxide (analytical grade), acetonitrile (analytical grade), dichloromethane (analytical grade) and toluene (analytical grade) were obtained from Honeywell Lab Chemicals

4.1.2 Hydrogenation procedure

The general procedure for carrying out tests on the new catalytic system was as follows: 0.39 g (2.5 mmol) of 4-chloronitrobenzene substrate (4-CNB) and 0.46 g (5 mmol) of toluene toluene internal standard were added to a 50 mL volumetric flask. The solvent (ethanol or hexane for testing) was then added to dissolve the substrate and internal standard, solution then topped to volume with solvent to prepare a 0.05 M substrate and 0.1 M internal standard solution.

A range of catalyst masses (0 mg to 50 mg) would be added to the batch reactor with 50 mL of the chloronitrobenzene solution. The solution would then be purged with nitrogen 3 times until all oxygen had been removed from the reaction vessel.

The solution was left to equilibrate under the nitrogen atmosphere for 30 minutes at the reaction temperature, between 25 °C and 80 °C, before 20 mmol of hydrogen donor compound (1 mL hydrazine monohydrate) was injected into the reaction.

After this point 250 µL aliquots of the solution were extracted at 0, 10, 20, 40, 60, 80, 100 and 120 minutes reaction time, these times were selected to obtain a full reaction profile across the reaction, opposed to a single end point. Each aliquot was analysed using a Varian 430 gas chromatograph equipped with a 30 m Stabilwax® capillary column (Restek), each aliquot was injected in triplicate in order to obtain the standard deviation and uncertainty in the measurements.

4.1.3 FTIR analysis

FTIR spectroscopy was carried out on the FeS₂ catalyst material pre- and post-catalysis. FTIR analysis was carried out using a Thermoscientific NicoletIS5 spectrometer with a Pike Miracle diamond ATR attachment carried out from 800 cm⁻¹ to 4000 cm⁻¹.

4.1.4 PXRD analysis

Powder X-ray diffraction (PXRD) carried out using a PANalytical Empyrean X-ray diffractometer with inline PIXcel detector. The monochromatic Cu Kα₁ radiation was used and the diffractograms were obtained in the 2θ range of 20–80°. A 1° divergence slit was used for all samples and a Ni anti-scatter filter, to minimise the fluorescence of iron under Cu Kα₁ radiation.

4.1.5 TEM and EDX analyses

Transmission Electron Microscopy (TEM) studies were performed in a high-resolution (HR) (0.18 nm) field emission JEOL 2200FS microscope operating at 200 kV, equipped with an in-column Ω energy filter, two High-Angle Annular Dark Field (HAADF) detectors for the so-called ‘Z-contrast’ imaging and an Energy Dispersive X-ray Spectrometer (EDX) for collecting X-ray spectra and X-ray mapping. The nanostructures were dispersed on holey copper grids for the observation.

4.2 Results and Discussion

4.2.1 Parameters for the optimisation of nitrobenzene hydrogenation

To characterise the catalytic behaviour of the new catalyst materials and system, the reaction-catalyst interaction was investigated and compared key reaction parameters with the view of optimising each of them within the context of the whole reaction system and its industrial applicability. The reaction metrics analysed are conversion, selectivity and initial rate and are defined by equations 4.1-4.3.

$$\text{Conversion (\%)} = \left(\frac{C_0 - C_t}{C_0} \right) * 100$$

Equation 4.1

$$\text{Selectivity (\%)} = \left(\frac{C_{XAN}}{C_{products}} \right) * 100$$

Equation 4.2

$$\text{Rate} = \frac{C_0 - C_t}{t}$$

Equation 4.3

where C_t = concentration of substituted nitrobenzene benzene at time t , C_0 = initial concentration of substituted nitrobenzene substrate, C_{XAN} = concentration of substituted aniline product, C_{products} = concentration of all products present in the reaction, t = reaction time elapsed.

4.2.1.1 Test reaction

To determine the initial effectiveness of pyrite as a hydrogenation catalyst via a hydrogen transfer route, test reactions were carried out using a modified methodology reported by B. Ma et al. 50 mL of a 0.05 M solution of 4-CNB in ethanol and⁹ 100 mg of pyrite (prepared in Section 3.2) was added to a 250 mL three-neck flask and connected to reactor shown in Fig 2.20 (see section 2.3.1.1), the reactor was purged with N_2 three times and left to equilibrate at 60 °C for 30 minutes. Once the reactor had been left to equilibrate for 30 minutes, 1 ml of hydrazine monohydrate was injected into the reactor through a silicon suba seal and reactor time started. At this point $t = 0$ time point extracted from the reaction mixture for GC analysis. Time points were taken from the reactor in ~250 μL aliquots at 1, 5, 10 minutes and every 5 minutes after this for a total of 90-minute reaction time. As this reaction was only used as a test, reaction was stopped after 90 minutes to give an approximate measure of reaction performance using extreme reaction conditions.

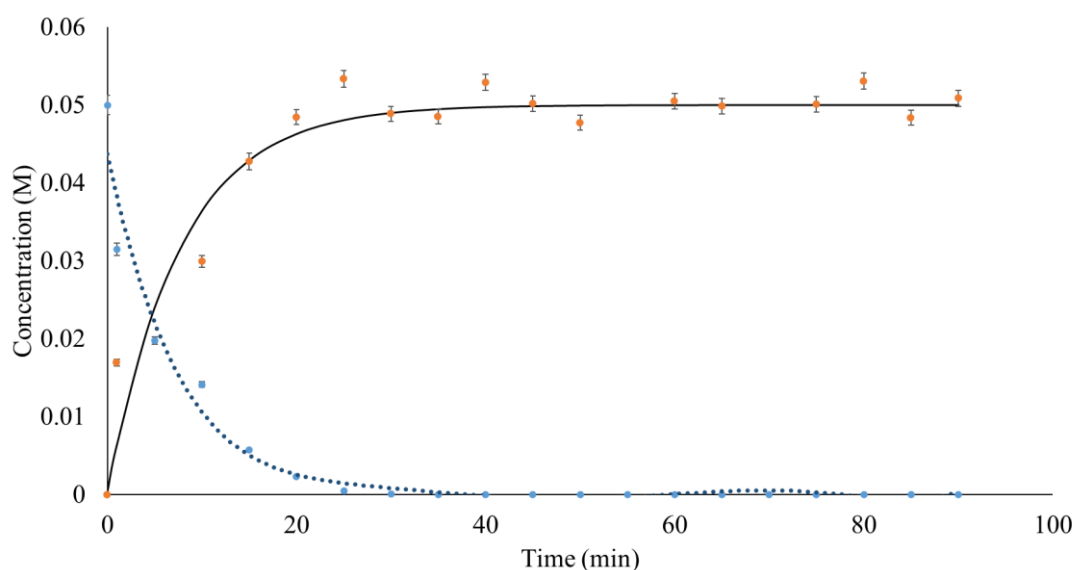


Figure 4. 2: Reaction profile for the FeS_2 catalysed hydrogen transfer hydrogenation in ethanol test reactions with decreasing 4-CNB concentration (blue) and increasing concentration of 4-CAN (black/orange) with time, averaged across 3 test reactions.

The test reactions, Figure 4.2, showed that FeS_2 was a highly effective catalyst for the hydrogen transfer reaction from 4-CNB to 4-CAN using hydrazine monohydrate as a hydrogen donor. In the conversion of nitroarenes using noble metal catalyst materials, published results report conversion of 50% in 5 hours.^{13, 87} In this work, using a FeS_2 nanoparticle catalyst and a hydrogen transfer agent, more than 99% conversion was obtained in less than two hour reaction time. Hence, using the FeS_2 and a hydrogen transfer agent, noticeable differences were observed in reaction rate and overall conversion of substrate material. The data obtained for 4-chloroaniline synthesis was fitted to a 1st order reaction plot as shown by the black line on the plot in Fig. 4.2, this yielded a rate constant of 0.1296 min^{-1} and initial rate of reaction of $6.5 \times 10^{-3} \text{ mol dm}^{-3} \text{ min}^{-1}$. Demonstration of this reaction rate fitting is shown in Fig. 4.3. This method of initial rate determination or close approximation was carried out for all data described.

Kinetic modelling of the reaction was carried out by plotting the data obtained from the test reactions according to first order and second order integrated rate equations, equations 4.4 and 4.5 respectively.

$$\ln[A] = \ln[A]_0 - kt \quad \text{Equation 4.4}$$

$$\frac{1}{[A]} = \frac{1}{[A]_0} + kt \quad \text{Equation 4.5}$$

From the plots obtained in Figures 4.3 a and b, the reaction kinetics observed for the selective hydrogen transfer reduction of chloronitrobenzene to chloroaniline by the FeS₂ nanoparticle catalyst is first order. The natural log of the change of concentration produces a linear plot against time, thus showing the reaction is first order. The first order kinetics of the reaction has been considered for future plots within this thesis when initial rate of reactions are compared.

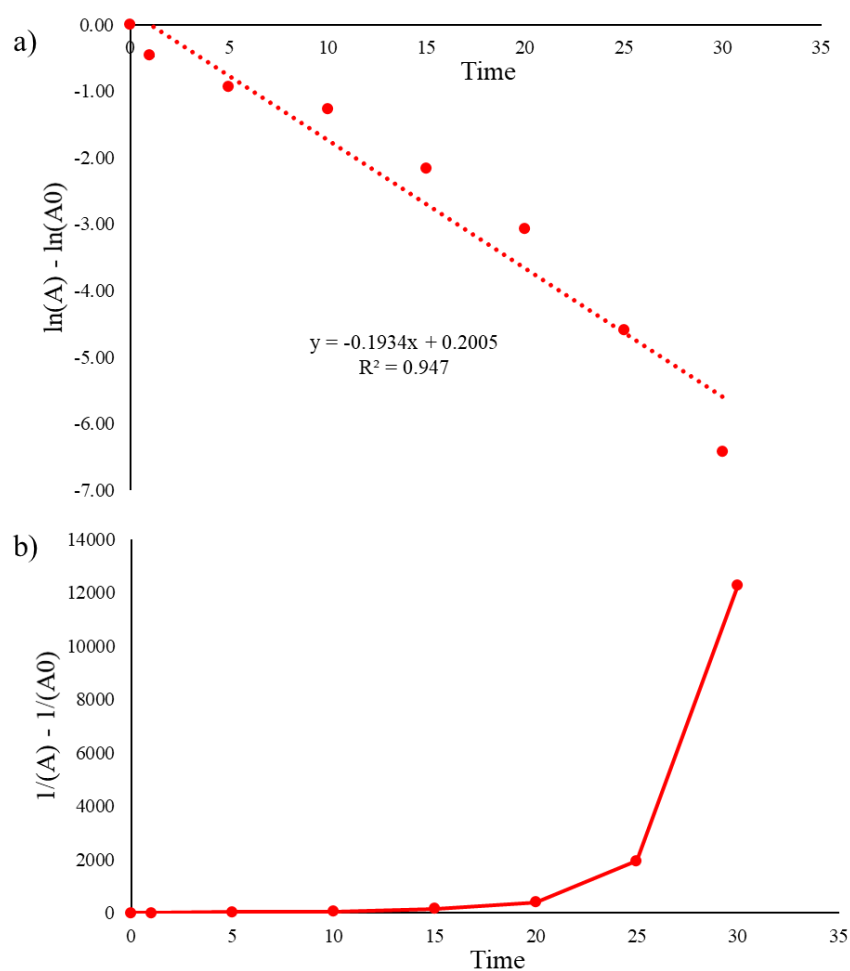


Figure 4. 3: a) 1st order kinetic plot for chloronitrobenzene consumption against time, b) 2nd order kinetic plot for chloronitrobenzene consumption against time, using data shown in figure 4.48.

One of the reasons for this increased efficiency, may be due to FeS_2 , which has been reported to show high selectivity towards CAN, thanks to the highly directional interaction of 4-CNB with the pyrite surface. 4-CNB is believed to interact at 90° to the pyrite surface with the nitro group bound to the disulfide ions.^{9, 72} This interaction makes the nitro group immobile on the surface, hence easier to be hydrogenated by dissociated hydrogen on the surface of the pyrite (Fig. 4.4). DFT analysis by Q. Xiao et al. showed that the strong nitrogen transition metal interaction prevented the movement of nitrobenzene across the catalyst surface and thereby reducing the likelihood of secondary reactions.²³⁵

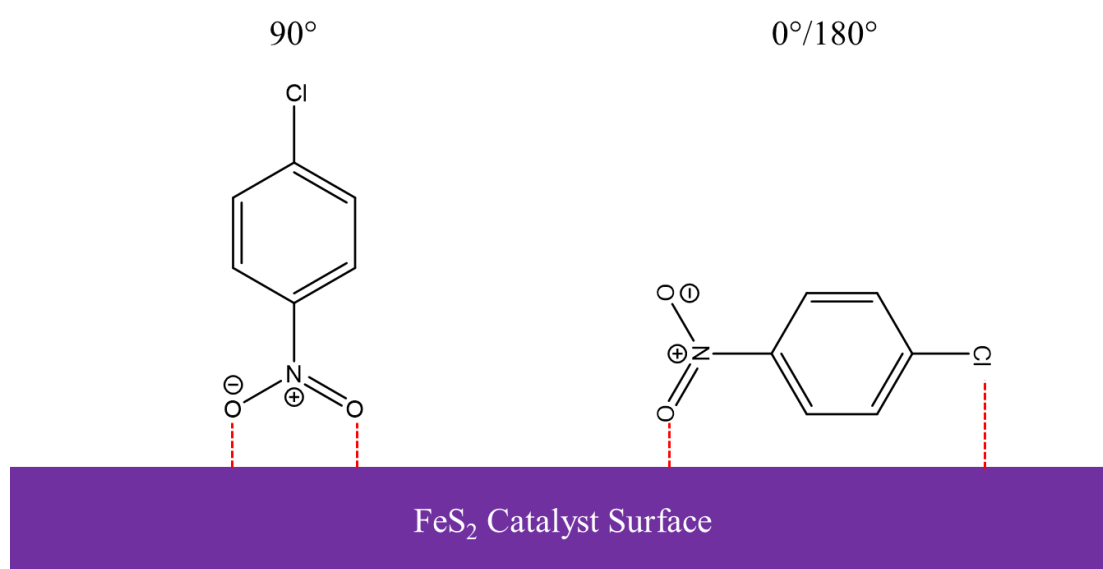


Figure 4. 4: graphical representation of 4-CNB binding to the FeS_2 catalyst surface at two different angles 90° and $0/180^\circ$.

Alternatively, some studies have promoted an interaction of nitrobenzenes at 180° to the catalyst surface, due to the resonance stabilised π ring promoting a parallel interaction with the catalyst surface. The perpendicular immobile interaction of nitrobenzene on the catalyst surface, prevents secondary reactions from occurring on the catalyst surface as the “tail” 4 position of the ring is placed at a distance where the activation energy of this reaction tends towards infinity (fig. 4.4). Conversely, should the substrate adsorb to the catalyst surface at an

angle of 0° or 180° , the 4 position becomes much more likely to interact with the catalyst and reaction may become possible, therefore reducing selectivity.

Due to the high selectivity of near 100% towards 4-chloroaniline seen in the test reactions, there is a high confidence that a perpendicular interaction is favoured by FeS_2 . This limited removal of functionalisation in the substituted aniline product shows the promise that FeS_2 as a catalyst shows. To study this 4-CNB was used as a model compound with the Cl acting as the functionality of the compound. Removal of the Cl was to be avoided as this would demonstrate a lack of selectivity in the catalyst as such the reaction conditions were optimised so that maximum conversion of 4-CNB was achieved, yet the reaction selectivity was maintained towards 4-CAN.

4.2.1.2 Optimisation of catalyst loading

The conversion of CNB to CAN is higher in our hydrogenation reaction, however, the reaction was too fast for the rate to be measured in a reliable way in our first tests. A reliable reaction rate measurement was needed to compare reaction conditions and optimise them. The rate can be reduced by reducing the amount of catalyst used. Reducing the amount of catalyst is also important to prevent over usage, which can lead to a lack of selectivity.^{9, 249} Therefore, the first aim in the process of optimisation of the hydrogenation process was to determine the minimum mass of catalyst required to obtain full conversion of CNB within two hours. A two hour window was selected as this would allow for rapid reactor reuse in an industrial application.¹ The selective hydrogenation of CNB to CAN was carried out using 0, 5, 15, 25, 40 and 50 mg of FeS_2 catalyst. The conversion of CNB during each reaction over time is shown in Fig 4.5.

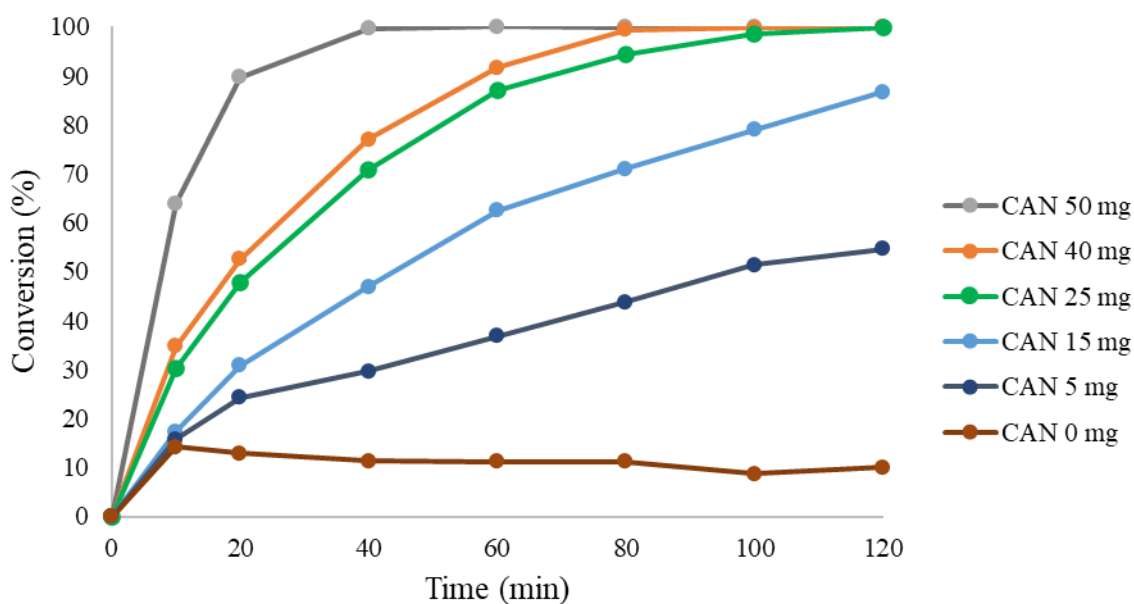


Figure 4. 5: Conversion percentages for hydrogenation reactions of 4-CNB at different reaction time points, using differing amounts of FeS_2 catalyst.

In agreement with literature, increasing the FeS_2 catalyst load causes a near linear effect on the initial rate of a given reaction calculated by the change in CAN concentration between the T_0 and T_{10} time points.² Fig. 4.4 shows that the reactions that reached complete 100% conversion of CAN to CNB within two hours were those with 50, 40 and 25 mg of FeS_2 catalyst loading. The optimum loading of catalyst was found be 25 mg. 10 mg and 5 mg of catalyst loading gave a conversion of 80% and 50% CNB respectively in 2 hours (Fig. 4.6). This lower conversion would lead to a longer reaction time for complete conversion, therefore limiting the turnover of an industrial reactor.

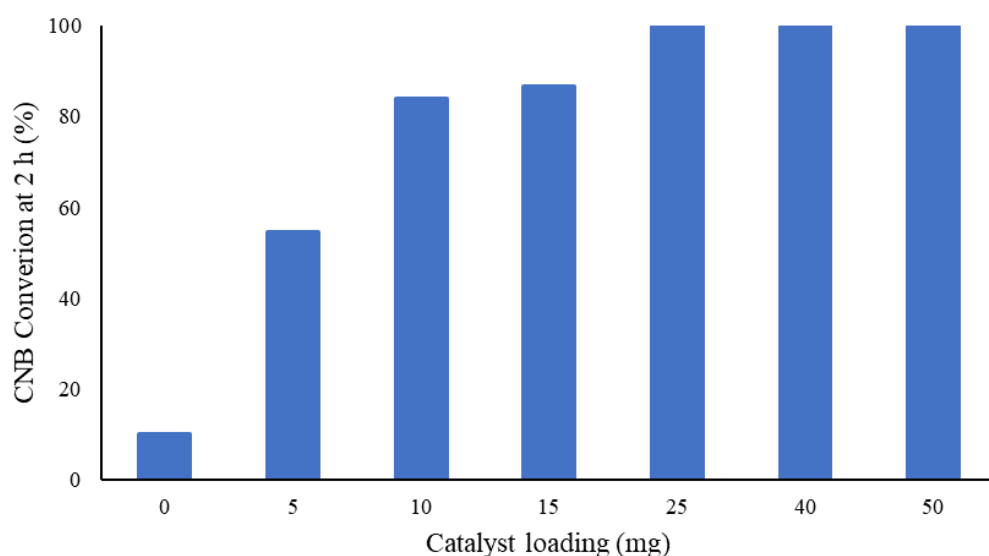


Figure 4. 6: Conversion of CNB after 2 hours against catalyst loading.

50 mg, 40 mg or 25 mg of catalyst loading showed complete CNB conversion at 2 hours and showed negligible difference after 60 minutes of reaction time. Therefore, using a higher loading than 25 mg of catalyst would offer little advantage. Future reactions were carried out using 25 mg of FeS₂ catalyst. Of note there was no loss of selectivity towards CAN with increased catalyst content, the selectivity maintained at >99.9%. As a further test, we carried out the reaction in the absence of the catalyst (fig. 4.8) and observed a 12% conversion of CNB to CAN. The loss of activity may be a result of the interaction of ethanol and hydrazine.^{250, 251,130}

To determine the most efficient loading of the catalyst for the reaction further, the rate of reaction was normalised to obtain which mass of catalyst gave the highest rate per gram of catalyst (Fig. 4.7).

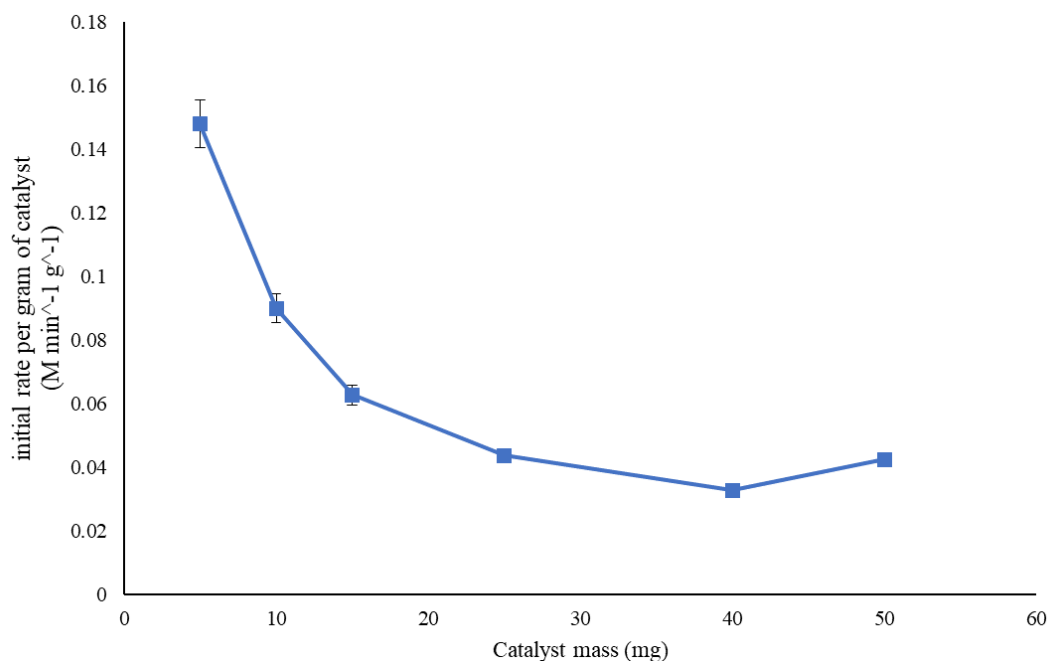


Figure 4. 7: Normalised rate of reaction against catalyst mass.

The normalisation of the rate, calculated by the change in CAN concentration between T_0 and T_{10} , confirmed that 25 mg loading offers the highest compromise between rate and conversion of 4-CNB in a two-hour time window. However, 5 mg of catalyst produced the most rate relative to the amount of catalyst loading. It could then be determined that, should reaction times be increased, catalyst loading would be conversely decreased to increase the catalytic systems efficiency. Further advantages are that the synthesis of FeS_2 is economical in that per gram of catalyst nanoparticles produced the combined costs are £14.18/gram, compared to approximately £30/gram for a comparable commercially available Pearlman's catalyst, making FeS_2 a promising environmentally and economical catalyst for aniline synthesis.^{9, 24, 51}

4.2.1.3 Solvent study

Solvent choice is an important factor in all chemical reactions as certain reactants may be insoluble in certain solvents or the solvent may become a reactant itself producing unwanted side reactions. Solvents affect the rate of reactions and product distributions, due to a solvent-substrate-catalyst interaction.^{24, 252} In heterogenous catalysis solvent plays another role in

transporting the substrate to the catalyst surface and then carrying away the product material. There are adsorption and desorption forces that play a role in determining how active/selective the reaction becomes in differing solvents and discrepancies in activity/selectivity can be attributed to how much of an affinity the reactants and products have to either the solvent or the catalyst surface. A higher affinity to the catalyst surface in the reactants will increase the activity of the reaction, a decreased affinity to the solvent by a product material may lead to further reactions occurring on the catalyst reducing the overall selectivity in a given solvent.

When rate of adsorption, (R_{ads}), is equal to the rate of product desorption, (R_{des}), the reaction rate is not dominated by either adsorption or desorption and reliant on the catalyst reaction. If $R_{ads} \ll R_{des}$, reaction kinetics are dominated by the slow rate of substrate adsorption to the catalyst surface. If $R_{ads} \gg R_{des}$, reaction kinetics become dominated by the slow rate of desorption of product material from the catalyst surface, in this case further reactions may occur on the catalyst surface whilst the substrate remains adsorbed.

To study the effect that a solvent had on the transfer hydrogenation of 4-chloronitrobenzene, a wide range of solvents were selected. These included nonpolar (hexane), polar protic (methanol, ethanol, butan-1-ol) and polar aprotic (dimethylsulfoxide, dichloromethane and acetonitrile).

Solvent	Dielectric Constant ($F\ m^{-1}$)	pKa
Hexane	1.89	50.00
dichloromethane	8.93	50.00
Butan-1-ol	17.80	16.95
Ethanol	25.30	16.00
Methanol	33.00	15.40

Acetonitrile	37.50	25.00
dimethylsulfoxide	47.00	31.00

Table 4.9: Solvents studied with their associated dielectric constants and pKa values.

These solvents were selected due to their prevalence in catalysis and general synthetic chemistry. These solvents show a wide range of pKa values and dielectric constants, as such it was theorised that they would show the differences such parameters play in the reaction, with the previously described adsorption/desorption phenomena.

To mitigate the effect that minor differences in catalyst amount would play, rates of reaction were normalised to the catalyst loading used. Fig. 4.8 showed that there is no correlation between the dielectric constant and the normalised rate of reaction. Hexane, dielectric constant 1.89 F m^{-1} , and dimethylsulfoxide, dielectric constant 47.00 F m^{-1} , showed the greatest rate and appeared to “bookend” the results.

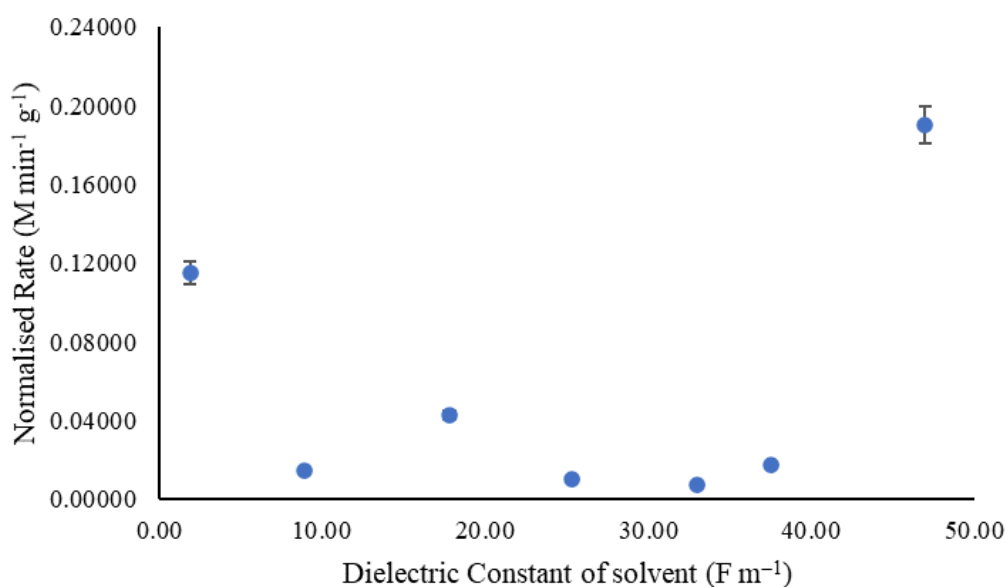


Figure 4. 8: Normalised rate plotted against dielectric constant for the seven solvents trialled in the solvent study.

Removing the two highest values for the dielectric constant from the plot in figure 4.8 gave a somewhat clearer picture of the random effect dielectric constant had on the normalised rate of reaction (Fig. 4.9).

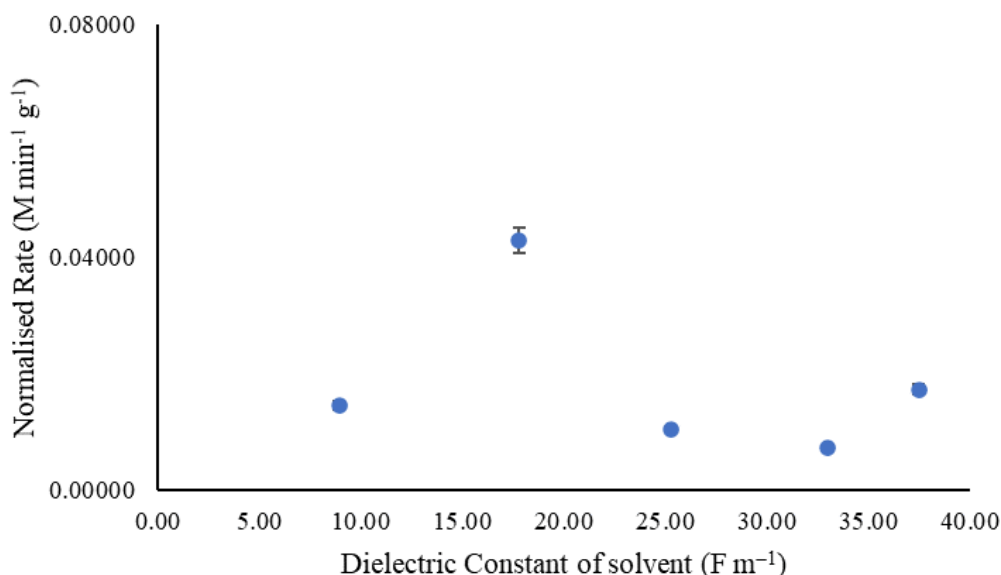


Figure 4. 9: Normalised rate against dielectric constant for the five remaining solvents after hexane and dimethylsulfoxide were removed.

When studying the effect each solvent had on the conversion of 4-CNB, within the 2 hour reaction window, two solvents were shown to be inferior to the others (Fig. 4.10). These two solvents, dichloromethane and methanol, showed a conversion of only 41.7 % and 69.4 % respectively, vastly lower than the 99.9 % observed in all other solvents. Dichloromethane has several environmental considerations in addition to its poor performance as a solvent and it is incompatible with many oxidizers including nitro compounds. As such it was not considered as a possible reaction solvent going forwards.

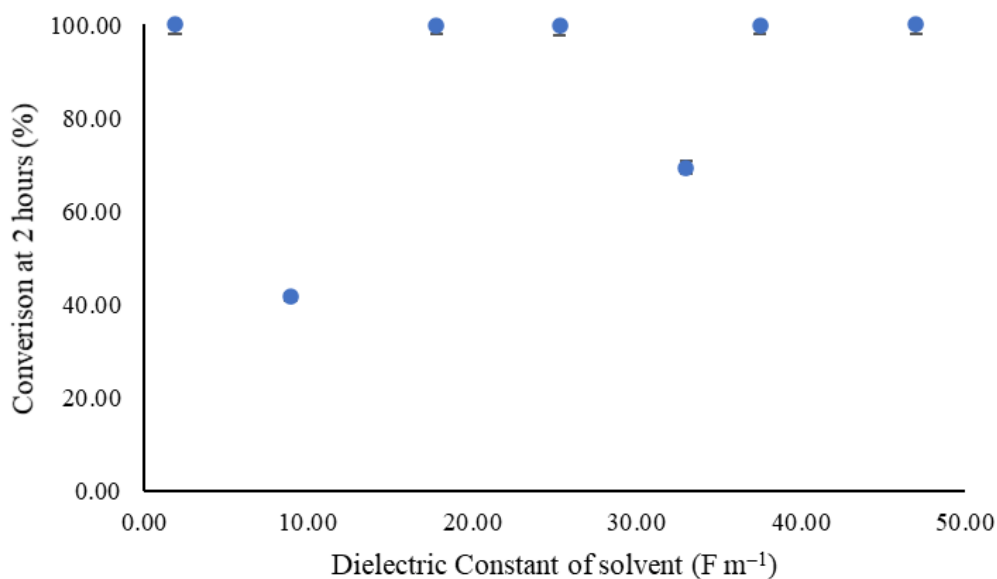


Figure 4. 10: Conversion of 4-CNB for seven solvents against their associated dielectric constants.

Methanol was still considered as a potential solvent as it had environmental advantages over other solvents due to its production from CO₂ conversion and cost effectiveness.

As noted in section 4.2.1.2, there was a small approximately 12 % conversion of CNB without the presence of the FeS₂ catalyst. This was deemed to be an instantaneous conversion as the conversion occurred in a short time, as such it could not be monitored *in situ*. When studying the solvent effect on the reaction, it was noted that this “instantaneous conversion” differed with each solvent studied. This “instantaneous conversion” effect was monitored for all solvents with the resultant plot shown in Fig. 4.11.

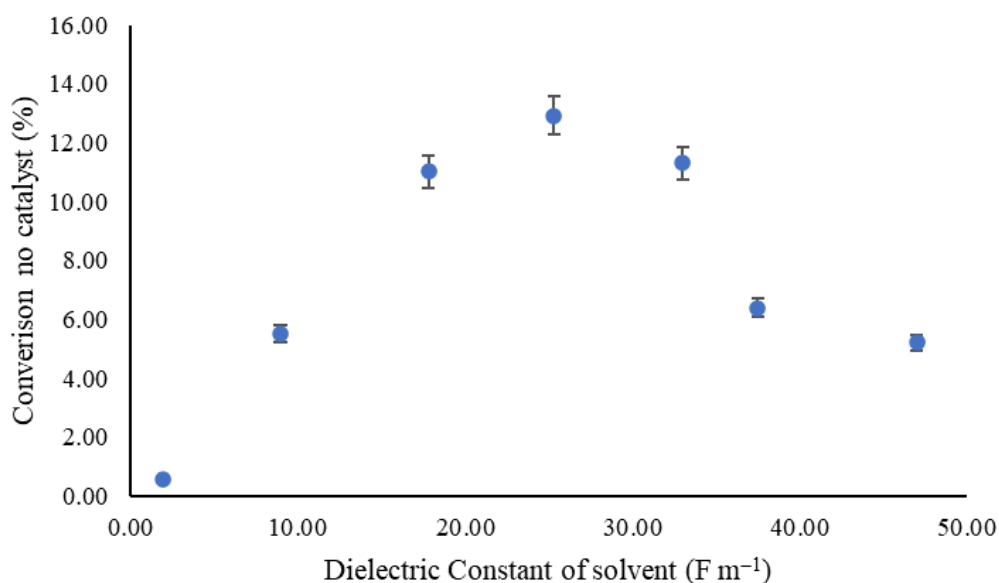


Figure 4. 11: instantaneous conversion in the absence of a FeS_2 catalyst for seven solvents against their associated dielectric constant.

When conversion in the absence of a catalyst is considered against the dielectric constant a clearer correlation can be seen. This “volcano like” distribution shows a maximum corresponding to ethanol. Of the solvents tested, alcohols all showed the greatest conversion of 4-CNB in the absence of the catalyst. To study this further, 4-CNB conversion in the absence of a catalyst was shown against the pKa of the selected solvents (Fig. 4.12). pKa is a measure of strength of acidity of a given compound, it is defined as the negative log of the dissociation constant K_a . A lower pKa value indicates a stronger acid; pKa of weak acids such as acetic acid is approximately 4 and for stronger mineral acids such as hydrochloric acid is approximately -6.

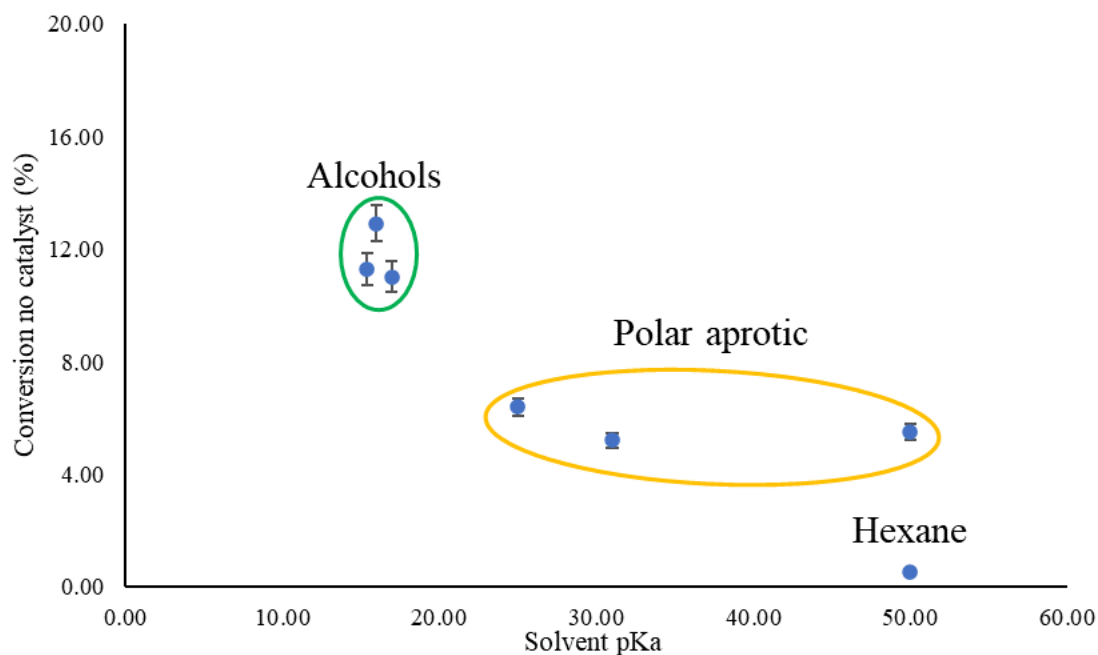


Figure 4. 12: Conversion of 4-CNB in the absence of a catalyst plotted against the pKa of the seven solvents tested, with areas corresponding to solvent classification highlighted.

With the conversion in the absence of the catalyst plotted against the solvent pKa clear groupings of results can be seen. Alcohols showed a tight grouping of conversion without the catalyst and their close pKa values, this group (green) was distinct from those of the polar aprotic solvents (yellow) and hexane. This showed that the acidity of the alcohols had a distinct effect on the hydrogenation of 4-CNB in the absence of a catalyst. The rationale for this difference in conversion in the presence of a protic solvent is that the highly basic hydrazine monohydrate partially reacts with the protons from the solvent molecules. The protons are more easily removed from alcohols compared to those present in DMSO, ACN, DCM and hexane, therefore, these free protons in the alcohol solvents convert a greater percentage of the 4-CNB via an interaction with the hydrazine than the higher pKa solvents. However, this increased interaction without the presence of a catalyst does not lead to a greater conversion of 4-CNB with FeS₂ being present as other factors such as miscibility of the hydrazine monohydrate with the reaction solvent appears to drive the reaction to a greater degree than the protic nature of the solvent, shown in Fig. 4.13. Once the catalyst is introduced, there is no observable trend for

how the solvent affects the initial rate when pKa is considered (Fig. 4.13). This lack of correlation between the pKa of the reaction solvent and the observed rate of reaction indicates that there are other factors in the overall interaction between the solvent, substrate, hydrogen donor and catalyst, these factors may have a far greater influence in the overall reaction kinetics than the pKa.

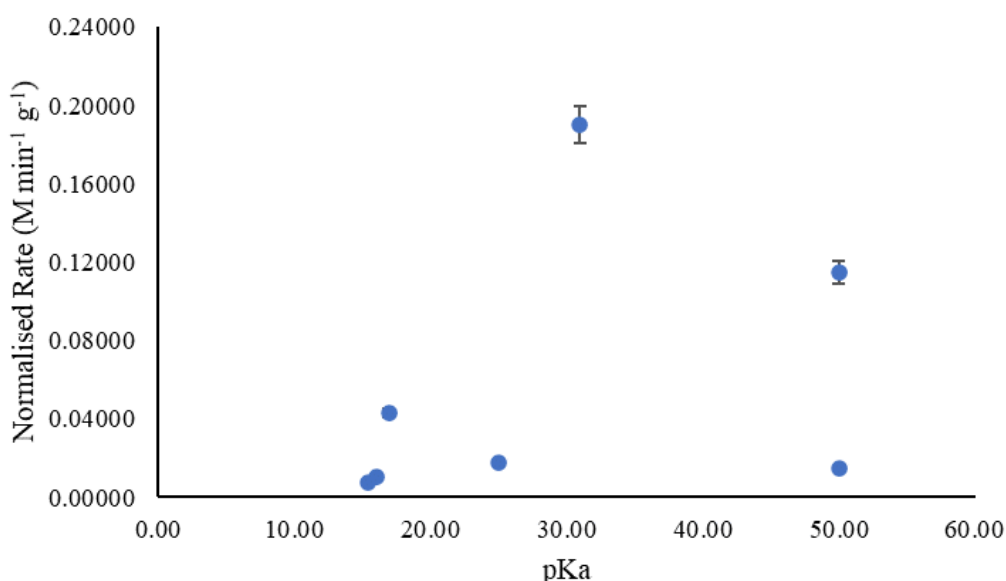


Figure 4. 13: Normalised rate of reaction for the hydrogen transfer hydrogenation of 4-CNB against the pKa of the reaction solvent.

Due to these findings many of the solvents were removed based on their environmental concerns as opposed to their reaction suitability. Acetonitrile, dichloromethane and dimethylsulfoxide (DMSO) were removed due to their impact on the environment. In spite of the high performance of DMSO, its environmental impact is significant and is not mitigated, as such it was removed from consideration. Hexane was further studied due to its prevalence as a solvent for industrial fine chemical synthesis, despite its environmental impact from its extraction from crude oil.²⁵³⁻²⁵⁵

Alcohols were studied in greater detail to determine the optimal solvent when combining its reaction characteristics and the environmental impact of its production/use. As discussed

earlier the hydrogen transfer reactions carried out in alcoholic solvents performed similarly, in terms on substrate conversion and selectivity, to hydrogen transfer reactions carried out in aprotic and polar solvents. Under a more detailed analysis isolating the solvents based on their respective pKa values and the conversion of 4-CNB in two hours (Fig. 4.14) a clear distinction can be made.

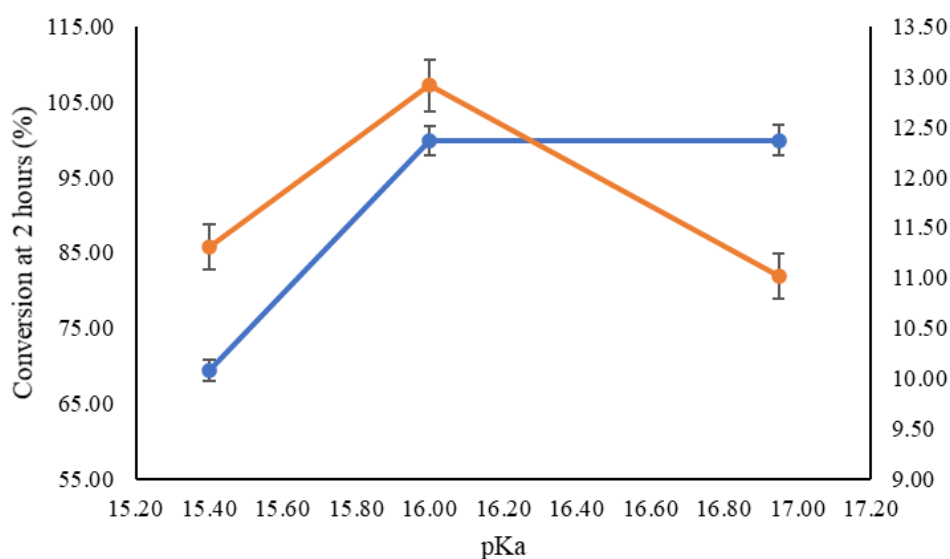


Figure 4. 14: Conversion of 4-CNB with 25 mg catalyst (blue, left side y-axis) and without catalyst (orange, right side y-axis) in a two hour reaction timeframe against their respective pKa (methanol left, butan-1-ol right).

From the comparison of ethanol, propan-1-ol and butan-1-ol, emerged that ethanol and butan-1-ol, both showed 4-CNB conversion of 99 ± 1 % within the two hour reaction window, in contrast to methanol, where only 69 ± 1 % of 4-CNB was converted in the two hour reaction window. All solvents maintained a 100 % selectivity towards the 4-CAN product. The significant decrease in conversion in a methanol solvated reaction eliminated methanol as a potential solvent in the catalyst system. Ethanol and butan-1-ol showed very similar characteristics in their solvation of reactions, with only minor differences in the normalised rate.

To determine the most optimal solvent their environmental impact was used to distinguish them. Ethanol is widely bioderived requiring little energy to produce, as such it is an abundant

and cheap solvent with a negligible environmental impact when appropriate disposal procedures are used.²⁵⁶⁻²⁵⁸ In contrast butan-1-ol production is still largely produced by the Reppe reaction between propylene and CO to produce butan-1-al, which is then reduced over a cobalt-rhodium catalyst in a hydrogen stream.^{259, 260} However, recent lab scale studies have shown that butan-1-ol can be synthesised from biomass using a bacterial fermentation, although such method has not been widely adopted in industrial scale synthesis.^{261, 262}

Ethanol was therefore deemed the most appropriate solvent; hence it was then studied in detail in comparison to the industrial standard of hexane.

Hexane is largely produced from the fractional distillation of petrochemicals, as such its environmental impact is significant. Yet it does have major advantages in industrial applications, as it is relatively inert in a hydrogenation reaction, can solubilise a wide variety of organic compounds and can be easily separated from the products due to its low boiling point of 67 °C.^{21, 89, 263}

In this more focused solvent study, hexane and ethanol were compared on their performance as a solvent in the desired reaction range. Low catalyst concentration (less than 0.2 mg mL⁻¹) was studied to impose an active site deficient situation and study the solvents behaviour (Fig. 4.15). The purpose of studying an active site deficient reaction was to determine how the movement of the substrate through each solvent affected the perceived rate of overall reaction.

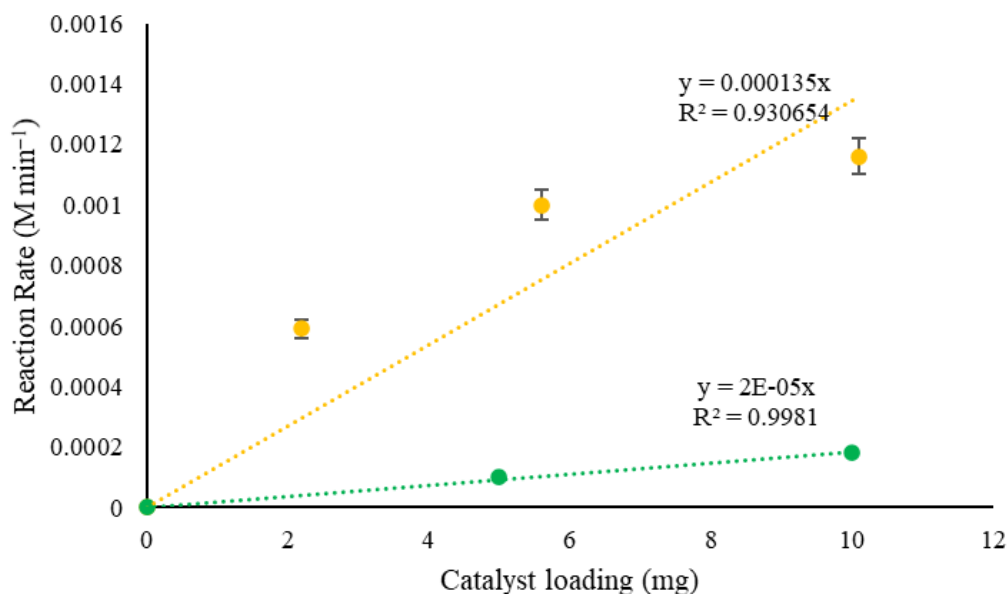


Figure 4. 15: the initial reaction rate of 4-CAN synthesis in hexane (yellow) and ethanol (green) using various catalyst loadings taken from the rate of change of CAN concentration between T_0 and T_{10} .

From the results obtained using a catalyst loading between 0 mg and 10 mg in both hexane and ethanol, the reaction was vastly more active in hexane across all catalyst loadings. This increased reaction rate has been theorised to be due to the increased solubility of the 4-CNB substrate in hexane allowing for a faster rate of adsorption to the catalyst surface, 4-CNB is only weakly soluble in alcohols. However, the 4-CAN product is readily soluble in both hexane and ethanol, as such its desorption from the catalyst surface is unaffected by either solvent. Reactions solvated by either solvent, maintained a selectivity towards 4-CAN of 100 % with no by-products observed in the GC analysis.

Previously described in section 4.2.1.2, the ideal FeS_2 catalyst loading is 25 mg, in ethanol. To determine the catalyst loading effect in hexane a comparison was drawn between ethanol and hexane at various loadings from 0 mg to 50 mg (Fig. 4.16). The catalyst loading study shows a similar result to the effect catalyst loading has on the rate of reaction in each solvent, with hexane showing complete conversion of 4-CNB in 2 hours with a 2 mg loading of catalyst.

Yet, ethanol does not achieve comparable conversion until a loading of 25 mg of catalyst is used.

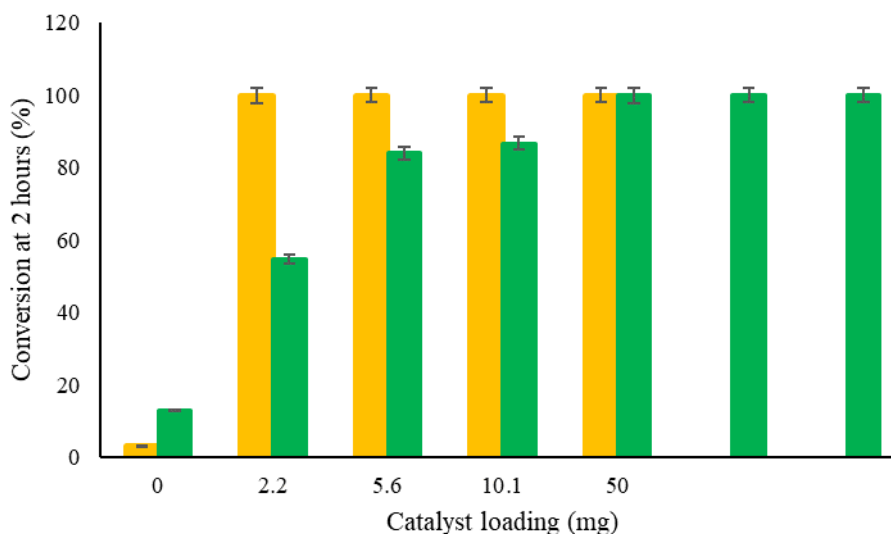


Figure 4. 16: Conversion of 4-CNB in two hours against the catalyst loading for reactions carried out in hexane (yellow) and ethanol (green).

The reaction performance of hexane outperformed ethanol at all catalyst loadings, in terms of the reaction rate and the conversion of 4-CNB in 2 hours. However, hexane has environmental concerns, as discussed previously in this section, and these must be taken into account. As such, it was ethanol that was selected as a reaction solvent, due to its environmental credentials, in addition to its admirable performance in the selective hydrogenation of 4-CNB at loadings above 25 mg.

4.2.1.4 The role of temperature

Temperature plays a key role in reaction kinetics as with increased temperature the number of molecules with sufficient energy to react (Fig. 4.17). The activation energy of a reaction can be higher than the energy required to decompose some reactant and when this happens a reaction does not occur. In general, the higher the reaction temperature the greater the reaction rate observed. The reaction temperature is another parameter of a catalytic system that needs refining, as it plays a key role in the kinetics of a given reaction.

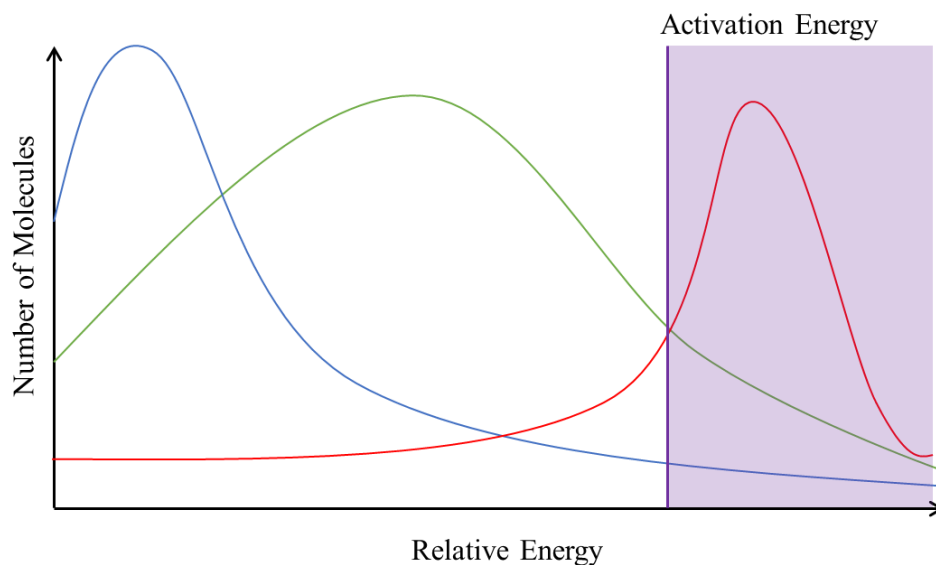


Figure 4. 17: Graphical depiction of how temperature (blue – low temperature, green – medium temperature, red – high temperature) affects the number of molecules with energy above the activation energy (purple region).

A catalyst does not increase the rate of a given reaction, instead a catalyst provides an alternative reaction pathway with a decreased activation energy. This route can involve intermediate compounds that are highly unstable but become stabilised by an interaction with the catalyst surface during the reaction. This stabilisation allows for the lower activation energy shown by a catalysed reaction (Fig. 4.18).

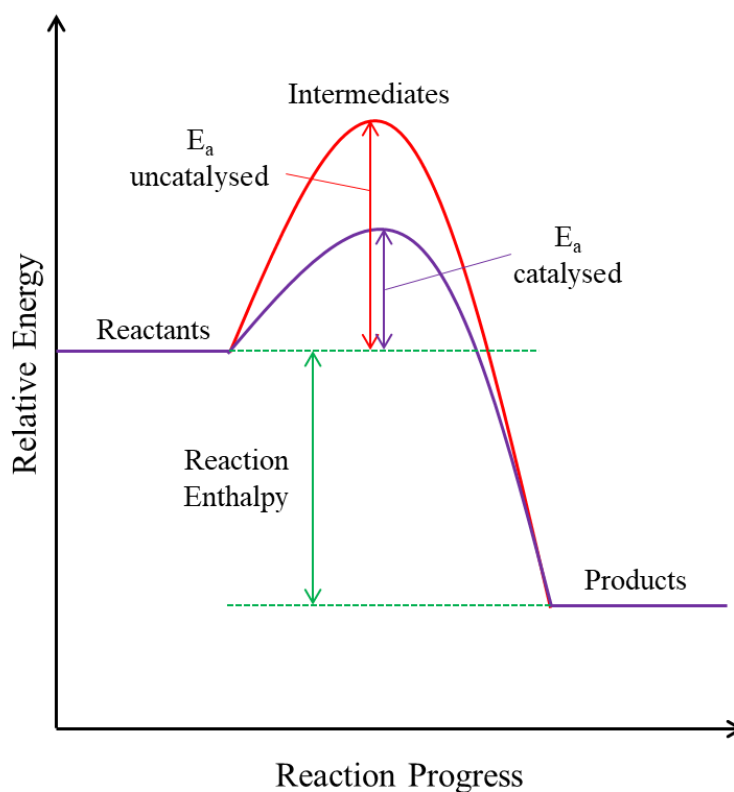


Figure 4. 18: Graphical representation of the effect of a catalyst on the activation energy of a given reaction, showing an uncatalysed reaction pathway in red and a catalysed pathway in purple.

In order to determine the activation energy of a given reaction the reaction must be carried out across a broad temperature range. To determine the activation energy of the selective hydrogenation of 4-CNB by the FeS₂ nanoparticle catalyst, several reactions were carried out across a temperature range of 25 °C to 80 °C. Up to this point all reactions had been carried out at 60 °C.

Reaction rates can be used to determine the activation energy using Arrhenius modelling, using the Arrhenius equation and its various forms (Equations 4.4 - 4.6).

$$k = Ae^{\frac{-E_a}{RT}} \quad \text{Equation 4.4}$$

$$\ln k = \ln A - \frac{E_a}{R} \frac{1}{T} \quad \text{Equation 4.5}$$

$$\ln k = \frac{-E_a}{R} \left(\frac{1}{T} \right) + \ln A \quad \text{Equation 4.6}$$

where k is the rate constant, A is the pre-exponential factor, E_a is the activation energy of the reaction, R is the universal gas constant and T is the absolute temperature in kelvin.

In the case of nitrobenzene hydrogenation using a hydrogen transfer reaction, the rate constant, k , becomes equal to the measured initial rate of reaction. As such, k is replaced with the initial reaction rate.

The reactions carried out across the temperature range showed an increase in initial rate with temperature as expected. Plotting the data as an Arrhenius plot where the x axis is $1/T$ (K) and y axis is $\ln(\text{rate (M s}^{-1}\text{)})$ the plot shown in Fig. 4.19 is obtained.

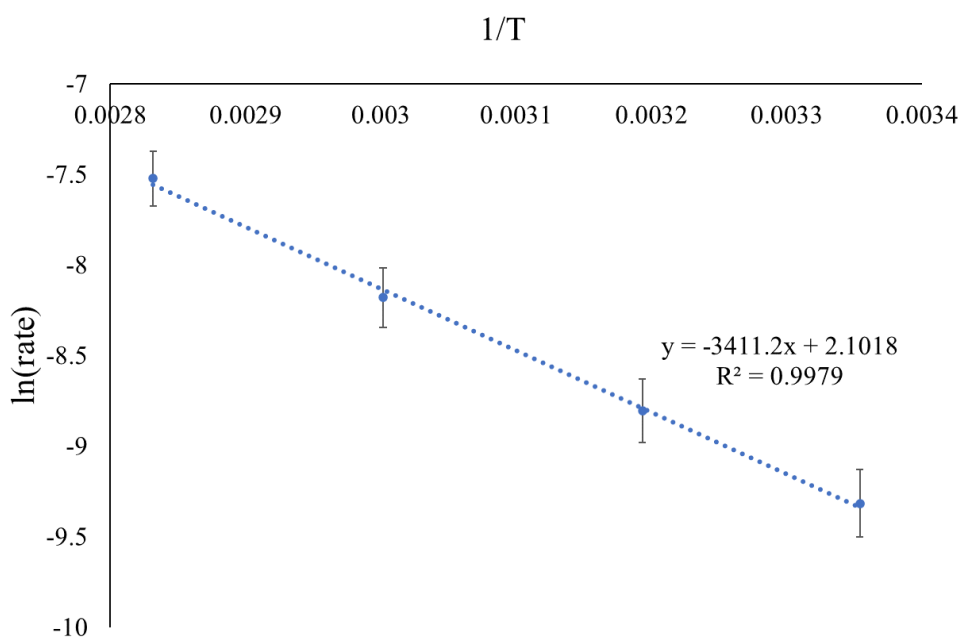


Figure 4. 19: Arrhenius plot $\ln(\text{rate})$ against $1/T$, for FeS_2 transfer hydrogenation of 4-chloronitrobenzene using hydrazine as the reducing agent across a temperature range of 25 °C to 80 °C.

Solving $y = mx + c$, where $c = \ln A$ (at $x = 1/T = 0$), $m = -E_a/R$, gives the activation energy of the system, 28.36 kJ mol⁻¹. The activation of molecular hydrogen with noble metal-based catalysts is typically ~90 kJ mol⁻¹, whereas the activation energy of reactions based on hydrogen transfer is ~55 kJ mol⁻¹.^{264, 265} The low activation energy of the hydrogenation

reaction may be due to the particular combination of the FeS₂ as a catalyst and the easily transferred hydrogen stored in the hydrazine, although this point is still under investigation.

The optimum reaction temperature was found to be 60 °C as this gave a rapid rate of reaction and total conversion of the material within a two-hour reaction frame. Higher temperatures may be applicable in producing more rapid reactions; however, these will be more energy intensive. A reaction carried out at room temperature may be the most environmentally friendly reaction temperature, yet it does lead to loss in time efficiency with a slow turnover of the reactor, resulting in less useful product within a given time window. Therefore, 60 °C was selected due to this increase turnover of reactions producing more useful product with a small increase in energy consumption across the reaction timescale.

4.2.1.5 The role of hydrazine concentration

Many potential hydrogen donors are available in the reduction of organic compounds, such as organic acids, hydrides or molecules such as tetralin.^{15, 136, 163} These compounds all possess different advantages and drawbacks in their use. Some of these compounds, such as tetralin, may require separation from the final product or various hydrides may leech inorganic components into the reaction, risking poisoning of the catalyst.^{15, 152} Hydrazine, the hydrogen transfer agent chosen in this work is toxic and corrosive, as such it carries substantial environmental concerns. However, hydrazine is widely used in industrial chemical synthesis, thanks to well established handling procedures. When utilised as hydrogen donor in hydrogen transfer reactions, in the presence of a catalyst, hydrazine decomposes completely to hydrogen and nitrogen, with hydrogen used in the transfer reaction and nitrogen, which does not carry any environmental concerns.

To address the hydrazine's environmentally unfriendly aspects as much as possible, an investigation to establish the minimum amount necessary for 4-CAN to 4-CNB conversion,

within the two hour time frame was carried out. Hydrogen transfer reactions were carried out using a range of hydrazine concentration, from 0 M to 0.8 M (0 mL to 2 mL). Fig. 4.20 shows the effect of hydrazine concentration on the rate of CNB consumption and conversion at 2 hours. There is a clear plateau in the conversion for solutions of hydrazine with concentration higher than 0.400 M. Importantly, there was no observed carryover of hydrazine observed within the GC chromatograms, evidence that all the hydrazine is consumed in the reaction.

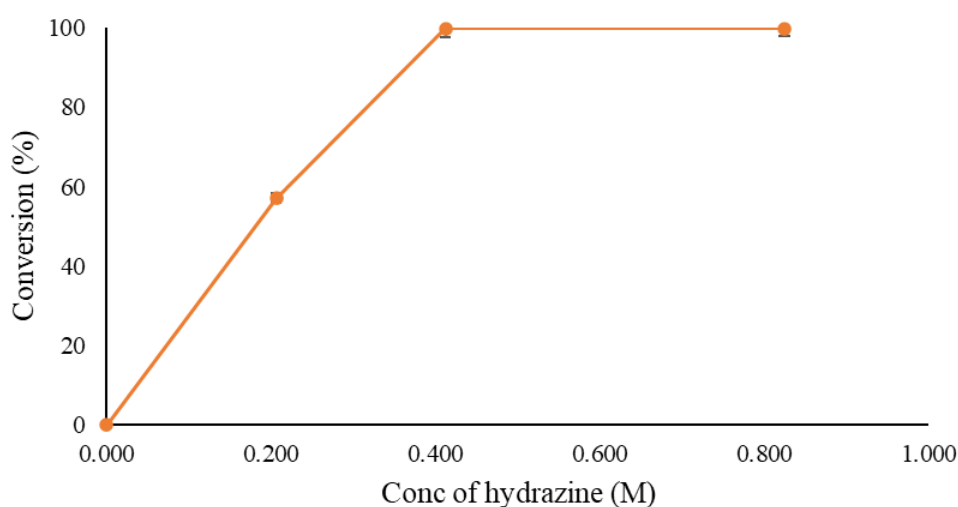


Figure 4. 20: Variation of hydrazine concentration and its effect on conversion of 4-chloronitrobenzene within a 2 hour time frame.

The plateau observed in the graph (Fig. 4.19), shows that 100 % conversion from p-CNB to p-CAN was achieved in two hours for 0.400 M hydrazine. Higher concentrations, such as 0.800 M, did not provide a worthwhile increase in rate of reaction, while a lower hydrazine content, 0.200 M, led to only 60% conversion of the 4-chloronitrobenzene in 2 hours. A hydrazine concentration of 0.400 M was selected as the optimum hydrazine amount, combining strong reaction performance and limiting the environmental concerns of hydrazine. 0.400 M hydrazine concentration corresponded to a 1 mL addition of hydrazine into the reactor containing 50 mL of 4-CNB solution (~2 % hydrazine). This lower concentration differed from more traditional molecular hydrogen activation as the atmosphere above the solution is typically 100 % hydrogen, with a significant concentration of the hydrogen dissolved in the reaction solution.

This hydrogen rich atmosphere poses several risks such as fire/explosion should the reactor leak, whereas, in this hydrazine mediated reaction the risk of fire is limited as the reaction atmosphere is nitrogen, and the amount of hydrogen possibly liberated from the hydrazine(unreacted) is low (240 mL) and diluted in the nitrogen atmosphere.

4.2.2 Mechanism of FeS₂ heterogenous hydrogenation

The mechanism of hydrogenation can often be difficult to determine, due to the number of factors involved, such as the active sites used in the reaction, molecule orientation and electronic effects within the catalyst material. Yet within this work there was a need to rationalise how FeS₂ was catalysing the hydrogen transfer reaction, using hydrazine as the hydrogen donor.

4.2.2.1 FeS₂ catalysed hydrogen transfer reaction - heterogeneous or homogeneous process?

Sulfide based materials have become increasingly scrutinised for their potential as catalysts, as such there has been some debate as to whether their mode of action is truly heterogenous.^{84, 266} Catalysts will often leech their material into the surrounding solution, causing parallel catalysed reactions interfering with the main reaction.^{85, 86, 177}

To determine if there was a significant impact of leached Fe(II) ions from the surface of the FeS₂ material, a hot filtration of the catalyst material was carried out. A hot filtration is the process of removing the catalyst from the reaction after an allotted time from the start and monitoring changes to the concentration of substrate or product. This process reveals if the catalyst has changed the reaction solution, through leeching of metal ions or other routes, to a point where the reaction can proceed unaided by the catalyst. Should this process have occurred a trend of increasing 4-CAN concentration would be observed in the reaction profile plot.^{267,}

In order to carry out the hot filtration, a reaction carried out in the same manner as described in section 4.1.2, however after 15 minutes of reaction time elapsed the reaction was hot-filtered through glass wool, into the reaction flask. After filtration, the reaction was placed back onto the reactor and reaction was continued as normal. Timepoints were pulled from the reactor at the same intervals as previously used. The reaction profiles for an unfiltered reaction and a hot filtered reaction using 25 mg of FeS_2 catalyst is shown in Fig. 4.21.

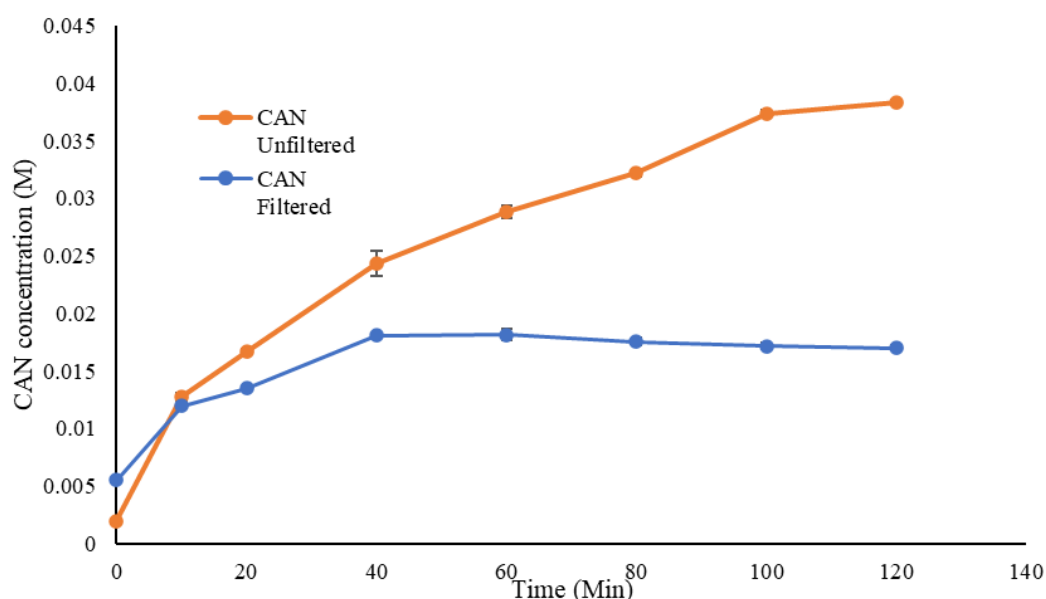


Figure 4. 21: Reaction profiles of 4-CAN concentration for a filtered reaction (blue) and an unfiltered reaction (orange).

From the reaction profiles for 4-CAN concentration shown in Fig. 4.20, there was a clear cessation of 4-CAN synthesis upon removal of the catalyst. 4-CNB conversion was constant at 21.5 % after catalyst was removed. The reaction did not proceed beyond the point of catalyst removal showing that if any Fe(II) had leached from the catalyst it was not playing a role in the continuation of the reaction and had been rendered inactive by the leaching process.

The lack of activity in the conversion of 4-CNB after the catalyst was removed from the reaction solution showed the catalyst is only acting in a heterogenous fashion for the hydrogen transfer and that any leached homogeneous Fe(II) ions did not play a role in the reaction. This

gave confidence in the application of FeS₂ as a heterogenous catalyst for study in further hydrogen transfer reactions (chapter 5).

4.2.2.2 Recyclability of FeS₂

The recyclability of the catalyst was also tested, taking into account that pyrite is known to decay into iron sulfate and iron oxide over time.^{9, 72} Structural and chemical changes in the catalysts structure during the reaction can influence the catalytic performance, therefore, post reaction characterisation is key. These structural changes to the catalyst material may create additional substrate reaction pathways, such as oxidation and bond cleavage, reducing the overall efficiency of the catalyst recyclability.^{228, 249, 269} FeS₂ nanocatalysts were used in several subsequent reactions, after centrifugation and drying. The nanoparticles were analysed via PXRD and FTIR after serving as catalyst in four consecutive reactions, to detect signs of decomposition. A graph showing the recyclability of the nanocatalyst is shown in Fig. 4.22.

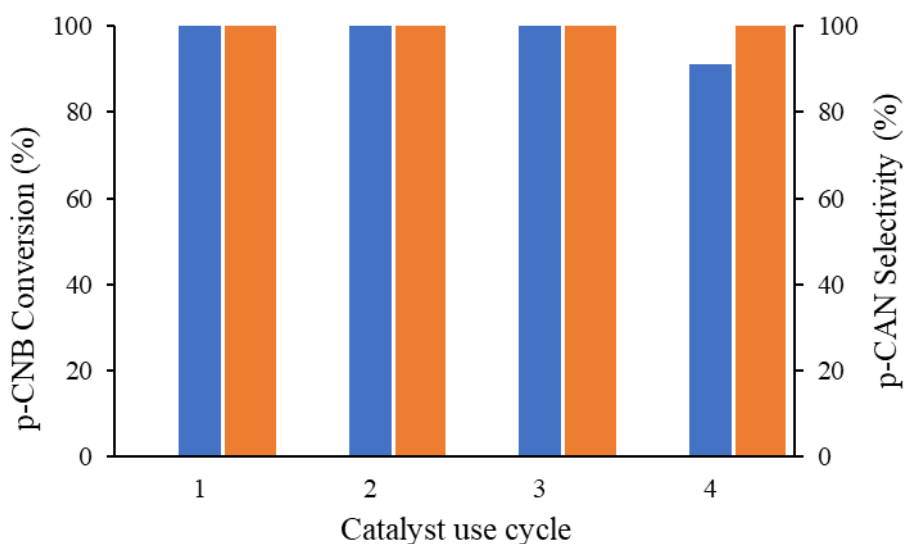


Figure 4. 22: recyclability of FeS₂ nanoparticles for the hydrogen transfer hydrogenation of 4-chloronitrobenzene, conversion of 4-chloronitrobenzene at 2 hours (blue) and selectivity towards 4-chloroaniline (orange).

FeS₂ proved to be recyclable across four reaction cycles, with conversion of 4-chloronitrobenzene reducing to less than 99% only after the third cycle (Fig. 4.21), allowing

for effective conversion of 4-CNB after each reaction. The loss of activity after the 3rd reaction cycle may not have been due to the deactivation of the catalyst material, instead to the fact that after each subsequent reaction, less catalyst was being recovered due to the incomplete recovery by centrifugation. This may have led to the reduced performance observed after the 3rd cycle. However, it is important to note that no loss of selectivity was observed across the recyclability study. The catalyst maintained a selectivity towards 4-chloroaniline of >99.9%.

The recyclability of the catalyst is important for potential scale up reactions. As in industrial reactions a catalyst is needed to be effective across a number of reaction cycles, with minimal loss in activity or selectivity.

4.2.2.3 Post reaction characterisation of FeS₂

During the catalysis reaction, it has been reported that FeS₂ may react to form α -Fe₂O₃, FeO and FeOOH.^{9, 72} Oxidation of the catalyst may occur during the reduction of the nitrogroup wherein oxygen is transferred to the FeS₂, possibly displacing sulfur. To determine these changes post reaction PXRD and FTIR were carried out on the catalyst material. PXRD would show presence of α -Fe₂O₃, whereas FTIR would show changes to the surface of the material such as changes to the surface thiol groups.

PXRD of the material, after separation from the reaction, was found to be identical to the starting material PXRD pattern, only with lower intensity due to decrease material present (~25 mg post catalysis). Comparison between the PXRD patterns of FeS₂ before and after the reaction (Fig. 4.23), show no peaks belonging to impurities deriving from FeS₂ decomposition or oxidation.^{9, 72} Small amounts of impurities may exist in minor quantities within the catalyst material post catalysis, however, due to the nature of PXRD of iron containing nanomaterials they are not visible due to the high background intensity. The crystallinity of the sample is changed during the reaction cycles as the FWHM of the FeS₂ before use was 1.7° and 2.3° for

the 200 and 311 with these values decreasing slightly to 1.3° and 2.0° for the 200 and 311 peaks respectively indicating a more uniform particle size suggesting some agglomeration of the particles had occurred.

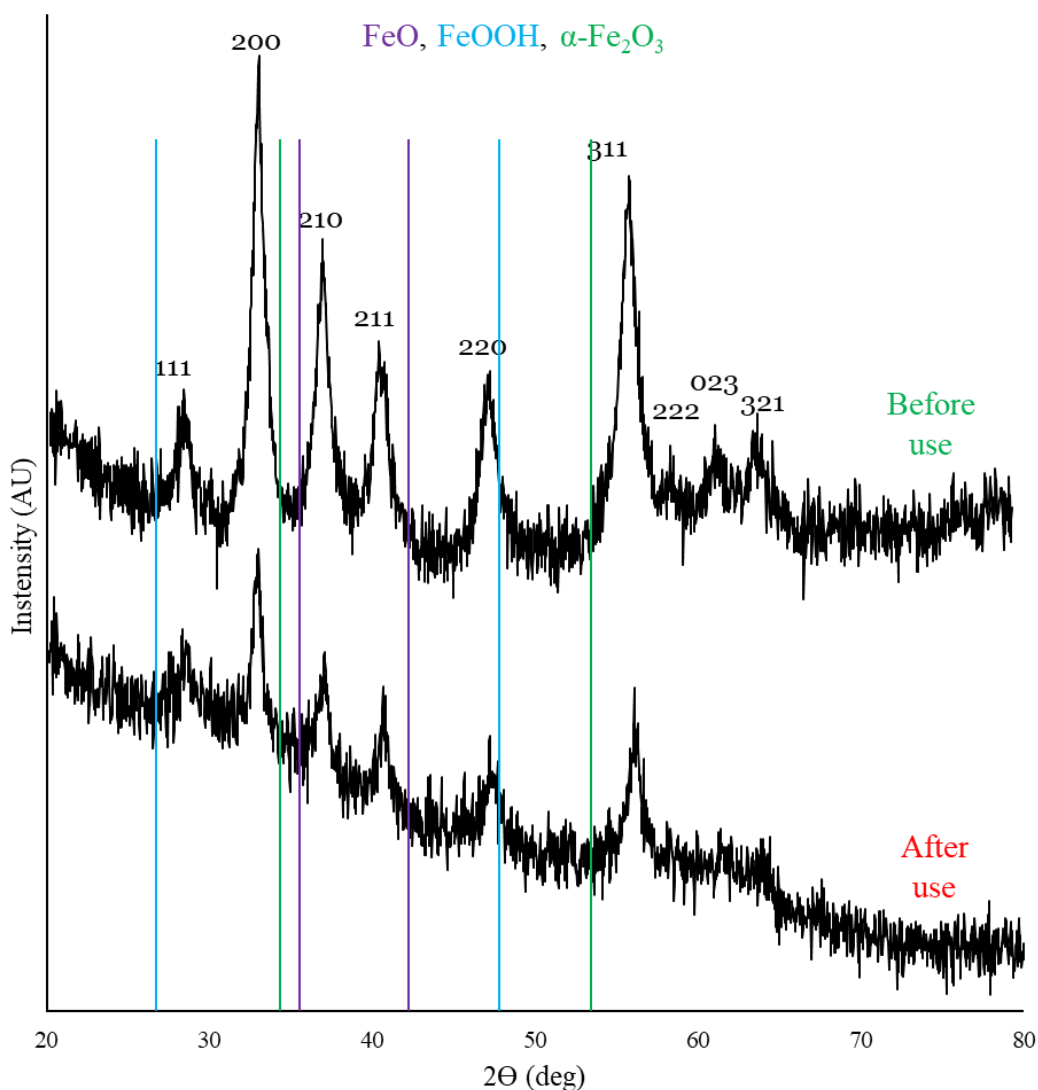


Figure 4. 23: PXRD pattern of FeS_2 nanoparticle catalyst before and after recycled reactions, with peaks indexed. most intense iron based impurities are identified and overlapped with the patterns to emphasise their absence.²⁷⁰⁻²⁷²

To determine any surface changes to the catalyst, FTIR was carried out on the FeS_2 material post catalysis. When comparing the pre and post catalysis FTIR results we found no observable differences in the sulfur bonding (Fig. 4.24). The thiol group stretch at 2800 cm^{-1} was maintained indicating that little surface oxidation had occurred during the catalysis process.

Furthermore, the peaks belonging to sulfur oxides, around 1400 cm^{-1} appear of similar intensity to the ones in the spectrum of the pre-catalysis material, suggesting a similar content of SO_x species. Therefore, no observable further oxidation of the catalyst material had taken place during the repeated reactions, suggesting that the FeS_2 catalyst was stable under these reaction conditions.

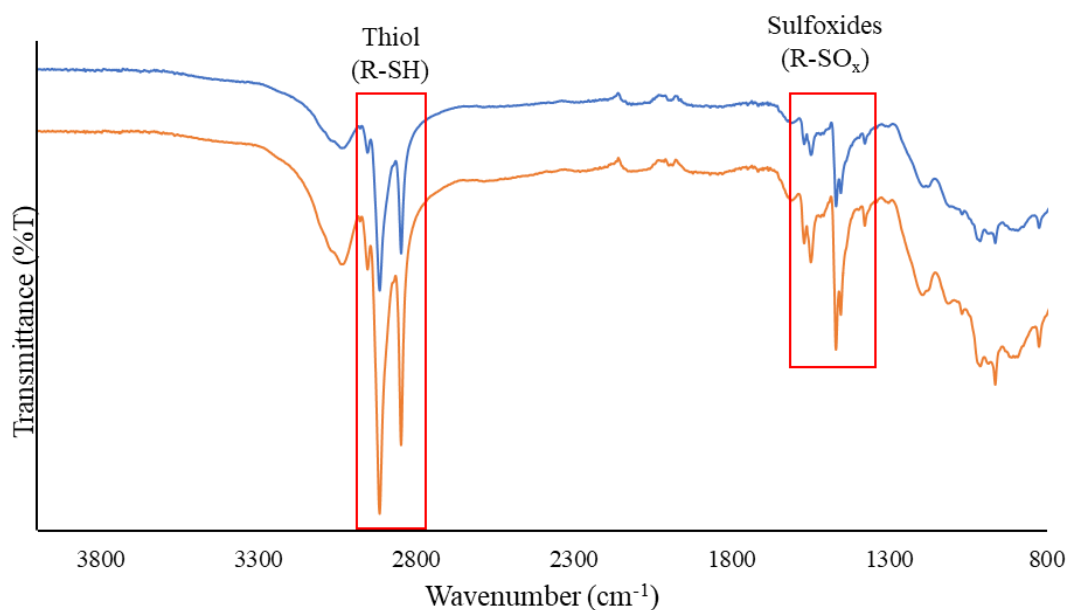


Figure 4. 24: FTIR spectra of FeS_2 catalyst before use (orange) and post reaction (blue).

From the results obtained from post reaction characterisation, there were minimal changes to the catalyst, even after 4 usage cycles. This was testament to the robust nature of the FeS_2 catalyst.

4.2.2.3 Comparison with NiS_2

To determine the effect the metal had in the catalytic performance of FeS_2 pyrite, the nickel pyrite (NiS_2), preparation described in section 3.4.1. NiS_2 and FeS_2 share the cubic pyrite structure. Both Ni and Fe metals exist in their 2+ oxidation state in a high spin configuration. Fe (II) and Ni (II) differ in their electronic structure having d^6 and d^8 electrons in their valence shell, respectively. High spin states combined with their d-electron numbers give them different electronic configurations within the same crystal structure (Fig. 4.25).

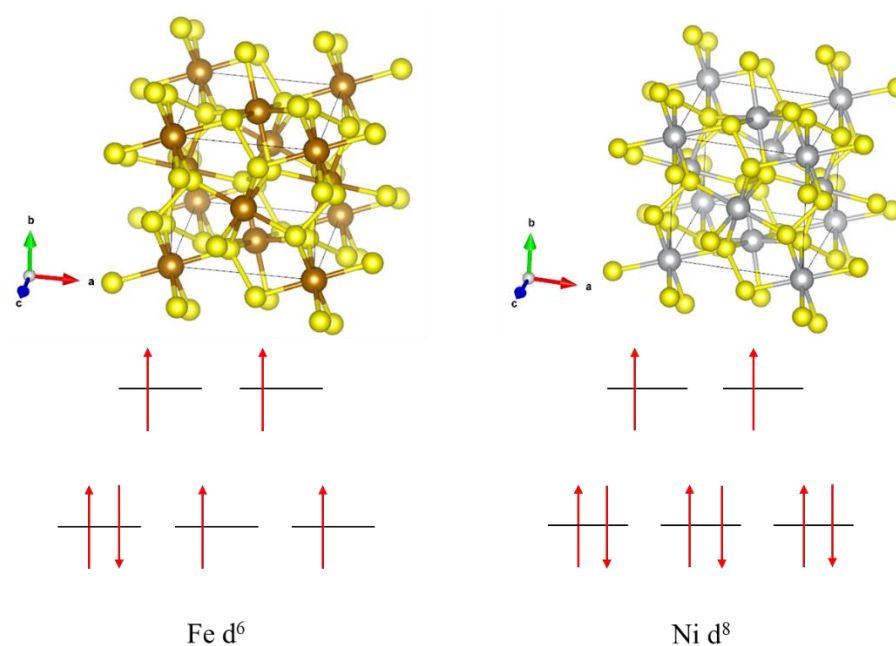


Figure 4. 25: Crystal structures of FeS_2 and NiS_2 (pyrites) with the d -electron configuration for the metals in 2+ oxidation state.^{222, 223, 273}

Both FeS_2 and NiS_2 were used as catalysts in the selective hydrogenation of 4-CNB in a transfer hydrogenation with hydrazine. Two reactions were prepared in an identical fashion to those prepared previously, with the exception of one reaction using 25 mg of NiS_2 in place of the FeS_2 catalyst used in other reactions.

The reactions were both left to equilibrate under nitrogen for 30 minutes before 1 mL of hydrazine was introduced into the reactor. The reaction profiles obtained for the reactions, with a reaction in absence of catalyst as a control, are shown in Fig. 4.26.

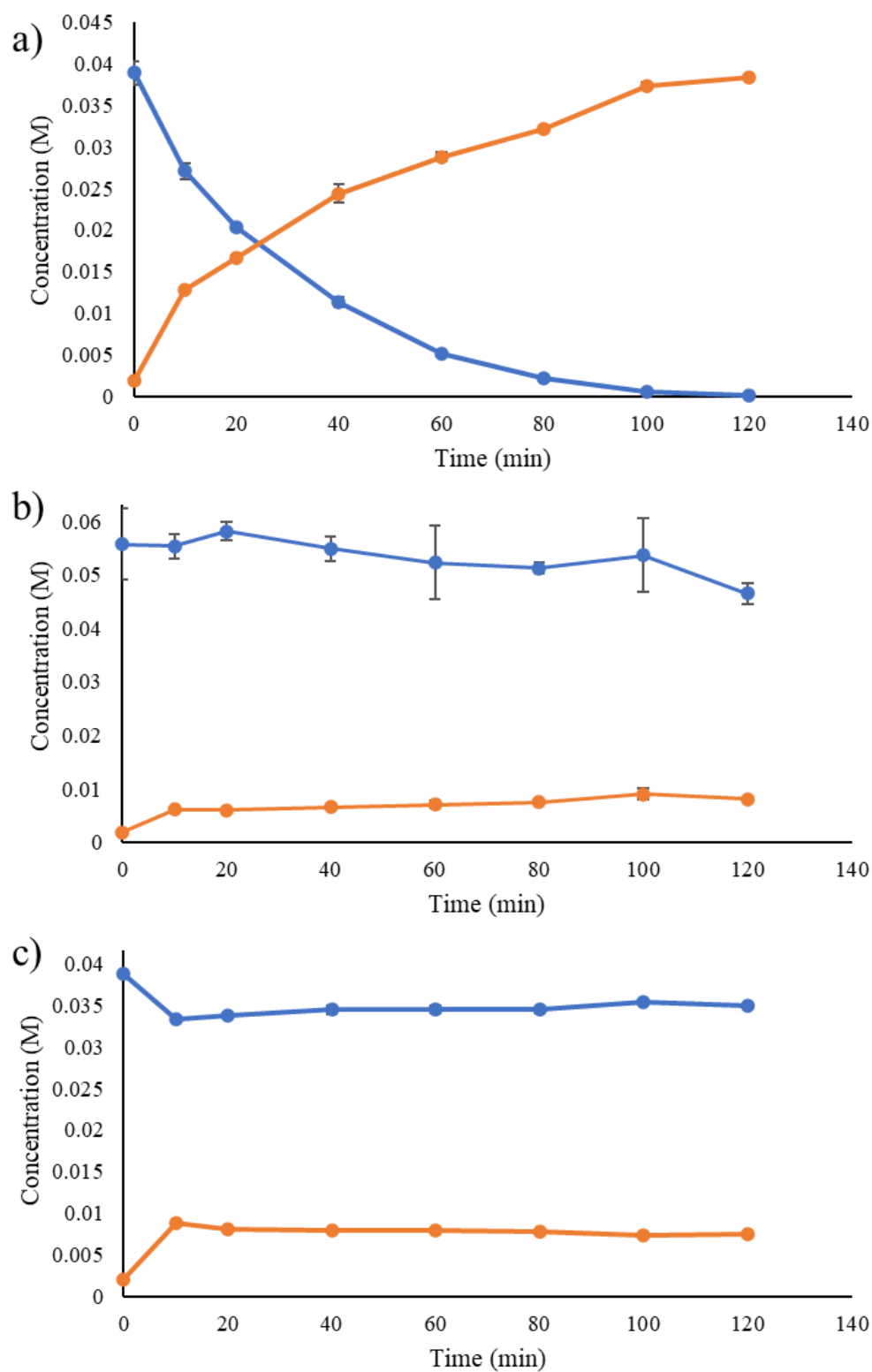


Figure 4. 26: Reaction profiles obtained for the selective hydrogenation of 4-CNB via a hydrogen transfer reaction using 1 mL of hydrazine monohydrate and a) 25 mg of FeS_2 catalyst, b) 25 mg of NiS_2 catalyst and c) 0 mg of catalyst.

NiS₂ nanoparticles did not produce a rapid reaction as was observed when using FeS₂ nanoparticles as a catalyst. The results obtained using NiS₂ nanoparticles are comparable to results when no catalyst is used, converting ~14 % of the initial 4-CNB concentration within a two hour reaction window. Compared to complete, >99.9 %, 4-CNB conversion displayed by the reaction catalysed by FeS₂.

It was theorised by B. Ma *et al.* that for the hydrogen transfer reaction to occur the catalyst material must donate an electron to the reaction, in the case of FeS₂ surface Fe (II) is oxidised to Fe (III), with the end point of the reaction reducing the Fe (III) back to Fe (II) leaving the catalyst in its starting state.⁹ This redox exchange on the surface of FeS₂, requires little energy as Fe (II) and Fe (III) are of a similar energy level, only differing by ~0.8 eV with both states remaining stable.^{223, 274} In contrast Ni (II) does not readily undergo this oxidation process as the energy difference between Ni (II) and Ni(III) is ~3.6 eV, thereby making the valence electrons needed for the reaction unobtainable by the reaction.^{236, 275} In addition to this oxidation being highly energetic the reduction of Ni (III) and Ni (IV) to a lower valency occurs readily. As such this process would compete with the catalysed reaction limiting the conversion of 4-CNB.

This surface redox phenomenon was determined to be the most likely reason for the reduced catalytic performance of NiS₂. From the reduced activity of NiS₂, all future catalytic work would be carried out using FeS₂ pyrite nanoparticles as it showed a vastly superior catalytic performance.

4.3 Conclusions

FeS₂ nanoparticles were successfully applied as a catalyst for the selective hydrogenation of 4-chloronitrobenzene, via a hydrogen transfer reaction using hydrazine monohydrate as a hydrogen donor compound. Using FeS₂ and hydrazine removed the noble metal catalysts

traditionally used in nitrobenzene reduction and the use of hydrogen gas, which are the two most significant aspects of traditional catalysis in terms of environmental impact. The parameters of the reaction were then optimised to obtain a >99.9 % conversion yet minimizing the environmental impact of the catalytic system. The ideal catalyst loading was determined to be 25 mg as this loading obtained a >99.9 % 4-chloronitrobenzene conversion with 100 % selectivity towards the 4-chloroaniline, the desired product. Temperature of reaction was optimised to produce the highest reaction rate and conversion using the minimal temperature, this was determined to be 60 °C. The concentration of hydrazine was also optimised to reduce the environmental impact of hydrazine yet still produce acceptable reaction performance, this was determined to be a hydrazine concentration of 0.400 M, 1 mL, molar ratio of hydrazine to catalyst 160:1.

The effect of solvent on the reaction performance was studied using seven different solvents, ranging from polar protic, polar aprotic and non-polar solvents to determine what effect the solvent polarity had on the reaction. It was determined that polarity of the solvent played only a minor role in the reaction with the pK_a of the solvent playing a role in the non-catalytic aspect of the reaction. The polar protic solvents such as ethanol, all displayed a non-catalytic component to the reaction as in the absence of the catalyst there was a small ~15 % conversion of the substrate. The conversion seen in this circumstance was proposed to be due to the interaction between the donated protons and hydrazine causing a small quantity of the 4-chloronitrobenzene to be converted to products. The solvents were judged based on their reaction performance and environmental impact. It was determined that ethanol was the ideal solvent for the reaction as it had appreciable performance in the reaction yet was the most environmentally friendly solvent due to its bio-derivability and ease of separation from the reactants and products.

Studies were carried out to determine the mechanism of action of FeS₂ as a catalyst. A hot filtration was carried out to determine if any of the Fe (II) ions had leached from the FeS₂ and if these leached ions played a role in the catalysis. After a hot filtration of the reaction solution 4-aniline synthesis completely halted, with no further reaction occurring. This showed that if any ions had leached into the reaction from the catalyst, they played no role in the catalysis, contrary to what had been previously reported. Recyclability of FeS₂ nanocatalyst was tested across 4 reaction cycles with little deterioration in the catalytic performance over the first 3 cycles only seeing deterioration in performance at the 4th cycle. Showing FeS₂ has potential as a catalyst for the selective hydrogenation of 4-chloronitrobenzene via a hydrogen transfer route. Analysis of the material after this recyclability study showed no observable changes to the crystal structure or the surface characteristics of the catalyst.

Comparisons of FeS₂ and NiS₂ was carried out to determine the role of the metal centre in the catalyst crystal structure. It was found that the NiS₂ nanoparticles were inactive in the catalysis of 4-chloronitrobenzene reduction. This was theorised to be due to the differences in the electronic structure of the two materials. Fe (II) can be readily oxidised to Fe (III) and then reduced in the reaction which Ni (II) cannot, as such the reaction with Fe based pyrite can facilitate the catalytic hydrogen transfer reaction whereas Ni is inactive in the reduction of the NO₂ group.

Chapter 5 FeS₂ Catalytic Hydrogen Transfer Reduction System - Further Development

This chapter discusses the general applicability of the catalytic system using FeS₂ as a catalyst for the hydrogen transfer reduction of nitrobenzenes. Building upon the work in chapter 4, this chapter applies the optimised catalyst system to other substituted nitrobenzenes to explore opportunities for wider applicability.¹⁴

To determine the wider applicability of FeS₂ pyrite for transfer hydrogenation of 4-chloronitrobenzene, further reactions were carried out using a range of halogenated nitrobenzene substrates. These halogenated nitrobenzenes would range from electron withdrawing fluorine substituents to electron donating iodine groups. Studying a series of halogenated nitrobenzenes gives a range of carbon-halogen (C-X) bond strengths, the strongest bond being the C-F bond with bonds becoming weaker going down the halogen series. This decrease in C-X bond strength across the halogen series causes certain bonds to be more thermodynamically unstable, thus the bound halogen may be released more easily. Comparing the relative selectivity of the hydrogen transfer reaction and the relative rate of reaction demonstrates how the catalyst interacts with a wide variety of substrate materials, aiding testing the true selectivity of the catalyst (section 4.2.1.1).

The position of the substituent group relative to the nitro group on the aromatic ring was tested using a range of chloronitrobenzenes, with the substituent group in the para (4), meta (3) or ortho (2) position relative to the nitro group. The relative positioning of the substituent group was used to test the selectivity of the catalytic system with the nitro group relative proximity to the substituent group position.

Finally, the choice of reducing agent is discussed due to the negative implications of hydrazine monohydrate, a range of potential reducing agents were proposed. These reducing agents

would be analysed relative to hydrazine monohydrate using the optimised system developed in chapter 4.

5.1 Experimental

5.1.1 Materials

1-chloro-4-nitrobenzene 98+ %, 1-fluoro-4-nitrobenzene 99 %, 1-bromo-4-nitrobenzene 98 %, 1-iodo-4-nitrobenzene 98+ %, 1-chloro-3-nitrobenzene 98 %, 1-chloro-2-nitrobenzene 99 %, 4-chloroaniline, 4-fluoroaniline 99 %, 4-bromoaniline 98+ %, 4-iodoaniline 99 %, 3-chloroaniline 99 %, 2-chloroaniline 98+ %, aniline 99+ %, nitrobenzene 99+ %, hydrazine monohydrate 98+ %, hypophosphorus acid 50 % w/w aq. solution, propan-2-ol 99.5 %, glycerol 99+ %, potassium hydroxide pellets 85 %, formic acid 97 % and acetic acid (glacial) 99 %, were purchased from Alfa Aesar.

Absolute ethanol and toluene (analytical grade) were obtained from Honeywell Lab Chemicals.

5.1.2 Hydrogenation procedure

The general procedure for carrying out tests on the new catalytic system was as follows: 2.5 mmol of substituted nitrobenzene substrate (4-fluoronitrobenzene, 4-chloronitrobenzene, 4-bromonitrobenzene, 4-iodonitrobenzene, 3-chloronitrobenzene or 2-chloronitrobenzene) and 0.46 g (5 mmol) of toluene internal standard were added to a 50 mL volumetric flask. The solvent (ethanol or hexane for testing) was then added to dissolve the substrate and internal standard, solution then topped to volume with solvent to prepare a 0.05 M substrate and 0.1 M internal standard solution.

25 mg of catalyst would be added to the batch reactor, shown in section 2.3.1.1, with 50 mL of the nitrobenzene solution. The solution would then be purged with nitrogen 3 times until all oxygen had been removed from the reaction vessel.

The solution was left to equilibrate under the nitrogen atmosphere for 30 minutes at 60 °C, before 20 mmol of hydrogen donor compound was injected into the reaction.

After this point 250 µL aliquots of the solution were extracted at 0, 10, 20, 40, 60, 80, 100 and 120 minutes reaction time, these times were selected to obtain a full reaction profile across the reaction, opposed to a single end point. Each aliquot was analysed using a Varian 430 gas chromatograph equipped with a 30 m Stabilwax® capillary column (Restek); each aliquot was injected in triplicate in order to obtain the standard deviation in the measurements.

5.2 Results and Discussion

5.2.1 Effect of the substituent in the substrate

The substituent effects on the transfer hydrogenation of nitrobenzenes were studied using a range of halogenated nitrobenzenes, categorised as ortho, meta, para and the halogen series. The substituents were studied to determine the effect of substituent on the selectivity and activity of the catalytic reduction of the nitro group. The wide variety of halogens and differing electronic effects of the substituent can affect the activation of the nitro group towards being reduced by the catalyst.

5.2.1.1 Ortho, Meta, Para effects

Initial studies on the effect of substituent focused on the relative substituent position has on the reduction of the nitro-group. 4-chloronitrobenzene (para-chloronitrobenzene), 3-chloronitrobenzene (meta-chloronitrobenzene) and 2-chloronitrobenzene (ortho-chloronitrobenzene), (Fig. 5.1) were chosen as substrates for hydrogen transfer reaction using the optimised catalytic system, described in chapter 4. These reactions were then compared based on the conversion of substrate, selectivity towards the substituted aniline product and the initial rate of reaction relative to the chloro substituent.

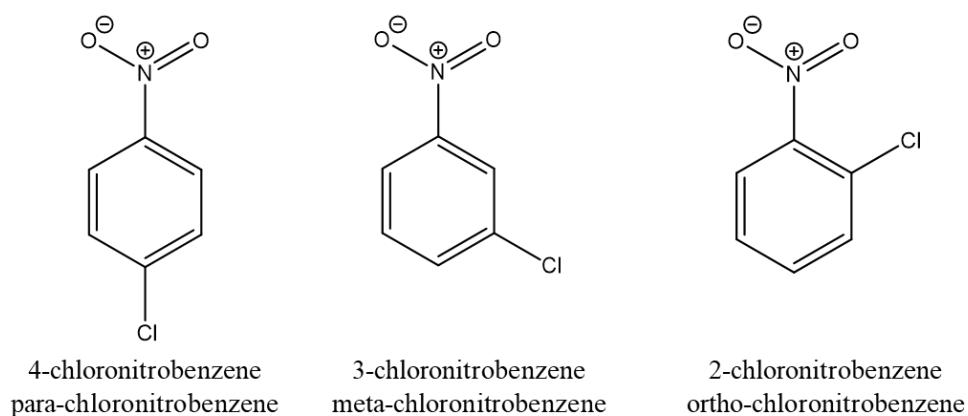


Figure 5. 1: Chemical structures of chloronitrobenzenes used in studying the effect of relative position on reaction characteristics.

The reactions were carried out using 50 mL of a solution containing 2.5 mmol of chloronitrobenzene substrate and 5 mmol of toluene internal standard, with 25 mg of FeS₂ pyrite catalyst. The reactions were heated at 60 °C and reduced using 1 ml of hydrazine monohydrate. The conversion of substrate in 2 hours and the selectivity towards the substituted aniline product is shown in table 5.1.

Substrate	Conversion of substrate in 2 hours (%)	Selectivity towards substituted aniline (%)
4-chloronitrobenzene	99.9	100.0
3-chloronitrobenzene	99.9	100.0
2-chloronitrobenzene	100.0	100.0

Table 5.10: Conversion of substrate and selectivity towards the substituted aniline product for reactions carried out using ortho, meta and para substituted chloronitrobenzenes, using hydrazine monohydrate as a reducing agent.

It was found that there was little dependence of the relative chloro position on the selectivity or conversion of the substrate, as all showed a conversion of substrate >99.9 % with a 100 % selectivity towards the desired product. However, when the initial rate of aniline synthesis is taken into consideration, a clearer trend is shown between the relative position of the chloro group and the nitro group (Fig. 5.3).

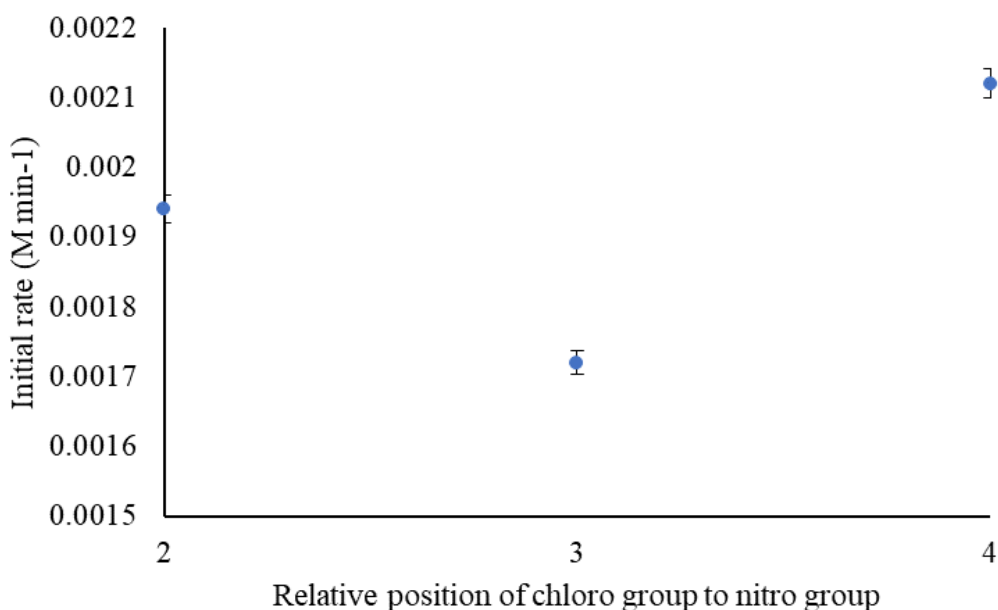


Figure 5. 2: Initial rate of substituted aniline synthesis for ortho, para, meta chloronitrobenzenes plotted against their relative positions. Reaction profile plots shown in appendix 14-16.

From studying the effect that relative position of the chloro substituent has on the initial rate of substrate conversion, there is a pronounced decrease in rate when the chloro group is present in the meta position. The decreased rate observed in the meta position relative to other positions may be due to the resonance effect displayed by the ortho and para positions.²⁷⁶ The resonance caused by the chlorine atom causes electrons to be withdrawn or donated into the π system of a substituted benzene ring.²⁷⁷ This donation effect observed with a chlorine substituent activates the ring in the para and ortho positions by the resonance effect whereby the chlorine donates into the π system and by extension onto the nitro group. The inductive effect of ortho and para chlorine groups are shown in Fig. 5.4.

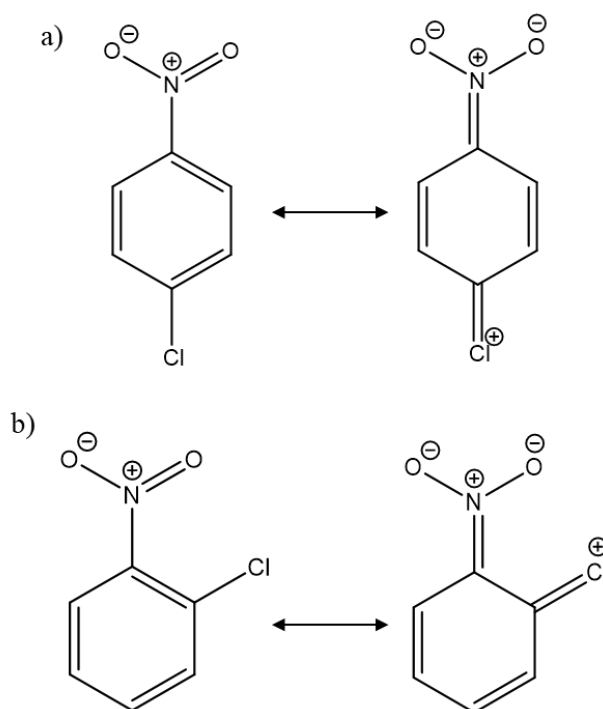


Figure 5. 3: Resonance stabilised structures of a) 4-chloronitrobenzene (para) and b) 2-chloronitrobenzene (ortho).

The resonance effect produced by the electron lone pairs on the chlorine substituent in either the ortho or para position pushes electron density towards the nitro group. This increased electron density provides and increased affinity of the nitro group towards the catalyst surface, thereby increasing the observed rate at which the substrate is taken out of solution.

Resonance within the meta substituted chloronitrobenzene the resonance stabilisation does not cause an increased electron density on the nitro group (Fig. 5.5). This instability caused by the induction requires a greater energy than that of the ortho or para positions, therefore it only occurs at increased reaction temperatures.

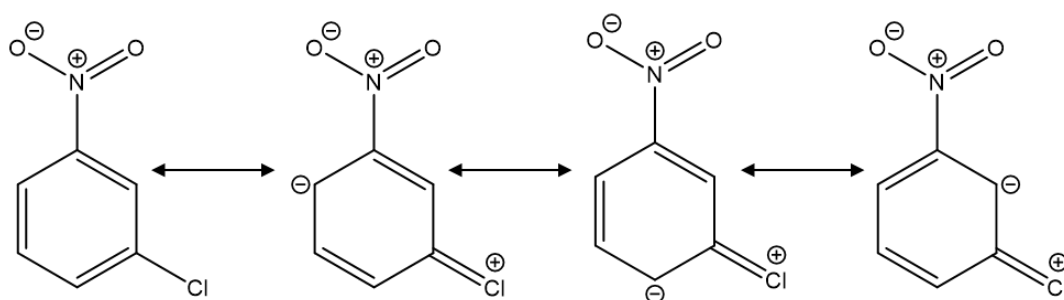


Figure 5. 4: Resonance displayed by 3-chloronitrobenzene (meta).

The resonance shown by the meta substituted chloronitrobenzene does not push electron density onto the nitro group, thereby, deactivating it relative to the para and ortho substituted nitrobenzenes. This deactivation leads to a relative decrease in initial rate between the meta substituted and ortho, para substituted nitrobenzenes.

5.2.1.2 Halogen series effect

As discussed in the previous section the para position of a substituent group has an influence on the activation or deactivation of the nitro group. To study this activation/deactivation effect various para halogenated nitrobenzenes were studied, using the optimised system (Chapter 4), to determine the effect of the para substituent on the catalysts conversion of substrate or the selectivity towards the desired aniline product. Halogens were chosen as the para substituent due to the electron donating or electron withdrawing nature across the series. Fluorine is relatively electron withdrawing due to its high electron negativity and iodine being moderately electron donating due to the diffuse outer electron shells being readily conjugated into the π system.

The reactions studied to determine the effect of electron donation on the catalytic characteristics, were carried out using 50 mL of a solution containing 2.5 mmol of chloronitrobenzene substrate and 5 mmol of toluene internal standard, with 25 mg of FeS₂ pyrite catalyst. The reactions were heated at 60 °C and reduced using 1 ml of hydrazine monohydrate. The conversion of substrate in 2 hours and the selectivity towards the substituted aniline product is shown in table 5.2.

Substrate	Conversion of substrate at 2 hours (%)	Selectivity towards substituted aniline (%)
4-fluoronitrobenzene	100.0	99.8
4-chloronitrobenzene	99.9	100.0
4-bromonitrobenzene	99.9	100.0
4-iodonitrobenzene	100.0	99.9

Table 5.11: conversion of substrate and selectivity towards the desired substituted aniline product for hydrogen transfer reactions of various para halogenated nitrobenzenes, using hydrazine monohydrate as a reducing agent.

The results for the conversion and selectivity of each of the para halogen substituted nitrobenzenes, showed little variation in the conversion or selectivity of the FeS₂ catalyst despite the electron donating effect of the substrate material. The electronic effects of the halogen showed very little influence on the selectivity of the catalyst this is promising as it indicates that the nature of the para substituent has very little influence on the final selectivity in product distribution.

As mentioned in section 4.2.1.1, the orientation of the substrate relative to the catalyst material is key to influencing the selectivity of the catalyst. In the case of halogenated nitrobenzenes there is a marked decrease in the bond strength as the halogen is changed from fluorine to iodine, with the carbon iodine bond being weakest with a bond energy of 209 kJ mol⁻¹ compared to a carbon fluorine bond being 536 kJ mol⁻¹.²⁷⁸ The decrease in relative bond energy across the halogenated nitrobenzenes should have led to a corresponding decrease in selectivity. However, due to the theorised interaction of the substrate molecule on the catalyst surface (discussed in Section 4.2.1.1), there is a greater distance between the carbon halogen bond and the catalyst active site. Therefore, the carbon halogen bond cannot be reacted. As such the selectivity of the system is not reduced regardless of the substrate compound.

The electron withdrawing and donating effect of the halogens is more clearly displayed when the initial rate of reaction is considered. Fig. 5.6 shows how the initial rate of reaction can be correlated to the atomic radius and the electron donating/withdrawing properties of the halogen. Fluorine, the smallest halogen, has the highest electronegativity and is the most electron withdrawing halogen. Iodine by contrast is the largest, with the most electron donating pressure due to its diffuse outer electron shells.²⁷⁹

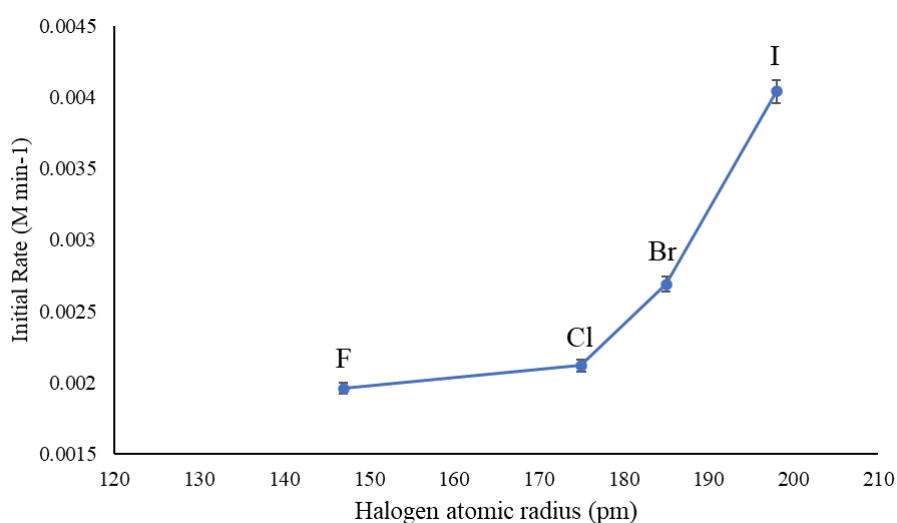


Figure 5. 5: Initial rate of reaction for various para halogenated nitrobenzenes in a hydrogen transfer reaction over FeS_2 catalyst using hydrazine monohydrate as a reducing agent. Reaction profile plots shown in Appendix 16-19.

In the graph displayed in Fig. 5.6, there is a plateau in the initial rate of halogenated nitrobenzene reduction observed between fluorine and chlorine substituted nitrobenzenes. This plateau may be caused by the electron withdrawing nature of fluorine and the relative inertness of the chlorine, being only weakly electron donating. This effect is shown in Fig. 5.7.

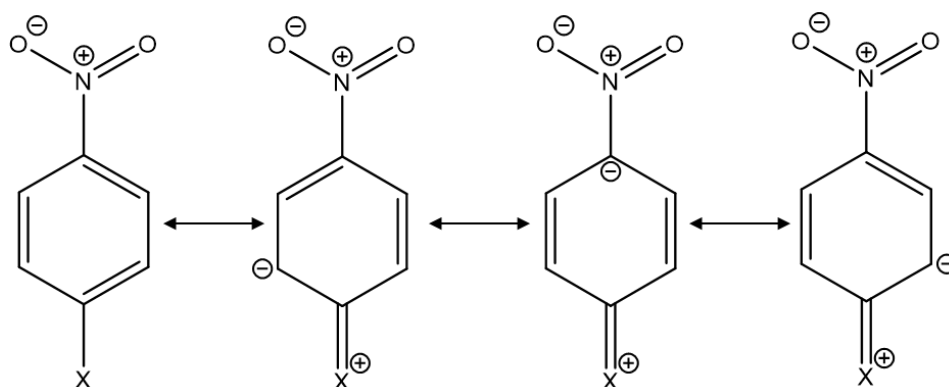


Figure 5. 6: Resonance structures from the electron withdrawing group in the para position relative to the nitro group.

The electron withdrawing effect of fluorine leads to the withdrawing of electron density from the ring making the ring more susceptible to nucleophilic attack. However, as there is no nucleophilic attack occurring in this reaction, this effect does not aid in the binding of the nitrobenzene to the catalyst surface. Therefore, the relative reaction rate appears lower in comparison to the other halogenated nitrobenzenes. As chlorine is only weakly electron donating the effect of the donation on the promotion of the nitrobenzene reduction is not pronounced.

The electron donation and promotion of the nitrobenzene reduction becomes more pronounced with a bromine or iodine substituent. The relative initial rate becomes much higher relative to fluorine and chlorine substituted nitrobenzene reduction, possibly due to the proposed electron donating resonance effect, as shown in Fig. 5.8.

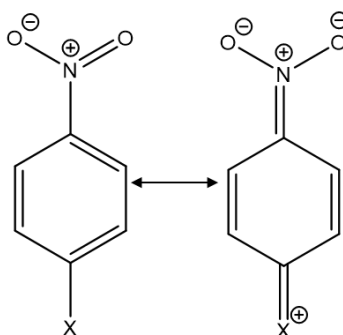


Figure 5. 7: Resonance structures of moderately electron donating halogens in the para position relative to the nitro group.

The resonance provided by the moderately electron donating bromine and iodine substituents pushes a greater electron density onto the nitro group (Fig. 5.8). The nitro group can then more readily be bound to the catalyst surface, thereby giving a greater observed rate of reaction as the catalyst substrate interaction becomes stronger.

5.2.1.3 Overall effect of substituent

The results obtained from studying the effect of different substituents on the hydrogen transfer catalytic performance of FeS₂ pyrite, have shown that the relative position of the substituent has little effect on the overall conversion of the substrate or the selectivity of the final product towards the substituted aniline. However, when studying the initial rate of reaction more closely there is a distinct decrease in the relative initial rate when the substituent group is in the 3 (meta) position relative to the nitro group. This was determined to be due to the resonance observed in the 2 (ortho) and 4 (para) substituted nitrobenzenes. Resonance in these positions pushes electron density towards the nitro group, thus giving the nitro group a greater affinity for the catalyst surface. As such the relative rate of reaction in the 2 and 4 positions is observed to be greater than the 3 position where resonance does not push the electron density onto the nitro group.

Resonance was also observed when studying the effect that a 4 (para) halogenated nitrobenzene has. This effect was observed to increase greatly the initial rate of reaction when the halogen is bromine or iodine. Resonance is greater with a bromine or iodine substituent due to the diffuse outer electron shells of these halogens, which are donated into the π system of the nitrobenzene. This resonance pushes electron density towards the nitro group resulting in an increased reaction rate. Fluorine is mildly electron withdrawing and as such it does not display this activation effect in relation to the reduction of the nitrobenzene. As such the rate is reduced in comparison to other halogenated nitrobenzenes.

The investigation of various halogenated nitrobenzenes substrates suggests that FeS₂ may display promising selective hydrogen transfer catalytic properties for a range of differing substrates. As the relative position or nature of the substituent group did not impact the selectivity of the catalyst, this system may be applied to the reduction of other substrates, such

as sulfates, sulfides and sulfoxide containing nitrobenzenes, due to the difficulty in selective reduction of these compounds using more traditional catalysis routes (section 6).^{280, 281}

5.2.2 Screening of other potential hydrogen donors

Hydrazine is toxic and corrosive, as such it requires careful handling, hence it carries the potential of being environmentally damaging. Yet, it has been shown to be an effective reducing agent requiring less energy for efficient reduction when compared to more traditional hydrogenation by hydrogen at elevated pressure.^{250, 251, 282} Furthermore, it is a chemical widely used in industry, hence appropriate handling procedures are available and well known. In this thesis the great potential of hydrazine monohydrate as a reducing agent for transfer hydrogenation reactions.

The use of hydrazine monohydrate as a reducing agent in the reduction of 4-CNB via a transfer hydrogenation, showed a conversion of substrate >99.9 %, with a selectivity towards 4-CAN of 100 %. This high level of conversion and selectivity would be used as a benchmark which other reducing agents would be compared to.

The use of alternative hydrogen transfer reagents was investigated, such as using alcohols and acids, which had previously shown potential in hydrogen transfer reductions on nitrobenzenes.^{66, 73, 136, 137, 283} The conditions under which the test reactions were carried out were those optimised in chapter 4, 25 mg FeS₂ pyrite catalyst, 50 ml of a 0.05 M 4-CNB solution in ethanol, 20 mmol reducing agent, 60 °C reaction temperature, 2 hour reaction time. The results of these tests are shown in table 5.3.

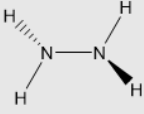
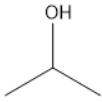
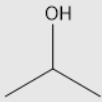
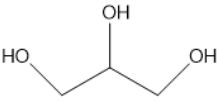
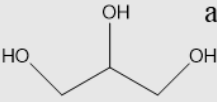
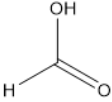
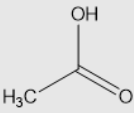
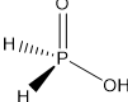
Reducing Agent	Conversion of p-CNB (%)	Selectivity towards p-CAN (%)
 hydrazine	99.9	100
 isopropanol	6.1	100
 a isopropanol	<1.0	99.2
 glycerol	0	N/A
 a glycerol	0	N/A
 formic acid	2.0	100
 acetic acid	0	N/A
 hypophosphorous acid	0	N/A

Table 5.12: Hydrogen donor compounds used in the selective transfer hydrogenation of 4-chloronitrobenzene to 4-chloroaniline, a) 5 mmol addition of a KOH base co-catalyst. Reaction profile plots shown in Appendix 16,20-26.

5.2.2.1 Alcoholic hydrogen donors

The use of alcohols in the reduction of nitrobenzenes has been widely explored, yet in many cases they require long reaction times (24 – 72 hours) to obtain acceptable conversion of the substrate material.²⁸⁴ The activation of alcohols traditionally requires the use of a platinum group metal (PGM, Rh, Pt, Pd or In) either in homogeneous or heterogeneous mode. In addition, a co-catalyst is required in order to aid in the activation of the alcohol, typically a base such as KOH or NaOH.^{66, 285} In this work, alcoholic hydrogen donors would be paired with a 5 mmol of KOH, to determine the effect the base has on the hydrogen transfer.

The alcohols that were studied in this work were glycerol and isopropanol, due to their wide use in previous work, in addition to their potential as green hydrogen donor compounds, with and without the addition of a 5 mmol KOH solution as co-catalyst.^{40, 66, 128, 285, 286}

It was clear from what was obtained that the alcoholic hydrogen donor compounds did not display similar performance to that obtained with hydrazine monohydrate (Table 5.3). Glycerol was not activated under either condition, possibly due to the intrinsic acidity of FeS₂ pyrite surface due to surface thiol groups. This acidity intrinsic to FeS₂ is neutralised by the addition of base, allowing for the deprotonation and transfer of hydrogen from the glycerol molecule onto the substrate. In the absence of the base, pyrite did not display the ability to activate glycerol and no reaction occurred. Isopropanol showed a low conversion (6.1 %) of nitrobenzene over the pyrite catalyst. However, when the base was added as a co-catalyst, the active sites became neutralised by the base thereby lowering the activity of the catalyst towards the activation of isopropanol.^{66, 283} Under the basic conditions the conversion of 4-CNB was reduced to just 2.0 %, relative to 6.1 % conversion when there was no base present. The conversion of 4-CNB remained comparatively low for isopropanol, yet the selectivity towards the 4-CAN product was maintained at 100 %. However, when the base was present the selectivity was reduced to 99.2 %, this may have been due to the deactivation of some of the

active sites, allowing for the 4-CNB to bind in orientations that allowed for the cleaving for the chloro substituent. Maintenance of a total selectivity towards the 4-CAN product by the FeS₂ pyrite catalyst showed that the nature of the reducing agent did not affect the overall selectivity of the catalyst and that the base had a slight deactivating effect on the pyrite, possibly due to the neutralisation of some acidic pyrite active sites.

5.2.2.2 Acidic reducing agent

Certain organic acids are another commonly used reducing agent for the reduction of organic compounds.^{136, 137} Most commonly used is formic acid, this is due to the degradation product of the acid being carbon dioxide (CO₂) which then diffuses out of the reaction solution, therefore, does not require an additional separation from the reaction.^{136, 137} Formic acid is a strong reducing agent than alcohols due to its low pK_a value and readily activated C-H bond that can be used in the transfer of hydrogen from one molecule to another.

The acids studied in this section are formic acid, acetic acid and hypophosphorus acid. These were selected due to their prevalence in organic reductions.^{15, 155} Due to the prevalence of formic acid in the reduction of organic compounds it was studied more closely as a potential to replace hydrazine in the reaction.

It was found that formic acid is weakly activated by the FeS₂ pyrite catalyst, converting 2.0 % of the 4-CAN, yet, maintaining 100 % selectivity towards 4-CAN. The small amount of conversion observed with a formic acid hydrogen donor may be due to the acidity of the pyrite, which may have been buffered by the formic acid therefore preventing any meaningful conversion of CNB.

There was no observed reaction when acetic acid or hypophosphorus acid was used as hydrogen donor compounds. This was believed to be due to a buffering effect similar to that observed with formic acid. The acetic acid does not decompose to a stable by-product

deprotonating into the acetate ion, which cannot react further without significant energy. Utilising hypophosphorus acid in reducing compounds that do not release water as a product of the reduction process, such as alkynes or carbonyls, allows for the activation of the hydrogen-phosphorus bonds within the hypophosphorus acid.¹⁵⁵ Any potential released oxygen driving the formation of phosphoric acid.¹⁵⁵ As the water by product from nitroarene reduction captures the oxygen, it cannot be reacted with the hypophosphorus acid driving the reduction forwards, as such the reaction did not proceed.

5.2.2.3 Comparisons of active hydrogen donors with hydrazine

From the comparison of the outcomes of the test reactions in table 5.1 and the discussion in sections 5.2.2.1 and 5.2.2.2, showed that isopropanol and formic acid show selectivities of 100 %, fully comparable with the selectivity of FeS₂ pyrite nanoparticles, when hydrazine was used as a reducing agent. However, all the alternative hydrogen transfer reagents displayed negligible conversion of p-CNB after the two-hour reaction time frame. This may have been due to the stringent reaction time frames, however, as this was a key advantage of the use of hydrazine extending the reaction time frame was unnecessary for comparison. Literature has stated that isopropanol has been used to reduce nitrobenzenes in a 24 – 72 hour time frame, a much longer time compared to that obtained using hydrazine monohydrate.

Hydrazine offered almost complete, 99.9 %, conversion of 4-CNB with 100 % selectivity towards the desired 4-CAN product. As such this will be the reducing agent of choice in future work.

5.3 Conclusions

FeS₂ pyrite has been shown to be highly active in the reduction of 4-chloronitrobenzene under a well optimised reaction using hydrazine monohydrate as a hydrogen donor compound. This optimised reaction has been applied to a range of halogenated nitrobenzenes with various

relative positioning of the halogen to the nitro group. These reactions showed that FeS₂ under these conditions maintained near 100 % conversion of the substrate material with a near 100 % selectivity towards the substituted aniline product. Minor differences were observed between compounds however, the end results were similar.

Substrates with differing relative positions of the halogen were demonstrated to be comparable at the end reaction time point. Yet, the observed initial rate of reaction of each was shown to vary, with the meta position showing a distinct decrease in relative reaction rate compared to the ortho and para positions. The inductive effect and resonance caused by the donating or withdrawing electron density to and from the aromatic ring was determined to be the key factor distinguishing each substrate. As with ortho and para halogenated nitrobenzenes, this electron density is pushed onto the nitro group thereby activating it towards the catalyst surface. Conversely, in the meta halogenated nitrobenzene this electron density is not directed towards the nitro group, therefore not aiding the nitro group in binding to catalyst, thus the observed rate of a meta substituted nitrobenzene is observed to be lower than that of the ortho and para halogenated nitrobenzenes.

The inductive effect and resonance was determined to be the key factor affecting the observed rate differences between different para halogenated nitrobenzenes. The lowest initial rate obtained from a para fluorinated nitrobenzene was due to the electron withdrawing nature of fluorine which prevented the directing of electron density towards the nitro group. Thus, the nitro group was deactivated relative to the other para halogenated nitrobenzenes. The activation was greater in the iodo and bromo nitrobenzenes, as the diffuse outer electrons of these groups donate their electrons strongly into the π system of the nitrobenzene, pushing electron density onto the nitro group which then gains a greater affinity towards the catalyst surface, thereby activating the nitro group for reduction.

The selectivity of the catalyst towards the substituted aniline product was maintained across all nitrobenzenes studied, thus showing that the inductive effect and resonance within the molecule does not affect the mode of action on the catalyst surface. Therefore, it may be that other substrates with different substituent groups may be used as potential substrates in future work, with possible other groups including sulfide, sulfate and sulfoxide groups that are currently difficult to avoid reducing under current hydrogenation conditions.

The use of different hydrogen donor compounds was explored with several alcohols and organic acids studied. The results obtained from studying these hydrogen donors in the presence of the FeS₂ pyrite catalyst showed that they were ineffective in the reduction of 4-chloronitrobenzene under the reaction conditions used for hydrazine monohydrate reactions. However, those hydrogen donors that did produce a small amount of substrate conversion, namely isopropanol and formic acid, did show that the catalyst maintained 100 % selectivity towards the desired substituted aniline product. As such in future experiments different amine based reducing agents may be explored to determine their effectiveness in the reduction of nitrobenzenes over the FeS₂ catalyst.

In this chapter, many substrates have been explored to determine the effect the substituent and relative positioning of this substituent has on the initial rate, conversion and selectivity of the reduction using an FeS₂ catalyst and hydrazine monohydrate as a hydrogen donor compound, in addition, to studying other potential hydrogen donor compounds such as organic acids and alcohols.

Chapter 6 Conclusions and Future Work

6.1 Conclusions

6.1.1 Metal sulfide synthesis

A flexible solvothermal synthesis method has been developed which, by altering the metal precursor and capping agent, can produce a single-phase iron pyrite with other transition metal sulfides being synthesised with impurity phases. The optimum solvothermal reaction conditions for producing single phase metal sulfides were found to be 15 mmol sulfur and 2.5 mmol of metal acetate, with 20 mL of ethanol as a solvent and 10 mL of oleylamine capping agent. Reaction temperature was 160 °C for 12 hours, with particles separated by centrifugation, washing with a mixture of hexane and ethanol.

This method has been demonstrated to produce monodisperse FeS₂ pyrite (space group $Pa\bar{3}$) with an elongated shape with lengths 3-5 nm. The method was applied to the synthesis of NiS₂ pyrite ($Pa\bar{3}$) producing similarly shaped particles with lengths of 5 nm.

Altering the capping agent used in the solvothermal synthesis from oleylamine to dodecane thiol produced a single phase FeS₂ marcasite ($Pnnm$). The obtained FeS₂ marcasite particles had anisotropic shape with two distinct morphologies making particle size determination difficult. The difficulty in measuring FeS₂ marcasite particle size was compounded by the lack of stability, as after just two weeks the material had begun to degrade into a mixed marcasite and pyrite material. Reactions were carried out in the absence of oleylamine. The particles obtained in the absence of a capping agent were a single phase FeS₂ pyrite nanoparticle material, particles have a spherical morphology with size of 16 ± 1 nm. Particles in the absence of oleylamine showed a tendency to aggregate together forming large ~ 0.75 μm aggregates, this is seen to a much lesser degree with oleylamine present.

6.1.2 Optimisation of the FeS₂ catalytic system

The synthesised FeS₂ nanoparticles were successfully applied as a catalyst for the selective hydrogenation of 4-chloronitrobenzene, via a hydrogen transfer reaction using hydrazine monohydrate as a hydrogen donor compound. The heterogeneous hydrogen transfer was carried out within a two-hour reaction timeframe, using ethanol as a solvent, hydrazine monohydrate as a hydrogen donor, a catalyst loading of 25 mg and a reaction temperature of 60 °C. These parameters were optimised using 4-chloronitrobenzene as a test substrate, with a view of reaching the best compromise between reaction performance and sustainability.

Studies were carried out to determine the mechanism of action of FeS₂ as a catalyst. A hot filtration was carried out to determine if any of the Fe (II) ions had leached from the FeS₂ and if these leached ions played a role in the catalysis. After a hot filtration, the reaction ceased with no further 4-chloroaniline production after the catalyst was removed. Importantly this demonstrated that FeS₂ nanoparticles play a purely heterogeneous role in the catalysis, not a potential homogeneous role as previously reported. Recyclability of FeS₂ nanocatalyst was tested over multiple reaction cycles, with no catalyst treatment between reaction cycles. The recyclability study demonstrated that FeS₂ nanoparticles used as a catalyst showed little degradation over 3 usage cycles, with noticeable reactivity differences only becoming apparent in after 4 reaction cycles. Analysis of the material after this recyclability study showed possible changes to the crystallinity of the pyrite post reaction. However, the pyrite crystal structure or the surface characteristics of the catalyst showed little change, indicating that there had been minimal structural or chemical changes after repeated use without reactivation between reaction cycles.

Comparative reactions using FeS₂ and NiS₂ nanoparticles were carried out as catalysts for the selective hydrogenation of 4-chloronitrobenzene to determine the role of the metal centre in the catalyst crystal structure. It was found that the NiS₂ nanoparticles were inactive in the

catalysis of 4-chloronitrobenzene reduction by hydrogen transfer. This was theorised to be due to the differences in the electronic structure of the two materials. Fe can readily undergo a redox reaction between Fe (II) and Fe (III), however, Ni cannot. Therefore, the reaction with Fe based pyrite can facilitate the catalytic hydrogen transfer reaction whereas Ni is inactive in the reduction of the NO₂ group.

6.1.3 FeS₂ catalytic system further development

FeS₂ pyrite nanoparticles were shown to be highly active in the hydrogen transfer reduction of 4-chloronitrobenzene using hydrazine monohydrate as a hydrogen donor compound. FeS₂ pyrite nanoparticles were applied in the catalytic hydrogen transfer reduction of a wider range of halogenated nitrobenzenes with various relative positioning of the halogen to the nitro group. These reactions showed that FeS₂ under these conditions maintained near 100 % conversion of the substrate material with a near 100 % selectivity towards the substituted aniline product. Minor differences in reactivity and catalyst effectiveness were observed between compounds however, the end results were similar.

Substrates with differing relative positions of the halogen were comparable at the end reaction time point. Yet, the observed initial rate of reaction of each was shown to vary, with the meta position showing a distinct decrease in relative reaction rate compared to the ortho and para positions.

The selectivity of the catalyst towards the substituted aniline product was maintained across all substrates studied, thus showing that the inductive effect or resonance within the molecule does not affect the mode of action once adsorbed to the catalyst surface. However, the electronic effects do somewhat determine the affinity a given substrate has towards the catalyst surface, thus, reducing the observed initial rate of reaction for these substrates.

The use of different hydrogen donor compounds was explored with several alcohols and organic acids studied, to determine what hydrogen donors were suitable for the hydrogen transfer reduction reaction. The results obtained from studying these hydrogen donors in the presence of the FeS₂ pyrite catalyst showed that they were ineffective in the reduction of 4-chloronitrobenzene under the reaction conditions used for hydrazine monohydrate reactions.

6.2 Future Work

Further development of transition metal sulfides for use as catalysts will be investigated as discussed in Section 3.4.2. The solvothermal method developed in this thesis has been applied to the successful synthesis of 5 first row transition metal sulfides. The most promising, not yet tested, metal sulfides synthesised were CuS and MnS, and these compounds may have potential uses in catalysis. Developing the synthesis method for CuS and MnS, may produce catalysts with a wide range of crystal structures and metal sulfur ratios, which may be tailored to produce highly active catalysts for both reduction and oxidation catalysts.

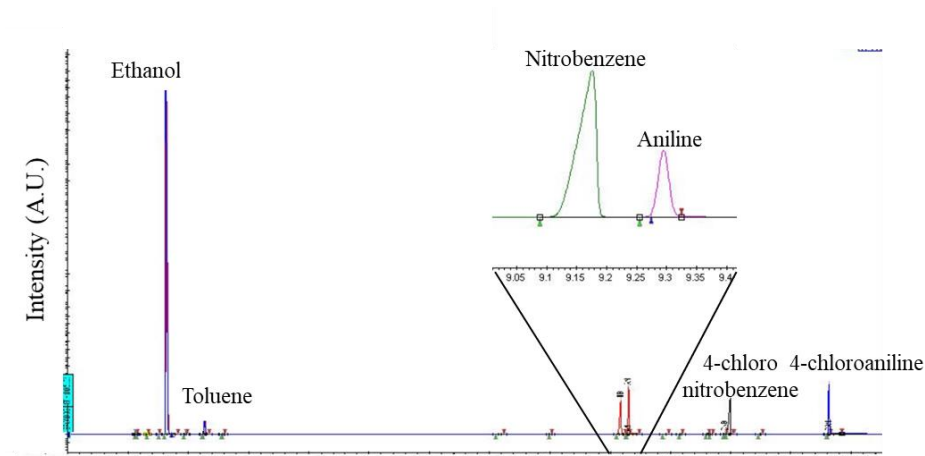
The presence of Fe₃S₄ within some FeS₂ syntheses is another area of exploration in the search for potential new catalysts. Being isostructural to Fe₃O₄, which has been demonstrated to show catalytic properties for various reactions, whilst being magnetically recoverable, Fe₃S₄ has been predicted to show similar catalytic properties. However, due to its instability and difficulty in separation from FeS₂ it has thus far been difficult to characterise its catalytic potential. Further development of the solvothermal synthesis method may give rise to selective phase control in the final product precipitate.

The application of FeS₂ as a catalyst in the selective hydrogen transfer reduction of nitroarenes will also be explored in greater depth. From what was found in Section 5.2, it has been deduced that other substrates with different substituent groups may be used as potential substrates in future work, with possible other groups including sulfide, sulfate and sulfoxide groups that are

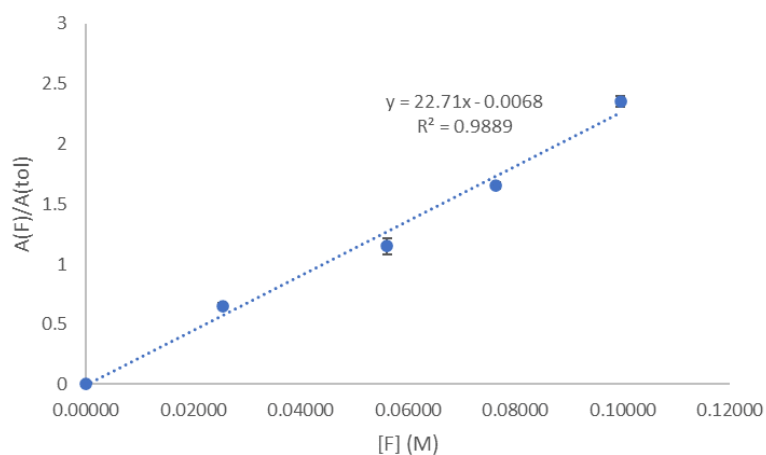
currently difficult to avoid reducing under current hydrogenation conditions. Whilst other aromatic substrates such as pyridines, furans and naphthalenes may also be possible substrates for future development and demonstration of metal sulfides as catalysts.

Other studies will involve the investigation of FeS_2 and other metal sulfides in the oxidation of organic molecules. Previous studies have indicated the potential of FeS_2 in oxidation catalysis. However, this catalyst is short lived and rapidly oxidised to iron oxide in the process. It may be that other metal sulfides show a greater stability within catalytic oxidation reactions, but this has not been reported as yet.

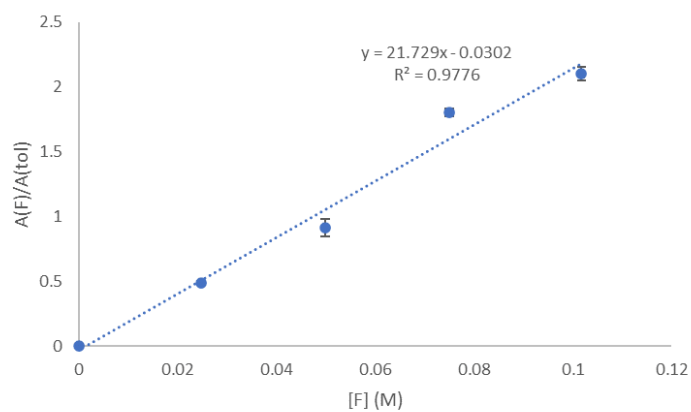
Appendices



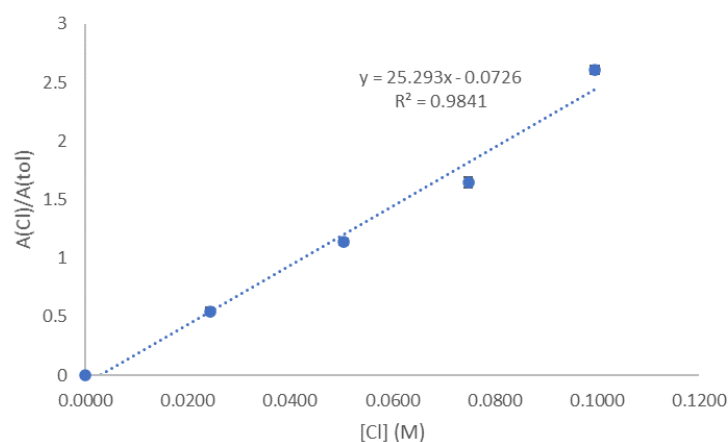
Appendix 1: Screenshots shown an example chromatogram at different scales of an aliquot from the selective hydrogenation of 4-chloronitrobenzene, the resolution of the nitrobenzene and aniline peaks have been shown to demonstrate good peak resolution.



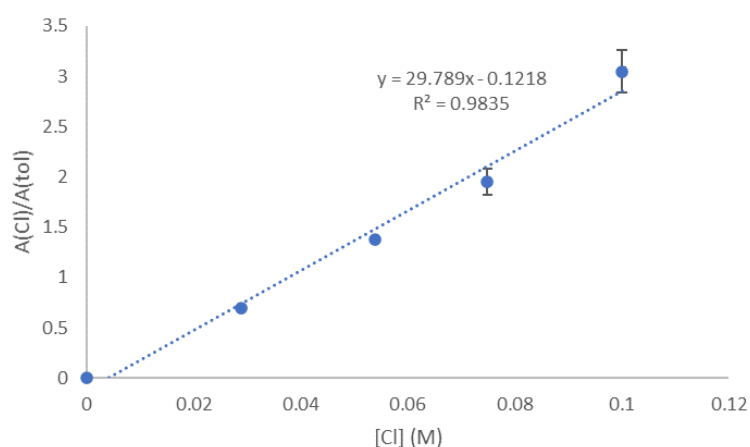
Appendix 2: Calibration curve obtained for 4-fluoronitrobenzene. Solutions of 4-fluoronitrobenzene prepared in ethanol with a 0.1 M toluene standard, peak areas measured as a ratio and calibration curve plotted.



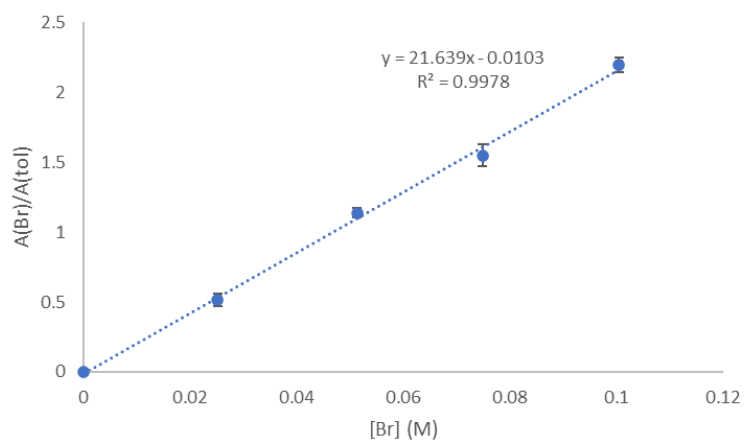
Appendix 3: Calibration curve obtained for 4-fluoroaniline. Solutions of 4-fluoroaniline prepared in ethanol with a 0.1 M toluene standard, peak areas measured as a ratio and calibration curve plotted.



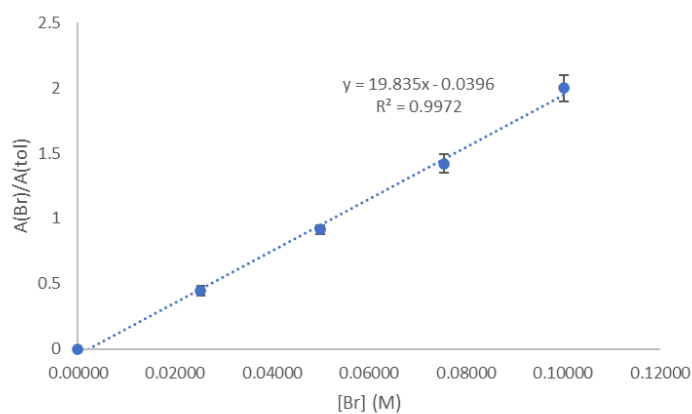
Appendix 4: Calibration curve obtained for 4-chloronitrobenzene. Solutions of 4-chloronitrobenzene prepared in ethanol with a 0.1 M toluene standard, peak areas measured as a ratio and calibration curve plotted.



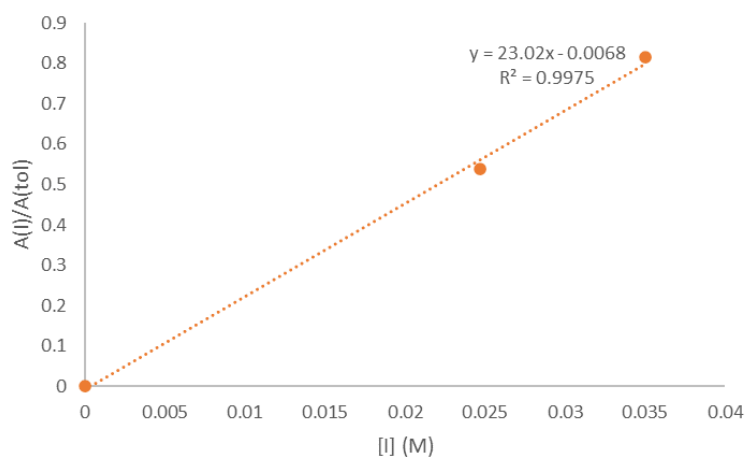
Appendix 5: Calibration curve obtained for 4-chloroaniline. Solutions of 4-chloroaniline prepared in ethanol with a 0.1 M toluene standard, peak areas measured as a ratio and calibration curve plotted.



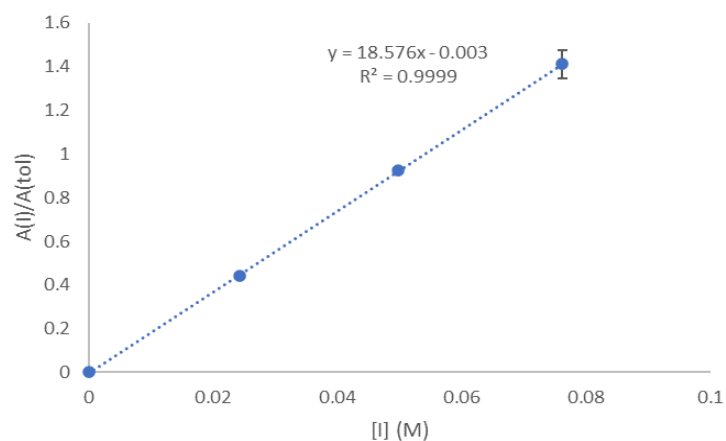
Appendix 6: Calibration curve obtained for 4-bromonitrobenzene. Solutions of 4-bromonitrobenzene prepared in ethanol with a 0.1 M toluene standard, peak areas measured as a ratio and calibration curve plotted.



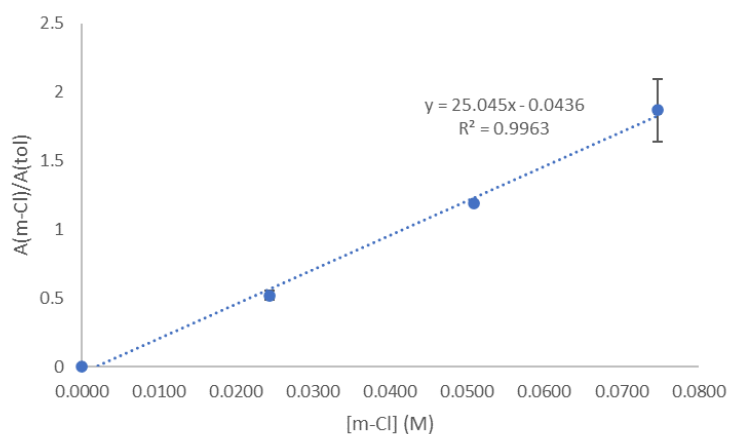
Appendix 7: Calibration curve obtained for 4-bromoaniline. Solutions of 4-bromoaniline prepared in ethanol with a 0.1 M toluene standard, peak areas measured as a ratio and calibration curve plotted.



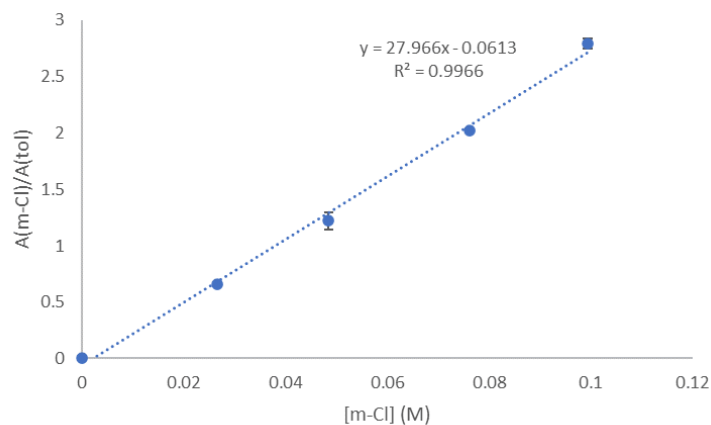
Appendix 8: Calibration curve obtained for 4-iodonitrobenzene. Solutions of 4-iodonitrobenzene prepared in ethanol with a 0.1 M toluene standard, peak areas measured as a ratio and calibration curve plotted.



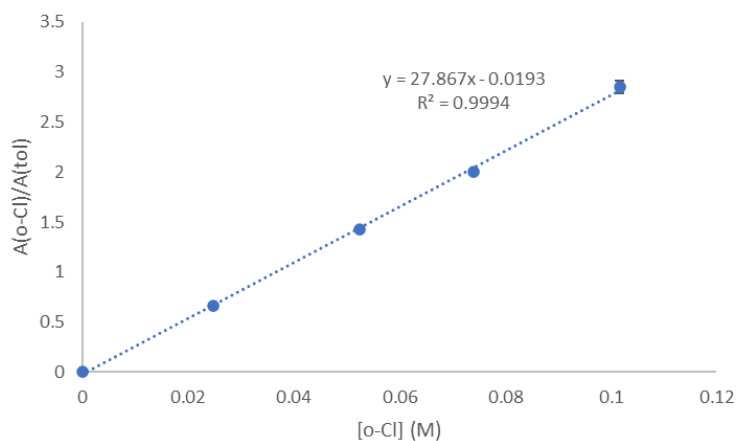
Appendix 9: Calibration curve obtained for 4-iodoaniline. Solutions of 4-iodoaniline prepared in ethanol with a 0.1 M toluene standard, peak areas measured as a ratio and calibration curve plotted.



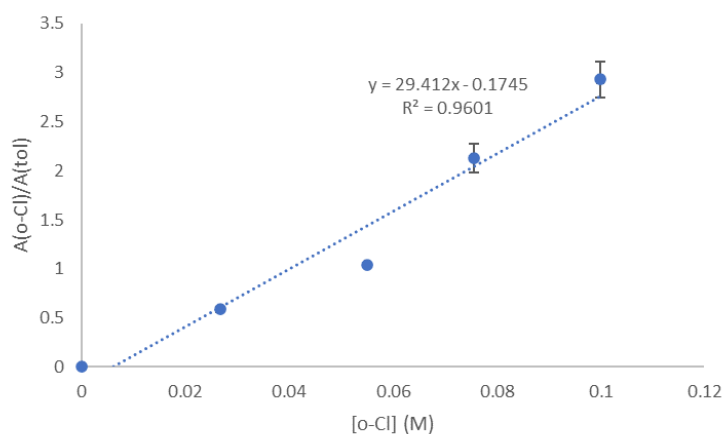
Appendix 10: Calibration curve obtained for 3-chloronitrobenzene. Solutions of 3-chloronitrobenzene prepared in ethanol with a 0.1 M toluene standard, peak areas measured as a ratio and calibration curve plotted.



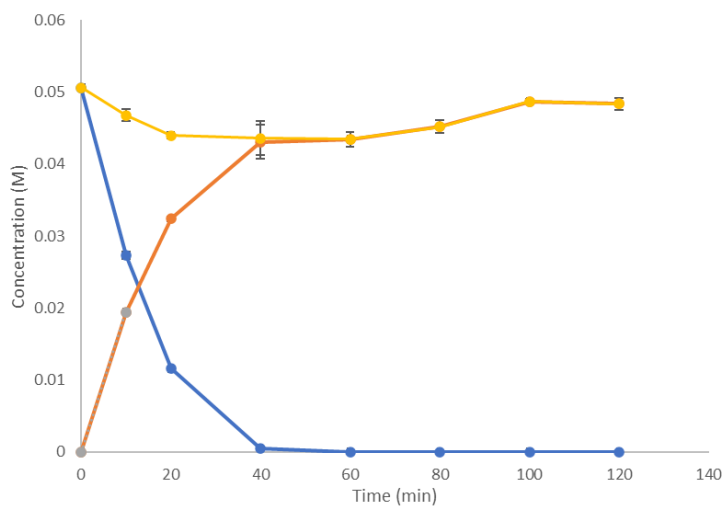
Appendix 11: Calibration curve obtained for 3-chloroaniline. Solutions of 3-chloroaniline prepared in ethanol with a 0.1 M toluene standard, peak areas measured as a ratio and calibration curve plotted.



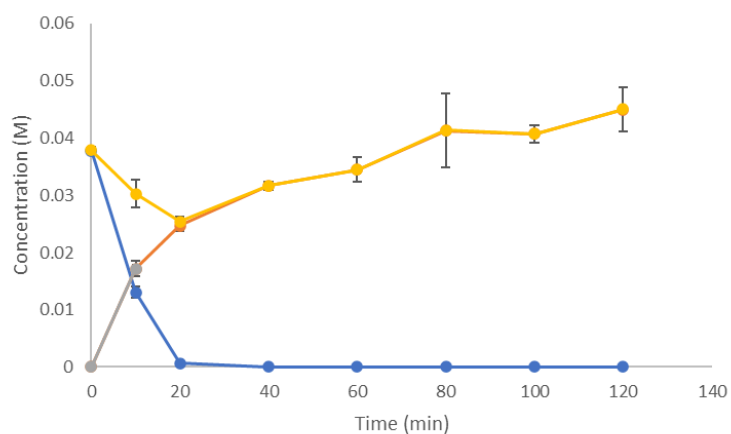
Appendix 12: Calibration curve obtained for 2-chloronitrobenzene. Solutions of 2-chloronitrobenzene prepared in ethanol with a 0.1 M toluene standard, peak areas measured as a ratio and calibration curve plotted.



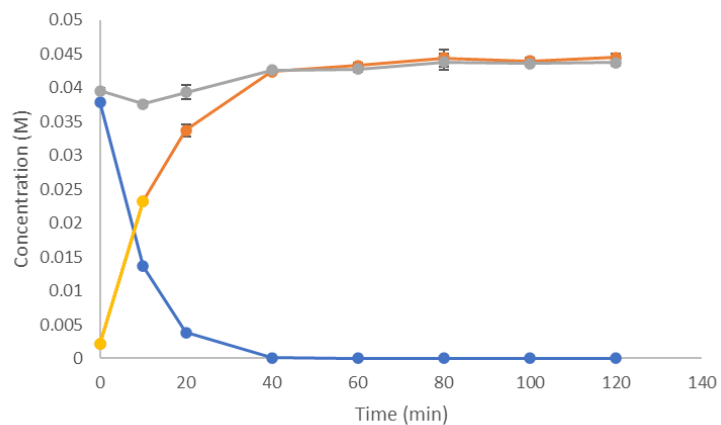
Appendix 13: Calibration curve obtained for 2-chloroaniline. Solutions of 2-chloroaniline prepared in ethanol with a 0.1 M toluene standard, peak areas measured as a ratio and calibration curve plotted.



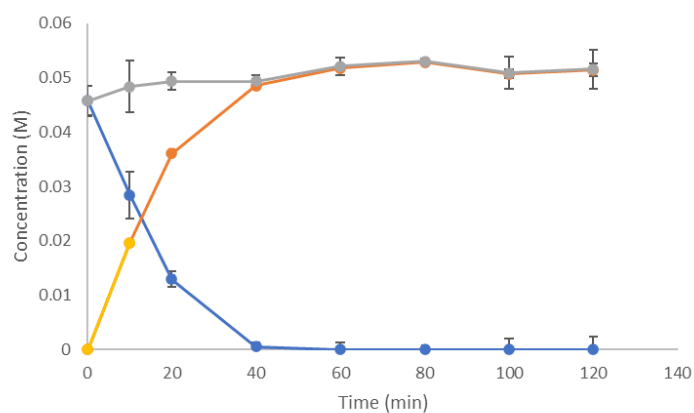
Appendix 14: Reaction profile plot of the catalytic hydrogen transfer reaction of 2-chloronitrobenzene (blue) to 2-chloroaniline (orange) with mass balance shown in yellow. 25 mg of catalyst loading, reaction carried out at 60 °C in ethanol, 20 mmol of hydrazine monohydrate used as hydrogen donor compound.



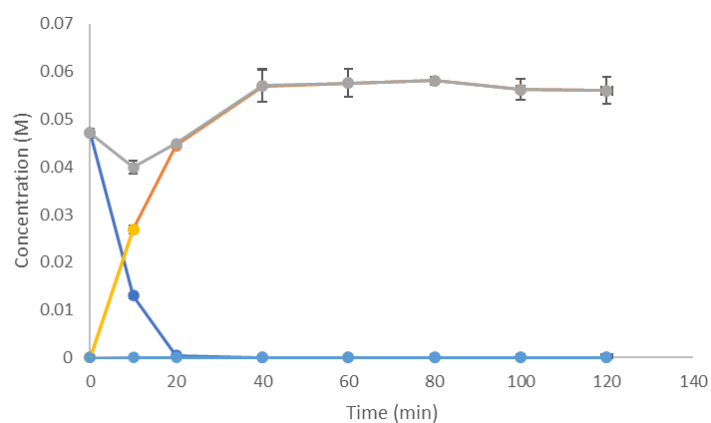
Appendix 15: Reaction profile plot of the catalytic hydrogen transfer reaction of 3-chloronitrobenzene (orange) to 3-chloroaniline (blue) with mass balance shown in yellow. 25 mg of catalyst loading, reaction carried out at 60 °C in ethanol, 20 mmol of hydrazine monohydrate used as hydrogen donor compound.



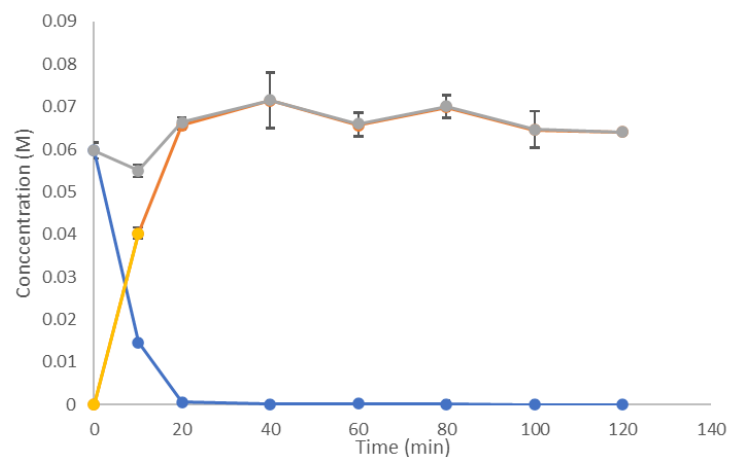
Appendix 16: Reaction profile plot of the catalytic hydrogen transfer reaction of 4-chloronitrobenzene (blue) to 4-chloroaniline (orange) with mass balance shown in grey. 25 mg of catalyst loading, reaction carried out at 60 °C in ethanol, 20 mmol of hydrazine monohydrate used as hydrogen donor compound.



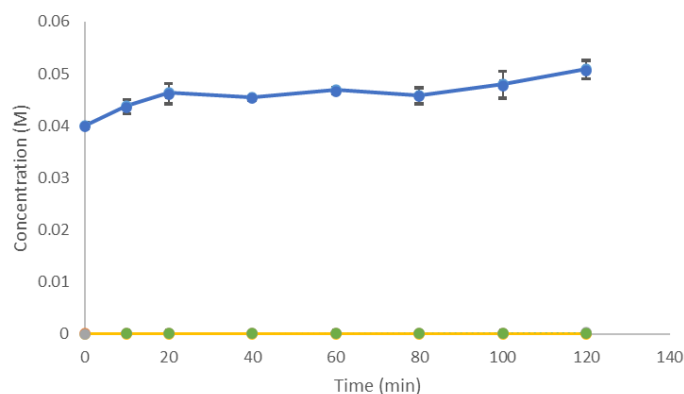
Appendix 17: Reaction profile plot of the catalytic hydrogen transfer reaction of 4-fluoronitrobenzene (blue) to 4-fluoroaniline (orange) with mass balance shown in grey. 25 mg of catalyst loading, reaction carried out at 60 °C in ethanol, 20 mmol of hydrazine monohydrate used as hydrogen donor compound.



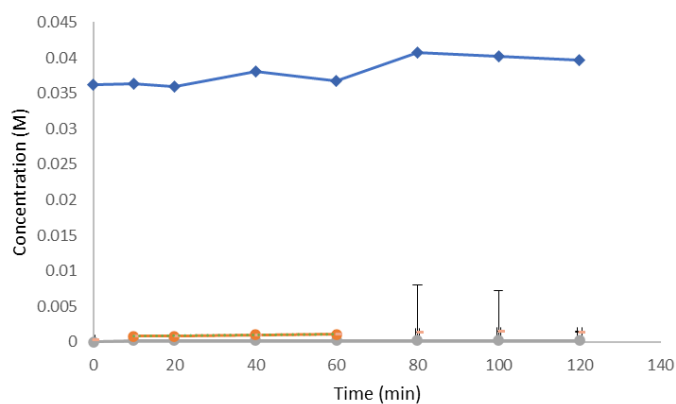
Appendix 18: Reaction profile plot of the catalytic hydrogen transfer reaction of 4-bromonitrobenzene (blue) to 4-bromoaniline (orange) with mass balance shown in grey. 25 mg of catalyst loading, reaction carried out at 60 °C in ethanol, 20 mmol of hydrazine monohydrate used as hydrogen donor compound.



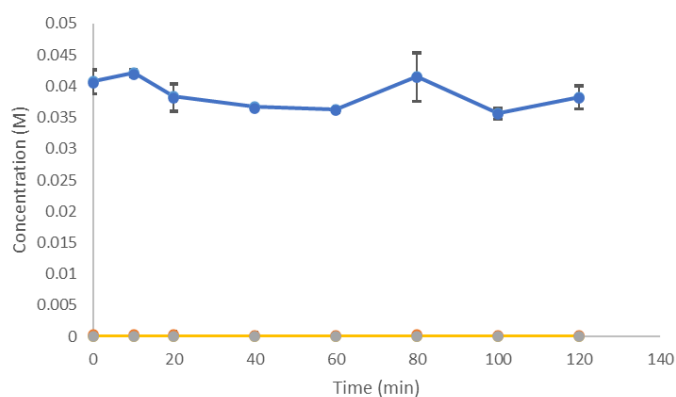
Appendix 19: Reaction profile plot of the catalytic hydrogen transfer reaction of 4-iodonitrobenzene (blue) to 4-iodoaniline (orange) with mass balance shown in grey. 25 mg of catalyst loading, reaction carried out at 60 °C in ethanol, 20 mmol of hydrazine monohydrate used as hydrogen donor compound.



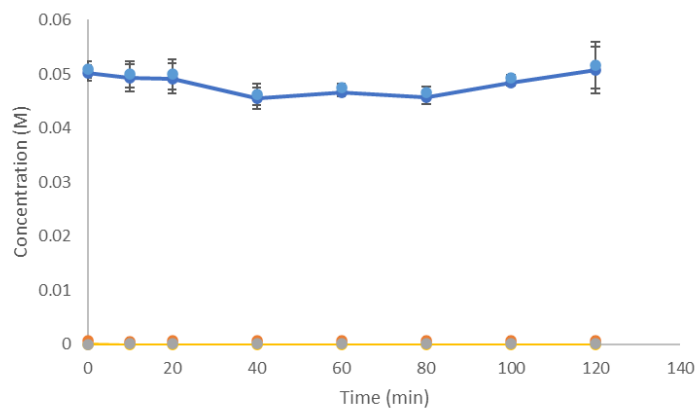
Appendix 20: Reaction profile plot of the catalytic hydrogen transfer reaction of 4-chloronitrobenzene (blue) to 4-chloroaniline (green) using glycerol as a hydrogen donor. 25 mg of catalyst loading, reaction carried out at 60 °C in ethanol, 20 mmol of glycerol used as hydrogen donor compound.



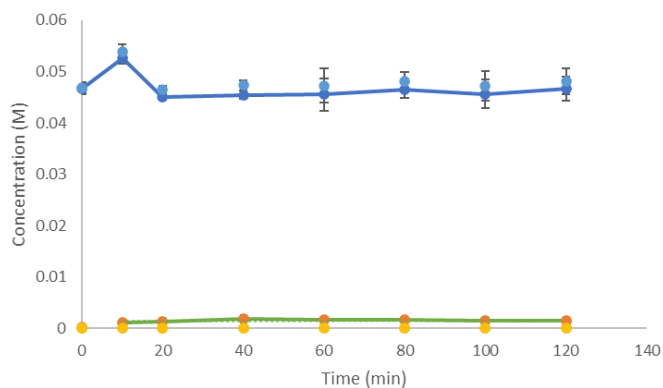
Appendix 21: Reaction profile plot of the catalytic hydrogen transfer reaction of 4-chloronitrobenzene (blue) to 4-chloroaniline (orange) using glycerol as a hydrogen donor and KOH as a co catalyst. 25 mg of catalyst loading, reaction carried out at 60 °C in ethanol, 20 mmol of glycerol and used as hydrogen donor compound.



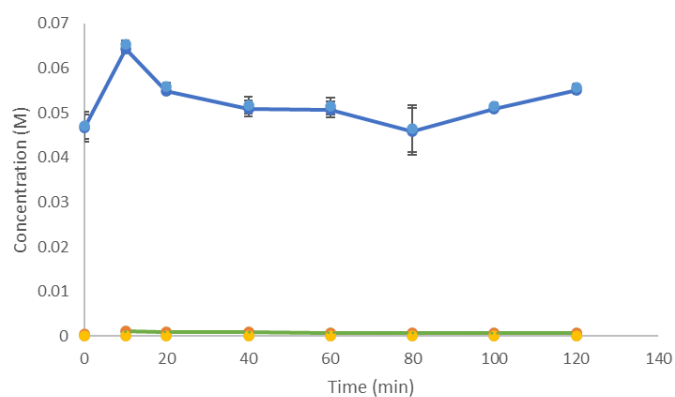
Appendix 22: Reaction profile plot of the catalytic hydrogen transfer reaction of 4-chloronitrobenzene (blue) to 4-chloroaniline (grey) using isopropanol as a hydrogen donor. 25 mg of catalyst loading, reaction carried out at 60 °C in ethanol.



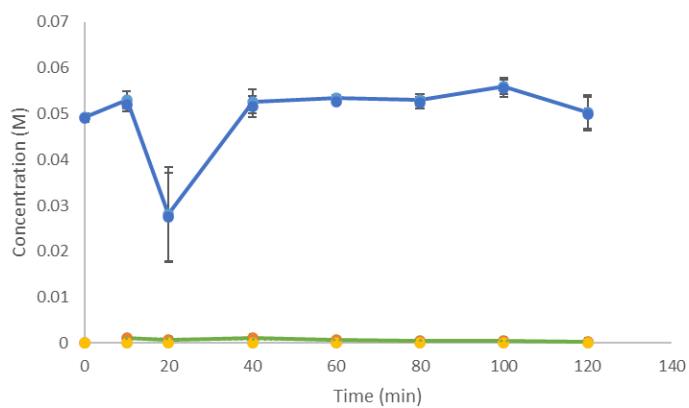
Appendix 23: Reaction profile plot of the catalytic hydrogen transfer reaction of 4-chloronitrobenzene (blue) to 4-chloroaniline (grey) using isopropanol as a hydrogen donor and 5 mmol of KOH as a co catalyst. 25 mg of catalyst loading, reaction carried out at 60 °C in ethanol.



Appendix 24 Reaction profile plot of the catalytic hydrogen transfer reaction of 4-chloronitrobenzene (blue) to 4-chloroaniline (green) using formic acid as a hydrogen donor. 25 mg of catalyst loading, reaction carried out at 60 °C in ethanol, 20 mmol of formic acid used as hydrogen donor compound.



Appendix 25 Reaction profile plot of the catalytic hydrogen transfer reaction of 4-chloronitrobenzene (blue) to 4-chloroaniline (green) using acetic acid as a hydrogen donor. 25 mg of catalyst loading, reaction carried out at 60 °C in ethanol, 20 mmol of acetic acid used as hydrogen donor compound.



Appendix 26 Reaction profile plot of the catalytic hydrogen transfer reaction of 4-chloronitrobenzene (blue) to 4-chloroaniline (green) using hypophosphorus acid as a hydrogen donor. 25 mg of catalyst loading, reaction carried out at 60 °C in ethanol, 20 mmol of hypophosphorus acid used as hydrogen donor compound.

References

1. Q. Haoa, J. Tiana, X. Li and L. Chena, *Resour., Conserv. Recycl.*, 2017, **122**, 106–113.
2. J. Heveling, *J. Chem. Educ.*, 2012, **89**, 1530–1536.
3. J. Baltrusaitis, *Sustainable Chem. Eng.*, 2017, **5**, 9527–9527.
4. A. Boulamanti and J. A. Moya, *Renewable Sustainable Energy Rev.*, 2017, **68**, 1205–1212.
5. H. Huang, X. Wang, X. Li, C. Chen, X. Zou, W. Dinga and X. Lu, *Green Chem.*, 2017, **19**, 809–815.
6. A. B. McEwen, M. J. Guttieri, W. F. Maier, R. M. Laine and Y. Shvo, *J. Org. Chem.*, 1983, **48**, 4438–4439.
7. M. Garcí'a-Mota, J. Go'mez-Dí'az, G. Novell-Leruth, C. Vargas-Fuentes, L. Bellarosa, B. Bridier, J. Pe'rez-Rami'rez and N. Lo'pez, *Theor. Chem. Acc*, 2011, **128**, 663–673.
8. A. J. McCue, A. Guerrero-Ruiz, C. Ramirez-Barria, I. Rodríguez-Ramos and J. A. Anderson, *J. Catal.*, 2017, **355**, 40–52.
9. B. Ma, X. Tong, C. Guo, X. Guo, X. Guo and F. J. Keilc, *RSC Adv.*, 2016, **6**, 55220–55224.
10. M. S. Faber, M. A. Lukowski, Q. Ding, N. S. Kaiser and S. Jin, *J. Phys. Chem. C*, 2014, **118**, 21347–21356.
11. M. Mirza-Aghayan, M. Kalantari and R. Boukherroub, *Appl. Organometal. Chem.*, 2019, **33**, 1–11.
12. P. Sangeetha, K. Shanthi, K. S. Rama Rao, B. Viswanathan and P. Selvam, *Appl. Catal.: A*, 2009, **353**, 160–165.
13. J. Wang, Y. Zhang, J. Diao, J. Zhang, H. Liu and D. Su, *Chinese J. Catal.*, 2018, **39**, 79–87.
14. J. P. Southouse, L. Lazzarini, A. O. Ibhaddon and M. G. Francesconi, *New J. Chem.*, 2021, **45**, 17808–17815.
15. H. K. Kadam and S. G. Tilve, *RSC Adv.*, 2015, **5**, 83391–83407.
16. A. Mahata, R. K. Rai, I. Choudhuri, S. K. Singh and B. Pathak, *Phys. Chem. Chem. Phys.*, 2014, **16**, 26365–26374.
17. O. A. Stasyuk, H. Szatylowicz, T. M. Krygowiski and C. Fonseca Guerra, *Phy. Chem. Chem. Phys.*, 2016, **18**, 11624–11633.
18. H.-U. Blaser, H. Steiner and M. Studer, *ChemCatChem*, 2009, **1**, 210–221.
19. W. Wang, W. Xu, K. B. Thapa, X. Yang, J. Liang, L. Zhu and J. i. Zhu, *Catalysts*, 2017, **7**, 292–305.
20. Y. Qiao, N. Said, M. Rauser, K. Yan, F. Qin, N. Theyssena and W. Leitner, *Green Chem.*, 2017, **19**, 9778–9986.
21. Y.-W. Chen and D.-S. Lee, *Mod. Res. Catal.*, 2013, **2**, 25–34.
22. R. Garcia-Garcia, O. Ortega-Zarzosa, M. E. Rincon and G. Orozco, *Electrocatalysis*, 2015, **6**, 263–273.
23. J. K. Nørskov, T. Bligaard, A. Logadottir, J. R. Kitchin, J. G. Chen, S. Pandelov and U. Stimming, *J. Electrochem.*, 2005, **152**, 23–26.
24. E. A. Gelder, S. D. Jackson and C. M. Lok, *Catal. Lett.*, 2002, **84**, 205–208.
25. L. Jiang, H. Gu, X. Xu and X. Yan, *J. Mol. Catal. A: Chem.*, 2009, **310**, 144–149.
26. H. Chen, D. He, Q. He, P. Jiang, G. Zhou and W. e. Fu, *RSC Adv.*, 2017, **7**, 29143–29148.
27. Y. Pei, Z. Qi, T. W. Goh, L. Wang, R. V. Maligal-Ganesh, H. L. MacMurdo, S. Zhang, C. Xiao, X. Li, F. Tao, D. D. Johnson and W. Huang, *J. Catal.*, 2017, **356**, 307–314.
28. S. Iihama, S. Furukawa and T. Komatsu, *ACS Catal.*, 2016, **6**, 742–746.
29. M. Sankar, N. Dimitratos, P. J. Miedziak, P. P. Wells, C. J. Kielye and G. J. Hutchings, *Chem. Soc. Rev.*, 2012, **41**, 8099–8139.
30. D. Lamey, O. Beswick, F. Cárdenas-Lizana, P. J. Dyson, E. Sulman and L. Kiwi-Minsker, *Appl. Catal. A*, 2017, **542**, 182–190.
31. G. X. Peia, X. Y. Liua, A. i. Wang, Y. Sua, L. Lia and L. a. Zhanga, *Appl. Catal.: A*, 2017, **545**, 90–96.

32. A. B. Merlo, V. Vetere, J. F. Ruggera and M. L. Casella, *Catal. Commun.*, 2009, **10**, 1665–1669.
33. L. Shen, S. Mao, J. Li, M. Li, P. Chen, H. Li, Z. Chen and Y. Wang, *J. Catal.*, 2017, **350**, 13-20.
34. A. C. Tsiapis, *Coord. Chem.*, 2017, **345**, 229-262.
35. R. V. Maligal-Ganesh, C. Xiao, T. W. Goh, L. Wang, J. Gustafson, Y. Pei, Z. Qi, D. D. Johnson, S. Zhang, F. Tao and W. Huang, *ACS Catal.*, 2016, **6**, 1754-1763.
36. S. K. Johnston, N. Cherkasov, E. Pérez-Barrado, A. Aho, D. Y. Murzin, A. O. Ibhadon and M. G. Francesconi, *Appl. Catal.: A*, 2017, **544**, 40-45.
37. L. B. Okhlopkovaa, S. V. Cherepanovaa, I. P. Prosvirina, M. A. Kerzhentseva and Z. R. Ismagilova, *Appl. Catal.: A*, 2018, **549**, 245-253.
38. S.-L. Xu, S.-C. Shen, S. Zhao, Y.-W. Ding, S.-Q. Chu, P. Chen, Y. Lin and H.-W. Liang, *Chem. Sci.*, 2020, **11**, 7933-7939.
39. R. Ferrando, J. Jellinek and R. L. Johnston, *Chem. Rev.*, 2008, **108**, 845-910.
40. E. Hong, S. Bang, J. H. Cho, K. D. Jung and C. Shin, *Appl. Catal. A*, 2017, **542**, 146-153.
41. G. Kyriakou, M. B. Boucher, A. D. Jewell, E. A. Lewis, T. J. Lawton, A. E. Baber, H. L. Tierney, M. Flytzani-Stephanopoulos and E. C. H. Sykes, *Science*, 2012, **335**, 1209-1212.
42. M. W. Tew, H. Emerich and J. A. van Bokhoven, *J. Phys. Chem.*, 2011, **115**, 8457–8465.
43. A. Han, J. Zhang, W. Sun, W. Chen, S. Zhang, Y. Han, Q. Feng, L. Zheng, L. Gu, C. Chen, Q. Peng, D. Wang and Y. Li, *Nat. Commun.*, 2019, **10**, 3787-3795.
44. K. G. Papanikolaou and M. Stamatakis, *Catal. Sci. Technol.*, 2020, **10**, 5815-5828.
45. R. Huang, G.-F. Shao, Y. Zhang and Y.-H. Wen, *ACS Appl. Mater. Interfaces*, 2017, **9**, 12486-12493.
46. V. Claude, J. G. Mahy, J. Geens and S. D. Lambert, *Mater. Today Chem.*, 2019, **13**, 98-109.
47. M. A. Aramendia, V. Borau, C. Jiménez, J. M. Marinas and J. A. Pajares, *J. Catal.*, 1982, **78**, 188-196.
48. N. Cherkasov, A. O. Ibhadon and E. V. Rebrov, *Lab Chip*, 2015, **15**, 1952-1960.
49. Y. Cui and W.-L. Dai, *Catal. Sci. Technol.*, 2016, **6**, 7752-7762.
50. Z. Wei, Y. Chen, J. Wang, D. Su, M. Tang, S. Mao and Y. Wang, *ACS Catal.*, 2016, **6**, 5816-5822.
51. A. B. Dongil, L. Pastor-Pérez, J. L. G. Fierro, N. Escalona and A. Sepúlveda-Escribano, *Catal. Commun.*, 2016, **75**, 55-59.
52. X. H. Lu, Y. Shena, J. Hea, R. Jing, P. P. Taaa, A. Hua, R. F. Niea, D. Zhoua and Q. H. Xiaa, *Mol. Catal.*, 2017, **444**, 53-61.
53. P. Mäki-Arvela and D. Y. Murzin, *Appl. Catal. A: Gen.*, 2013, **451**, 251-281.
54. J. T. Miller, M. Schreier, A. J. Kropf and J. R. Regalbuto, *J. Catal.*, 2004, **225**, 203-212.
55. W. Yu, Z. Xin, S. Niu, T.-W. Lin, W. Guo, Y. Xie, Y. Wu, X. Ji and L. Shao, *Catal. Sci. Technol.*, 2017, **2017**, 4934-4939.
56. K. Esumi, T. Tano, K. Torigoe and K. Meguro, *Chem. Mater.*, 1990, **2**, 564-567.
57. I. Robinson, S. Zacchini, L. D. Tung, S. Maenosono and N. T. K. Thanh, *Chem. Mater.*, 2009, **21**, 3021-3026.
58. W. Li, X. Cui, K. Junge, A.-E. Sarkus, C. Kreyenschulte, S. Bartling and M. Beller, *ACS Catal.*, 2019, **9**, 4302-4307.
59. V. R. Remya and M. Kurian, *Int. Nano Lett.*, 2019, **9**, 17-29.
60. X. Chen, X. Chen, S. Cai, J. Chen, W. Xu, H. Jia and J. Chen, *Chem. Eng. J.*, 2018, **334**, 768-779.
61. B. Gole, U. Sanyal, R. Banerjee and P. S. Mukherjee, *Inorg. Chem.*, 2016, **55**, 2345-2354.
62. J. D. Wright and J. M. Sommerdijk, *Sol-Gel Materials: Chemistry and Applications*, CRC Press, London, 200.
63. M. A. Cauqui and J. M. Rodríguez-Izquierdo, *J. Non Cryst. Solids*, 1992, **147-148**, 724-738.
64. S. Riyaz, A. Parveen and A. Azam, *Perspect. Sci.*, 2016, **8**, 632-635.
65. S. Zhao, Q. Li, F. Li and Z. Liang, *J. Sol-Gel Sci. Technol.*, 2017, **84**, 544-555.

66. M. B. Gawande, A. K. Rath, P. S. Branco, I. D. Nogueira, A. Velhinho, J. J. Shrikhande, U. U. Indulkar, R. V. Jayaram, C. A. A. Ghumman, N. Bundaleski and O. M. N. D. Teodoro, *Chem. Eur. J.*, 2012, **18**, 12628-12632.
67. K. J. Datta, A. K. Rath, M. B. Gawande, V. Ranc, G. Zoppellaro, R. S. Varma and R. Zboril, *ChemCatChem*, 2016, **8**, 2351-2355.
68. S. Xu, D. Yu, S. Liao, T. Yeac and H. Sheng, *RSC Adv.*, 2016, **6**, 96431-96435.
69. R. Poreddy, C. Engelbrekt and A. Riisager, *Catal. Sci. Technol.*, 2015, **5**, 2467-2477.
70. L. Petitjean, R. Gagne, E. S. Beach, D. Xiao and P. T. Anastas, *Green Chem.*, 2016, **18**, 150-156.
71. C. Guo, X. Tong and X. Guo, *Mater. Lett.*, 2015, **161**, 220-223.
72. J. R. Morse, J. F. Callejas, A. J. Darling and R. E. Schaak, *Chem. Commun.*, 2017, **53**, 4807-4810.
73. S. Farhadi and F. Siadatnasab, *J. Mol. Catal. A Chem.*, 2011, **339**, 108-116.
74. J. W. Thomson, K. Nagashima, P. M. Macdonald and G. A. Ozin, *J. Am. Chem. Soc.*, 2011, **133**, 5036-5041.
75. N. Zhang, R. Yi, Z. Wang, R. Shi, H. Wang, G. Qiu and X. Liu, *Mater. Chem. Phys.*, 2008, **111**, 13-16.
76. S. H. Chaki, S. M. Chauhan, J. P. Tailor and M. P. Dashpande, *J. Mater. Res. Technol.*, 2017, **6**, 123-128.
77. D.-W. Wang, Q.-H. Wang and T.-M. Wang, *CrystEngComm*, 2010, **12**, 755-761.
78. N. L. N. Broge, F. S ndergaard-Pedersen, M. Roelsgaard, X. Hassing-Hansen and B. B. Iversen, *Nanoscale*, 2020, **12**, 8511-8518.
79. W. L. Liu, X. H. Rui, H. T. Tan, C. Xu, Q. Y. Yan and H. H. Hng, *RSC Adv.*, 2014, **4**, 48770-48776.
80. B. Yuan, W. Luan and S. Tu, *Dalton Trans.*, 2012, **41**, 772-776.
81. X. Chen and R. Fan, *Chem. Mater.*, 2001, **13**, 802-805.
82. B. Ma, Y. Wang, X. Tong, X. Guo, Z. Zheng and X. Guo, *Catal. Sci. Technol.*, 2017, **7**, 2805-2812.
83. K. W. Cheah, M. J. Taylor, A. Osatiashtiani, S. K. Beaumont, D. J. Nowakowski, S. Yusup, A. V. Bridgewater and G. Kyriakou, *Catal. Today*, 2019, **324**, 115-125.
84. J. Li, Z. Xia, M. Zhang, S. Zhang, J. Li, Y. Ma and Y. Qu, *J. Mater. Chem. A*, 2019, **7**, 17775-17781.
85. I. S daba, M. L pez Granados, A. Riisager and E. Taaring, *Green Chem.*, 2015, **17**, 4133-4145.
86. W. Yang, B. Vogler, Y. Lei and T. Wu, *Environ. Sci. Water Res. Technol.*, 2017, **3**, 1143-1151.
87. C. Zhang, Z. Zhang, X. Wang, M. Li, J. Lu, R. Si and F. Wang, *Appl. Catal. A-Gen.*, 2016, **525**, 85-93.
88. I. Sorribes, L. Liu and A. Corma, *ACS Catal.*, 2017, **7**, 2698-2708.
89. J. Zhang, L. Wang, Y. Shao, Y. Wang, B. C. Gates and F.-S. Xiao, *Angew. Chem. Int. Ed.*, 2017, **56**, 9747-9751.
90. A. Corma and P. Serna, *Science*, 2006, **313**, 332-334.
91. M. Zhao, *Chem. Asian J.*, 2016, **11**, 461-464.
92. S. Carenco, A. Levya-Perez, P. Concepcion, C. Boissiere, N. Mezailles, C. Sanchez and A. Corma, *Nano Today*, 2012, **7**, 21-28.
93. H. Wang, Y. Shu, M. Zheng and T. Zhang, *Catal. Lett.*, 2008, **124**, 219-225.
94. J. L. Hauser, G. Amberchan, M. Tso, R. Manley, K. Bustillo, J. Cooper, J. H. Golden, B. Singaram and S. R. J. Oliver, *ACS Appl. Nano Mater.*, 2019, **2**, 1472-1483.
95. Y. Bonita, T. P. O'Connell, H. E. Miller and J. C. Hicks, *Ind. Eng. Chem. Res.*, 2019, **58**, 3650-3658.
96. S. Wang, H. Ge, S. Sun, J. Zhang, F. Liu, X. Wen, X. Yu, L. Wang, Y. Zhang, H. Xu, J. C. Neuefeind, Z. Qin, C. Chen, C. Jin, Y. Li, D. He and Y. Zhao, *J. Am. Chem. Soc.*, 2015, **137**, 4815-4822.
97. B. Jiang, H. Song, Y. Kang, S. Wang, Q. Wang, X. Zhou, K. Kani, Y. Guo, J. Ye, H. Li, Y. Sakka, J. Henzie and Y. Yusuke, *Chem. Sci.*, 2020, **11**, 791-796.

98. N. Kalyon, K. Hofmann, J. Malter, M. Lucas, P. Claus and B. Albert, *J. Catal.*, 2017, **352**, 436-441.
99. L. Chen, L.-R. Zhang, L.-Y. Yao, Y.-H. Fang, L. He, G.-F. Wei and Z.-P. Liu, *Energy Environ. Sci.*, 2019, **12**, 3099-3105.
100. F. Cárdenas-Lizana, D. Lamey, L. Kiwi-Minsker and M. A. Keane, *J. Mater. Sci.*, 2018, **53**, 6707-6718.
101. T.-N. Ye, S.-W. Park, Y. Lu, J. Li, M. Sasase, M. Kitano and H. Hosono, *J. Am. Chem. Soc.*, 2020, **142**, 14374-14383.
102. L. Yu, S. Song, B. McElhenny, F. Ding, D. Luo, Y. Yu, S. Chen and Z. Ren, *J. Mater. Chem. A*, 2019, **7**, 19728-19732.
103. S. Hu, C. Feng, S. Wang, J. Liu, H. Wu, L. Zhang and J. Zhang, *ACS Appl. Mater. Interfaces*, 2019, **11**, 13168-13175.
104. T. Jin, X. Sang, R. R. Unocic, R. T. Kinch, X. Liu, J. Hu, H. Liu and S. Dai, *Adv. Mater.*, 2018, **30**, 1707512-1707516.
105. R. Gao, L. Pan, H. Wang, X. Zhang, L. Wang and J.-J. Zou, *ACS Catal.*, 2018, **8**, 8420-8429.
106. Y. Bonita, V. Jain, F. Geng, T. P. O'Connell, N. X. Ramos, N. Rai and J. C. Hicks, *Appl. Catal. B.: Environ.*, 2020, **277**, 119272-119283.
107. Y. Kanda, K. Kawanishi, T. Tsujino, A. M. F. M. Al-Otaibi and Y. Uemichi, *Catalysts*, 2018, **8**, 160-171.
108. Y. Zhu, S. Yang, C. Cao, W. Song and L.-J. Wan, *Inorg. Chem. Front.*, 2018, **5**, 1094-1099.
109. D. J. Collins and A. D. Smith, *Ind. Eng. Chem. Prod. Res. Dev.*, 1982, **21**, 279-281.
110. F. Cárdenas-Lizana, D. Lamey, S. Gómez-Quero, N. Parret, L. Kiwi-Minsker and M. A. Keane, *Catal. Today*, 2011, **173**, 53-61.
111. A. Borgschulte, R. J. Westerwaal, J. H. Rector, H. Schreuders, B. Dam and R. Griessen, *J. Catal.*, 2006, **239**, 263-271.
112. L. Rodríguez-García, K. Hungerbühler, A. Baiker and F. Meemken, *J. Am. Chem. Soc.*, 2015, **137**, 12121-12130.
113. B. Amin-Ahmadi, D. Connétable, M. Fivel, D. Tanguy, R. Delmelle, S. Turner, L. Malet, S. Godet, T. Pardoën, J. Proost, D. Schryvers and I. H., *Acta Mater.*, 2016, **111**, 253-261.
114. B. Li and Z. Xu, *J. Am. Chem. Soc.*, 2009, **131**, 16380-16382.
115. K. Fulajtárovaa, T. Sotáka, M. Hroneca, I. Vávrab, E. Dobrořckab and M. Omastová, *Appl. Catal., A*, 2015, **502**, 78-85.
116. M. J. Taylor, L. J. Durndell, M. A. Isaacs, C. M. A. Parlett, K. Wilson, A. F. Lee and G. Kyriakou, *Appl. Catal. B.-Environ.*, 2016, **180**, 580-585.
117. A. Malouche, Y. Oumellal, C. M. Ghimbeu, A. Martínez de Yuso and C. Zlotea, *J. Nanopart. Res.*, 2017, **19**, 270.
118. M. J. Young, J. C. Carson, P. H. Pfromm, M. E. Rezac and B. M. Law, *Ultramicroscopy*, 2017, **181**, 42-49.
119. S. Schaefer, V. Fierro, A. Szczurek, M. T. Izquierdo and A. Celzard, *Int. J. Hydrog. Energy*, 2016, **41**, 17442-17452.
120. N. C. Nelson and J. Szanyi, *ACS Catal.*, 2020, **10**, 5663-5671.
121. P. Jia, X. Lan, X. Li and T. Wang, *ACS Sustainable Chem. Eng.*, 2019, **7**, 15221-15229.
122. F. Chen, C. Topf, J. Radnik, C. Kreyenschulte, H. Lund, M. Schneider, A. Surkus, L. He, K. Junge and M. Beller, *J. Am. Chem. Soc.*, 2016, **138**, 8781-8788.
123. M. Crespo-Quesada, M. Grasemann, N. Semagina, A. Renken and L. Kiwi-Minsker, *Catal. Today*, 2009, **147**, 247-254.
124. Y. Li, H. Cheng, W. Lin, C. Zhang, Q. Wu, F. Zhao and M. Arai, *Catal. Sci. Technol.*, 2018, **8**, 3580-3589.
125. H. Takagi, T. Isoda, K. Kasukabe and S. Morooka, *Energy Fuels*, 1999, **13**, 1191-1196.
126. S. Fujita, Y. Onodera, H. Yoshida and M. Arai, *Green Chem.*, 2016, **18**, 4934-4940.

127. K.-i. Shimizu, Y. Miyamoto, T. Kawasaki, T. Tanji, Y. Tai and A. Satsuma, *J. Phys. Chem. C*, 2009, **113**, 17803-17810.
128. Z. Hu, Y. Ai, L. Liu, J. Zhou, G. Zhang, H. Liu, X. Lu, Z. Liu, J. Hu, H. Sun and Q. Liang, *Adv. Synth. Catal.*, 2019, **361**, 3146-3154.
129. D. Wand and D. Astruc, *Chem. Rev.*, 2015, **115**, 6621-6686.
130. C. Zhang, J. Lu, M. Li, Y. Wang, Z. Zhang, H. Chen and F. Wang, *Green Chem.*, 2016, **18**, 2435-2442.
131. M. M. Villaverde, T. F. Garetto and A. J. Marchi, *Catal. Commun.*, 2015, **58**, 6-10.
132. V. K. Das, S. Mazhar, L. Gregor, B. D. Stein, D. G. Morgan, N. A. Maciulis, M. Pink, Y. Losovyj and L. M. Bronstein, *ACS Appl. Mater. Interfaces*, 2018, **10**, 21356-21364.
133. Y. Wang, P. Prinsen, K. S. Triantafyllidis, S. A. Karakoulia, A. Yepez, C. Len and R. Luque, *ChemCatChem*, 2018, **10**, 3459-3468.
134. H. P. R. Kannapu, C. A. Mullen, Y. Elkasabi and A. A. Boateng, *Fuel Process. Technol.*, 2015, **137**, 220-228.
135. H. Chen, H. Ruan, X. Lu, J. Fu, T. Langrish and T. Lu, *Mol. Catal.*, 2018, **445**, 94-101.
136. H. Guo, G. R. M. Sun, H. Guo, B. Wang and L. Chen, *Chem. Sus. Chem.*, 2019, **12**, 487-494.
137. X. Zhan, S. Michaud-Chevallier, D. Hérault and F. Duprat, *Org. Process Res. Dev.*, 2019.
138. C. Guyon, E. Méta, F. Popowycz and M. Lemaire, *Orb. Biomol. Chem.*, 2015, **13**, 7879-7906.
139. M. Oba, K. Kojima, M. Endo, H. Sano and K. Nishiyama, *Green Chem. Lett. Rev.*, 2013, **6**, 233-236.
140. I. D. Entwistle, T. Gilkerson, R. A. W. Johnstone and R. P. Telford, *Tetrahedron*, 1978, **34**, 213-215.
141. J. Du, J. Zhang, Y. Sun, W. Jia, Z. Si, H. Gao, X. Tang, X. Zeng, T. Lei, S. Liu and L. Lin, *J. Catal.*, 2018, **368**, 69-78.
142. G. Li, H. Yang, H. Zhang, Z. Qi, M. Chen, W. Hu, L. Tian, R. Nie and W. Huang, *ACS Catal.*, 2018, **8**, 8396-8405.
143. R. Ne, X. Peng, H. Zhang, X. Yu, X. Lu, D. Zhou and Q. Xia, *Catal. Sci. Technol.*, 2017, **7**, 627-634.
144. S. Tian, M. Hu, Q. Xu, W. Gong, W. Chen, J. Yang, Y. Zhu, C. Chen, J. He, Q. Liu, H. Zhao, D. Wang and Y. Li, *Sci. China Mater.*, 2020, **1**, 1-7.
145. X. Zhou and M. Zhou, *Chemistry*, 2020, **2**, 960-968.
146. R. F. Nystrom and W. G. Brown, *J. Am. Chem. Soc.*, 1948, **70**, 3738-3740.
147. I. Pogorelic, M. Filipan-Litvic, S. Merkaš, G. Ljubic, I. Cepanec and M. Litvic, *J. Mol. Catal. A Chem.*, 2007, **274**, 202-207.
148. R. O. Hutchins, D. W. Lamson, L. Rua, C. Milewski and B. Maryanoff, *J. Org. Chem.*, 1971, **36**, 803-806.
149. T. B. Nguyen, C. P. Huang and R. Doong, *Appl. Catal. B*, 2019, **240**, 337-347.
150. K. Bhaduri, B. D. Das, R. Kumar, S. Mondal, S. Chatterjee, S. Shah, J. J. Bravo-Suàrez and B. Chowdhury, *ACS Omega*, 2019, **4**, 4071-4081.
151. M. Ghadermazi, S. Moradi and R. Mozafari, *RSC Adv.*, 2020, **10**, 33389-33400.
152. K. Zhang, J. M. Suh, J.-W. Choi, H. W. Jang, M. Shokouhimehr and R. S. Varma, *ACS Omega*, 2019, **4**, 483-495.
153. J. Wang, Y. Zhang, J. Diao, J. Zhang, H. Liu and D. Su, *Chinese J. Catal.*, 2018, **39**, 79-87.
154. R. K. Rai, A. Mahata, S. Mukhopadhyay, S. Gupta, P.-Z. Li, K. T. Nguyen, Y. Zhao, B. Pathak and S. K. Singh, *Inorg. Chem.*, 2014, **53**, 2904-2909.
155. R. A. W. Johnstone and A. H. Wilby, *Chem. Rev.*, 1985, **85**, 129-170.
156. A. A. Vernekar, S. Patil, C. Bhat and S. G. Tilve, *RSC Adv.*, 2013, **3**, 13243-13250.
157. Z. Zhao, H. Yang, Y. Li and X. Guo, *Green Chem.*, 2014, **16**, 1274-1281.
158. Y.-M. Lu, H.-Z. Zhu, W.-G. Li, B. Hu and S.-H. Yu, *J. Mater. Chem. A*, 2013, **1**, 3783-3788.
159. Z. Hu, J. Zhou, Y. Ai, L. Liu, L. Qi, R. Jiang, H. Bao, J. Wang, J. Hu, H. Sun and Q. Liang, *J. Catal.*, 2018, **368**, 20-30.

160. H. Shafaghat, P. S. Rezaei and W. M. A. W. Daud, *J. Taiwan Inst. Chem. Eng.*, 2016, **65**, 91-100.
161. G. Fraga, Y. Yin, M. Konarova, M. D. Hasan, B. Laycock, Q. Yuan, N. Batalha and S. Pratt, *Int. J. Hydrog. Energy*, 2020, **45**, 27281-27391.
162. B. Quiclet-Sire and S. Z. Zard, *J. Am. Chem. Soc.*, 1996, **118**, 9190-9191.
163. K. W. Cheah, S. Yusup, G. Kyriakou, M. Ameen, M. J. Taylor, D. J. Nowakowski, A. V. Bridgewater and Y. Uemura, *Int. J. Hydrog. Energy*, 2019, **44**, 20678-20689.
164. L. Li, Y. Hou, W. Wu, S. Liang and S. Ren, *Fuel Process. Technol.*, 2019, **191**, 202-210.
165. P. T. Aakko-Saksa, M. Vehkamäki, M. Kemell, L. Keskiäli, P. Simell, M. Reinikainen, U. Tapper and T. Repo, *Chem. Commun.*, 2020, **56**, 1657-1660.
166. Z. Kou, Z. Zhi, G. Xu, Y. An and C. He, *Appl. Catal. A-Gen.*, 2013, **467**, 196-201.
167. P. Modisha, P. Gqogqa, R. Garidzirai, C. N. M. Ouma and D. Bessarabov, *Int. J. Hydrog. Energy*, 2019, **44**, 21926-21935.
168. P. M. Modisha, C. N. M. Ouma, R. Garidzirai, P. Wasserscheid and D. Bessarabov, *Energy Fuels*, 2019, **33**, 2778-2796.
169. A. Devaraj, M. Vijayakumar, J. Bao, M. F. Guo, M. A. Derewinski, Z. Xu, M. J. Gray, S. Prodingier and K. K. Ramasamy, *Sci. Rep.*, 2016, **6**.
170. B. Liu, D. Slocombe, M. AlKinany, H. AlMegren, J. Wang, J. Arden, A. Vai, S. Gonzalez-Cortes, T. Xiao, V. Kuznetsov and P. P. Edwards, *Appl. Petrochem. Res.*, 2016, **6**, 209-215.
171. L. Malet-Sanz and F. Susanne, *J. Med. Chem.*, 2012, **55**, 4062-4098.
172. D. M. Roberge, B. Zimmermann, F. Rainone, M. Gottsponer, M. Eyholzer and N. Kockmann, *Org. Process Res. Dev.*, 2008, **12**, 905-910.
173. A. Borodziński and G. C. Bond, *Catal. Rev.*, 2006, **48**, 91-144.
174. M. C. Bryan, Z. Fei, K. Fraunhoffer, J. Hayler, M. Hickey, S. Hughes, L. Humphreys, P. Richardson, M. Schober, A. Steven, T. White, S. Wuyts and Y. Jingjun, *Org. Process Res. Dev.*, 2017, **21**, 153-164.
175. R. Porta, M. Benaglia and A. Puglisi, *Org. Process Res. Dev.*, 2016, **20**, 2-25.
176. S. Chakraborty and K. Pulindindi, *Synthetic & Bio-based Aniline Market Size by Process (Reduction, Substitution), By Product (Synthetic, Bio-Based) By Application (MDI, Rubber Processing Chemicals, Agrochemicals, Dyes and Pigments) By End-User (Construction, Rubber Products, Transportation, Consume Goods, Adhesives and Sealants, Packaging Industry, textile, Agriculture) Industry Analysis Report, Regional Outlook, Growth Potential, Price trends, Competitive Market Share & Forecast 2017-2024*, Global Market Insights, GMIInsights, 2017.
177. M. Turáková, M. Králik, P. Lehoc'ý, L. u. Pikna, M. Smrcová, D. Remeteiová and A. Hudák, *Appl. Catal.: A*, 2014, **476**, 103-112.
178. M. Audemar, Y. Wang, D. Zhao, S. Royer, F. Jerome, C. Len and K. D. O. Vigier, *Energies*, 2020, **13**, 1002-1011.
179. H. G. Manyar, C. Hardacre, D. J. Cole-Hamilton and J. Coetzee, *ChemCatChem*, 2013, **5**, 2843-2847.
180. R. A. Sheldon, *Green Chem.*, 2017, **19**, 18-43.
181. F. Fanelli, G. Parisi, L. Degennaro and R. Luisi, *13*, 2017, 520-542.
182. E. Comer and M. G. Organ, *J. Am. Chem. Soc.*, 2005, **127**, 8160-8167.
183. A. Tanimu, S. Jaenicke and K. Alhooshani, *Chem. Eng. J.*, 2017, **327**, 792-921.
184. A. Adamo, R. L. Beingessner, M. Behnam, J. Chen, T. F. Jamison, K. F. Jensen, J.-C. M. Monbaliu, A. S. Myerson, E. M. Revalor, D. R. Snead, T. Stelzer, N. Weeranoppanant, S. Y. Wong and P. Zhang, *Science*, 2016, **352**, 61-67.
185. N. Kockmann, M. Gottsponer, B. Zimmermann and D. M. Roberge, *Chem. Eur. J.*, 2008, **14**, 7470-7477.
186. N. Cherkasova, M. m. Al-Rawashdehb, A. O. Ibadon and E. V. Rebrov, *Catal. today*, 2016, **273**, 205-212.

187. J. Li, F. Wu, L. Lin, Y. Guo, H. Liu and X. Zhang, *Chem. Eng. J.*, 2018, **333**, 146-152.
188. E. V. Rebrov, A. Berenguer-Murcia, H. E. Skelton, B. F. G. Johnson, A. E. H. Wheatley and J. C. Schouten, *Lab Chip*, 2009, **9**, 503-506.
189. E. V. Rebrov, E. A. Klinger, A. Berenguer-Murcia, E. M. Sulman and J. C. Schouten, *Org. Process Res. Dev.*, 2009, **13**, 991-998.
190. N. Cherkasov, Y. Bai and E. Rebrov, *Catalysts*, 2017, **7**, 358-373.
191. K. K. Yeong, A. Gavriilidis, R. Zapf and V. Hessel, *Chem. Eng. Sci.*, 2004, **59**, 3491-3494.
192. K. K. Yeong, A. Gavriilidis, R. Zapf and V. Hessel, *Catal. Today*, 2003, **81**, 641-651.
193. R. D. Chambers, M. A. Fox, D. Holling, T. Nakano, T. Okazoe and G. Sandford, *Lab on a Chip*, 2005, **5**, 191-198.
194. S. Jang, B.-J. Jung, M.-J. Kim, W. Lee and D.-P. Kim, *React. Chem. Eng.*, 2019, **4**, 1752-1756.
195. X. Zhu, H. Feng, R. Chen, Q. Liao, D. Ye, B. Zhang, J. Liu, M. Liu and G. Chen, *RSC Adv.*, 2018, **8**, 5661-5669.
196. G. Chen, X. Zhu, Q. Liao, R. Chen, D. Ye, M. Liu and K. Wang, *Chem. Eng. Sci.*, 2021, **229**, 116004-116013.
197. C. S. Couto, L. M. Madiera, C. P. Nunes and P. Araújo, *Ind. Eng. Chem. Res.*, 2017, **56**, 3231-3242.
198. D. Li, P. Ashikari, J.-A. Shin, J.-H. Lee, Y.-J. Kim, X.-M. Zhu, J.-N. Hu, J. Jin, C. C. Akoh and K.-T. Lee, *LWT - Food Sci. Technol.*, 2010, **43**, 458-464.
199. E. Fernandez-Puertas, A. J. Robinson, H. Robinson, S. Sathiyalingam, H. Stubbs and L. J. Edwards, *Org. Process Res. Dev.*, 2020, **24**, 2147-2156.
200. J. Yue, *Catal. Today*, 2017, **41**, 1-16.
201. J. Yue, *Catal. Today*, 2018, **308**, 3-19.
202. A. Tanimu, S. Jaenicke and K. Alhooshani, *Chem. Eng. J.*, 2017, **327**, 792-821.
203. R. Dinnebier, *Principles of Powder Diffraction*, Max Plank Institute for Solid State Research, 2014.
204. A. Khorsand Zak, W. H. Abd. Majid, M. E. Abrishami and R. Yousefi, *Solid State Sci.*, 2010, **13**, 251-256.
205. R. C. Reynolds, *Rev. Mineral.*, 1989, **20**, 1-17.
206. D. L. Bish and J. E. Post, *Rev. Mineral.*, 1989, **20**, 17-20.
207. W. Friedrich and P. Knipping, *Sitz. ber. Bayer. Akad. Wiss.*, 1912, 311-322.
208. M. von Laue, presented in part at the Nobel Lecture, 1920.
209. M. Eckert, *Ann. Phys.*, 2012, **524**, A83-A85.
210. N. S. Goncalves, J. A. Carvalho, Z. M. Lima and J. M. Sasaki, *Mat. Lett.*, 2012, **72**, 36-38.
211. N. S. Ramgir, Y. K. Hwang, I. S. Mulla and J. Chang, *Solid State Sci.*, 2006, **8**, 359-362.
212. P. Scherrer and R. Zsigmondy, *Kolloidchemie*, 3rd edn. edn., 1920.
213. P. A. L., *Phys. Rev.*, 1939, **56**, 978-982.
214. M. Adhikari, A. Singh, E. Echeverria, D. N. McIlroy and Y. Vasquez, *ACS Omega*, 2020, **5**, 14104-14110.
215. I. Mukhtar, S. Ali, S. Jamil, S. urRehman and S. R. Khan, *Chem. Phys. Lett.*, 2020, **754**, 137649-137658.
216. Y. Liu, Y. Li, J. A. Anderson, J. Feng, A. Guerrero-Ruiz, I. Rodriguez-Ramos, A. J. McCue and D. Li, *J. Catal.*, 2020, **383**, 51-59.
217. C. Maheu, E. Puzenat, C. Geantet, L. Cardenas and P. Afanasiev, *Int. J. Hydrog. Energy*, 2019, **44**, 18038-18049.
218. I. n. Sorribes, L. Liu and A. Corma, *ACS Catal.*, 2017, **7**, 2698-2708.
219. F. Cao, R. Liu, L. Zhou, S. Y. Song, Y. Lei, W. Shi, F. Zhao and H. Zhang, *J. Mater. Chem.*, 2010, **20**, 1078-1085.
220. H. T. E. Jr., *Science*, 1970, **167**, 621-623.
221. Y. Takeuchi and W. Nowacki, *Schweiz. Mineral. Petrogr. Mitt.*, 1964, **44**, 105-120.
222. K. Momma and F. Izumi, *J. Appl. Crystallogr.*, 2011, **44**, 1272-1276.

223. S. Finklea, L. Cathey and E. L. Amma, *Acta Crystall. A-Cryst*, 1976, **32**, 529-537.
224. T. Li, Z. Guo, L. X., Z. Wu, K. Zhang, H. Liu, H. Sun, Y. Liu and H. Zhang, *RSC Adv.*, 2015, **5**, 98967-98970.
225. G. Li, B. Zhang, F. Yu, A. A. Novakova, M. S. Krivenkov, T. Y. Kiseleva, L. Chang, J. Rao, A. O. Polyakov, G. R. Blake, R. A. de Groot and T. T. M. Palstra, *J. Mater. Chem.*, 2014, **26**, 5821-5829.
226. D. Rickard and G. W. Luther, *Chem. Rev.*, 2007, **107**, 514-562.
227. H. E. King and C. T. Prewitt, *Acta Crystallogr. B*, 1982, **38**, 1877-1887.
228. R. Sun, M. K. Y. Chan and G. Ceder, *Phys. Rev.*, 2011, **83**, 235311-235311-235312.
229. G. Brostigen and A. Kjekshus, *Acta Chim. Scand.*, 1970, **25**, 1925-1940.
230. M. J. Buerger, *Z Kristallogr Krist*, 1937, **97**, 504-513.
231. J. Li, J. Zhu and X. Liu, *Dalton Trans.*, 2014, **43**, 132-137.
232. R. V. Jagadeesh, K. Natte, H. Junge and M. Beller, *ACS Catal.*, 2015, **5**, 1526-1529.
233. S. Phimsen, W. Kiatkittipong, H. Yamada, T. Tagawa, K. Kiatkittipong, N. Laosiripojana and S. Assabuumrungrat, *Energ. Convers. Manage.*, 2017, **151**, 324-333.
234. P. George and P. Chowdhury, *Analyst*, 2019, **144**, 3005-3012.
235. Q. Xiao, S. Sarina, E. R. Waclawik, J. F. Jia, J. Chang, J. D. Riches, H. S. Wu, Z. F. Zheng and H. Y. Zhu, *ACS Catal.*, 2016, **6**, 1744-1753.
236. E. Nowack, D. Schwarzenbach and T. Hahn, *Acta Crystallogr. B.*, 1991, **47**, 650-659.
237. S. Ogawa, *J. Appl. Phys.*, 1979, **50**, 2308-2311.
238. Y. M. Mos, A. C. Vermeulen, C. J. N. Buisman and J. Weijma, *Geomicrobiol. J.*, 2018, **35**, 511-517.
239. T. K. Chattopadhyay, H. G. von Schnering, R. F. D. Stansfield and G. J. McIntyre, *Z. Kristallogr.*, 1992, **199**, 13-24.
240. A. Kjekshus and T. Rakke, *Acta Chem. Scand.*, 1979, **A33**, 617-620.
241. G. Varga, A. S ápi, T. Varga, K. Ba án, I. Szent, G. Halasi, R. Mucsi, L. Óv ári, J. Kiss, Z. Fogarassy, B. P écz, Á. Kukovecz and Z. K ónya, *J. Catal.*, 2020, **386**, 70-80.
242. H. E. King and C. T. Prewitt, *Am. Mineral.*, 1979, **64**, 1265-1271.
243. B. Wang, W. An, L. Liu, W. Chen, Y. Liang and W. Cui, *RSC Adv.*, 2015, **5**, 3224-3231.
244. M. J. Buerger and B. J. Wuensch, *Science*, 1963, **141**, 276-277.
245. Y. Tak éuchi, Y. Kudoh and G. Sato, *Z. Krist.-Cryst. Mater.*, 1985, **173**, 119-128.
246. K. Koto and N. Morimoto, *Acta Cryst.*, 1970, **26**, 915-924.
247. L. M. Corliss, N. Elliott and J. Hastings, *Phys. Rev.*, 1956, **104**, 924-928.
248. H. Ott, *Z. Krystallog.*, 1926, **63**, 222-230.
249. I. Temprano, T. Liu and S. J. Jenkins, *Catal. Today*, 2017, **286**, 101-113.
250. A. Furst, R. C. Berlo and S. Hooton, *Chem. Rev.*, 1965, **65**, 51-68.
251. H. W. Lucien, *J. Chem. Eng. Data*, 1961, **6**, 584-586.
252. X. Jia, I. K. M. Yu, D. C. W. Tsang and A. C. K. Yip, *Micropor. Mesopor. Mat.*, 2019, **284**, 43-52.
253. S. K. Johnston, T. A. Bryant, J. Strong, L. Lazzarini, A. O. Ibhadon and M. G. Francesconi, *ChemCatChem*, 2019, **11**, 2909-2918.
254. S. K. Johnston, N. Cherkasov, E. Pérez-Barrado, A. Aho, D. Y. Murzin, A. O. Ibhadon and M. G. Francesconi, *Appl. Catal. A*, 2017, **544**, 40-45.
255. D. E. Stewart, B. H. Sage and W. N. Lacey, *Ind. Eng. Chem.*, 1954, **46**, 2529-2531.
256. S. Cimino, L. Lisi and S. Romanucci, *Catal. Today*, 2018, **304**, 58-63.
257. C. Zhang, H. Chen, S. Pang, C. Su, M. Lv, K. Wang, D. Cai and P. Qin, *Renew. Energy*, 2020, **146**, 1444-1450.
258. F. Xu, J. Sun, N. V. S. N. M. Konda, J. Shi, T. Dutta, C. D. Scown, B. A. Simmons and S. Singh, *Energy Environ. Sci.*, 2016, **9**, 1042-1049.
259. B. Ndaba, I. Chiyanzu and S. Marx, *Biotechnol. Rep.*, 2015, **8**, 1-9.
260. B. Kolesinska, J. Fraczyk, M. Binczarski, M. Modelska, J. Berłowska, P. Dziugan, H. Antolak, Z. J. Kaminski, I. A. Witonska and D. Kregiel, *Materials*, 2019, **12**, 350-371.

261. J. Li, Y. Du, T. Bao, J. Dong, M. Lin, H. Shim and S. Yang, *Bioresource Technol.*, 2019, **289**, 121749-121756.
262. S. Atsumi and J. C. Liao, *Appl. Environ. Microbiol.*, 2008, **74**, 7802-7808.
263. K. H. Lee, B. Lee, K. R. Lee, M. H. Yi and N. H. Hur, *Chem. Commun.*, 2012, **48**, 4414-4416.
264. Z. Hu, S. Tan, R. Mi, X. Li, D. Li and B. Yang, *Catal. Lett.*, 2018, **148**, 1490-1498.
265. J. B. Santos, G. P. Valenca and J. A. J. Rodrigues, *J. Catal.*, 2002, **210**, 1-6.
266. M. E. Castillo, T. A. Gad-Allah, M. E. M. Ali, A. H. Salem, A. S. G. Khalil, M. G. Francesconi and D. C. Lupascu, *Proceedings of the 4th World Congress on New Technologies*, 2018, **1**, 1-6.
267. C. Deraedt, R. Ye, W. T. Ralston, F. D. Toste and G. A. Somorjai, *J. Am. Chem. Soc.*, 2017, **139**, 18084-18092.
268. P. D. Cara, R. Crirminna, N. R. Shiju, G. Rothenberg and M. Pagliaro, *ChemSusChem*, 2014, **7**, 835-840.
269. G. W. Luther, *Geochim. Cosmochim. Ac.*, 1991, **55**, 2839-2849.
270. R. L. Blake, R. E. Hessevick, T. Zoltai and L. W. Finger, *Amer. Miner.*, 1966, **51**, 123-129.
271. R. W. G. Wyckoff and E. D. Crittenden, *Z. Kristallogr. Cryst. Mater.*, 1926, **63**, 144-147.
272. H. Christensen and A. N. Christensen, *Acta Chem. Scand.*, 1978, **32**, 87-88.
273. T. Fujii, K. Tanaka, F. Marumo and Y. Noda, *Miner. Journ.*, 1987, **13**, 448-454.
274. I. Suzuki, L. Gura and A. Klein, *Phys. Chem. Chem. Phys.*, 2019, **21**, 6238-6246.
275. B. Sasi and K. G. Gopchandran, *Nanotechnology*, 2007, **18**, 115613-115620.
276. W. M. Schubert, J. M. Craven and H. Steadly, *J. Am. Chem. Soc.*, 1959, **81**, 2695-2698.
277. V. Arjunan, A. Raj, S. Sakiladevi, K. Carthigayan and S. Mohan, *J. Mol. Struct.*, 2012, **1007**, 122-135.
278. R. J. Ouellette, *Organic Chemistry - Structure, Mechanism, Synthesis*, Academic Press, 2018.
279. R. H. Petrucci, *General Chemistry: Principles and Modern Applications*, Pearson Education Inc., New Jersey, 9th edn., 2007.
280. L. Zhang, M. Zhou, A. Wang and T. Zhang, *Chem. Rev.*, 2020, **120**, 683-733.
281. S. Sharma, D. Bhattacharjee and P. Das, *Adv. Synth. Catal.*, 2018, **360**, 2131-2137.
282. W. M. N. Ratnayake, J. S. Grosserf and R. G. Ackman, *J. Am. Oil Chem. Soc.*, 1990, **67**, 940-946.
283. J. Wang, Z. Ge, L. Pei, P. Kong, R. Wang, P. Zhu, M. Liu, X. Gu and Z. Zheng, *Catal. Sci. Technol.*, 2019, **9**, 6681-6690.
284. S. Tagliapietra, L. Orio, G. Palmisano, A. Penoni and G. Cravotto, *Chem. Pap.*, 2015, **69**, 1519-1531.
285. D. Tavor, I. Gefen, C. Dlugy and A. Wolfson, *Synth. Commun.*, 2011, **41**, 3409-3416.
286. J. Wang, Z. Ge, L. Pei, P. Kong, R. Wang, P. Zhu, M. Liu, X. Gu and Z. Zheng, *Catal. Sci. Technol.*, 2019, **9**, 6681-6690.

Project Outputs

Research Articles

Ultra-small FeS₂ nanoparticles for highly efficient chemoselective transfer hydrogenation of nitroarenes, **J. P. Southouse**, L. Lazzarini, A. O. Ibadon, M. G. Francesconi, New Journal of Chemistry, 2021

Oral Presentations

A SUSTAINABLE HETEROHGENEOUS CATALYTIC SYSTEM FOR THE HIGHLY SELECTIVE HYDROGENATION OF NITROARENE DERIVATIVES, **J. P. Southouse**, M. G. Francesconi and A. O. Ibadon, Mercia Group AGM, Wolverhampton, UK, 2019

NON-NOBLE METAL HETEROGENEOUS CATALYSTS FOR SUSTAINABLE FINE CHEMICAL SYNTHESIS, **J. P. Southouse**, A. O. Ibadon and M. G. Francesconi, Intermetallic Compounds in Catalysis (IMCAT) International Symposium, Chemnitz, Germany, 2019

FeS₂ AS AN HETEROGENEOUS CATALYST FOR SUSTAINABLE FINE CHEMICAL SYNTHESIS, **J. P. Southouse**, A. O. Ibadon and M. G. Francesconi, RSC Dalton Northern Group AGM, York, UK, 2019

Poster Presentations

Pd-based Catalysts for the Semi-Hydrogenation of 2-Methyl-3-Butyne-2-ol (MBY), S. K. Johnston, **J. P. Southouse**, T. A. Bryant, E. Pérez-Barrado, J. Strong, N. Cherkasov, L. Lazzarini, A. Aho, D. Y. Murzin, M. G. Francesconi and A. O. Ibadon, Intermetallic Compounds in Catalysis (IMCAT) International Symposium, Chemnitz, Germany, 2019

NON-NOBLE METAL HETEROGENEOUS CATALYSTS FOR SUSTAINABLE FINE CHEMICAL SYNTHESIS, **J. P. Southouse**, A. O. Ibadon and M. G. Francesconi, Solid-State Chemistry Group Christmas General Meeting, London, UK, 2018

NON-NOBLE METAL HETEROGENEOUS CATALYSTS FOR THE SELECTIVE HYDROGENATION OF NITROARENES TO ANILINES, **J. P. Southouse**, A. O. Ibadon and M. G. Francesconi, RSC Dalton Northern Group AGM, Leeds, UK, 2018

NON-NOBLE METAL SULFIDES AS HETEROGENEOUS CATALYSTS FOR THE SELECTIVE HYDROGENATION OF NITROARENES TO ANILINES, **J. P. Southouse**, M. G. Francesconi and A. O. Ibadon, Mercia Group AGM, Keele, UK, 2017